University of Sheffield

Fault Modelling and Analysis of Permanent Magnet Machines for Offshore Wind Power Application

Zeting Mei

A thesis submitted in partial fulfilment of the requirements

for the degree of Doctor of Philosophy

Department of Electronic and Electrical Engineering

The University of Sheffield, UK

April 2023

ABSTRACT

Wind energy, as one of the most promising renewable energy sources, has been well developed in the past 30 years. However, the improvement in reliability and availability of wind turbine systems is still an important topic to both academia and industry due to the high operation and maintenance cost. As two of the key components of a wind turbine system, the wind generator and gearbox, have the longest downtime although they are less prone to failure than the power converters and their associated control units. Therefore, it is necessary to study the faults of wind generators and try to reduce their downtime by detecting their faults at an early stage and then implementing effective maintenance.

Among all the faults of these wind generators, the winding fault, as the second most frequent fault, has attracted significant interest. It has been reported by the Electrical Apparatus Service Association (EASA) that there are five major winding faults, namely (1) inter-turn (turn-to-turn) short circuit (ITSC), (2) coil-to-coil short circuit, (3) open circuit of one phase, (4) phase-to-phase short circuit, and (5) coil-to-ground short circuit. Amongst all the faults, the ITSC fault, often regarded as one of the root causes of other winding faults, has attracted increasing attention from researchers over the last few years. This thesis will mainly focus on modelling and analysis of permanent magnet machines under ITSC fault for wind power application.

Firstly, a general analytical fault model of permanent magnet (PM) machines with series-connected coils has been developed to extend the fault analysis to surface-mounted permanent magnet (SPM) machines with any power rating. Two modelling approaches have been used: analytical and numerical FE methods. It is found that the determination of inductances in the fault model is the key to ensure a good accuracy of the proposed fault model. Subsequently, finite element (FE) and Matlab/Simulink simulations of a 96-slot 32-pole SPM machine have been done to validate the proposed fault model. Fault performance comparisons of SPM machines with different power ratings have been carried out to see their difference in the fault-tolerant ability. Finally, a small scale 12-slot 4-pole SPM machine prototype has been built and the proposed fault model is further validated by a series of experiments on the 12-slot 4-pole machine prototype.

Then, a relatively simple general analytical model in a compact matrix form for SPM wind generators with parallel-connected coils under ITSC fault is developed. To simplify the fault model with analytical inductances, the multiphase Clarke transformation has been proposed. Such model simplification method may be extended to other types of electrical machines with similar winding configurations, no matter how many phases the machines have. FE and Matlab/Simulink simulations of a 96-slot 32-pole SPM machine with parallel-connected windings have been done to validate the proposed fault model. The analytical model developed can be very useful for model-based fault detection and mitigation for large wind power generators, for which the FE or magnetic equivalent circuit modelling can be very

time-consuming due to large number of slots and poles. Finally, the accuracy of the proposed fault model is further validated on the small-scale 12-slot 4-pole SPM machine prototype when its winding connections are changed from series to parallel.

To see whether the multiphase Clarke transformation can be used to simplify the fault model with analytical inductances for series-parallel connected coils, further studies have been carried out. The proposed fault models of a 3kW 96-slot 32-pole SPM machine with different series-parallel coil connections have been built in Matlab/Simulink and validated by time-stepping 2D FE simulations. Simulation results show that different series-parallel coil connections have little influence on the amplitude of the ITSC current. Finally, a small-scale 24-slot 8-pole SPM machine prototype has been built to further validate the accuracy of the proposed fault model.

When the fault model with analytical inductances is extended to analyse the performance of large-power SPM wind generators, it is found that some relative errors between analytical and FE linear inductances having large values in the fault model are large, which makes the accuracy of the fault model with analytical inductances questionable. However, it is found that the multiphase Clarke transformation can be used to simplify the proposed fault model with FE linear or nonlinear inductances. Thus the accuracy of fault model with analytical inductances can be easily validated by the fault model with FE linear inductances. If more accurate predictions are required, nonlinear FE inductances can be used in the simplified fault model. In addition, studies of scaling effect and influence of fault location considering series-parallel coil connections of PM machines with different power ratings (3kW, 500kW, 3MW) have been carried out. Simulation results show that large-power SPM wind generators are vulnerable to ITSC faults when relatively small number of turns are short-circuited and the single turn short-circuit fault at the top of the slot is the worst case.

Based on the proposed fault model and model simplification method, fault performance comparisons of SPM machines with overlapping and modular windings have been carried out. A number of Matlab/Simuink and FE simulations on a 96-slot 32-pole SPM machine have been carried out. Simulation results show that the healthy machine performances for a SPM machine with overlapping or modular windings are the same, but their fault performances are very much different. For example, for overlapping windings, the same fault in different phases will lead to different variations in branch currents. In addition, compared with the modular windings, the same fault in the overlapping windings will lead to greater imbalance in branch currents. Thus, compared with the overlapping windings, the modular windings generally are more fault-tolerant. However, these differences in the large-power SPM machines are negligible because ITSC faults will cause very little imbalance in branch currents for large-power SPM machines.

ACKNOWLEDGEMENTS

During the completion of this PhD thesis, I would like to express my sincere gratitude to my supervisor, Prof. Guang-jin Li, for his invaluable guidance, and daily encouragement throughout this PhD project. Without him, the finish of paper and thesis writing would be impossible. I am also very grateful to Prof. Z.Q. Zhu and the engineers from Siemens Gamesa for offering me the opportunity to work with them and keeping funding me in the past four years, otherwise the fruits of my research would not be so enjoyable.

I would also like to acknowledge the PhD students and technicians in the Electrical Machines and Drives Research Group in our electronic and electrical engineering department. Many of them helped me with their professional knowledge and warm personalities during the FE modelling and experiments. They are Dileep, Rajesh, Alex, Liren Huang, Wei Zhang, Guangbo Zhang, Thomas J. Templeman, and Clive Thompson, to just name a few. Without them, the life during the PhD study would be not so colourful.

Finally, I would like to show my deepest appreciation for the understanding and support of my parents, who are kind peasants, knowing nothing of what I am doing. Their continuous love and support nurtured a man what he is becoming now.

NOMENCLATURES

Abbreviation	
2D	Two dimensional
3D	Three dimensional
AC	Alternating current
DC	Direct current
EMF	Electromotive force
FEM	Finite element method
ITSC	Inter-turn short-circuit
MEC	Magnetic equivalent circuit
PM	Permanent magnet
SPM	Surface-mounted permanent magnet
SPP	Slot/pole/phase
WFA	Winding function approach

Variables	
r_e	Mean air-gap radius
g_e	Effective air-gap length
l_e	Effective stack length
n_c	The number of turns per coil
n_f	The number of short-circuited turns in one coil
p	The number of pole pairs

CONTENTS

Chapter 1 Introduction

This PhD research topic "fault modelling and analysis of permanent magnet machines for offshore wind power applications" is originated from the necessity of online fault detection and mitigation of wind power generators in offshore wind turbines (WTs) to reduce the operation and maintenance cost of wind turbine systems.

1.1 State-of-the-art of Wind Energy Conversion System (WECS)

Due to exhausting traditional fossil fuels such as petroleum, coal and natural gas, and environmental concerns about global warming, renewable energy sources have emerged as a promising alternative to meet the energy needs of our modern society. In recent years, electricity production from the hydro, solar, wind, geothermal, tidal, wave and biomass energy sources has come under increasing attention [1]. Amongst all these renewable energy sources, wind energy is becoming dominant. It has been reported that in 2021, approximately 93.6 GWs of new wind power was added, which brings the total installed wind capacity to 837GW [2]. In 2021, the world's top five markets of onshore wind installations were China, the USA, Brazil, Vietnam, and United Kingdom, making up 75.1% of the global installations. As for the world's top five markets of offshore wind installations, they were China, United Kingdom, Denmark, Vietnam, the Netherlands. These five markets combined made up 99.5% of new installations. These facts highlight that wind energy industry is an essential part of modern industries and it contributes much to the economic development in these countries. On the other hand, the scenarios of achieving net zero emission by 2050 are shown in Fig. 1.1, it can be seen that wind energy is not growing fast or widely enough to realise a secure and resilient global energy transition, thus there is still a huge demand in wind turbine installations.

With the wind power capacity becoming larger and larger, the size of a single commercial wind turbine is also bigger and bigger, as shown as Fig. 1.2. If these big wind turbines break down, wind energy production process will be stopped and maintenance of them is required, which often causes a big financial and time loss. It has been reported that the relatively high cost of operation and maintenance are estimated to be 10-15% of the total income for a wind farm. As for the offshore wind turbine, the costs are estimated to be 20-25% of the total income [3].Therefore, improving the reliability of a whole wind turbine system is becoming more and more important to keep the competitive advantages of power generation from the wind energy.

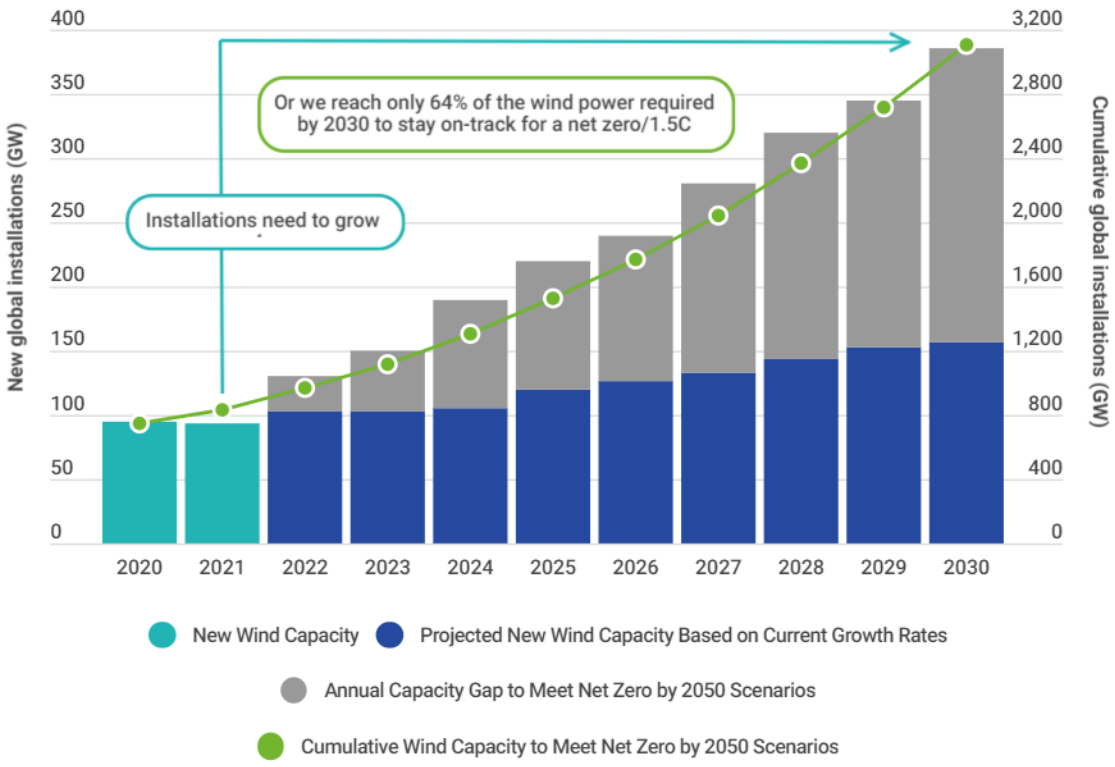

Fig. 1.1 Wind capacity to meet net zero by 2050 scenarios [2].

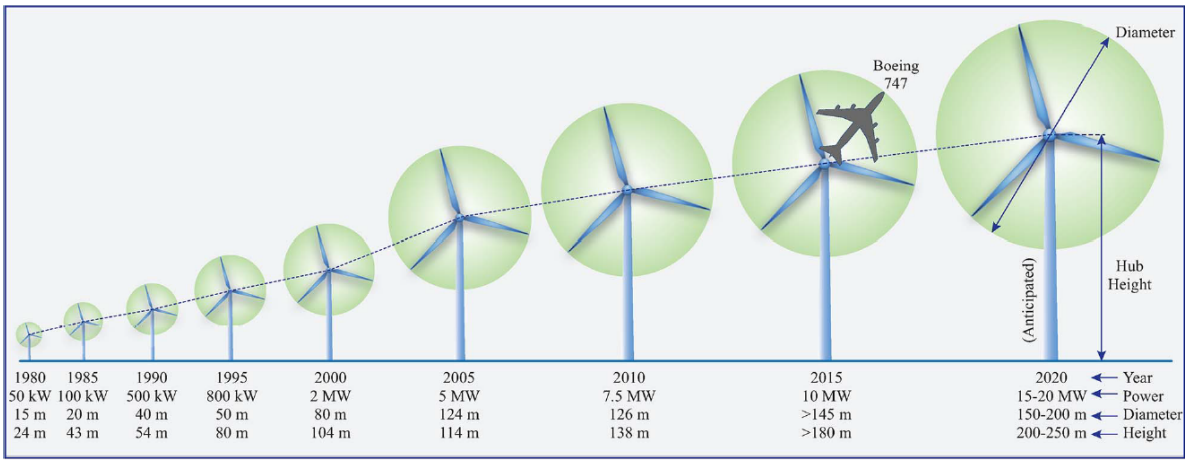

Fig. 1.2 Evolution in the size of commercial wind turbines [1].

The major components of a typical wind turbine system as shown in Fig. 1.3 are blades, gearbox (non-direct drive), generator, power converters and the associated microcontroller units. If these major components failed, they often incur costly and difficult maintenance work because it is often difficult to access the tower, the height of which often reaches hundreds of meters. For offshore wind turbine systems shown in Fig. 1.4, it is much more important to implement effective maintenance. This is because access to these offshore wind turbine systems is much more difficult than their onshore counterparts shown in Fig. 1.3. It has been

reported that maintenance technicians need to approach the tower by boat and then reach the nacelle by climbing the tower, or alternatively be landed directly onto the nacelle by a helicopter. The ability to carry out the related maintenance work will also be limited under extreme weather conditions [4].

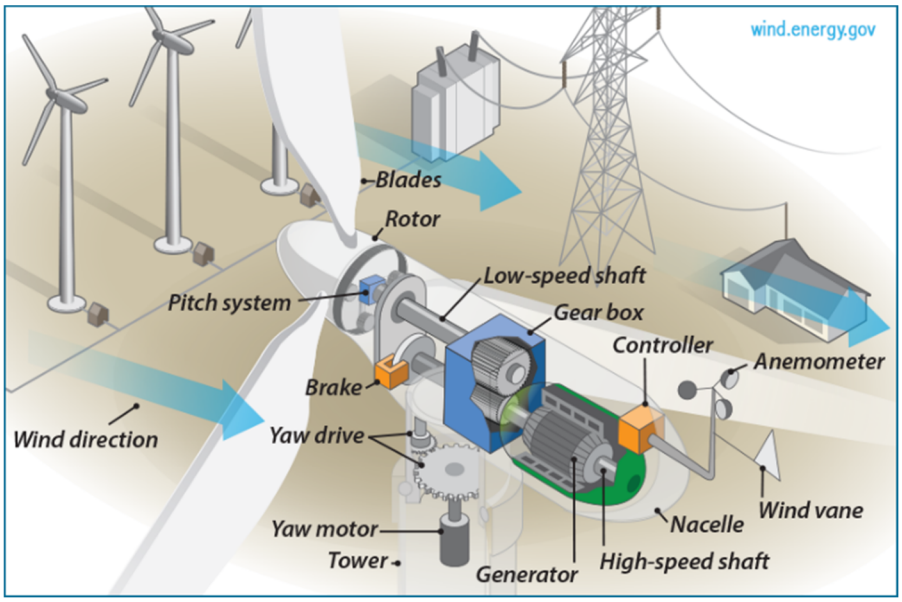

Fig. 1.3 A typical land-based wind turbine system [5].

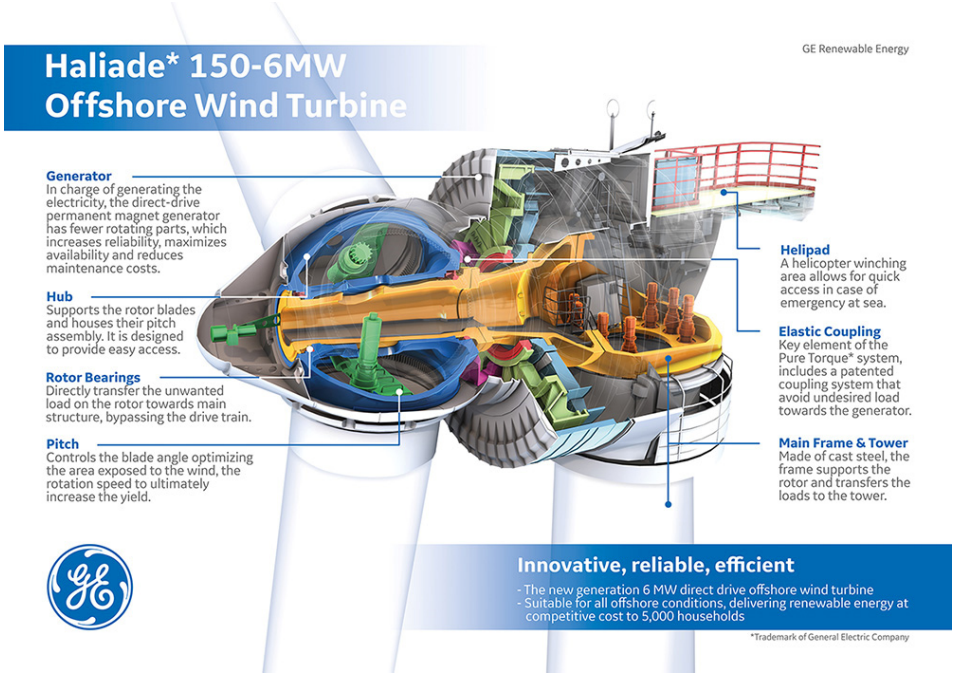

Fig. 1.4 Inside of an offshore wind turbine from GE renewable energy [6].

To sum up, there are three main reasons for performing condition monitoring, fault detection and diagnosis of an offshore wind turbine system:

- A wind turbine system has many components and each component would break down or have a failure at some point.
- It is much more difficult to access the faulty wind turbine to carry out the maintenance work compared to onshore wind turbine system. This is particularly the case during extreme weather conditions.
- Downtime of wind turbines will cause energy production loss, and operation and maintenance costs account for a large amount of their total income.

It should be noted that the study of reliability in wind turbine systems nowadays is moving from a statistically based approach that has been proven to be unsatisfactory in achieving higher safety levels to a physics based approach which involves the study of fault mechanisms that lead to failures of different components of the entire wind turbine [7]–[9].

In contrast with Fig. 1.3 and Fig. 1.4, the basic configurations of some existing WECS in Fig. 1.5 show how the electricity generated by the WECS are processed and transmitted to the grid. Nowadays there are five major types of WECSs, which could be summarized as follows [10]:

- **Type 1:** Fixed-speed WECS with squirrel cage induction generator (SCIG)
- **Type 2:** Semi-variable-speed WECS with wound rotor induction generator (WRIG)
- **Type 3:** Semi-variable-speed WECS with doubly fed induction generator (DFIG)
- **Type 4:** Full-variable-speed WECS with SCIG, permanent magnet synchronous generator (PMSG), wound rotor synchronous generator (WRSG), or high-temperature superconducting synchronous generator (HTS-SG)
- **Type 5:** Full-variable-speed WECS with WRSG and mechanical converter

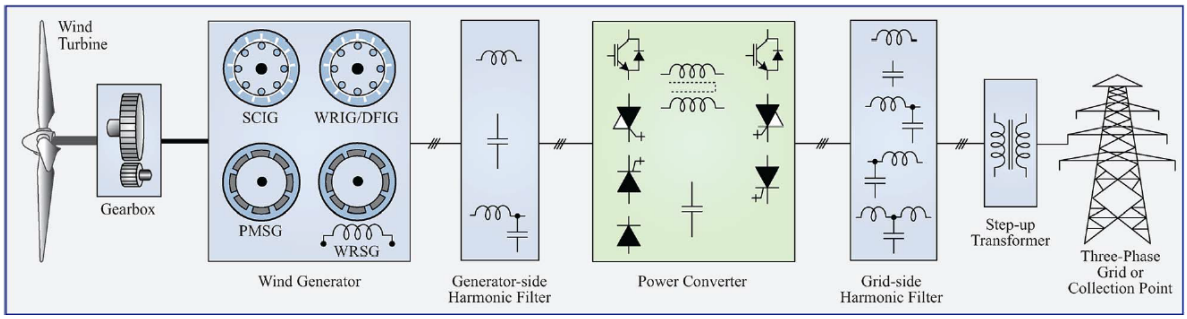

Fig. 1.5 Basic configuration of a grid-connected megawatt wind turbine [1].

1.2 Failure Distribution of a Wind Turbine System

To improve the reliability of wind turbine systems, major failures of wind turbine should be investigated first, and remedial strategies could be implemented subsequently. Fig. 1.6 shows a typical configuration of a grid-connected megawatt wind turbine. In this wind turbine system, turbine, gearbox, generator, power converter, and the associated control units are major

components. Fig. 1.7 shows the annual failure rate and down time of a wind turbine system corresponding to Fig. 1.6.

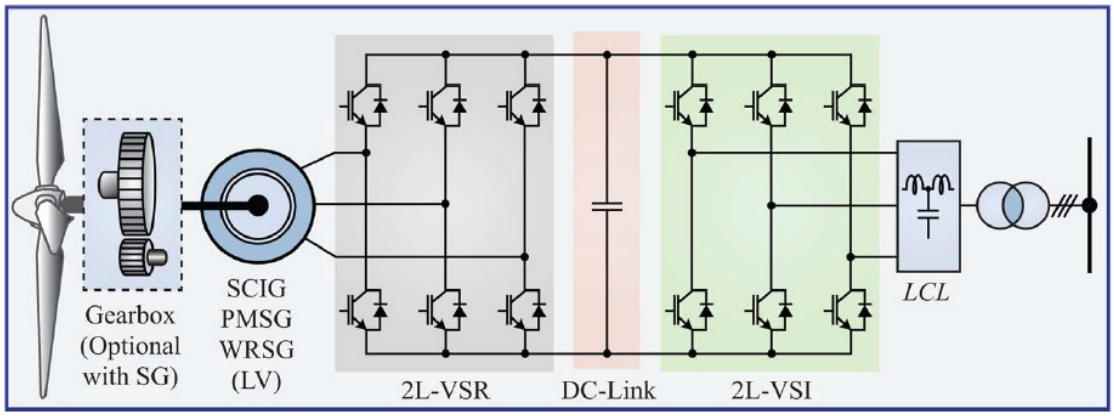

Fig. 1.6 Two-level BTB voltage source converters [1]. (Mainstream commercial power converter configuration).

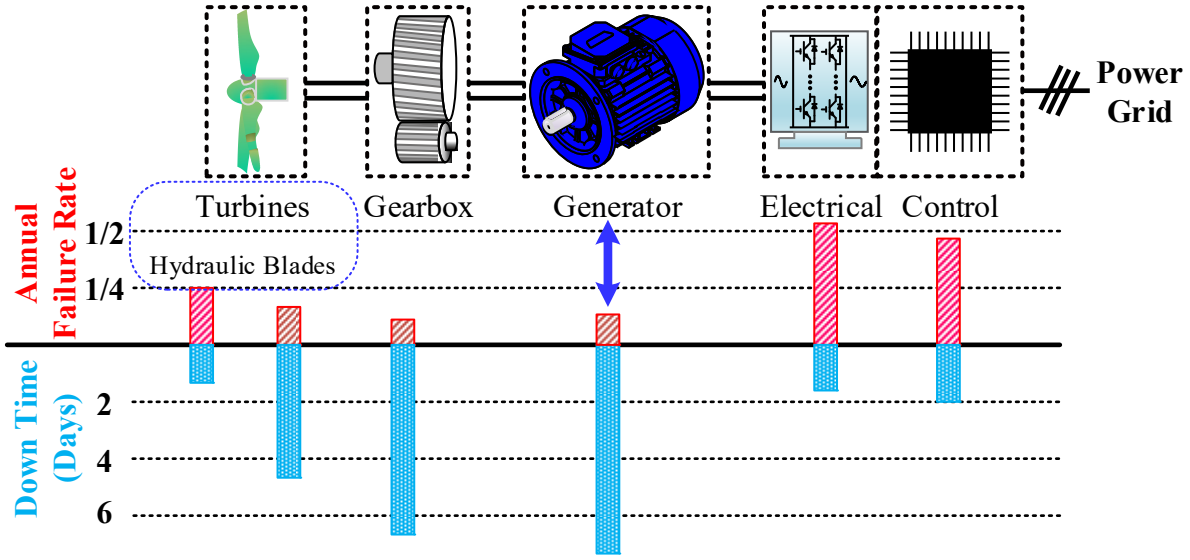

Fig. 1.7 Wind turbine overview in respect to reliability [7].

Some conclusions can be made from Fig. 1.7:

- The power electronic converters and control units have the highest and second highest annual failure rates, but the downtime of power electronic converters is the lowest.
- Although the annual failure rate of generators is around 12.5% (lowest), the downtime is the longest, up to 7 days.

Therefore, it is necessary to study the faults of wind generators and try to reduce their downtime by detecting their faults at an early stage in order to optimize the maintenance schedule.

1.3 Failure Distribution and Mechanism in Electrical Machines

1.3.1 Failure Distribution

There have been many review papers [8], [9], [11]–[20] about failure distribution and fault diagnosis of electrical machines, some of which are amongst the most cited papers in journal database like IEEE Xplore and ScienceDirect. Up to now, most researchers have paid significant attention to induction machines (IMs), which are regarded as the main workhorses of the industry. This is why there were so many surveys about fault types and distribution of IMs.

In [21], statistical data about distribution of breakdown of failed components of IMs was shown as Fig. 1.8 (a), based on the petroleum and chemical industries. One conclusion was made that the fault distribution could be applied to most industrial applications where totally enclosed fan cooled (TEFC) motors are employed. After a slight modification of the distribution of failure of IMs in Fig. 1.8 (a), Fig. 1.8(b) could be obtained to get a general conclusion about the failure distribution of IMs. In 2014, ABB issued an electronic booklet "Motors don't just fail...do they? A guide to preventing failure", in which the failure distribution of IMs was given in Fig. 1.9 [22]. This report also reflects that fault diagnosis of electrical machines has attracted much more attention in industry.

According to the failure distribution shown above, the major faults of IMs can be broadly classified as following:

(1) bearing and gearbox failures [23]–[28];

(2) stator winding faults [29]–[34];

(3) broken rotor bar or cracked rotor end-rings [35]–[39];

(4) static and/or dynamic air-gap irregularities [40]–[43];

(5) short-circuited rotor field winding [44]–[47];

Of the above types of faults, (1) bearing, (2) stator or armature faults, (3) broken rotor bar and end ring faults of IMs, and (4) eccentricity-related faults, are the most prevalent ones and, thus, received special attention [11].

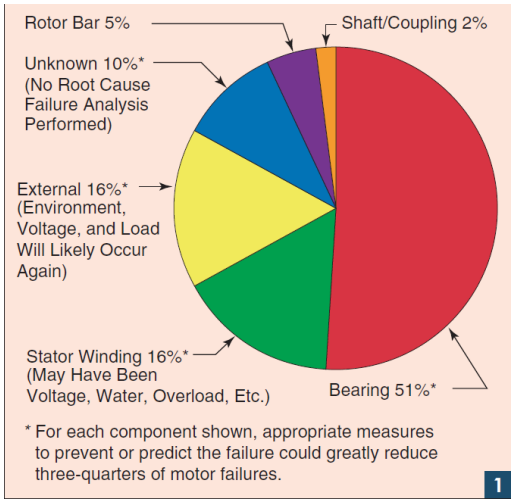

(a) Breakdown of failed components

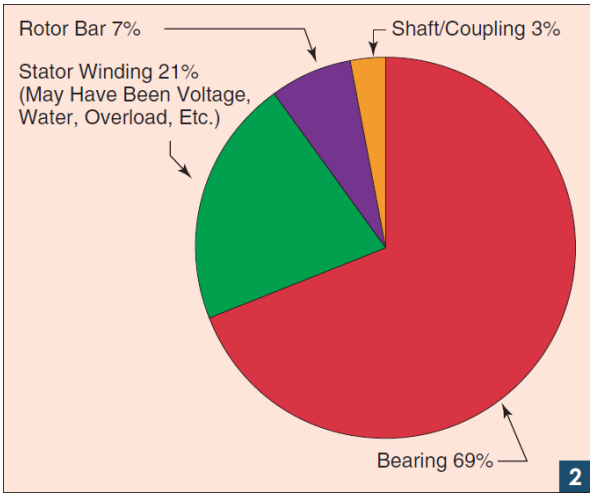

(b) Extrapolated distribution of failure by machine component

Fig. 1.8 Distribution of induction machine failures [21].

As for permanent magnet (PM) machines, it seems that no statistical data for their fault distribution has been published by industry. One reason is that nowadays IMs are still the main workhorses in industry due to their ruggedness and simple squirrel-cage construction although there is considerable progress made in PM machines. However, the fault types and distribution of PM machines could be inferred from the fault distribution of IMs, which is shown in Fig. 1.10. This is because the main components of PM machines are the same as those of IMs. Amongst all these faults, the stator winding faults [13], [48]–[53], the rotor demagnetization [54]–[61], and the static and/or dynamic air-gap irregularities [62]–[67] have been received more attention from both academia and industry.

As for the fault distribution of PM wind generators, it has been investigated by main wind turbine manufacturers and shown in Fig. 1.11. This survey was based on a sample of more than 1200 wind turbine generators repaired or replaced since 2005, which has revealed that fewer than half of the failures were electrical in nature and most of those were due to mechanical failures of the insulation support structure [68]. On the other hand, Fig. 1.12 shows a comparison between wind turbine failures and industrial machine failures, based on data compiled by Peter Tavner and his team at Durham University (Durham, UK) [68].

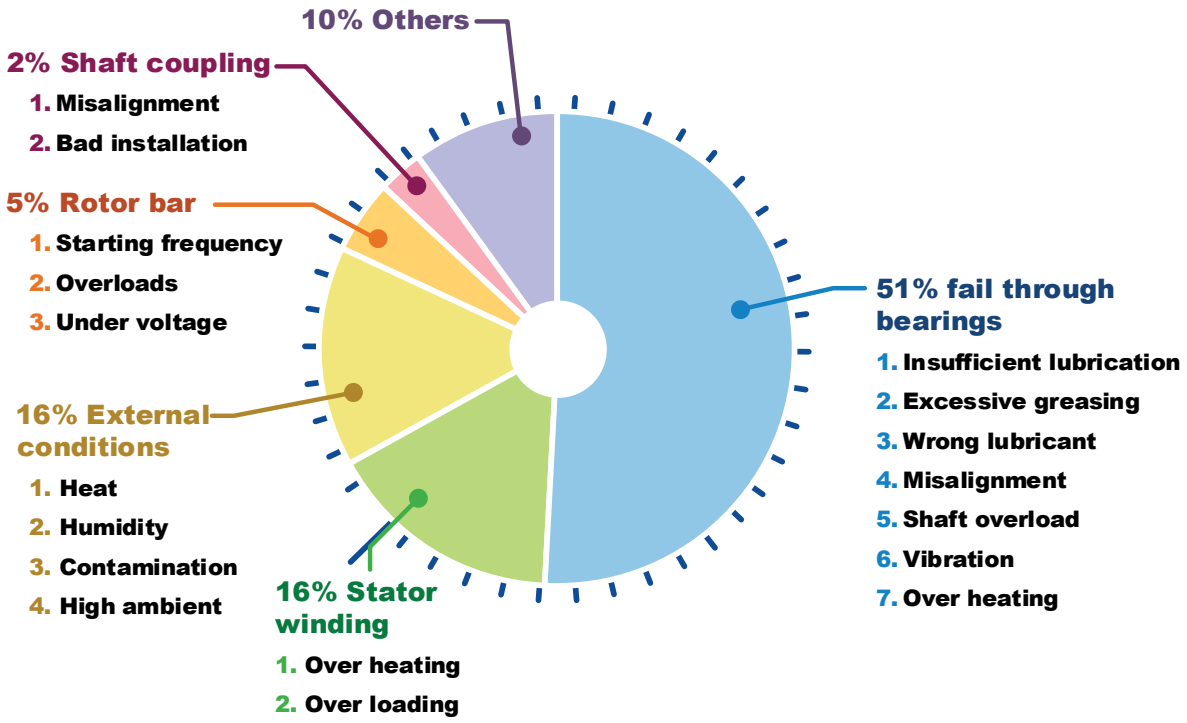

Fig. 1.9 Failure distribution of induction machines (IMs) [22].

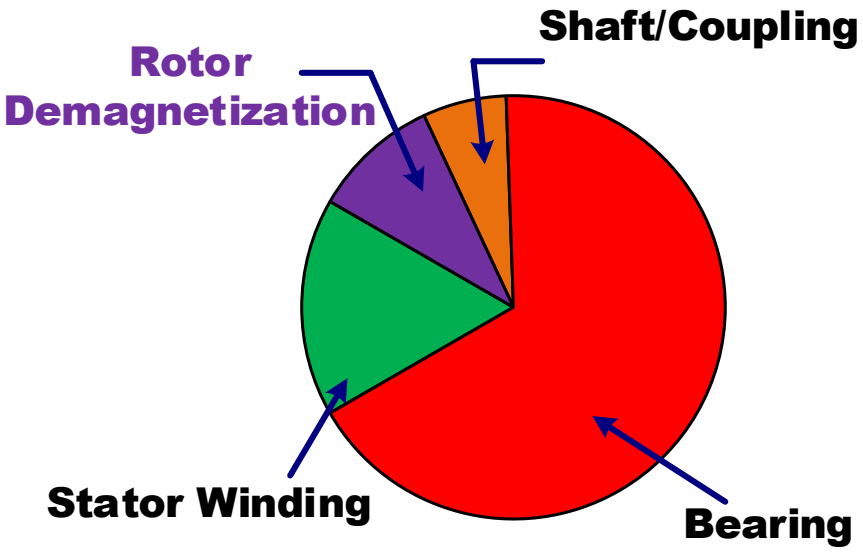

Fig. 1.10 Fault distribution of permanent magnet machines [21].

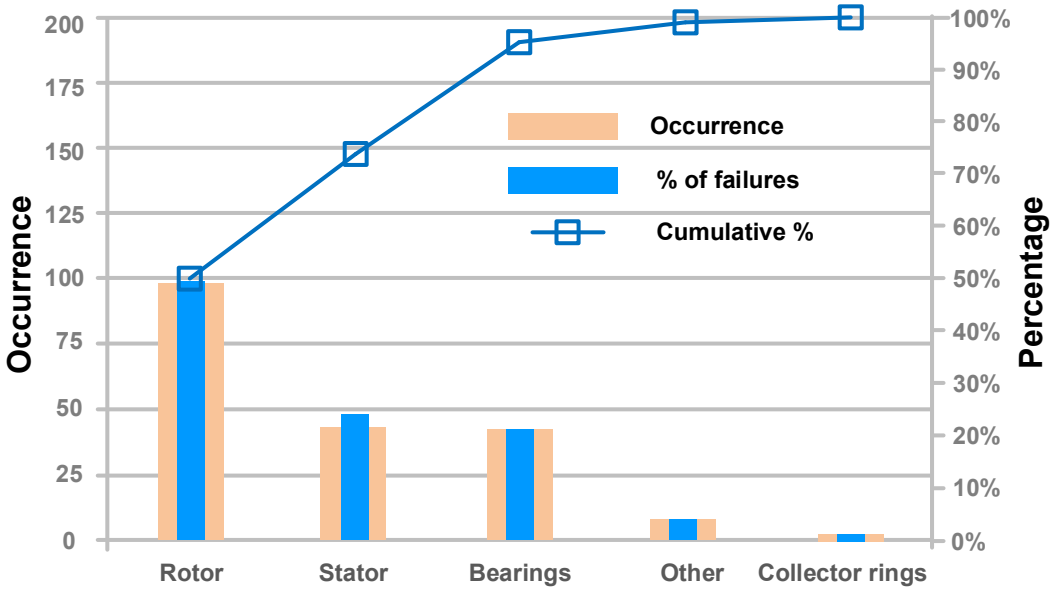

(a) Power rating <1 MW

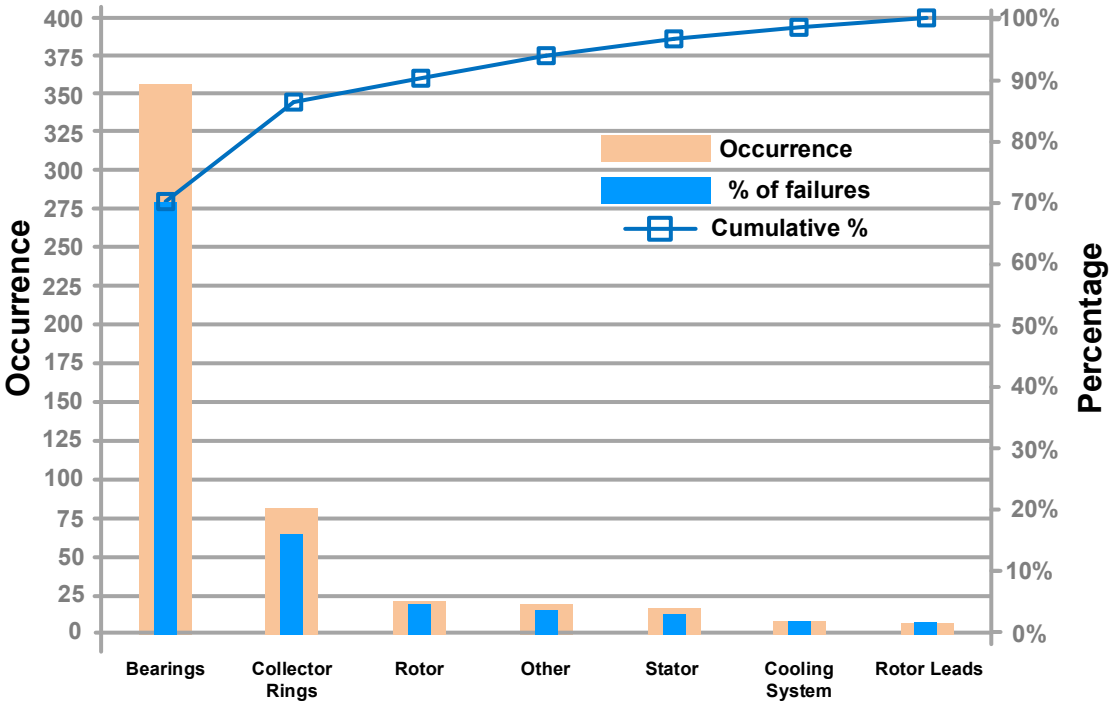

(b) Power rating 1 to 2 MW

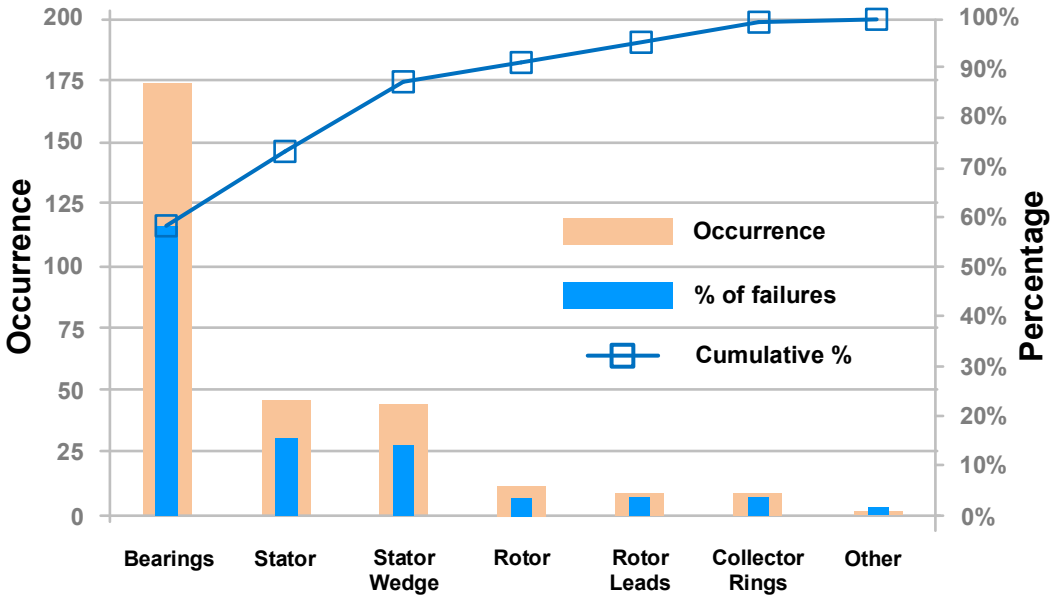

(c) Power rating >2 MW

Fig. 1.11 Failure types and occurrences for generators [68].

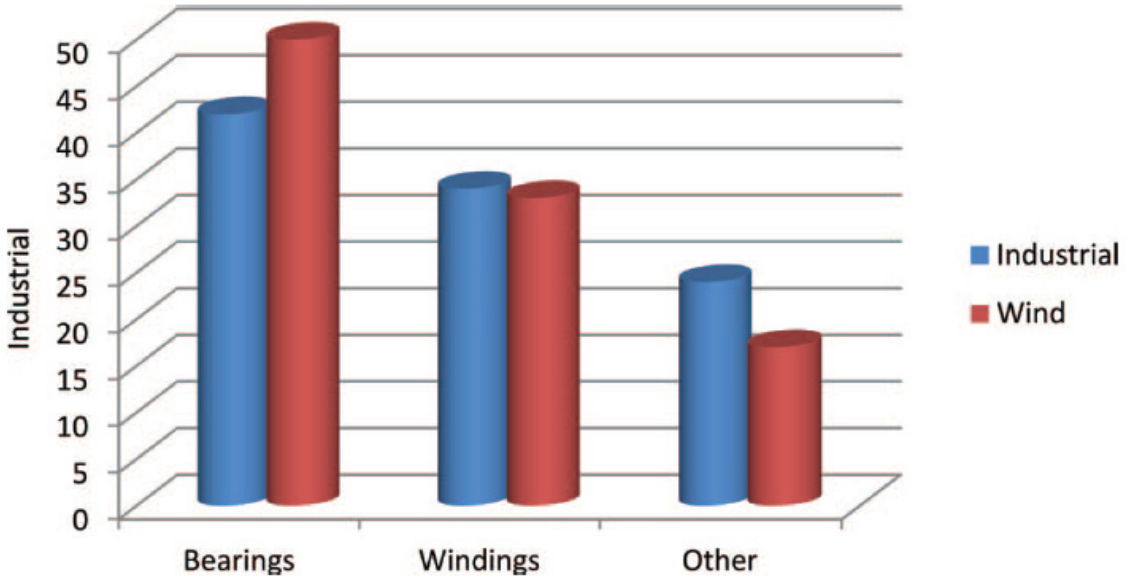

Fig. 1.12 Comparison of wind turbine failures with industrial machine failures. Distribution (%) of failure types [68].

It could be seen from Fig. 1.12 that failures due to bearing and winding damages are the two most important root causes to catastrophic consequences in both wind and industrial rotating electrical machinery sectors. This is one of the reasons that this thesis has chosen to focus on the stator winding faults of offshore wind PM power generators.

1.3.2 Failure Mechanism

1.3.2.1 Failure mechanism inside machines

The causes of the majority of the above mentioned faults are due to a combination of thermal, electrical, mechanical, and environmental stresses acting on the stator windings, as listed in Table 1.1 [69]. Corresponding to Table 1.1, Fig. 1.13 shows some typical stator winding faults due to different causes.

Table 1.1 Various stresses lead to stator winding faults

A) Thermal	**B) Electrical**
1) thermal aging 2) thermal overloading	1) dielectric 2) tracking (over 600V) 3) corona (above 5kV)
C) Mechanical	**D) Environmental**
1) coil movement 2) rotor strike 3) abrasion	1) moisture (condensation) 2) contamination

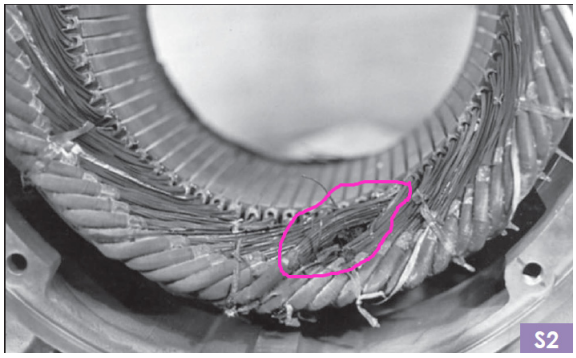

(a) A typical phase-to-phase fault caused by a breakdown in phase insulation

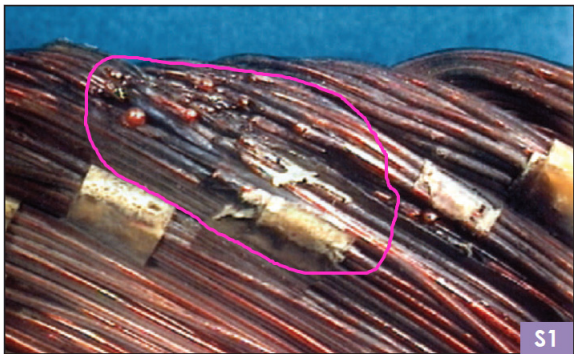

(b) A typical turn-to-turn short-circuit caused by voltage spikes from an inverter

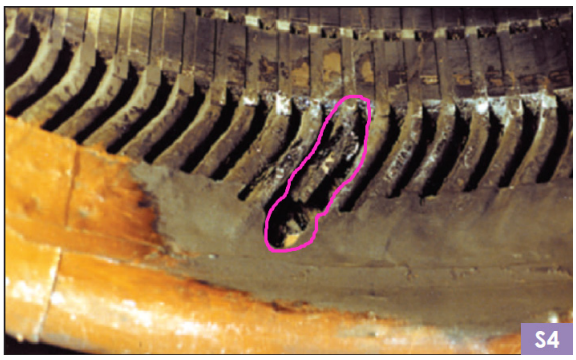

(c) A turn-to-turn short-circuit caused by a defective magnet wire insulation

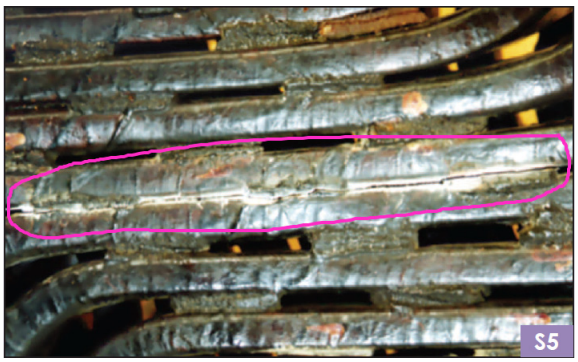

(d) Breakdown of ground insulation caused by corona

Fig. 1.13 Stator winding faults due to different causes [70].

1.3.2.2 Failure mechanism outside machines

Nowadays electrical machines especially PM machines are often driven by inverters. It is very natural that inverter faults would also possibly cause machine failure. In [71], four types of inverter faults have been considered, which are shown as Fig. 1.14. Moreover, single-phase open circuit and symmetrical 3-phase short-circuit of some 3-phase machines due to inverter faults, have been investigated in [72]–[75].

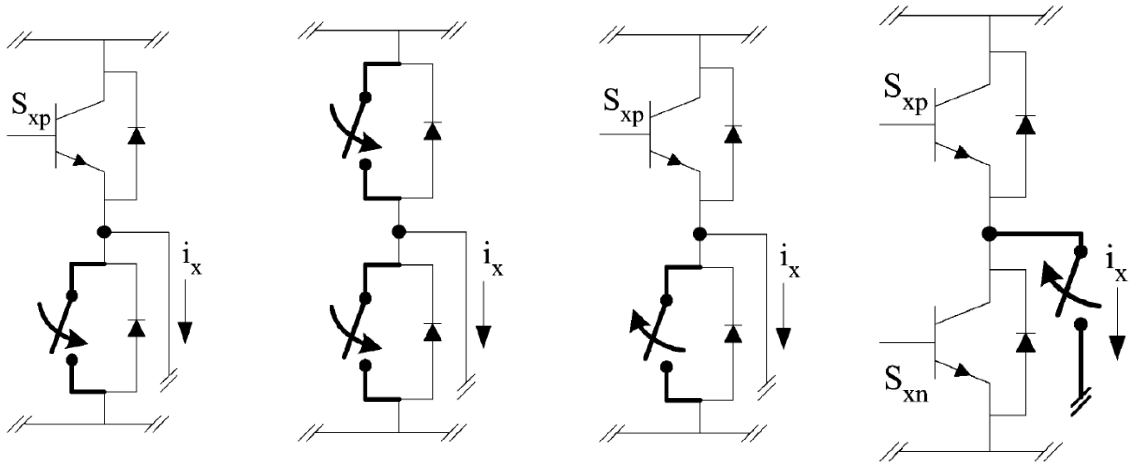

(a) single switch short-circuit (b) phase-leg short-circuit (c) single inverter switch open-circuit (d) single-phase open-circuit

Fig. 1.14 Some inverter faults that will lead to machine winding failures[71].

1.4 Typical Failures in 3-Phase Stator Windings

Visual inspection into the typical failures in the stator windings of 3-phase electrical machines are shown in Fig. 1.15 [76]. Actually, it has been surveyed by industry that there are five major types of stator winding faults, as shown in Fig. 1.16 [69]: (1) open-circuit of one phase, (2) inter-turn (turn-to-turn) short-circuit (ITSC), (3) coil-to-coil short-circuit, (4) phase-to-phase short-circuit, and (5) coil/phase to ground short-circuit.

It has been reported that the ITSC faults were one of the root causes of other more severe faults. ITSC faults are usually very difficult to detect because the fault symptoms are not obvious. However, if they are left unattended, it could quickly escalate to become a phase short-circuit, and eventually lead to the breakdown of the entire machine system [69].

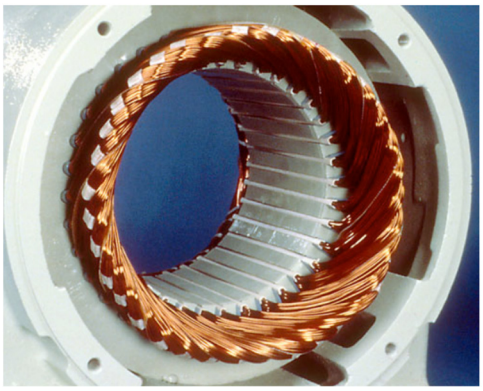

(a) Healthy stator windings

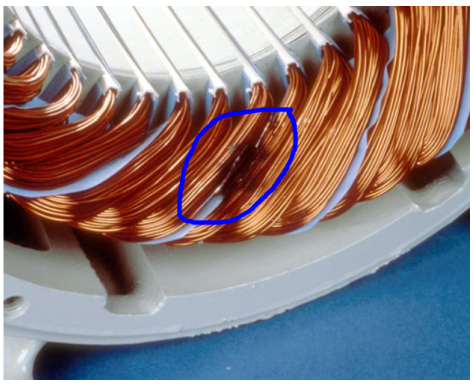

(b) Windings with phase-to-phase short-circuit

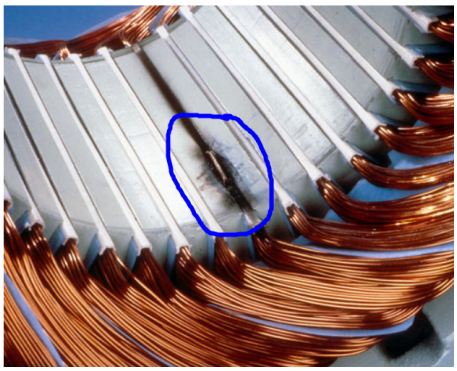

(c) Winding with phase to ground short-circuit in the slot

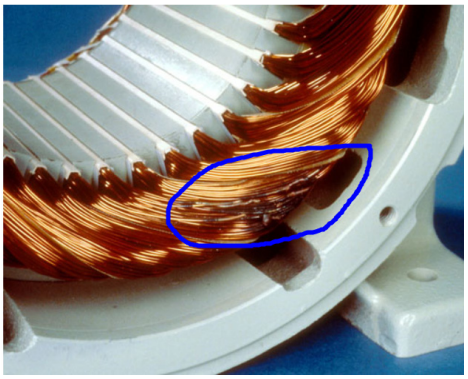

(d) Winding with inter-turn (turn-to-turn) short-circuit

Fig. 1.15 Conditions of three-phase stator windings [77].

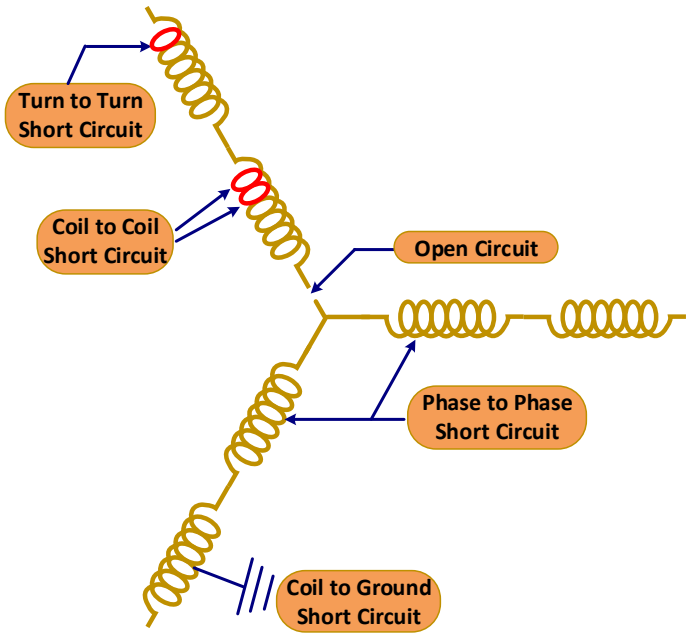

Fig. 1.16 Y-connected 3-phase windings with possible stator winding failure modes[69].

Apart from the five major failure modes, there are some aspects that should be taken into consideration to accurately diagnose the cause of a winding failure. This includes the failure pattern, machine appearance, application and maintenance history. The failure pattern could be classified into four groups: (1) symmetrical, (2) single phasing, (3) asymmetric with grounding, and (4) miscellaneous asymmetric excluding grounding.

Combining the five major failure mode and four failure patterns can help analyse the causes of failure. This will be detailed in the following sections.

1.5 Inter-Turn Short-Circuit (ITSC) Fault

As mentioned in the section 1.4, the ITSC fault was one of the root causes of other more severe faults, as shown in Fig. 1.17. Another example of the ITSC fault in a large-power electrical machine has been shown in Fig. 1.18. If the ITSC fault can be detected and mitigated in time, the amount of maintenance work could be reduced, and the wind generators will be able to operate more efficiently during their designed life span. Hence, an in-depth investigation of the ITSC faults and their impact on the performance of electrical machines are necessary.

Fig. 1.17 A turn-to-turn short-circuit leading to a ground fault in a 6.6 kV, 8MW motor [78].

From the fault detection and protection perspective, it would be much better if the changes in machine currents and voltages under ITSC fault can be predicted and understood. This will help develop a model-based fault detection method or increase the sensitivity and accuracy of the available techniques before doing any test [79]. The cost-effective fault model is especially useful for large-power electrical machines because doing fault tests on them are costly, difficult and probably destructive. Therefore, this PhD thesis will focus on ITSC fault modelling and analysis of permanent magnet machines for offshore wind power application.

Fig. 1.18 Turn insulation failure in the end winding of a 6.6-kV, 1678-kW primary air fan motor [80].

An illustration of the ITSC fault occurring in one coil is shown in Fig. 1.19. When the insulation coating of any two turns degrades, it could establish an electrical contact between normally insulated copper wires, such as between points *a* and *b* shown in Fig. 1.19 (a), leading to an ITSC fault. The corresponding circuit schematic is shown in Fig. 1.19 (b). When this fault happens, there will be a large short-circuit current flowing in the short-circuited path marked as red, causing serious local heating. Under this situation, the previous healthy winding can be deemed to be divided into two windings: the remaining healthy winding and the faulty winding.

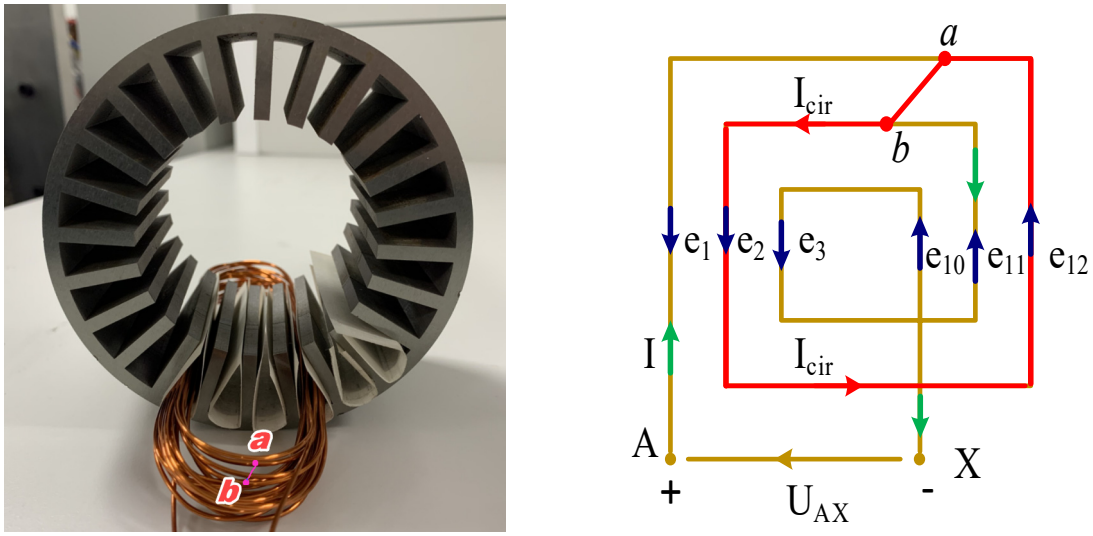

(a) ITSC fault (b) Circuit schematic [29]

Fig. 1.19 ITSC fault in one coil.

In addition, it is worth mentioning that the structure of the stator coils for large-power electrical machines is a little more complex than that shown in Fig. 1.19. A comparison of some

typical coil structures for electrical machines with different power ratings has been shown in Fig. 1.20. It has been reported in [78] that the random-wound stator coils are used widely for machines less than several hundred kilowatts and operating at voltages less than 1000V. The multi-turn coils of one phase winding of an electrical machine with random-wound stator are often connected in series. However, for form-wound stators used in most large motors and many generators rated up to 50MVA, the multi-turn coils will often form series-parallel connections, which complicates the ITSC fault modelling.

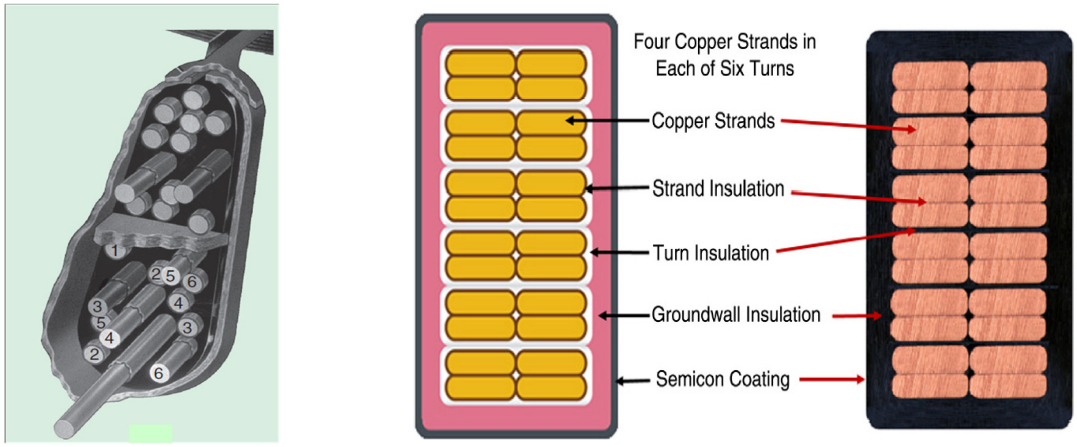

(a) Random-wound stator coil for small power machines [81]

(b) Form wound stator coil for large power machines [82]

Fig. 1.20 Stator coil structures for machines with different power ratings.

1.6 Modelling and Analysis of Inter-Turn Short-Circuit Fault

Some prior work on the ITSC fault modelling of different electrical machines has been carried out by researchers in [31], [51], [83]–[91]. In the literature, there are three well-established methods to model the ITSC faults, i.e., analytical approach, magnetic equivalent circuit (MEC), and finite element method (FEM). Modelling electrical machines under ITSC faults by analytical approach uses electric circuits to describe the machine behaviour, as shown in Fig. 1.21. When the ITSC fault occurs in the stator phase *as* winding, it has to be split into two windings as_1 and as_2, and voltage equations have to be written for these two windings in terms of lumped parameters such as resistances, inductances and back-EMFs. As for MEC modelling, as shown in Fig. 1.22, it has been used as a tool for decades for machine analysis [92].

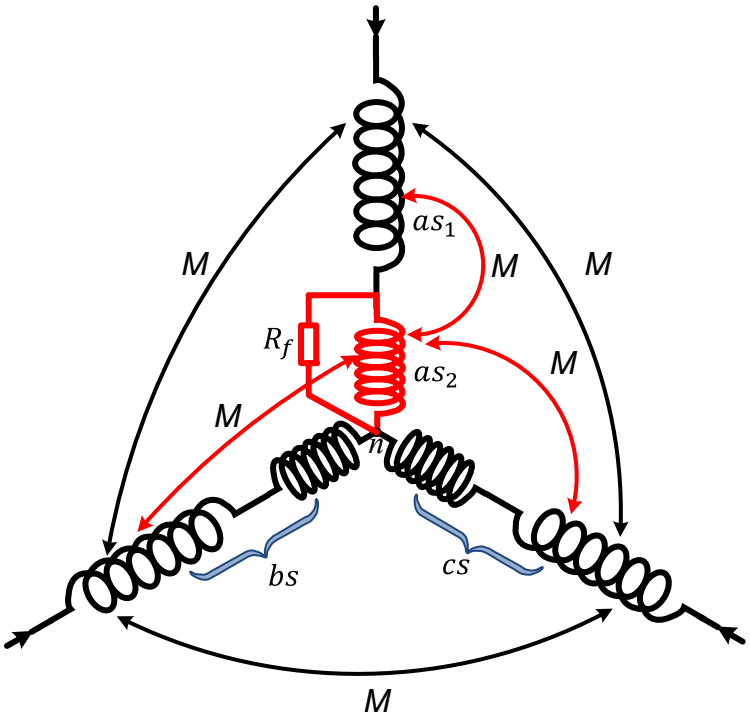

Fig. 1.21 Circuit schematic with ITSC fault in the stator phase *as* winding [93].

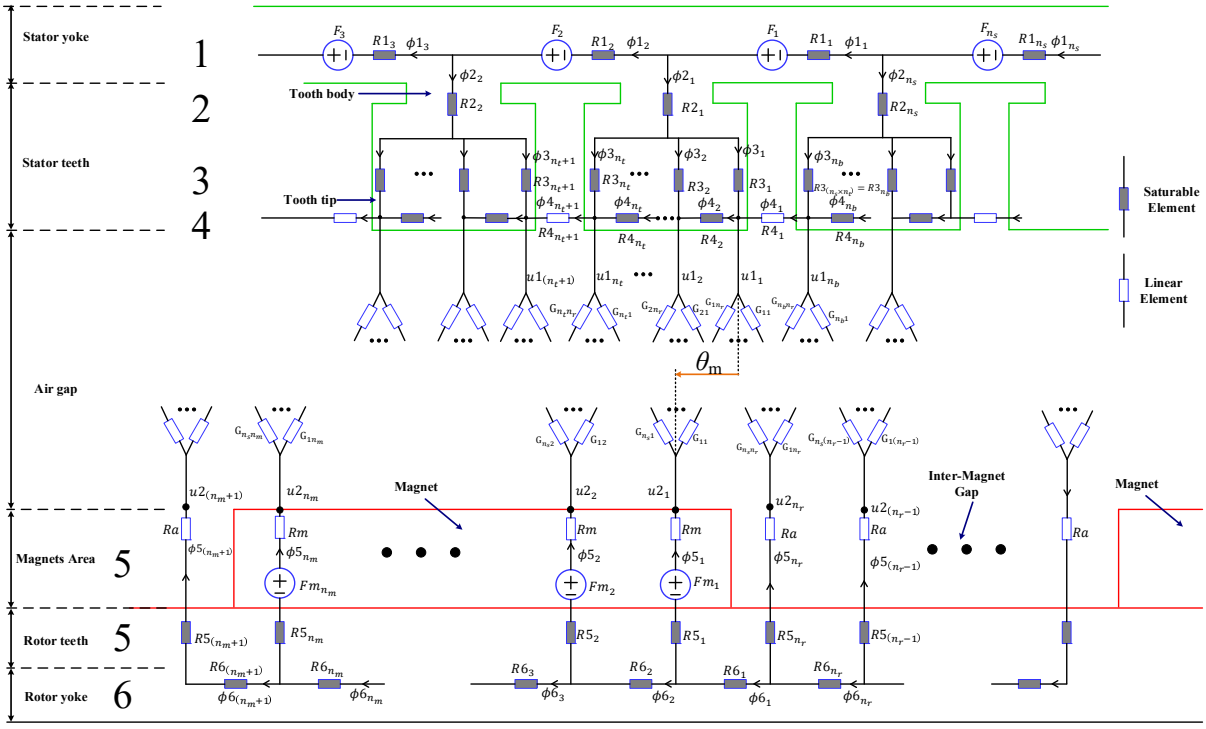

Fig. 1.22 A MEC-based model of a studied SPM machine with ITSC faults [51].

In the early days it was used to analyse machine behaviour considering magnetic saturation [94], now it has also been used for fault studies [31], [32], [90], [92], [94]–[97]. In a MEC model, reluctances, permeances, fluxes, magneto-motive forces are used to establish equations by applying the Kirchhoff's voltage and current laws to magnetic circuits. Compared with

MEC, FEM can give more detailed and accurate information such as the cogging torque, back electromotive forces (back-EMFs), inductances, magnetic field distribution inside the machine by converting the corresponding partial differential equations of the nonlinear magnetic field into a system of algebraic equations and solving them numerically. As one example, the frequently used time-stepping 2-D FEM is shown in Fig. 1.23, which has also been used for ITSC fault studies [93], [98], [99].

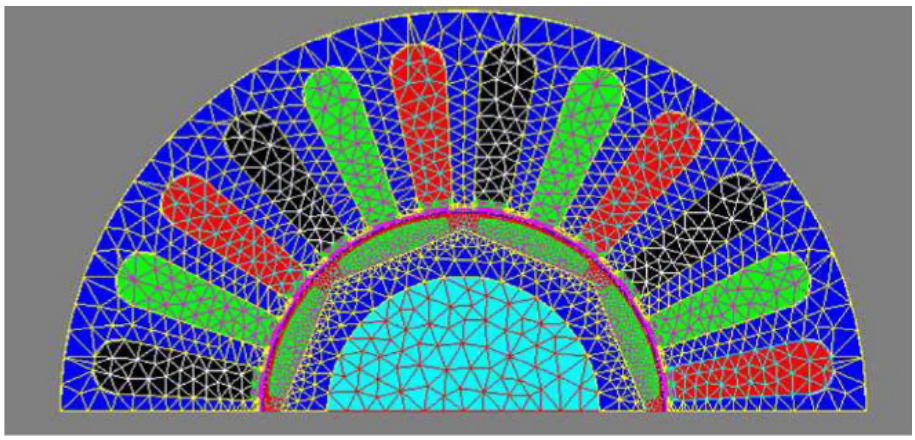

(a) Geometry model

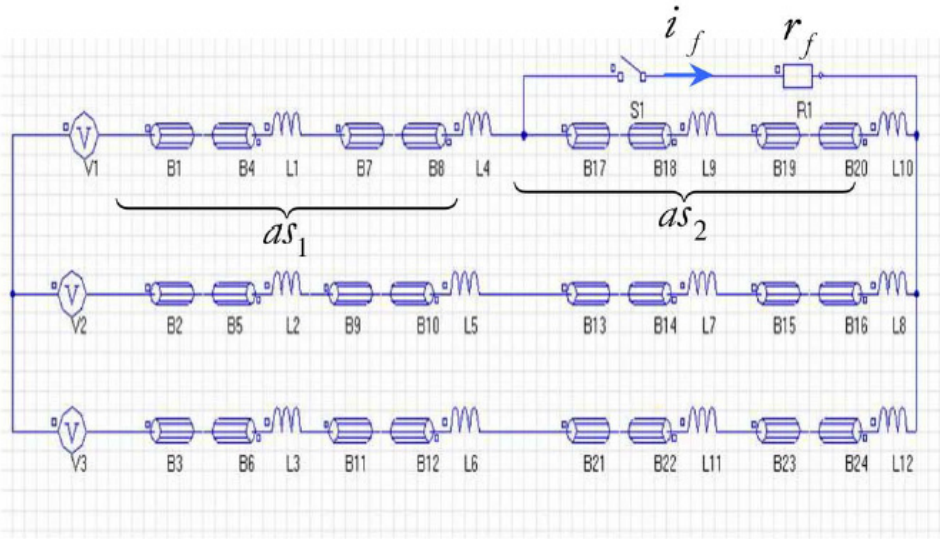

(b) Electric model

Fig. 1.23 Coupled models in Flux 2D for a 8-pole PM motor with ITSC faults [93].

The advantage of analytical approach using circuit representation is that it can be generic and applicable to machines with any power ratings although it could be less accurate, and the analytical calculation of inductances used in the fault model sometimes can be complex. As for the magnetic equivalent circuit (often called as reduced-order FEM) and FEM, although they have better accuracy, they are often much more time consuming particularly for large-power

electrical machines under ITSC faults. This is mainly because full models required for large-power electrical machines with ITSC faults will lead to much more mesh elements in the FE models or flux tubes in the MEC models, hence they need much more time to solve at each time step when current sources are used to excite the electrical machines. For example, the simulation time for current excited large-power SPM machines over one electrical period is often several hours. However, if the electrical machines are voltage fed, the machine models are more complex than the corresponding current fed ones so that they have to be reformulated. One method proposed by Nabeel A.O. Demerdash employs combined systems of ordinary differential equations (ODEs) and partial differential equations (PDEs) shown in Fig. 1.24 [100]–[104] to describe the machine behaviour for voltage fed electrical machines. In order to accurately predict the future states of state variables in the ODEs, a small-time step usually has to be chosen. In addition, it is found that the voltage fed large-power SPM machines often needs more time to reach steady state. Thus, a compromise between accuracy and computational burden typically has to be made for FE simulation of large-power electrical machines with voltage sources. If the full models of large-power electrical machines with large number of slots and poles are interfaced with voltage sources such as balanced 3-phase sinusoidal voltages or PWM converters (co-simulation) to simulate the faulty machine performance under real operating conditions, to keep good accuracy, the simulation time using common office computers would be too long and unacceptable for fault analyses.

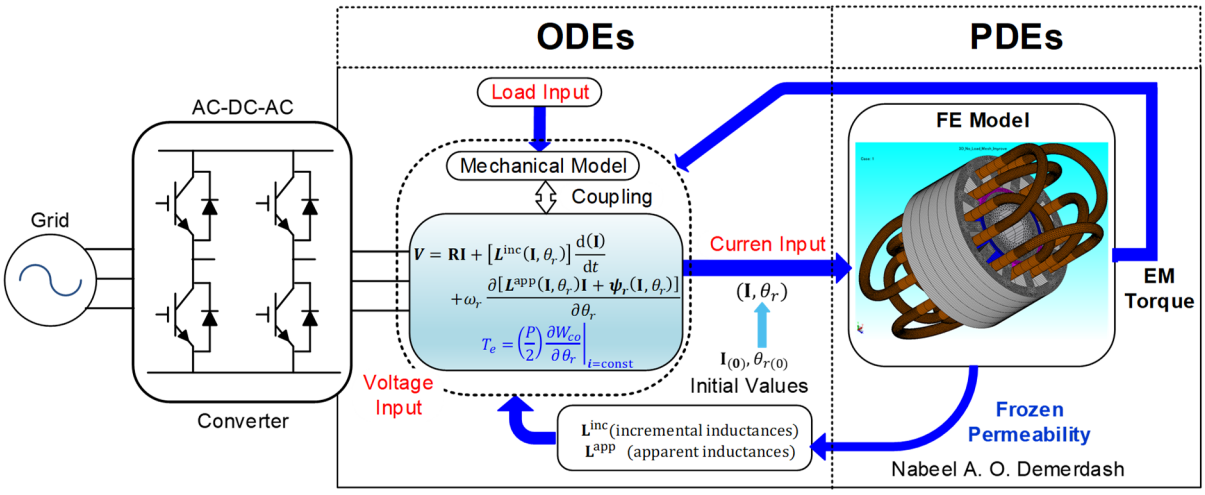

Fig. 1.24 Time-stepping coupled finite element state space(TSCFE-SS) machine model proposed by Nabeel A.O. Demerdash [101].

In addition, it should be mentioned that although the analytical modelling principles of healthy machines, i.e., the basic principles of electromechanical energy conversion, have been well established [105]–[108], the fault modelling for large-power electrical machines will also

require a good understanding of these basic principles, otherwise a general analytical fault model could not be developed.

In 1995, the authors in [83] developed a fault model for induction machines with squirrel-cage rotors. One characteristic of the fault model is that it uses a large number of first-order differential equations to predict the machine behaviour under ITSC faults. This is because the squirrel-cage rotor has many inductively coupled loops, constructed by many rotor bars and two end rings. When an ITSC fault occurs, they cannot be approximated to 3-phase windings any more. In addition, the model parameters especially the large number of inductances have been calculated by an analytical method called winding function approach. It is worth mentioning that the derivation of the inductance expressions for a general fault model is difficult, and this is why the inductances calculated are only based on two specific machines. On the other hand, some assumptions have been made such as neglecting the slot opening and rotor bar skew effects to simplify the inductance calculation.

In 2002, the authors in [30] developed a transient model for an induction machine with series-connected windings under ITSC faults. The main contribution in [30] is that the authors divided the fault model into two parts. The part of the healthy machine model uses 3-phase currents as state variables, and the faulty part is represented by the current in the external short-circuited path and inductances related to the short-circuited turns. As for the determination of inductances in the fault model, the authors made some simple assumptions, i.e., the self-inductance is proportional to the square of the number of turns, and the mutual inductance is proportional to the number of turns. This treatment does not consider the influence of spatial distribution of the coils on the inductance values. In addition, the rotor of the induction machine considered is represented by a 3-phase winding, instead of the complex squirrel-cage structure.

Meanwhile, the authors in [109] modelled the transient behaviour of salient-pole synchronous machines with ITSC faults to predict the resulting currents and voltages. The proposed fault model considered the practical winding structure (stator branches, rotor damper circuit loops) of the large-power synchronous machines. A large-scale system of first-order differential equations is also required to characterize the fault model. In addition, the cumbersome inductance calculation considering the practical distributed winding arrangement and nonuniform air gaps also makes the ITSC fault modelling for large salient-pole synchronous generators quite complex and challenging. Although the stator branch currents have been transformed into loop currents to represent the fault model in another way, it seems that the analytical model is not simplified.

A few years later, the authors in [86], [87] also proposed internal fault models in matrix forms for synchronous machines. Although not specifically stated, the focused internal faults include ITSC faults. In [86], based on the winding function approach, the machine inductances have been calculated directly from the machine winding distribution to include all the space harmonics produced by the machine windings and the calculation of the machine inductances has been made easier by the effective use of the machine electrical parameters instead of the geometrical ones. Although the ITSC fault is not directly involved, the modelling of one phase-to-ground short-circuit fault actually is equivalent to that of one-coil short-circuit fault. In [87], simulation models to investigate the internal fault currents of large synchronous generators with parallel-connected windings under different internal faults have been presented. It is worth mentioning that the ITSC fault is one of the 8 internal faults investigated. In addition, the branch currents are used as state variables to describe the machine behaviours under normal and faulty conditions. Finally, the internal fault models for a few different machines including the more complicated 370MVA salient-pole synchronous generator were implemented in a real-time simulator of large power networks called Hypersim. The simulation models developed in [87] provide all the currents flowing in the machine stator windings, which may be very useful to develop an accurate protection plan. However, it should be mentioned that the internal fault models developed in [86], [87] assume that the rotor is equipped with a field winding and 2 damper windings, which is not the case for PM machines.

Compared with the analytical fault modelling for squirrel-cage induction machines and salient-pole synchronous machines, the analytical fault modelling for PM machines is easier, especially for series-connected coils. This is because there is no winding on the rotor of PM machines. In [110], fault analysis of a PM brushless dc motor with parallel-connected coils using FEM has been carried out. The fault conditions considered are external (phase-to-phase) short-circuit, internal turn-to-turn short-circuit, and open-circuit faults. Considering the fact that the ITSC faults will lead to asymmetric current distribution, a full 2D FE model has been used. In addition, the demagnetization issue of the studied PM brushless dc motor under ITSC faults have also been investigated. However, it should be mentioned that the reasons why fault analysis of the studied PM brushless dc motor using direct FEM can be carried out are that the number of mesh elements of this small machine is not large, and the control strategy is very simple.

Some other interesting studies of the ITSC fault modelling of PM machines using FEM have also been carried out in [93], [98], [99]. As mentioned earlier, theoretical calculation of inductances by an analytical approach is often complex and not very accurate. However, the

inductance calculation using FEM is more straightforward. In [98], the authors first extracted the inductances and back-EMFs of the studied PM machines by FEM, then loaded them into the analytical fault model to simulate the fault performance of the studied PM machines under different fault conditions. In this way, to some extent, the accuracy of the FE model can be retained in the analytical fault model and the simulation time is shortened significantly. In [93], [99], the authors have found that the inductance expressions in the general analytical fault model are related with the pole pair number of the studied machine. However, the influence of the pole pair number on the inductance expressions has not been considered in [49], [111], [112]. As a result, although the proposed fault models can predict the fault performance of the investigated machines to some extent, such models may not be easily generalized and made applicable to other machines.

In addition, other researchers showed some interest about ITSC fault modelling for fractional-slot PM machines [88], [89], [113]–[118], the theory and design of which have attracted increasing interest in the electrical machine community [119]–[124] in the past few decades. Unlike the traditional integer-slot PM machines, the mutual inductive couplings between phases of some fractional-slot PM machines are almost zeros, meaning that the fault in one phase will not affect the other healthy phases. Therefore, they are much more fault-tolerant. This inherent fault-tolerant characteristic also results in simple fault models, as investigated in [113], [116]–[118].

1.7 Organization and Contributions

1.7.1 Organization

This thesis aims for developing a simple general analytical model for large-power SPM wind generators under ITSC fault to predict their machine performance. The thesis is organized as follows:

Chapter 2 Fault Modelling and Analysis of SPM Machines with Series-Connected Coils

In this chapter, a general analytical model for (SPM) machines with series-connected coils under ITSC fault has been developed, how to calculate the inductances in the fault model has been detailed. The proposed fault model built in Matlab/Simulink is validated by time stepping FE simulations for a 3kW 96-slot 32-pole SPM machine. In addition, other power ratings (0.5MW and 3MW) have also been investigated to study the scaling effect on machine fault-tolerant capability.

Chapter 3 Fault Modelling and Analysis of SPM Machines with Parallel-Connected Coils

This chapter presents a general analytical fault model in a compact matrix form for surface-mounted permanent magnet (SPM) machines with parallel-connected coils, and inductances for its winding configuration have also been calculated by the same analytical approach used in the chapter 2. Then the multiphase Clarke transformation has been proposed to simplify the fault model. In the model, the branch currents rather than the phase currents have been employed as state variables to describe machine behaviours under fault. Finally, the proposed analytical fault model is applied to a 3 kW 96-slot 32-pole SPM machine and the analytical fault model built in Matlab/Simulink is validated by time-stepping FE simulations.

Chapter 4 In-depth Investigation of Inter-Turn Short-Circuit Faults of SPM Machines with Series-Parallel Coil Connections

Based on the developed general analytical fault model for SPM machines with parallel-connected coils in chapter 3, this chapter proposes the general analytical fault model for SPM machines with series-parallel coil connections. The inductances in the fault model are derived for SPM machines with series-parallel coil connections by the same analytical method as in the previous two chapters. Based on the characteristics of the calculated inductances and the developed fault model, the multiphase Clarke transformation is found to be still useful for simplifying the fault model. The proposed fault models of a 3kW 96-slot 32-pole SPM machine with different series-parallel coil connections have been built in Matlab/Simulink and validated by time-stepping 2D FE simulations.

Chapter 5 Modelling and Analysis of Inter-Turn Short-Circuit Fault for Large-Power SPM Wind Generators

Based on the developed general analytical fault model in chapter 4, this chapter focuses on the fault model simplification for large-power surface-mounted permanent magnet (SPM) wind generators. It is found that the multiphase Clarke transformation can be used to simplify the proposed fault model with FE linear or nonlinear inductances. For the fault modelling of large power rating machines due to larger electrical loading and heavier magnetic saturation, nonlinear inductances can be used in the fault model to achieve more accurate prediction of the changes in machine currents and voltages under ITSC faults. With the developed fault model, studies of the scaling effect (different power ratings such as 3kW, 500kW and 3MW) and the influence of fault location on the electromagnetic performance of SPM generators with series-parallel coil connections have been carried out.

Chapter 6 Analysis of SPM Machines with Different Winding Configurations under Inter-Turn Short-Circuit Faults

Based on the developed general analytical fault model in chapter 4 and general model simplification method using the multiphase Clarke transformation in chapter 5, this chapter compares the performance of SPM machines with two different winding configurations under ITSC fault. The two different winding configurations are the non-modular and modular overlapping windings. It is found that the healthy machine performances for a SPM machine with non-modular or modular overlapping windings are the same, but their fault performances are different. Simulation results of the 96-slot 32-pole SPM machine under ITSC faults have confirmed this conclusion. In addition, fault performances of the same fault occurring in different phases have been studied when these two winding configurations are considered. Finally, fault simulations using the 500kW SPM machine with modular windings have been carried out to see these differences in the large-power SPM machines.

Chapter 7 Experimental Validation

This chapter is dedicated to the experimental validations of the fault models of the SPM machines with series-connected coils, parallel-connected coils, and series-parallel connected coils on two different small-scale machine prototypes.

Chapter 8 General Conclusions

This chapter summarizes the research work that has been carried out in this thesis and proposes some meaningful future works.

1.7.2 Contributions

- General and simple analytical models for SPM machines with series, parallel and series-parallel connected coils under ITSC faults have been developed. Calculation of inductances in the fault models of SPM machines with single-layer, full-pitch and distributed winding arrangements [slot/pole/phase (SPP) is equal to 1] by an analytical approach (winding function approach + slot permeance method) and FEM have been carried out. To simplify the fault models with analytical inductances, the multiphase Clarke transformation has been proposed. Then the fault models and model simplification method have been validated by direct FE and Simulink simulations of a 96-slot 32-pole SPM machine with different series-parallel coil connections. However,

only the developed fault models have been validated by experimentation on two different machine prototypes.

- The model simplification method using multiphase Clarke transformation for analytical models of large-power SPM wind generators under ITSC faults has also been proved if the FE linear and nonlinear inductances are used in the fault model. As a result, simulations for large-power SPM wind generators under ITSC faults can be carried out directly in an easier and more time-saving way while keeping adequate accuracy. It is worth mentioning that the proposed fault model and model simplification method are generic and may be applied to other types of non-PM machines and also their multiphase counterparts with practical winding configurations. In addition, based on the simplified fault model, studies of scaling effect and influence of fault location on the amplitude of ITSC current of PM machines with different power ratings (3kW, 500kW, 3MW) have been carried out. It is found that large-power SPM wind generators are vulnerable to ITSC faults when relatively small number of turns are short-circuited and the single-turn short-circuit fault at the slot top (slot opening) is the worst-case scenario.
- A comparison of the performance of SPM machines with two different winding configurations under ITSC faults has been made. The two different winding configurations are the non-modular and modular overlapping windings. It is found that the healthy machine performances for a SPM machine with non-modular or modular windings are the same, but their fault performances are different. Compared with the non-modular windings, the modular windings are generally more fault-tolerant. However, these differences in the large-power (500kW and beyond) SPM machines become negligible because ITSC faults often cause very little imbalance in branch currents for large-power SPM machines with many parallel branches and many coils connected in series for one branch.

Related Publications:

(1) [Mei21] Z. T. Mei, G. J. Li, Z. Q. Zhu, R. Clark, A. Thomas, and Z. Azar, “Scaling Effect on Inter-Turn Short-Circuit of PM Machines for Wind Power Application”, in 2021 IEEE International Electric Machines & Drives Conference (IEMDC), Hartford, CT, USA, 2021, pp. 1-8.

(2) [Mei23a] Z. T. Mei, G.J. Li, Z. Q. Zhu, R. Clark, A. Thomas, and Z. Azar, “Scaling Effect On Inter-Turn Short-Circuit Fault of PM Machines for Wind Power Application,” *IEEE Trans. Ind. Appl.*, vol. 59, no. 1, pp. 789–800, Jan.-Feb. 2023.

(3) [MEI23b] Z. T. Mei, G. J. Li, Z. Q. Zhu, R. Clark, A. Thomas, and Z. Azar, “Modelling and Analysis of Inter-Turn Short-Circuit Fault of PM Machines with Parallel-Connected Coils,” *IEEE Trans. Energy Convers.*, vol. 38, no. 2, pp. 1268-1279, Jun. 2023.

(4) [Mei23c] Z. T. Mei, G. J. Li, Z. Q. Zhu, R. Clark, A. Thomas, and Z. Azar, “In-depth Investigation of Inter-Turn Short-Circuit Faults of PM Machines with Series-Parallel Coil Connections,” *IET Electr. Power Appl.*, pp. 1–9, Apr. 2023.

(5) [Mei23d] Z. T. Mei, G. J. Li, Z. Q. Zhu, R. Clark, A. Thomas, and Z. Azar, “Modelling and Analysis of Inter-Turn Short-Circuit Fault for Large-Power SPM Wind Generators” *Energies*, vol. 16, no. 12, 2023.

(6) [Mei23e] Z. T. Mei, G. J. Li, Z. Q. Zhu, R. Clark, A. Thomas, and Z. Azar, “Analysis of SPM Machines with Different Winding Configurations Under Inter-Turn Short-Circuit Fault” Energies, 2023. (To be submitted)

Chapter 2 Fault Modelling and Analysis of SPM Machines with Series-Connected Coils

This chapter proposes a general analytical model of surface-mounted permanent magnet (SPM) machines with series-connected coils under inter-turn short circuit (ITSC) fault. One prominent feature of this fault model is that the air-gap and slot-leakage components of inductances under fault are calculated separately when core saturation is neglected, and the influences of pole number and spatial distribution of coils have been considered in the calculations. In the model, the winding function approach (WFA) is used to calculate the air-gap inductance components by considering all space harmonics whilst slot-leakage inductance components are obtained by using slot permeance method. The proposed fault model built in Matlab/Simulink is validated by time stepping FE simulations for a 3kW 96-slot 32-pole SPM machine. The fault model has acceptable accuracy and is suitable for the fast evaluation of fault performance of SPM machines and its accuracy considering core saturation can be improved using FE-based results. Other power ratings (0.5MW and 3MW) have also been investigated to study the scaling effect on machine fault-tolerant capability.

Related Publications:

[Mei21] Z. T. Mei, G. J. Li, Z. Q. Zhu, R. Clark, A. Thomas, and Z. Azar, "Scaling Effect on Inter-Turn Short-Circuit of PM Machines for Wind Power Application", in 2021 IEEE International Electric Machines & Drives Conference (IEMDC), Hartford, CT, USA, 2021, pp. 1-8.

[Mei23a] Z. T. Mei, G.J. Li, Z. Q. Zhu, R. Clark, A. Thomas, and Z. Azar, "Scaling Effect On Inter-Turn Short-Circuit Fault of PM Machines for Wind Power Application," *IEEE Trans. Ind. Appl.*, vol. 59, no. 1, pp. 789–800, Jan.-Feb. 2023.

2.1 Introduction

As a starting point for theoretical analysis, this chapter will mainly focus on analytical modelling and analysis of inter-turn short-circuit (ITSC) faults in PM machines with series-connected coils. It is worth noting that the large-power PM machines with series-parallel connected coils are very common in practice and they will be analysed in later chapters.

It should be mentioned that for physics-based modelling of permanent magnet (PM) machines under ITSC fault, there are three major methods in literature: (1) winding function approach (WFA) [87], [125], [50], [126], [127], (2) finite element (FE) approach [128]–[130], and (3) magnetic equivalent circuit (MEC) approach [51], [90]. WFA is a circuit-based modelling method in essence, and it is the foundation of the analytical derivation and calculation of inductances of integer-slot AC machines [106]. Researchers in [83], [87] have tried to use this method to analyse the fault performance of induction and synchronous machines in the last 30 years. The disadvantage of this method for calculating the inductances is that it neglects the core saturation and also space harmonics. If space harmonics are considered, the derivation of general inductance expressions under faulty conditions for machines with complex winding configurations will become significantly difficult.

Considering this difficulty in employing WFA, researchers in [49], [111], [112] made assumptions to simplify the determination of the inductances in the fault model based on the relationship between the healthy inductances and the number of turns. However, when large number of coils per phase are distributed in different slots around the stator periphery, such assumptions may not be valid. Unlike WFA, both FE and MEC can consider the core saturation. However, they require detailed geometrical dimensions of the machines, and simulations using these two methods are much more time-consuming. Using the FE model as an example, with a typical current desktop PC, the total computation time would be several days or even months if sinusoidal voltage sources and a full FE model are employed for large direct-drive wind power generators with large numbers of stator slots and rotor poles.

Therefore, WFA will be adopted for the analyses of integer-slot SPM machines with a slot/pole/phase (SPP) of 1 in this chapter. However, it was found that the simulated results using the air-gap inductance components calculated by WFA with all space harmonics considered cannot match well with that of 2D FE simulations even when linear magnetic material was used. This is due to the fact that for surface-mounted PM (SPM) machines, the slot-leakage inductance components will also have some influence on machine performance due to large effective air gaps.

To establish a more accurate analytical fault model, the slot-leakage inductances will be calculated based on the slot permeance method and are added to the corresponding air-gap inductance components. The proposed fault model built in Matlab/Simulink is validated by time stepping FE simulations. In addition, a comparison between the developed model in this chapter against the analytical model proposed in [49] has been carried out. The comparison results show that the influence of the pole number and the spatial distribution of coils on the determination of inductance values under faulty conditions cannot be neglected when the number of short-circuited turns in one coil is large.

Furthermore, a method taking the full advantages of the proposed analytical and FE models to develop a more accurate fault model considering core saturation has been proposed. The SPM machines with different power-ratings, e.g., 3kW, 0.5MW and 3MW, will also be investigated to analyse the effect of scaling on the ITSC fault performance by using the proposed model. To validate the developed fault model, a small scale 12-slot 4-pole SPM machine has been built and tested in chapter 7. It is worth mentioning that for most part of this chapter, the core saturation has been neglected when inductance calculations and simulations are carried out. In addition, considering that different SPM machines have different saturation levels, the influence of inductance parameters on the accuracy of prediction of phase currents and ITSC currents have not been conducted. However, in chapter 7, to fully validate the developed fault model, nonlinear inductances obtained from measurement and 3D FE models will be used.

2.2 Modelling of ITSC Fault of SPM Wind Generator

This section will give a brief introduction to the analytical and FE modelling of ITSC fault of SPM wind generator with series-connected coils.

2.2.1 Analytical Modelling Neglecting the Core Saturation

An example of ITSC fault in a stator armature coil of wind power generator is shown in Fig. 2.1. Due to a turn insulation breakdown, two electrically isolated points will have an electrical contact, leading to an ITSC fault and a large short-circuit current, which can cause local overheating, speeding up the insulation breakdown of the entire armature windings.

The equivalent circuit of the ITSC fault in a Y-connected stator winding of a PM machine is shown in Fig. 2.2, where the fault is assumed to occur in phase A. This equivalent circuit will be used to build the electrical model of the studied SPM machines. Together with the

mechanical model, tools like Matlab/Simulink can be used to investigate the influence of ITSC fault on the performance of the SPM machines.

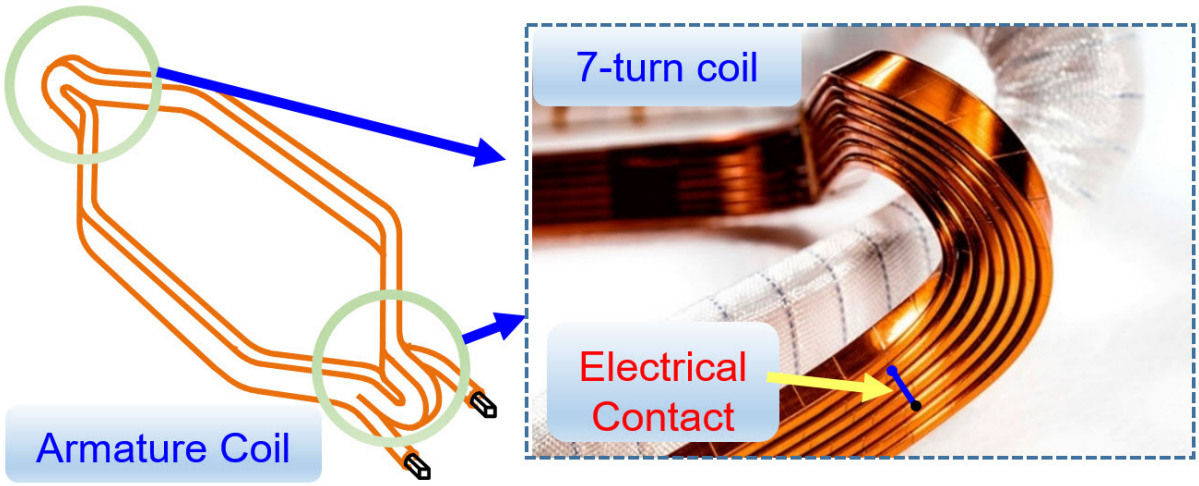

Fig. 2.1 ITSC fault in armature coils.

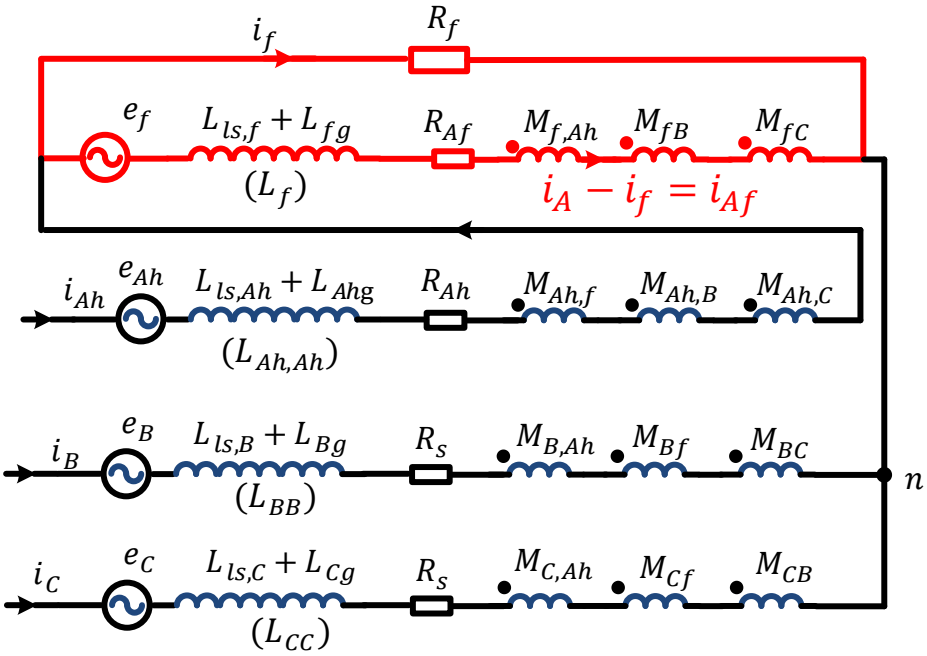

Fig. 2.2 Equivalent circuit of SPM machines under ITSC fault in the phase A.

From Fig. 2.2, the circuit-based voltage equations representing the relationship between phase voltages, EMFs and also currents under ITSC fault can be expressed as (2.1), where R_s is the phase resistance, R_{Af} is the resistance of short-circuited turns, and R_f (assumed to be zero for the 3kW machine) is the contact resistance between short-circuited points. $M_{Ah,f}$, M_{Bf}, and M_{Cf} are the mutual inductances between the remaining healthy winding Ah, healthy

windings B, C and short-circuited turns, respectively. L_f is the self-inductance of short-circuited turns. $i_{Ah}(=i_A)$, i_B and i_C are the currents of remaining healthy windings Ah, B and C, respectively. Similarly, e_A, e_B, and e_C are the phase back-EMFs of healthy phase windings. In addition, $e_{Ah}=(1-\mu)e_A$, $e_f=\mu e_A$, in which the phase faulty turns ratio in one phase winding is defined as $\mu=\frac{1}{p}\mu_1=\frac{1}{p}\frac{n_f}{n_c}$ for the studied integer-slot SPMs with a SPP of 1. The corresponding coil faulty turns ratio in one elementary coil is defined as $\mu_1=n_f/n_c$, where n_f denotes the number of short-circuited turns in one coil, and n_c describes the number of turns per coil. Furthermore, p is the number of pole pairs.

$$\begin{bmatrix} v_A \\ v_B \\ v_C \\ 0 \end{bmatrix} = \begin{bmatrix} R_s & 0 & 0 & -R_{Af} \\ 0 & R_s & 0 & 0 \\ 0 & 0 & R_s & 0 \\ R_{Af} & 0 & 0 & -R_{Af}-R_f \end{bmatrix} \begin{bmatrix} i_A \\ i_B \\ i_C \\ i_f \end{bmatrix} + \begin{bmatrix} e_A \\ e_B \\ e_C \\ e_f \end{bmatrix} + \begin{bmatrix} L_{AA} & M_{AB} & M_{AC} & -(M_{Ah,f}+L_f) \\ M_{BA} & L_{BB} & M_{BC} & -M_{Bf} \\ M_{CA} & M_{CB} & L_{CC} & -M_{Cf} \\ (M_{f,Ah}+L_f) & M_{fB} & M_{fC} & -L_f \end{bmatrix} \frac{\mathrm{d}}{\mathrm{d}t} \begin{bmatrix} i_A \\ i_B \\ i_C \\ i_f \end{bmatrix} \tag{2.1}$$

If the phase back-EMFs in (2.1) contain harmonics and no neutral line is introduced, then the phase voltages cannot be directly obtained from the line voltages under ITSC fault. Under this situation, it is found that the sum of the 3 phase voltages can be expressed as

$$v_A+v_B+v_C=(e_A+e_B+e_C)-R_{Af}i_f-\left(L_f+M_{Ah,f}+M_{Bf}+M_{Cf}\right)\frac{\mathrm{d}i_f}{\mathrm{d}t} \tag{2.2}$$

Equation (2.2) together with (2.3) and (2.4) could be used to calculate the phase voltages from line voltages.

$$v_{AB}=v_A-v_B \tag{2.3}$$

$$v_{BC}=v_B-v_C=v_A+2v_B-(v_A+v_B+v_C) \tag{2.4}$$

Once the currents in the healthy and faulty windings are determined, the electromagnetic torque under ITSC fault can be calculated by

$$T_e=p\frac{\left(e_Ai_A+e_Bi_B+e_Ci_C-e_fi_f\right)}{\omega_r}+T_{cog} \tag{2.5}$$

where ω_r is the rotor electrical speed (rad/s), T_{cog} is the cogging torque.

The above equations will be used in the Matlab/Simulink to analytically predict the machine performance before and after ITSC faults. It should be mentioned that the phase back-EMFs and cogging torque obtained from FE simulations of healthy machines are imported into the

Matlab/Simulink to accurately predict the torque ripple before and after introducing the ITSC fault. In addition, inductances in the fault model will be calculated based on the analytical method (which requires the machine's geometrical dimensions) in the section 2.3.1.

2.2.2 Analytical Modelling Considering the Core Saturation

If the core saturation needs to be fully included into the analytical modelling based on Matlab/Simulink, its influence on apparent and differential inductances together with PM flux linkages should be taken into account. In order to consider the saturation effect, in [131], the flux linkage lookup table based model is used. However, such a model does not provide meaningful physical insights into the fault phenomena and multiple fault scenarios might not be easily incorporated. Furthermore, there is no detailed discussion about how to determine the current profiles as inputs to obtain the stator flux linkages. In [132], lookup tables using differential inductances considering the core saturation are employed. However, only the influence of the core saturation on the differential/incremental inductances is considered, and the influence of the core saturation on the on-load PM flux linkages and the apparent inductances has not been included because the frozen permeability method such as the one investigated in [100], [133] has not been employed.

In order to overcome the shortcomings in the existing methods, the frozen permeability method has been used to obtain the saturated apparent inductances and the on-load PM flux linkages of the studied machines under different operating conditions.

In the frozen permeability method, accurate determination of the current profiles as inputs to obtain the permeability in every mesh element in the FE model is the key to achieving the saturated apparent inductance and the on-load PM flux linkage look-up tables. For 3-phase healthy machines, the currents are often balanced, and their waveforms are sinusoidal. However, this is no longer the case for faulty machines, especially when significant harmonics exist in their phase back EMFs. A proposed method making full use of the linear analytical model (based on Matlab/Simulink) developed is shown in Fig. 2.3.

As illustrated in Fig. 2.3, the current profiles as inputs into non-linear FE fault models could be determined by the linear analytical model. This can help to update the saturated apparent inductance and on-load PM flux-linkage under different operating conditions. If necessary, this method can be iterated to further improve the accuracy of the fault model. Meanwhile, a predefined current accuracy of 5% (deemed acceptable for most cases) or a maximum number of iterations of 5 can be selected to terminate the iteration, which are similar to the settings in the FE modelling (JMAG software package).

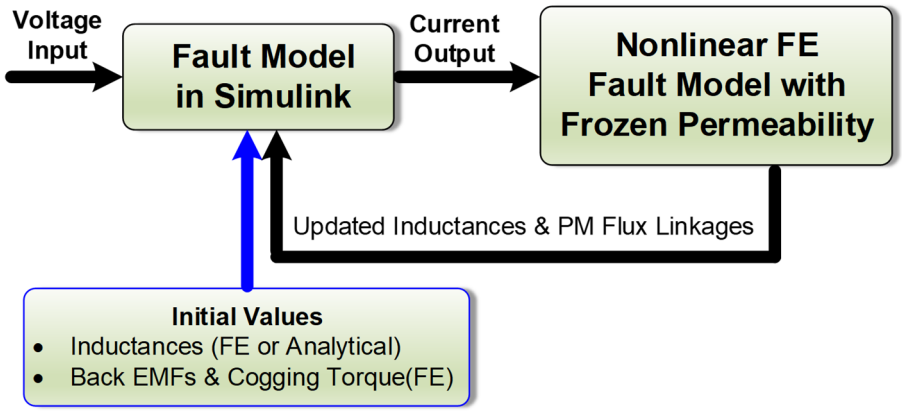

Fig. 2.3 Analytical modelling (based on Matlab/Simulink) of ITSC fault with consideration of core saturation.

2.2.3 FE Numerical Modelling

To validate the results obtained by the developed analytical models, 2D FE simulations (JMAG software package) for the outer rotor 3kW 96-slot/32-pole SPM machine have been carried out in this chapter. Since the symmetrical machines become asymmetric under ITSC faults, a full FE model is necessary as shown in Fig. 2.4, where only part of the model is shown to have a clearer view of the ITSC fault.

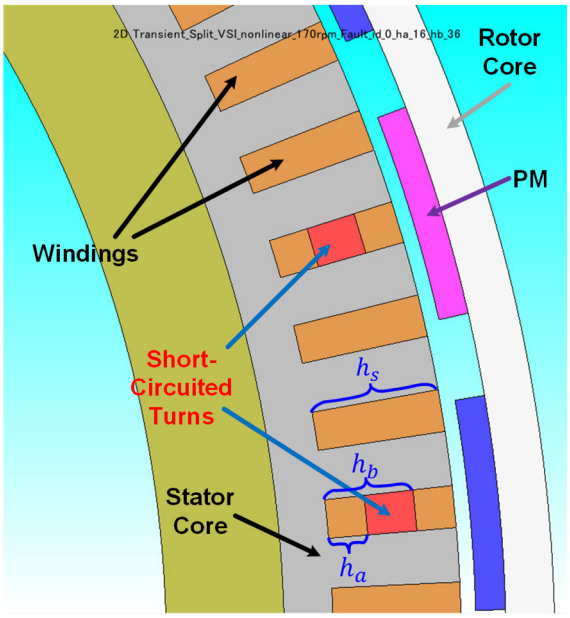

Fig. 2.4 Cross-sectional view of the machines with the ITSC fault for FE simulations. In this figure, only one section of the full model is shown.

Furthermore, the faulty machine is excited by voltage sources to fully reflect the fault characteristics in FE simulations, as shown in Fig. 2.5.

In Fig. 2.4, the 15 healthy coils are represented by one FEM coil (A_1_15) in the FE simulation and the faulty coil with the ITSC fault is represented by three FEM coils in Fig. 2.5. For example, the remaining healthy turns at the bottom, the top, and the short-circuited turns in the middle of the affected slot are represented by A_16_hb, A_16_ht, and A_16_fm, respectively. This arrangement will lead to balanced three phase back-EMFs when the switch in Fig. 2.5 is off, i.e., the machine is healthy.

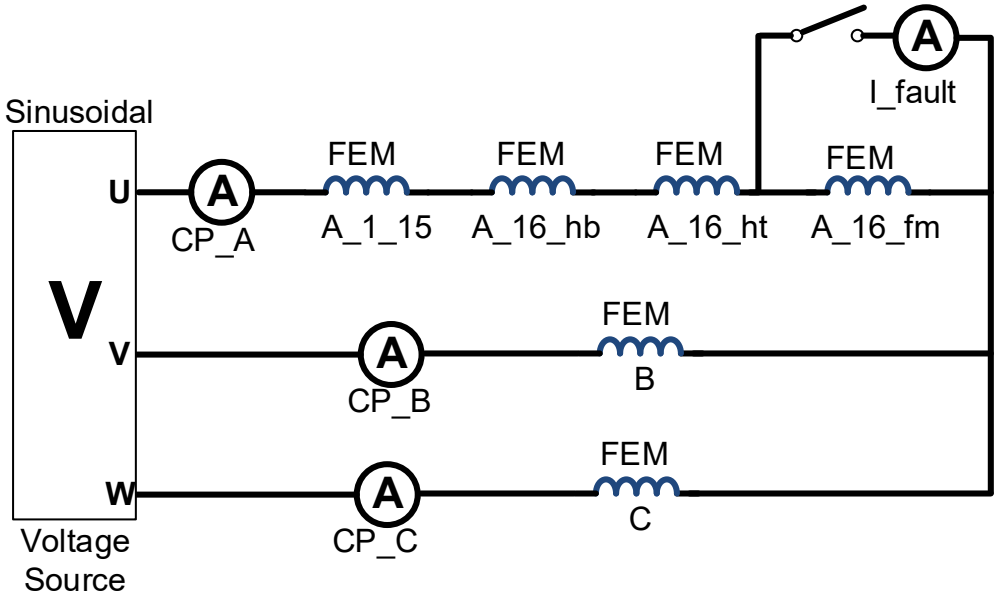

Fig. 2.5 External circuit for the ITSC fault simulations.

2.3 Inductance Calculation

One of the most important parts of fault modelling is to determine the parameters in the fault model, especially the inductances. Experimental measurement and theoretical calculation are two typical ways to obtain inductances in the healthy and fault models. However, experimental measurement of inductances for different fault scenarios (under ITSC faults) would be impossible at a machine design stage.

In [49], [111], [112], the researchers have made a simple assumption about the determination of the elements in the faulty inductance matrix (under ITSC fault), which assumes that they could be obtained from the inductances of the healthy machines. However, the validity of that assumption under fault are neither confirmed by FE simulations nor by the conventional analytical method for inductance calculation, i.e., WFA. Hence, whether it could be applied to multipole SPM machines is questionable. The only advantage of making that simple

assumption is that the faulty inductance matrix in the fault model could be determined from the calculated or measured phase self- and mutual-inductances of the healthy machines.

In [99], a more accurate approach, based on FE modelling only, is adopted to calculate the inductances under ITSC fault. One important conclusion in [99] is that the pole number has a significant influence on the values of the inductance of the short-circuited turns under ITSC faults. However, the assumption that the mutual-inductances between any two coils are the same is not valid, which can be proven by WFA and FE. This is mainly because two coils that are closer to each other will have larger mutual-inductance values, whilst the ones that are further apart will have smaller values.

2.3.1 Calculation of Inductances

In [134], the phase self- and mutual-inductances are considered to have three components:

$$\begin{cases} L_{ph} = L_g + L_{ls} = L_g + L_{slot} + L_{end} \\ M_{ph} = M_g + M_{ls} = M_g + M_{slot} + M_{end} \end{cases} \tag{2.6}$$

where L_g, M_g are the air-gap components and L_{ls}, M_{ls} are the leakage components, respectively. L_{slot}, M_{slot} are the slot-leakage components, and L_{end} and M_{end} are the end-turn leakage components, respectively. It is worth noting that for long-drum-type SPM machines, the aspect ratio of which, defined as the ratio of stack length to pole pitch, is large and therefore the end-winding leakage components can be neglected. For the studied 3kW, 0.5MW and 3MW machines, the aspect ratios of them are 2.92, 8.32, and 12.64, respectively. Hence 2D FE simulations are enough to ensure the accuracy of the calculated inductances.

The final inductance matrix now is split into two parts, i.e., air-gap component $\boldsymbol{L}'_{ms}$ and slot-leakage component $\boldsymbol{L}'_{ls}$.

$$\begin{bmatrix} L_{AA} & M_{AB} & M_{AC} & -(M_{f,Ah} + L_f) \\ M_{BA} & L_{BB} & M_{BC} & -M_{Bf} \\ M_{CA} & M_{CB} & L_{CC} & -M_{Cf} \\ (M_{f,Ah} + L_f) & M_{fB} & M_{fC} & -L_f \end{bmatrix} = \boldsymbol{L}'_{ms} + \boldsymbol{L}'_{ls} \tag{2.7}$$

Calculation of air-gap inductance components is done by WFA. Air-gap component of inductances can be calculated by [135]:

$$L_{ij} = \frac{\mu_0 r_e l_e}{g_e} \int_0^{2\pi} N_i(\phi_s) N_j(\phi_s)\, \mathrm{d}\phi_s \tag{2.8}$$

where l_e is the effective stack length, r_e is the mean air-gap radius, g_e is the effective air-gap length, μ_0 is the permeability of free space. Both g_e and r_e for SPM machines can be

calculated using the method in [134]. $N_i(\phi_s)$ and $N_j(\phi_s)$ are the winding functions of the ith and jth windings, respectively. When an ITSC fault happens, the healthy phase winding is split into two parts: faulty winding and remaining healthy winding. The corresponding winding functions after fault (the influence of the slot opening on the derivation of winding functions is neglected) is illustrated in Fig. 2.6, which will be used to get the air-gap components of the inductances in these two windings.

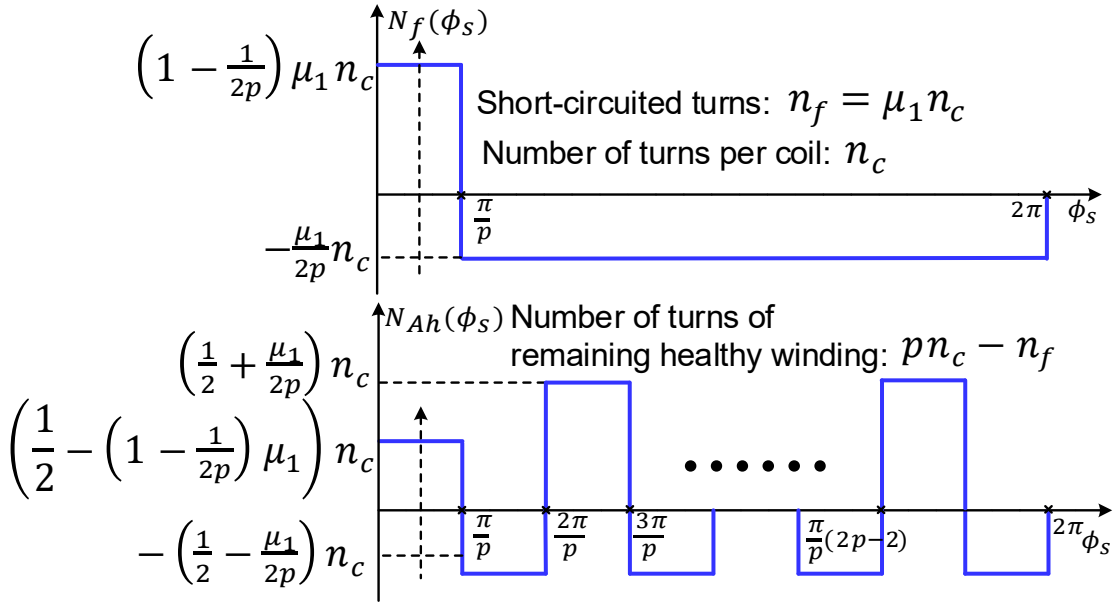

Fig. 2.6 Winding functions of the faulty winding (Phase A).

The air-gap inductance component of phase A is

$$L_{Ag} = \frac{\mu_0 r_e l_e}{g_e}\frac{\pi}{2}(n_c)^2 \tag{2.9}$$

After some arrangements, the air-gap component inductance matrix is expressed as follows:

$$\boldsymbol{L}'_{ms} = L_{Ag}\begin{bmatrix} 1 & -\frac{1}{3} & -\frac{1}{3} & -\mu \\ -\frac{1}{3} & 1 & -\frac{1}{3} & \frac{\mu}{3} \\ -\frac{1}{3} & -\frac{1}{3} & 1 & \frac{\mu}{3} \\ \mu & -\frac{\mu}{3} & -\frac{\mu}{3} & -\mu^2(2p-1) \end{bmatrix} \tag{2.10}$$

Slot-leakage inductance component calculation is based on the slot permeance method in [113]. For the studied PM machines with open slot shown in Fig. 2.7, the slot-leakage inductance components can be written as

$$\boldsymbol{L}'_{ls} = \begin{bmatrix} L_{ls,A} & 0 & 0 & -(M_{ls\_Ah,f} + L_{ls,f}) \\ 0 & L_{ls,B} & 0 & 0 \\ 0 & 0 & L_{ls,C} & 0 \\ M_{ls\_Ah,f} + L_{ls,f} & 0 & 0 & L_{ls,f} \end{bmatrix} \tag{2.11}$$

where $L_{ls,A}$, $L_{ls,B}$, $L_{ls,C}$, $L_{ls,f}$ are the slot-leakage components of self-inductances of phases A, B and C and the short-circuited turns, respectively. $M_{ls\_Ah,f}$ is the slot-leakage component of mutual inductance between the remaining healthy phase winding and the short-circuited turns.

According to Fig. 2.7, the unknown inductances in the slot-leakage inductance matrix are derived as

$$L_{ls,A} = L_{ls,B} = L_{ls,C} = 2p\mu_0 l_e \left(\frac{n_c}{h_s}\right)^2 \frac{(h_s)^3}{3S_\omega} \tag{2.12}$$

$$L_{ls,f} = 2\mu_0 l_e \left(\frac{n_c}{h_s}\right)^2 \frac{(h_b - h_a)^2}{S_\omega} \left(h_s - \frac{1}{3}h_a - \frac{2}{3}h_b\right) \tag{2.13}$$

$$M_{ls\_f,Ah} = M_{ls\_Ah,f} = 2\mu_0 l_e \left(\frac{n_c}{h_s}\right)^2 \left[\frac{h_a(h_b - h_a)^2}{2S_\omega} + \frac{(h_b - h_a)}{2S_\omega}\{(h_s - h_b + h_a)^2 - h_a^2\}\right] \tag{2.14}$$

where S_ω is the slot width, h_s is the slot height, h_a and h_b represent the fault locations along the slot (see Fig. 2.4), and $n_f = n_c(h_b - h_a)/h_s$ represents the number of short-circuited turns.

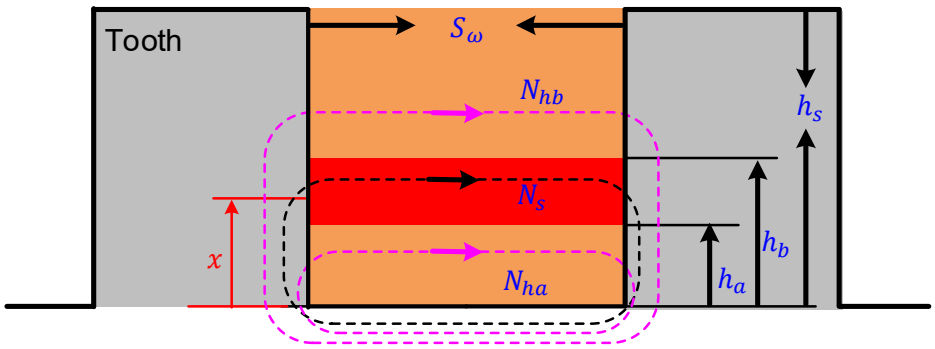

Fig. 2.7 Flux distribution in open slot caused by remaining healthy winding.

2.3.2 Results of Inductances

To simplify the inductance calculation by FE simulations, one coil short-circuit fault is assumed first for the 3kW, 0.5MW and 3MW SPM machines. The machine specifications are given in Table 2.1, in which the rated voltage and current of the 0.5MW, 3MW machines have been adjusted due to the change of series/parallel connected coils into series connected coils.

To be consistent with WFA, in the FE model, the permanent magnets have been replaced by air, and the stator and rotor cores are assumed to be linear magnetic material with a relative permeability $\mu_r = 10000$. The inductances required in the fault model of the 3kW, 0.5MW, and 3MW machine calculated by FE and analytical methods are shown in Table 2.2, Table 2.3, and Table 2.4.

Table 2.1 Key parameters of the studied SPM machines

Rated power	3kW	0.5MW	3MW
Rated speed (rpm)	170	32	15
Line-line rated voltage (Vrms)	690	4830	13800
Phase current (Arms)	2.5	62.6	139.5
Series turns/coil	52	23	14
Numbers of slots/poles	96/32	294/98	480/160
Rotor outer diameter (mm)	426.4	2195.5	5000
Stack length (mm)	110	550	1200
Airgap length (mm)	2	2.15	5

Table 2.2 Some inductances in mH of the 3kW machine under one coil short-circuit fault

Method	$L_{AA}/L_{BB}/L_{CC}$	$M_{AB}/M_{BC}/M_{CA}$	M_{Bf}/M_{Cf}	$M_{Ah,f}$	L_f
2D FE	31.62	-6.1	-0.382	-1.038	3.02
Analytical	31.96	-6.627	-0.414	-1.165	3.16
RE (%)	1.1	8.6	8.4	12.2	4.8

Note: 'relative error' is abbreviated to 'RE'.

Table 2.3 Some inductances in mH of the 0.5MW machine under one coil short-circuit fault

Method	$L_{AA}/L_{BB}/L_{CC}$	$M_{AB}/M_{BC}/M_{CA}$	M_{Bf}/M_{Cf}	$M_{Ah,f}$	L_f
2D FE	182.55	-25.33	-0.518	-1.42	5.14
Analytical	188.98	-27.37	-0.559	-1.64	5.5
RE (%)	3.52	8	7.9	15.6	7

Note: 'relative error' is abbreviated to 'RE'.

Table 2.4 Some inductances in mH of the 3MW machine under one coil short-circuit fault

Method	$L_{AA}/L_{BB}/L_{CC}$	$M_{AB}/M_{BC}/M_{CA}$	M_{Bf}/M_{Cf}	$M_{Ah,f}$	L_f
2D FE	150	-18.9	-0.24	-0.66	2.53
Analytical	145.98	-20.1	-0.25	-0.74	2.57
RE (%)	-2.7	6.35	6.4	13	1.5

Note: 'relative error' is abbreviated to 'RE'.

It can be found that there is generally a reasonably good match between the FE and analytical results although the discrepancy for the mutual inductances is relatively larger. This relatively large difference in the mutual inductances is mainly due to the fact that, in WFA, the negative part of the air-gap flux density (or magneto-motive force) generated by the short-circuited coil is assumed to be constant at different angular positions, as shown in Fig. 2.6. This is not the case as predicted by the FE model, which shows that the air-gap flux density far away from the short-circuited coil has reduced value.

2.4 Simulation Results

2.4.1 One Coil Short-Circuit Fault

Due to the limitation of voltage source excitation in the FE simulations, three phase balanced sinusoidal voltages are fed to the studied 3kW SPM machine and its rotor mechanical speed is kept constant during the whole operation period. It is worth mentioning that the FE simulations for the 0.5MW and 3MW SPM machines using the same method with the Dell Precision Tower 5820 PC workstation would take more than one month to complete, hence the FE simulations for those machines using voltage source excitation have not been carried out. In this section, one coil short-circuit fault has been selected as an example, and the results for a single turn short-circuit fault will be introduced in section 2.4.2.

2.4.1.1 Linear Magnetic Core Material

To validate the proposed analytical model, a core material with a relative permeability $\mu_r = 10000$ is used first. Fig. 2.8 shows the currents in the healthy and short-circuited coils before and after one coil short-circuit. Here, the 3kW machine operates under rated condition and with $i_d = 0$ control. In Fig. 2.8, the legend of the proposed analytical model is marked as "Proposed", the direct FE simulation results are labelled with "FE", and the results obtained using the analytical model proposed in [49] have also been added for the purpose of comparison.

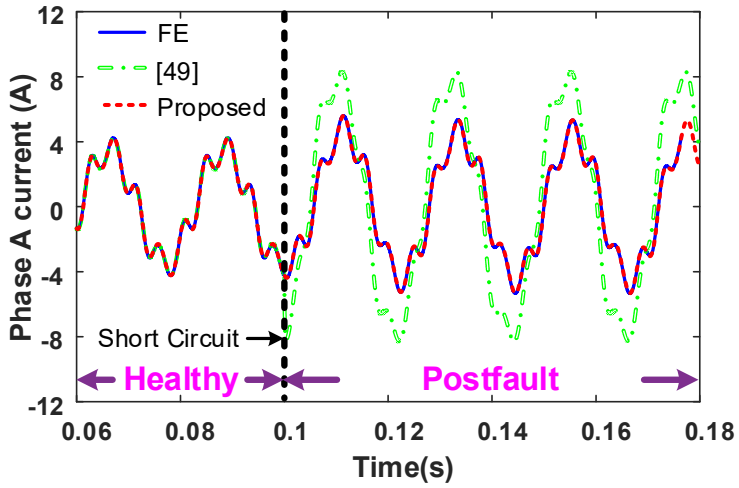

(a) Current in healthy coils

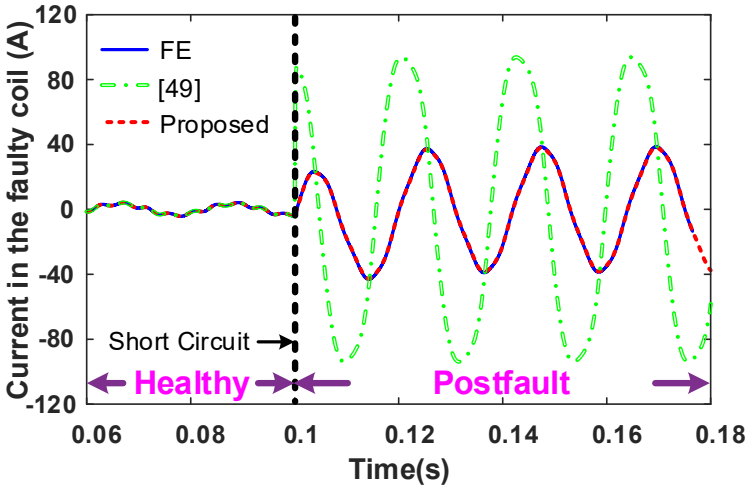

(b) Currents in the short-circuited coil

Fig. 2.8 Currents in the healthy coils and the short-circuited coil before and after one coil short-circuit.

From Fig. 2.8, without considering the core saturation, a very good match (the errors between the currents of the analytical and FE models are less than 1%) can be observed between the results obtained by the proposed analytical (based on Matlab/Simulink) and the FE models. However, if the influence of the pole number and the spatial distribution of coils on the determination of the inductances under the ITSC faults is neglected like that in [49], the phase current and the faulty coil current will be overestimated. In addition, the change in currents due to the one-coil short-circuit fault is also obvious. This is particularly the case for the current in the faulty coil, the peak value of which has increased from 4.24A to 38.6A. The change in phase currents and faulty coil current will also have an impact on the electromagnetic torque generated by the machine, as shown in Fig. 2.9.

It is worth noting that the cogging torque obtained by the FE model has already been incorporated into the Simulink model to accurately capture the torque ripple characteristic before and after the one coil short-circuit fault. It can be observed that although there is a slight discrepancy, both models predict a slight increase in torque ripple after the one-coil short-circuit fault.

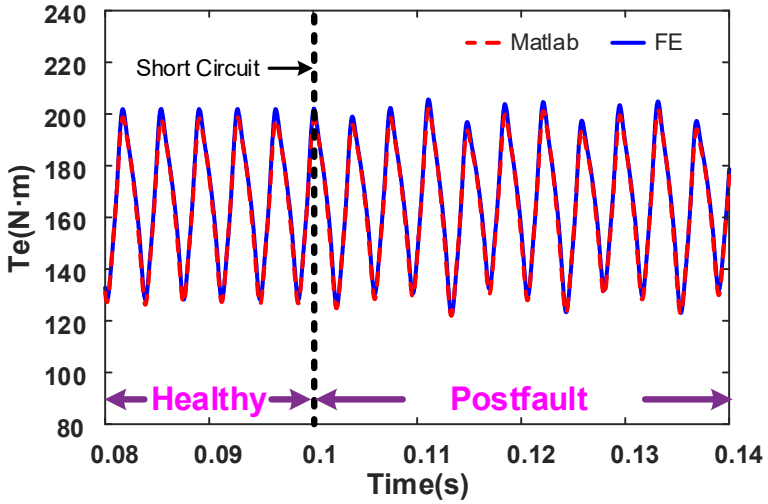

Fig. 2.9 Change of on-load torque of the 3kW SPM machine before and after the one coil short-circuit fault.

To validate the accuracy of the proposed analytical model under different operating conditions, Fig. 2.10 shows the results of peak currents of phase A and the short-circuited coil before and after the one coil short-circuit fault.

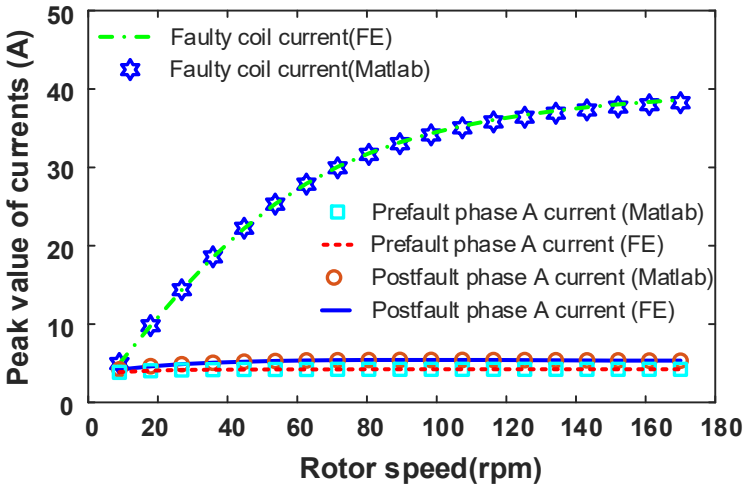

Fig. 2.10 Peak values of phase A currents of the 3kW SPM machine before and after one coil short-circuit fault.

As with the previous analysis, the phase current (essentially *q*-axis current) is maintained constant to produce the rated torque and only the rotor speed is changed. The good agreement in the simulated results at different rotor speeds further confirms that the proposed analytical model is accurate.

2.4.1.2 Nonlinear Magnetic Core Material

If the core saturation is considered, there will be some discrepancy between the simulated results obtained by the proposed analytical (based on Matlab/Simulink) and the non-linear FE models, as shown in Fig. 2.11. In order to improve the model accuracy while considering the core saturation effect in the Simulink model, the proposed method in Fig. 2.3 has been employed. As can be seen from Fig. 2.11 that the error between the currents of the analytical and FE models is now reduced from 16% to 8%. It should be mentioned that only one iteration in Fig. 2.3 is used to obtain the on-load PM flux linkages and the saturated inductances in the Simulink model. This is why there is still an 8% difference between the analytical and FE fault currents. More iterations will reduce this difference further but will be more time consuming and add extra model complexity.

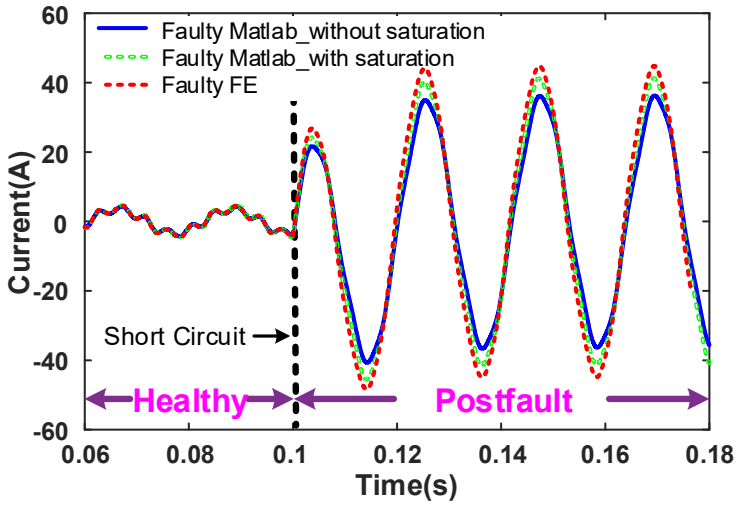

Fig. 2.11 Currents in the faulty coil when the saturation is considered in the analytical and FE models.

2.4.2 Single Turn Short-Circuit Fault

Similar to the one coil short-circuit fault, the single turn short-circuit fault has also been investigated, and the results are shown in Fig. 2.12. A generally good agreement can be observed between the results obtained by the analytical (based on Matlab/Simulink) and the FE models.

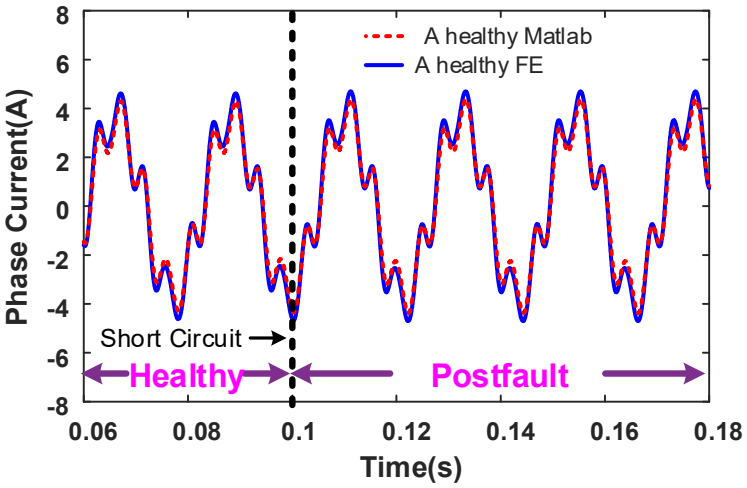

(a) Current in the healthy coils

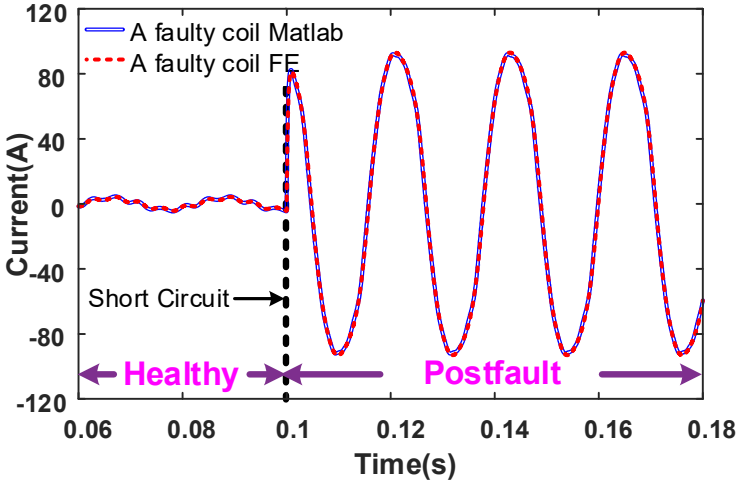

(b) Current in the short-circuited turn

Fig. 2.12 Currents in the healthy coils and short-circuited turn before and after one turn short-circuit fault.

It is noticed that under the single turn short-circuit fault, the faulty phase turn ratio is $\mu = 1/832$, which is too small to cause variations in current waveforms in the healthy windings. However, as expected, the single turn short-circuit leads to the highest short-circuit current (almost 27 times the rated current while for the one coil short circuit fault, it is about 10 times). This extremely large single turn short-circuit current could lead to serious local overheating problems. Therefore, it is still important to detect such faults in order to take measures to prevent further damage to the machine. However, this is out of scope of this thesis and would be part of our future research.

The peak currents at different rotor speeds under single turn short-circuit fault have also been simulated, as shown in Fig. 2.13. Interestingly, the single turn short circuit current seems to

increase linearly with the rotor speed for the full investigated speed range. This phenomenon can be explained by using the voltage equation of the short-circuited path to predict the amplitude of the short-circuited current.

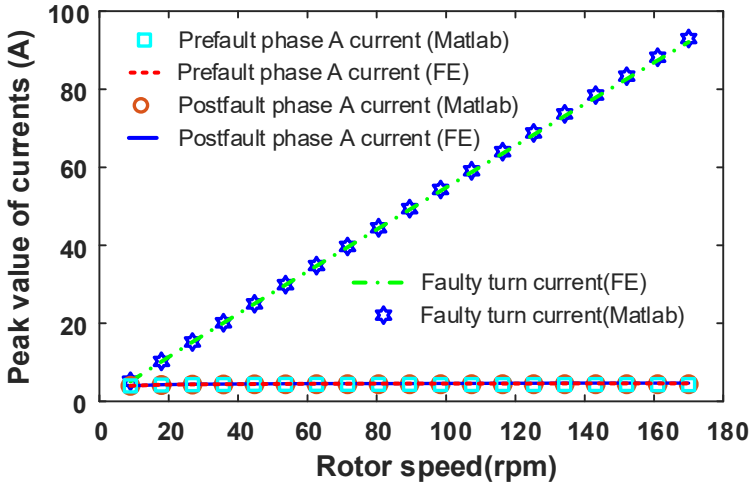

Fig. 2.13 Peak currents in phase A of the 3kW SPM machine before and after single turn short-circuit fault.

To simplify the analysis, it is assumed that after the ITSC fault, the motor currents are almost unchanged. If all harmonics in the phase currents and back-EMFs are neglected, then the following equation to predict the amplitude of the short-circuited current for the 3kW SPM machine is valid

$$I_f \approx \frac{\mu\omega_r\lambda_m}{\sqrt{(\mu R_s)^2 + \left(\omega_r L_f\right)^2}} \tag{2.15}$$

where λ_m is the amplitude of the open-circuit phase flux linkage. When the rotor speed is low, the resistance in the denominator of (2.15) is much greater than the reactance, thus the amplitude of the short-circuited current increases linearly with the rotor speed. If the rotor speed goes higher and higher, the reactance will become the more important term in the denominator, and the amplitude of the short-circuited current will become almost constant, similar to what is shown in Fig. 2.10. It is estimated that the maximum short-circuit current for the one coil short-circuit fault is about 40.5A. However, the maximum single-turn short-circuit current is much higher, up to 1419.9A. If $\omega_r L_f = 1/3\mu R_s$ is used as the critical point for the "linear region" in the current-speed curves, then for the one-coil short-circuit fault, the critical rotor speed is about 23rpm, beyond which the increase rate of short-circuit current reduces. However, for the single turn short-circuit fault, the critical rotor speed for the "linear region"

is around 803rpm. This means that the single-turn short-circuit current will increase linearly with rotor speed within a quite wide speed range.

2.4.3 Performance Comparison of Different Power Ratings

It is worth noting that the proposed analytical model is general for all SPM machines with series-connected coils and can be used to investigate the fault performance of SPM machines with different power ratings. A comparison in terms of fault tolerant capability amongst SPM machines with different power ratings, e.g. 3kW, 0.5MW and 3MW has been carried out, and the results are shown in Fig. 2.14 and Fig. 2.15.

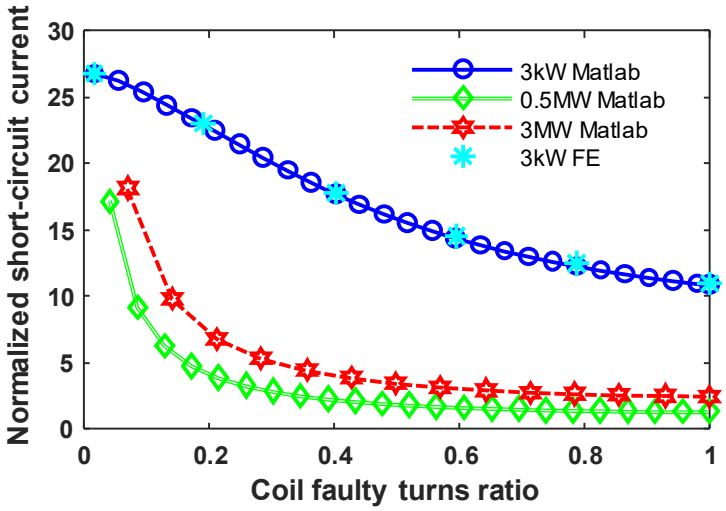

Fig. 2.14 Normalized short-circuit current *vs* coil faulty turns ratio.

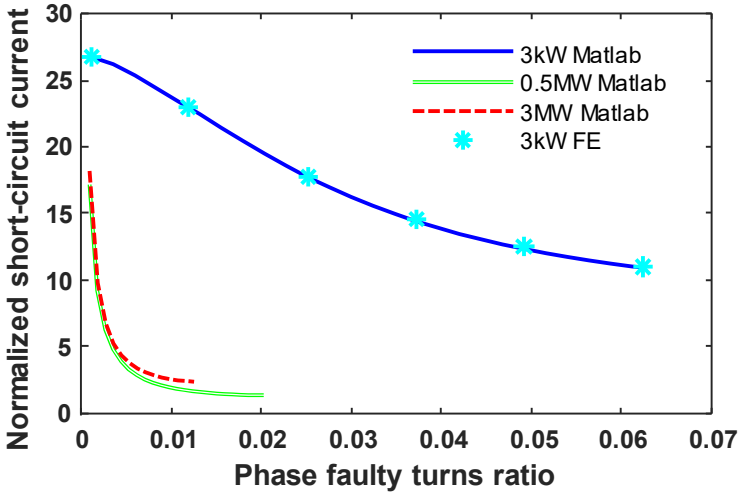

Fig. 2.15 Normalized short-circuit current *vs* phase faulty turns ratio.

In this comparative study, considering that the core saturation will not lead to a big difference in predictions of the short-circuited current, hence the linear model is used for simplicity. In Fig. 2.14 and Fig. 2.15, FE simulations of single turn, 10 turns, 21 turns, 31turns, 41 turns and

one entire coil short-circuited faults for the 3kW machine have been carried out to compare against the analytical model based on Matlab/Simulink.

However, the FE modelling for higher power ratings is significantly time consuming because large number of slots and poles exist and full models are needed when inter-turn short-circuits occur, and hence it has not been carried out in this chapter. In addition, all data points in Fig. 2.14 and Fig. 2.15 are obtained when the machine operates under rated condition and with i_d = 0A control. It is apparent from Fig. 2.14 and Fig. 2.15 that large-power SPM machines with series-connected coils are generally more fault-tolerant to the ITSC fault, but they are still vulnerable to ITSC fault when a relatively small number of turns are short-circuited.

2.5 Conclusion

This chapter presents a general analytical model for evaluation of fault performance of multipole PM wind power generators with different power ratings under inter-turn short-circuit (ITSC) faults. Simulation results from 2D FE and Simulink models match quite well when a linear magnetic material is used, which verifies the accuracy of the proposed analytical model. It is found that the influence of pole number and spatial distribution of the coils on the determination of inductances under ITSC faults cannot be neglected when the number of short-circuited turns in one coil is large. It is also found that the developed analytical model could be used to obtain current profiles, which can be used as inputs in the nonlinear FE fault model to obtain the saturated inductances and on-load PM flux linkages in order to improve the accuracy of the predicted fault performance under core saturation. As for the fault-tolerant capability, large power machines with all coils connected in series are generally much more fault-tolerant to ITSC fault. However, they are still vulnerable to ITSC faults when relatively small number of turns are short-circuited.

Chapter 3 Fault Modelling and Analysis of SPM Machines with Parallel-Connected Coils

This chapter presents a general analytical fault model in a compact matrix form for surface-mounted permanent magnet (SPM) machines with parallel-connected coils, which is useful to study the machine performance under the inter-turn short circuit (ITSC) fault. Then the multiphase Clarke transformation has been proposed to simplify the fault model. In the model, the branch currents rather than the phase currents are employed as state variables to describe machine behaviours under fault. Additionally, self- and mutual-inductances are obtained by winding function approach (WFA) plus slot permeance method. The proposed analytical fault model is applied to a 3 kW 96-slot 32-pole SPM machine and validated by time-stepping FE simulations.

Related Publications:

[MEI23b] Z. T. Mei, G. J. Li, Z. Q. Zhu, R. Clark, A. Thomas, and Z. Azar, "Modelling and Analysis of Inter-Turn Short-Circuit Fault of PM Machines with Parallel-Connected Coils," *IEEE Trans. Energy Convers.*, vol. 38, no. 2, pp. 1268-1279, Jun. 2023.

3.1 Introduction

In chapter 2, a general analytical model of surface-mounted permanent magnet (SPM) machines with series-connected coils under ITSC faults was proposed, in which the inductances neglecting the end-turn leakage component under faults were calculated by analytical method, i.e., WFA plus slot permeance method. However, the fault modelling of medium and large-power electrical machines equipped with series-parallel-connected windings, although much more complicated, is more desirable [86], [87], [109].

In [109], the transient behaviour of the salient-pole synchronous machines with internal stator winding faults including ITSC fault was modelled by the multi-loop circuit method. In the developed fault model, stator branch currents were transformed into loop currents and used as state variables to consider the practical series-parallel winding configurations of salient-pole synchronous machines. The authors in [109] also concluded without proof that the accuracy of the simulation results using inductances determined by analytical techniques was similar to those with inductances obtained by linear FEA.

In [86], the authors calculated the machine inductances of a synchronous machine with series-parallel windings based on the WFA to study different internal faults like ground fault and phase-to-phase short circuit fault.

In [87], the authors explained the reason for choosing branch currents as state variables when a large-power electrical machine was subject to one type of internal faults. Furthermore, eight types of faults including the ITSC fault for a 370MVA salient-pole synchronous generator with fractional-slot winding are simulated using a Hypersim real-time simulator. However, the inductance calculation involved, and the large number of first-order differential equations required to establish the fault model make the internal fault modelling of large salient-pole synchronous generators quite complex and challenging. Furthermore, not much physical insight is provided.

Other researchers in [109] tried to simplify the calculation of large number of inductances in the analytical fault model. However, their assumptions may not be easily applicable to other types of machines.

Despite the progress made by the authors in [86], [87], [109], [136], no relatively simple and general analytical fault model has been developed, which is mainly due to the saliency and complex winding arrangement of synchronous machines.

In [88], the authors proposed some ITSC fault models of fractional-slot SPM machines employing series and parallel winding connections. It was assumed that all branch currents in

healthy phases (phases B and C) were equal when the ITSC fault occurred in one of the faulty phase (phase A) branches of a 6-pole-9-slot SPM motor. This may not be true for integer-slot SPM machines. In [89], the authors analysed different modes of ITSC fault in SPM motors with multi-strand windings and made the same assumption as that of [88]. However, both [88] and [89] did not provide a relatively simple analytical method to obtain the inductances in the fault model.

Unlike the progress made by [86]–[89], [109], this chapter proposes a relatively simple general analytical model in a compact matrix form for SPM machines with parallel-connected coils under inter-turn short circuit (ITSC) fault. Then the multiphase Clarke transformation has been proposed to simplify the fault model. It is worth mentioning that, in this chapter, the core saturation has been neglected for inductance calculation using the developed analytical technique and for fault model simplification using the multiphase Clarke transformation.

In the fault model, branch currents rather than the phase currents are used as state variables to describe the machine behaviours under ITSC fault. In addition, to simplify the process of inductance calculation, the windings of the analysed SPM machines are integer slot, single-layer, and distributed (slot/pole/phase (SPP) equal to 1), which are often the cases for winding structures adopted by large SPM wind power generators. Based on this simple winding configuration, inductances in the fault model have been obtained by winding function approach (WFA) plus slot permeance method.

Particular attention has also been paid to the one-coil short-circuit fault, which is equivalent to the phase short-circuit fault for the winding configuration (one coil per parallel branch) investigated in this chapter. The proposed fault model is applied to a 3kW 96-slot 32-pole SPM machine, which is built in Matlab/Simulink and validated by time stepping FE simulations. It is worth mentioning that in this chapter, the core saturation has been neglected during the inductance calculation and simulations. However, in chapter 7, on the experimental validation of the developed fault model, nonlinear inductances obtained from both measurement and 3D FE models are employed. More details will be given in chapter 7.

3.2 Modelling of ITSC Fault of SPM Wind Generator

This section gives a brief introduction to the analytical and FE modelling of ITSC fault of SPM wind generator with parallel-connected coils.

3.2.1 Analytical Modelling Neglecting the Core Saturation

One example of the parallel-connected coils of the studied SPM machine under an ITSC fault is shown in Fig. 3.1, where the fault is assumed to occur in the first branch of phase A. As mentioned previously, the winding of the analysed SPM machines is integer slot, single-layer, and distributed, as shown in Fig. 3.2. This means that the number of coils in one phase winding is identical to the number of pole pairs p, and for the studied 96-slot 32-pole SPM machine, $p = 16$. This can be seen in Fig. 3.1, i.e., when one parallel branch has one coil only, 16 parallel branches will contain 16 coils in total.

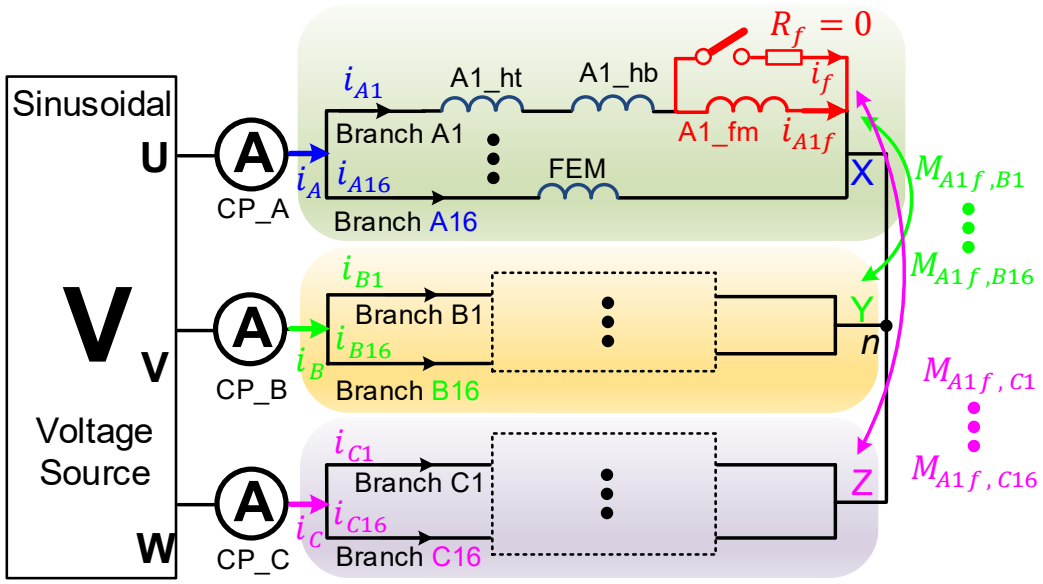

Fig. 3.1 Circuit schematic of the studied PM machines under an ITSC fault.

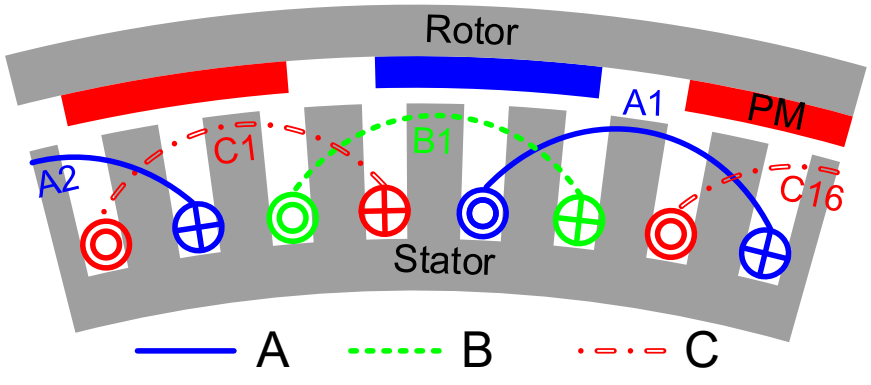

Fig. 3.2 Cross-section of the studied SPM machine with overlapping windings.

In addition, to simplify the analyses, the short-circuited turns of the faulty coil A1 are labelled as A1_fm, and the remaining healthy turns are marked as A1_ht and A1_hb, the meanings of which will be detailed in section 3.2.2. The mutual inductances between the short-

circuited turns and other coils such as $M_{A1f,A16}$, $M_{A1f,B1}$, and $M_{A1f,C16}$, etc. are also shown in Fig. 3.1.

From Fig. 3.1, the circuit branch voltage equations representing the relationship between branch-to-neutral voltages, EMFs, and branch currents under ITSC fault can be written in a compact matrix form as

$$\begin{bmatrix}\mathbf{v}_A\\ \mathbf{v}_B\\ \mathbf{v}_C\end{bmatrix}=\begin{bmatrix}\mathbf{L}_{AA} & \mathbf{M}_{AB} & \mathbf{M}_{AC}\\ \mathbf{M}_{BA} & \mathbf{L}_{BB} & \mathbf{M}_{BC}\\ \mathbf{M}_{CA} & \mathbf{M}_{CB} & \mathbf{L}_{CC}\end{bmatrix}\frac{\mathrm{d}}{\mathrm{d}t}\begin{bmatrix}\mathbf{i}_A\\ \mathbf{i}_B\\ \mathbf{i}_C\end{bmatrix}+R_{\mathrm{coil}}\begin{bmatrix}\mathbf{i}_A\\ \mathbf{i}_B\\ \mathbf{i}_C\end{bmatrix}+\begin{bmatrix}\mathbf{e}_A\\ \mathbf{e}_B\\ \mathbf{e}_C\end{bmatrix}-\begin{bmatrix}R_{A1f}\\ 0\\ \vdots\\ 0\end{bmatrix}i_f-\begin{bmatrix}\mathbf{M}_{Af}\\ \mathbf{M}_{Bf}\\ \mathbf{M}_{Cf}\end{bmatrix}\frac{\mathrm{d}i_f}{\mathrm{d}t} \tag{3.1}$$

where **v, i,** and **e** are column vectors representing branch-to-neutral voltages (v), branch back-EMFs (e) or branch currents (i) for the phases A, B and C windings. Each column vector has p entries, and p is the number of pole pairs as mentioned previously. For example, the column vector $\mathbf{v}_A=[v_{A1}\quad v_{A2}\quad\cdots\quad v_{Ap}]^T$ has a size of $p\times 1$. Additionally, i_f is the current in the short-circuit path as shown in Fig. 3.1. As for $\mathbf{L}_{AA}$, $\mathbf{M}_{AB}$, $\mathbf{M}_{AC}$ and $\mathbf{M}_{BC}$, they describe the inductive coupling between two coils/branches in the same phase or in two different phases. In this thesis, they are termed as branch inductance matrices and expressed as

$$\mathbf{L}_{xx}=\begin{bmatrix}L_{x1x1} & M_{x1x2} & M_{x1x3} & \cdots & M_{x1xp}\\ M_{x2x1} & L_{x2x2} & M_{x2x3} & \cdots & M_{x2xp}\\ M_{x3x1} & M_{x3x2} & L_{x3x3} & \cdots & M_{x3xp}\\ \vdots & \vdots & \vdots & \ddots & \vdots\\ M_{xpx1} & M_{xpx2} & M_{xpx3} & \cdots & L_{xpxp}\end{bmatrix} \tag{3.2}$$

$$\mathbf{M}_{xy}=\left(\mathbf{M}_{yx}\right)^T=\begin{bmatrix}M_{x1y1} & M_{x1y2} & M_{x1y3} & \cdots & M_{x1yp}\\ M_{x2y1} & M_{x2y2} & M_{x2y3} & \cdots & M_{x2yp}\\ M_{x3y1} & M_{x3y2} & M_{x3y3} & \cdots & M_{x3yp}\\ \vdots & \vdots & \vdots & \ddots & \vdots\\ M_{xpy1} & M_{xpy2} & M_{xpy3} & \cdots & M_{xpyp}\end{bmatrix} \tag{3.3}$$

where x and y designate the phase windings, namely, A, B and C. $\mathbf{L}_{xx}$ describes all the inductive couplings of the same or different coils/branches in the same phase winding, and $\mathbf{M}_{xy}$ describes the inductive couplings between two different coils/branches in two different phase windings. In addition, both of them have the size of $p\times p$, and p is the number of pole pairs.

For example, in (3.2), L_{AiAi} $(i=1,2,\cdots,p)$ is the self-inductance of branch Ai winding, and M_{AiAj} $(i\neq j; i=1,2,\cdots,p; j=1,2,\cdots,p)$ is the mutual inductance between two different branches Ai and Aj in phase A winding. Similar explanation applies to other branch inductance matrices. It is worth noting that all these branch inductance matrices are circulant matrices.

One important characteristic of circulant matrices is that the elements of each row are identical to those of the previous row, but are moved one position to the right and wrapped around [105], [137]. Its mathematical form is as follows

$$\operatorname{circ}(c_0, c_1, \cdots, c_{p-1}) = \begin{bmatrix} c_0 & c_1 & c_2 & \cdots & c_{p-1} \\ c_{p-1} & c_0 & c_1 & \cdots & c_{p-2} \\ c_{p-2} & c_{p-1} & c_0 & \cdots & c_{p-3} \\ \vdots & \vdots & \vdots & \ddots & \vdots \\ c_1 & c_2 & c_3 & \cdots & c_0 \end{bmatrix} \tag{3.4}$$

In addition, R_{coil} in (3.1) is the coil resistance, and R_f is the contact resistance between short-circuited points. In the following case studies for the 3kW machine, R_f is set to be zero for simplicity.

For the short-circuited path, the voltage equation is expressed as

$$\begin{aligned} &\left(R_f + R_{A1f}\right) i_f + L_{A1f,A1f} \frac{\mathrm{d}i_f}{\mathrm{d}t} - e_{A1f} - R_{A1f} i_{A1} \\ &\qquad = \left(\mathbf{M}_{Af}\right)^T \frac{\mathrm{d}\mathbf{i}_A}{\mathrm{d}t} + \left(\mathbf{M}_{Bf}\right)^T \frac{\mathrm{d}\mathbf{i}_B}{\mathrm{d}t} + \left(\mathbf{M}_{Cf}\right)^T \frac{\mathrm{d}\mathbf{i}_C}{\mathrm{d}t} \end{aligned} \tag{3.5}$$

Regarding the short-circuited turns, R_{A1f}, $L_{A1f,A1f}$, and e_{A1f} are their resistance, self-inductance, and back EMF. It could be easily found that $e_{A1f} = \mu_1 e_A$, in which the coil faulty turn ratio in one phase winding is defined as $\mu_1 = n_f/n_c$ for the studied integer-slot SPM machines. As for n_f and n_c, they are the number of short-circuited turns in one coil and the total number of turns per coil, respectively. The last remaining terms, $\mathbf{M}_{Af}$, $\mathbf{M}_{Bf}$, and $\mathbf{M}_{Cf}$, are faulty inductance vectors related to the short-circuited turns and they can be written as

$$\begin{cases} \mathbf{M}_{Af} = [L_{A1f,A1f} + M_{A1h,A1f} \quad M_{A2,A1f} \quad \cdots \quad M_{Ap,A1f}]^T \\ \mathbf{M}_{Bf} = [M_{B1,A1f} \quad M_{B2,A1f} \quad \cdots \quad M_{Bp,A1f}]^T \\ \mathbf{M}_{Cf} = [M_{C1,A1f} \quad M_{C2,A1f} \quad \cdots \quad M_{Cp,A1f}]^T \end{cases} \tag{3.6}$$

It can be seen that $L_{A1f,A1f}$ is the self-inductance of the short-circuited turns and $M_{A1h,A1f}$ represents the mutual inductance between the remaining healthy turns and short-circuited turns of the faulty coil, A1.

For the Y-connected stator windings with parallel coil connection, the sum of three phase currents must be zero as described by

$$\sum_{k=1}^{p} i_{Ak} + \sum_{k=1}^{p} i_{Bk} + \sum_{k=1}^{p} i_{Ck} = 0 \tag{3.7}$$

Furthermore, if the branch back-EMFs in (3.1) contain harmonics and no neutral line is introduced, then the branch-to-neutral voltages cannot be directly obtained from the line

voltages under ITSC fault. Considering the "circulant" characteristic of the above branch inductance matrices and current constraints, the sum of the 3-phase voltages will be

$$v_A + v_B + v_C = (e_A + e_B + e_C) - \frac{1}{p}\left[R_{A1f} i_f + \left(\sum_{k=1}^{p} \left(\mathbf{M}_{Af} + \mathbf{M}_{Bf} + \mathbf{M}_{Cf}\right)_k\right) \frac{\mathrm{d}i_f}{\mathrm{d}t}\right] \tag{3.8}$$

where v_A, v_B, and v_C are the three branch-to-neutral voltages. On the other hand, e_A, e_B, and e_C are the three branch back-EMFs. It is worth noting that all the branch-to-neutral voltages belonging to the same phase such as v_{A1} to v_{Ap} and the corresponding branch back-EMFs are equal in the study. In the meantime, to be concise, $\left(\mathbf{M}_{Af} + \mathbf{M}_{Bf} + \mathbf{M}_{Cf}\right)_k$ is used to denote the k^{th} element of the sum of three faulty inductance vectors $\mathbf{M}_{Af}$, $\mathbf{M}_{Bf}$, and $\mathbf{M}_{Cf}$.

In addition, line voltages v_{AB} and v_{BC} can be expressed in terms of branch-to-neutral voltages v_A and v_B as

$$v_{AB} = v_A - v_B \tag{3.9}$$

$$v_{BC} = v_B - v_C = v_A + 2v_B - (v_A + v_B + v_C) \tag{3.10}$$

Equations (3.8), (3.9) , and (3.10) can be used to find the phase voltages (or branch-to-neutral voltages) from line voltages.

Once the currents in the healthy and faulty windings are determined, the torque under ITSC fault can be calculated by

$$T_e = p\frac{(\mathbf{e}_A)^T \mathbf{i}_A + (\mathbf{e}_B)^T \mathbf{i}_B + (\mathbf{e}_C)^T \mathbf{i}_C - e_{A1f} i_f}{\omega_r} + T_{cog} \tag{3.11}$$

where ω_r is the rotor electrical speed (rad/s), T_{cog} is the cogging torque calculated by using FEA.

From the above equations for the fault model, it can be seen that the complexity of the analytical fault model using branch currents as state variables in the stationary reference frame depends on the number of parallel branches. It is worth noting that the number of differential equations in the equivalent first-order system to describe the machine behaviour under ITSC fault is $3p + 2$ for the studied machine with parallel-connected coils. The larger the number of parallel branches, the more effort is required to build the analytical fault model in Matlab/Simulink. In section 3.4, one model simplification method using the multiphase Clarke transformation will be proposed to significantly reduce the model complexity.

3.2.2 FE Modelling

To verify the results obtained by the proposed analytical fault model, 2D FE simulations (using JMAG software package) for the outer rotor 3 kW 96-slot 32-pole SPM machine with parallel coils have been carried out in this chapter. Under ITSC fault, considering that the current distribution in the three phase windings of the machine becomes asymmetric, full rather than partial FE model is employed and illustrated in Fig. 2.4, in which only part of the full model is used to show the potential location of the ITSC fault more clearly.

Additionally, the faulty machine is fed by voltage sources (as shown in Fig. 3.1) to more accurately predict the changes in phase currents and short-circuit current in FE simulations. The coil having ITSC fault shown in Fig. 2.4 is represented by three FEM coils, as illustrated in Fig. 3.1. One of the three FEM coils represents the remaining healthy turns at the bottom of the two slots where ITSC fault occurs, marked as A1_hb, and one at the top, named as A1_ht. The short-circuited turns in the middle are described by the A1_fm FEM coil. This arrangement will lead to balanced three phase back-EMFs when the switch in Fig. 3.1 is open, i.e., the machine is healthy and open-circuited.

3.3 Inductance Calculation

One of the most important tasks of fault modelling is to determine the parameters in the fault model, especially the inductances in all branch inductance matrices. Experimental measurement and theoretical calculation are two typical ways to obtain inductances in the machine model.

In the past, for the purpose of machine control, the equivalent phase self- and mutual inductances or *dq*-axis inductances of healthy machines were often measured. Actually they represent the combined effect of all elements in branch inductance matrices, which can be seen in section 3.4.1. However, under fault, it is required that the value of every individual element of branch inductance matrices is known prior to establishing the fault model. When large number of fault scenarios need to be investigated, the measurement of individual inductance element in the branch inductance matrices will become impractical. In addition, it is not realistic to measure many inductances at the machine design stage. Due to these reasons, theoretical calculation especially analytical calculation of inductances in those branch inductance matrices without considering the core saturation as a first approximation becomes important for initial study of ITSC fault modelling.

3.3.1 Calculation of Inductances

As mentioned in chapter 2, the three components of the phase self- and mutual inductances are air-gap, slot-leakage, and end-turn leakage inductances. As mentioned in chapter 2, for the 3kW machine, the end-turn leakage component has also been neglected due to its relatively shorter end-windings.

The air-gap component of inductances can be also calculated by WFA shown in (2.8) of chapter 2. When an ITSC fault happens, the healthy coil A1 is divided into two parts: faulty turns and remaining healthy turns. The corresponding winding functions after fault is illustrated in Fig. 3.3, which will be used to calculate the air-gap component of inductances related to these two "coils" with different numbers of turns.

After determining the winding functions of other coils according to the winding layout shown in Fig. 3.3, all elements of the branch inductance matrices can be evaluated by calculating the air-gap and slot-leakage inductances separately, using similar method as in [127]. It is worth noting that these branch inductance matrices are all circulant matrices, meaning that once the elements in the first row of a circulant matrix are known, all the elements of the whole matrix can be determined. The final results are given as

$$\begin{cases} L_{A1A1} = L_{B1B1} = L_{C1C1} = L_1 \ (j = 1, 2, \cdots, p) \\ M_{A1Aj} = M_{B1Bj} = M_{C1Cj} = M_1 \ (j = 2, 3, \cdots, p) \\ M_{A1B1} = M_{B1C1} = M_{A1Cp} = M_2 \\ M_{A1Bj} = M_{B1Cj} = M_1 \ (j = 2, 3, \cdots, p) \\ M_{A1Cj} = M_{A1C1} = M_1 \ (j = 2, 3, \cdots, p-1) \end{cases} \tag{3.12}$$

with

$$\begin{cases} L_1 = \dfrac{\mu_0 r_e l_e}{g_e} \dfrac{(2p-1)}{2p^2} \pi (n_c)^2 + 2(n_c)^2 \mu_0 l_e \left[\dfrac{h_s}{3S_\omega} \right] \\ M_1 = \dfrac{\mu_0 r_e l_e}{g_e} \left(-\dfrac{1}{2p^2} \right) \pi (n_c)^2 \\ M_2 = \dfrac{\mu_0 r_e l_e}{g_e} \left(\dfrac{2p-3}{6p^2} \right) \pi (n_c)^2 \end{cases} \tag{3.13}$$

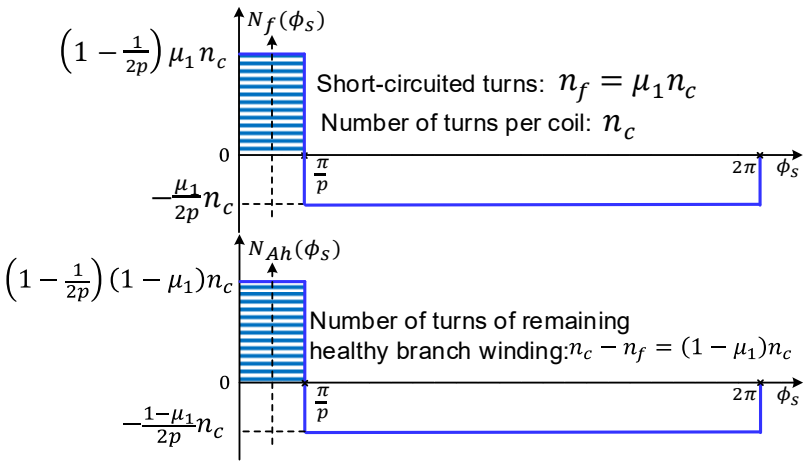

Fig. 3.3 Winding functions of the faulty coil/branch A1 in Phase A.

As for the elements in the faulty inductance vectors, for brevity, they are redefined as

$$\begin{cases} L_{A1f,A1f} + M_{A1h,A1f} = L_{11} \\ M_{Aj,A1f} = M_{Bj,A1f} = M_{11}\ (j = 2,3,\cdots,p) \\ M_{B1,A1f} = M_{Cp,A1f} = M_{22} \\ M_{Cj,A1f} = M_{11}\ (j = 1,2,\cdots,p-1) \end{cases} \tag{3.14}$$

In terms of calculating $L_{A1f,A1f}$ and $M_{A1h,A1f}$, the air-gap and slot-leakage inductance components (indicated by subscripts "g" and "slot", respectively) same as those shown in chapter 2 have to be calculated separately as follows

$$\begin{aligned} L_{11} = L_{A1f,A1f} + M_{A1h,A1f} = \left(L_{A1f,A1f}\right)_g + \left(L_{A1f,A1f}\right)_{slot} \\ + \left(M_{A1h,A1f}\right)_g + \left(M_{A1h,A1f}\right)_{slot} \end{aligned} \tag{3.15}$$

with

$$\left(L_{A1f,A1f}\right)_g = \frac{\mu_0 r_e l_e}{g_e}\frac{(2p-1)}{2p^2}(\mu_1)^2\pi(n_c)^2 \tag{3.16}$$

$$\left(M_{A1h,A1f}\right)_g = \frac{\mu_0 r_e l_e}{g_e}\frac{(2p-1)}{2p^2}[\mu_1 - (\mu_1)^2]\pi(n_c)^2 \tag{3.17}$$

In addition, the expressions for $\left(L_{A1f,A1f}\right)_{slot}$ and $\left(M_{A1h,A1f}\right)_{slot}$ are the same as (2.13) and (2.14).

In addition, M_{11} and M_{22} in (3.14) can be expressed as

$$\begin{cases} M_{11} = -\dfrac{\mu_0 r_e l_e}{g_e}\dfrac{\mu_1}{2p^2}\pi(n_c)^2 \\ M_{22} = \dfrac{\mu_0 r_e l_e}{g_e}\dfrac{(2p-3)}{6p^2}\mu_1\pi(n_c)^2 \end{cases} \tag{3.18}$$

Equation (3.18) clearly shows that the mutual inductances between the short-circuited turns and other healthy coils do not have slot-leakage inductance component. With the above equations, all the inductance elements in the fault model have now been determined.

3.3.2 Results of Inductance Calculation

The machine specifications are given in Table 3.1. The winding configuration of the 3kW SPM machine has been changed from series-connected coils in [127] to parallel-connected coils. In addition, the inductance characteristics of the 3kW 96-slot 32-pole SPM healthy machine with parallel-connected coils calculated by FE simulations and analytical approach are shown in Fig. 3.4. To be consistent with the conditions that the analytical method adopts in determining the inductances, in the FE model, all permanent magnets have been replaced by air, and the stator and rotor core are assumed to be linear magnetic material with a relative permeability $\mu_r = 10000$. Only the coil A1 is excited by 1A DC current. It should be mentioned that $\mathbf{L}_{AA} = \mathbf{L}_{BB} = \mathbf{L}_{CC}$ and $\mathbf{M}_{AB} = \mathbf{M}_{BC}$ due to symmetrical overlapping windings adopted by the studied SPM machines. Considering the large number of elements in a branch inductance matrix and the circulant property of these branch inductance matrices, only the absolute values [see Fig. 3.4 (a)] and the relative errors [see Fig. 3.4 (b)] of the inductances related to A1 coil are shown in Fig. 3.4.

Table 3.1 Specifications of the studied SPM machine

Rated power(kW)	3	Numbers of slots/poles	96/32
Rated speed (rpm)	170	Rotor outer diameter (mm)	426.4
Line voltage (Vrms)	43.1	Stator outer diameter (mm)	401.1
Phase current (Arms)	40	Airgap length (mm)	2
Series turns/coil	52	Stack length (mm)	110

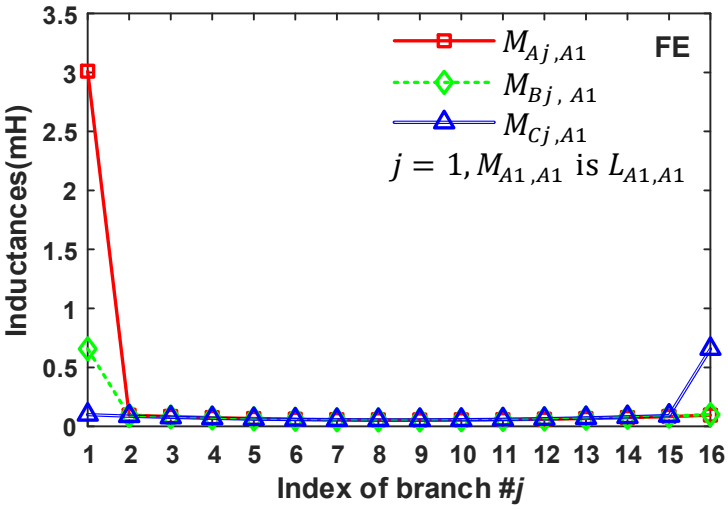

(a) Absolute values of some 2D FE inductances

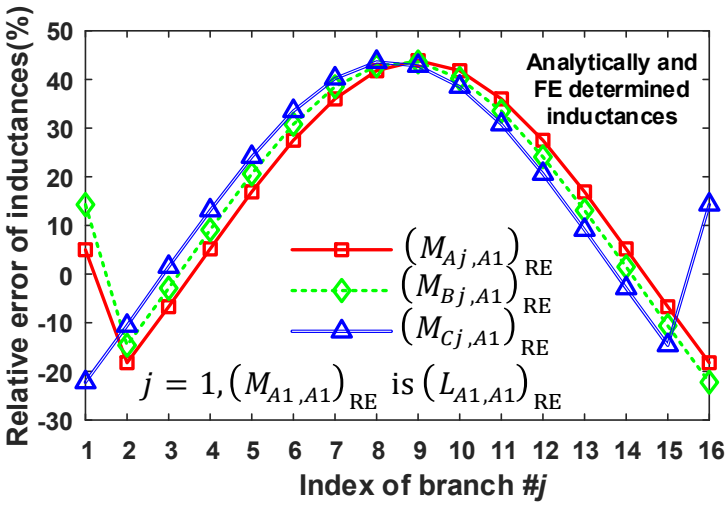

(b) Relative errors of some inductances

Fig. 3.4 Characteristics of inductances between A1 branch/coils and other branches/coils.

The relative error $[(M_{AjA1})_{\mathrm{RE}}]$ using M_{AjA1} as an example in Fig. 3.4 (b) is given by

$$(M_{AjA1})_{\mathrm{RE}} = \frac{(M_{AjA1})_{\mathrm{Analytical}} - (M_{AjA1})_{\mathrm{FE}}}{(M_{AjA1})_{\mathrm{FE}}} \times 100 \tag{3.19}$$

where $(M_{AjA1})_{\mathrm{Analytical}}$ is the mutual inductance calculated by analytical approach, and $(M_{AjA1})_{\mathrm{FE}}$ is obtained by FE simulations.

From Fig. 3.4 (b), the following conclusions could be drawn:

- The self-inductance can be accurately predicted with a relative error of around 5%.
- The relative errors of mutual inductances between two adjacent coils are generally the smallest, which is smaller than 20%.

- The relative errors of mutual inductances between two coils farthest apart from each other is the biggest, up to 50%.

However, when two coils/branches are farther apart (the difference between the indices of branches will be bigger), their mutual inductances are much smaller compared to those of coils close to each other, as shown in Fig. 3.4 (a). Therefore, although larger relative error is observed between some analytically calculated and FE inductances, this may not have a significant impact on the performance prediction such as healthy and short-circuit currents, torque, etc.

A further calculation of the equivalent phase self- and mutual inductances of 3-phase windings has been carried out, and it is shown in Table 3.2. The calculation of the equivalent inductances of 3-phase windings with parallel-connected coils will be detailed in the section 3.4.1.

Table 3.2 Equivalent self- and mutual-inductances (mH) of 3-phase windings

Method	L_{AA}	M_{AB}	M_{AC}
FE	0.1233	-0.02388	-0.02386
Analytical	0.1246	-0.02589	-0.02589
Relative error (%)	1.1	8.4	8.4

Again, as explained previously, the much smaller differences in equivalent phase self- and mutual-inductances of 3-phase windings indicate that there would only be small errors in predicting phase currents of healthy machines by analytical and linear FE models. On the other hand, the results of relative errors of some inductances related to the short-circuited turns (see Fig. 3.5) are very much the same as those shown in Fig. 3.4, i.e., similar conclusions can also be made. It should be mentioned that all the inductance results are obtained without considering the core saturation.

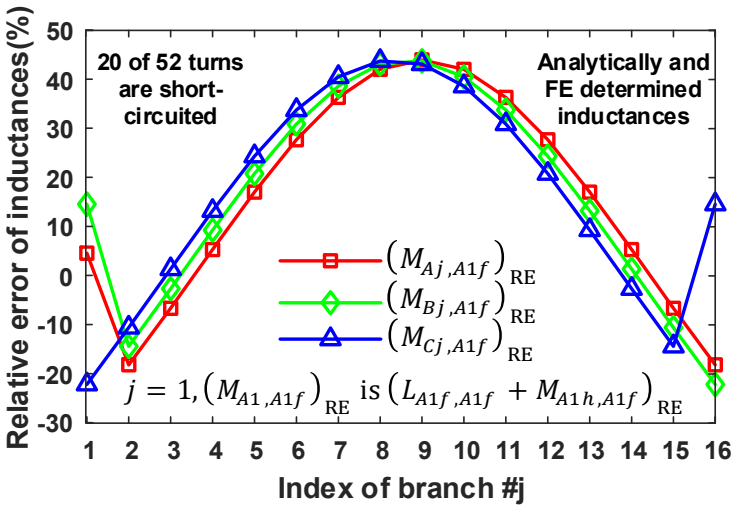

Fig. 3.5 Relative error of inductances related with short-circuited turns. Here 20 out of 52 turns are short-circuited. $M_{A1h,A1f}$ is the mutual inductance between the healthy and faulty turns in the branch/coil A1.

3.4 Model Simplification using Multiphase Clarke Transformation

Although the fault model in a compact matrix form is proposed using branch currents as state variables in the stationary reference frame, not much physical insight can be provided. In addition, it is difficult to build the fault model using Matlab/Simulink if the number of pole pairs is large. Therefore, it would be much better if the fault model could be simplified. After all the branch inductance matrices are determined analytically, it is found that all of them are circulant matrices like those of a healthy multiphase machine. Therefore, when the original branch currents, voltages, and back-EMFs are transformed into new variables using a multiphase Clarke transformation matrix $\mathbf{C}$, the fault model can be simplified. This simplification process can be expressed as

$$\begin{bmatrix} \mathbf{f}'_A \\ \mathbf{f}'_B \\ \mathbf{f}'_C \end{bmatrix} = \begin{bmatrix} \mathbf{C} & \mathbf{0} & \mathbf{0} \\ \mathbf{0} & \mathbf{C} & \mathbf{0} \\ \mathbf{0} & \mathbf{0} & \mathbf{C} \end{bmatrix} \begin{bmatrix} \mathbf{f}_A \\ \mathbf{f}_B \\ \mathbf{f}_C \end{bmatrix} \tag{3.20}$$

where $\mathbf{f}'_A$, $\mathbf{f}'_B$, $\mathbf{f}'_C$ are the corresponding transformed branch current, voltage, and back-EMF vectors. In this thesis, the multiphase Clarke transformation matrix $\mathbf{C}$ adopts the power invariant form, expressed as (3.31). This means that $\mathbf{C^{-1}} = \mathbf{C}^T$, so that

$$\begin{bmatrix}\mathbf{f}_A\\ \mathbf{f}_B\\ \mathbf{f}_C\end{bmatrix}=\begin{bmatrix}\mathbf{C}^T & \mathbf{0} & \mathbf{0}\\ \mathbf{0} & \mathbf{C}^T & \mathbf{0}\\ \mathbf{0} & \mathbf{0} & \mathbf{C}^T\end{bmatrix}\begin{bmatrix}\mathbf{f}'_A\\ \mathbf{f}'_B\\ \mathbf{f}'_C\end{bmatrix} \tag{3.21}$$

3.4.1 General Case: ITSC Fault

The new voltage equations after the multiphase Clarke transformation can be written as

$$\begin{aligned}\begin{bmatrix}\mathbf{v}'_A\\ \mathbf{v}'_B\\ \mathbf{v}'_C\end{bmatrix}=&\begin{bmatrix}\mathbf{L}'_{AA} & \mathbf{M}'_{AB} & \mathbf{M}'_{AC}\\ \mathbf{M}'_{BA} & \mathbf{L}'_{BB} & \mathbf{M}'_{BC}\\ \mathbf{M}'_{CA} & \mathbf{M}'_{CB} & \mathbf{L}'_{CC}\end{bmatrix}\frac{\mathrm{d}}{\mathrm{d}t}\begin{bmatrix}\mathbf{i}'_A\\ \mathbf{i}'_B\\ \mathbf{i}'_C\end{bmatrix}+R_{\mathrm{coil}}\begin{bmatrix}\mathbf{i}'_A\\ \mathbf{i}'_B\\ \mathbf{i}'_C\end{bmatrix}\\ &+\begin{bmatrix}\boldsymbol{e}'_A\\ \boldsymbol{e}'_B\\ \boldsymbol{e}'_C\end{bmatrix}-\begin{bmatrix}\mathbf{C} & \mathbf{0} & \mathbf{0}\\ \mathbf{0} & \mathbf{C} & \mathbf{0}\\ \mathbf{0} & \mathbf{0} & \mathbf{C}\end{bmatrix}\left(\begin{bmatrix}R_{A1f}\\ 0\\ \vdots\\ 0\end{bmatrix}i_f+\begin{bmatrix}\mathbf{M}_{Af}\\ \mathbf{M}_{Bf}\\ \mathbf{M}_{Cf}\end{bmatrix}\frac{\mathrm{d}i_f}{\mathrm{d}t}\right)\end{aligned} \tag{3.22}$$

where $\mathbf{L}'_{xx}=\mathbf{C}\mathbf{L}_{xx}\mathbf{C}^{\boldsymbol{T}}$, $\mathbf{M}'_{xy}=\mathbf{C}\mathbf{M}_{xy}\mathbf{C}^{\boldsymbol{T}}$. "$x$" and "$y$" represent different windings of phases A, B, and C. If the inductances calculated by analytical method are employed in this analytical model, then $\mathbf{L}'_{xx}$ and $\mathbf{M}'_{xy}$ become diagonal or block diagonal matrices as follows:

$$\mathbf{L}'_{xx}=\mathrm{diag}\big((L_1+(p-1)M_1),(L_1-M_1),(L_1-M_1),\cdots,(L_1-M_1)\big) \tag{3.23}$$

and

$$\mathbf{M}'_{AB}=\mathbf{M}'_{BC}=\mathrm{diag}\big((M_2+(p-1)M_1),(M_2-M_1),(M_2-M_1),\cdots,(M_2-M_1)\big) \tag{3.24}$$

and

$$(\mathbf{M}'_{AC})_{ij}=\begin{cases}M_2+(p-1)M_1 & i=j=1\\ (M_2-M_1)\cos\left(\dfrac{2\pi k}{p}\right) & i=j=2k \text{ or } 2k+1\\ (M_2-M_1)\sin\left(\dfrac{2\pi k}{p}\right) & i=2k, j=2k+1\\ -(M_2-M_1)\sin\left(\dfrac{2\pi k}{p}\right) & i=2k+1, j=2k\\ -(M_2-M_1) & i=j=p\end{cases} \tag{3.25}$$

In (3.25), p is assumed to be an even integer, and the integer k can vary from 1 to $(p-2)/2$. Other elements equal to zero in $(\mathbf{M}'_{AC})_{ij}$ are not listed. If p is odd, then the integer k can only vary from 1 to $(p-1)/2$.

Therefore, the model is greatly simplified considering that the number of state variables in every first-order differential equation is reduced from $3p+1$ to the minimum value (only 3 to 5 state variables exist after transformation).

The new voltage equation for the short-circuited path can be written by

$$\begin{aligned}\left(R_f + R_{A1f}\right)i_f + L_{A1f,A1f}\frac{\mathrm{d}i_f}{\mathrm{d}t} - e_{A1f} - R_{A1f}(\mathbf{C}^T\mathbf{i}'_A)_1 \\ = \left(\mathbf{CM}_{Af}\right)^T\frac{\mathrm{d}\mathbf{i}'_A}{\mathrm{d}t} + \left(\mathbf{CM}_{Bf}\right)^T\frac{\mathrm{d}\mathbf{i}'_B}{\mathrm{d}t} + \left(\mathbf{CM}_{Cf}\right)^T\frac{\mathrm{d}\mathbf{i}'_C}{\mathrm{d}t}\end{aligned} \tag{3.26}$$

where $(\mathbf{C}^T\mathbf{i}'_A)_1$ is the first element of the vector $\mathbf{C}^T\mathbf{i}'_A$. Finally, the torque equation now can be expressed as

$$T_e = \frac{p}{\omega_r}\left(e_A i_A + e_B i_B + e_C i_C - e_{A1f} i_f\right) + T_{cog} \tag{3.27}$$

It should be mentioned that $\mathbf{v}'_x = [v_x \quad 0 \quad \cdots \quad 0]^T$, $\mathbf{e}'_x = [e_x \quad 0 \quad \cdots \quad 0]^T$. If $i_f = 0$, indicating that the machine is healthy, then only three transformed voltage equations with nonzero excited voltages and back-EMFs are useful, others are redundant. This means that, by using the multiphase Clarke transformation, the healthy machine model using branch currents as state variables can be reduced to that using phase currents as state variables. In other words, the mathematical model for machines with parallel-connected coils is the same as that with equivalent series-connected coils under healthy operation if the relationship of equivalent phase (self- and mutual-) inductances between the series and parallel windings are used

$$L_{\text{parallel}} = \frac{1}{p^2}L_{\text{series}} \quad M_{\text{parallel}} = \frac{1}{p^2}M_{\text{series}} \tag{3.28}$$

Similarly, the relationship of resistance between series and parallel windings can also be established. Finally, the equivalent phase self- and mutual-inductances for parallel-connected coils can be expressed by

$$\begin{cases}(L_{xx})_{\text{parallel}} = \dfrac{1}{p^2}\displaystyle\sum_{i=1}^{p}\sum_{j=1}^{p}(\mathbf{L}_{xx})_{ij} = \frac{1}{p}\sum_{j=1}^{p}(\mathbf{L}_{xx})_{1j} \\ \left(M_{xy}\right)_{\text{parallel}} = \dfrac{1}{p^2}\displaystyle\sum_{i=1}^{p}\sum_{j=1}^{p}\left(\mathbf{M}_{xy}\right)_{ij} = \frac{1}{p}\sum_{j=1}^{p}\left(\mathbf{M}_{xy}\right)_{1j}\end{cases} \tag{3.29}$$

3.4.2 Special Case: One-Coil Short-Circuit Fault

For the studied machine with parallel-connected coils, the one-coil short-circuit fault is equivalent to one-phase short-circuit fault. When this fault occurs, the circuit branch voltage equations are changed to the following form

$$\begin{bmatrix}\mathbf{v}_A \\ \mathbf{v}_B \\ \mathbf{v}_C\end{bmatrix} = \begin{bmatrix}\mathbf{L}_{AA} & \mathbf{M}_{AB} & \mathbf{M}_{AC} \\ \mathbf{M}_{BA} & \mathbf{L}_{BB} & \mathbf{M}_{BC} \\ \mathbf{M}_{CA} & \mathbf{M}_{CB} & \mathbf{L}_{CC}\end{bmatrix}\frac{\mathrm{d}}{\mathrm{d}t}\begin{bmatrix}\mathbf{i}_{Af} \\ \mathbf{i}_B \\ \mathbf{i}_C\end{bmatrix} + R_{\text{coil}}\begin{bmatrix}\mathbf{i}_{Af} \\ \mathbf{i}_B \\ \mathbf{i}_C\end{bmatrix} + \begin{bmatrix}\mathbf{e}_A \\ \mathbf{e}_B \\ \mathbf{e}_C\end{bmatrix} \tag{3.30}$$

where $\mathbf{i}_{Af} = [i_{A1} - i_f \quad i_{A2} \quad \cdots \quad i_{Ap}]^T$. The multiphase Clarke transformation in (3.20) now should be applied to $\mathbf{i}_{Af}$ vector directly, and it can be proven that all coil currents under one-

phase short-circuit fault are equal. Here, the current of the first coil A1 is $i_{A1} - i_f$. Under this situation, it is sufficient to use 3-phase currents as state variables to describe the machine behaviour, and a system of 5 first-order differential equations is enough to model the machine behaviour under the one-coil short-circuit fault (one-phase short-circuit fault). This will make the analysis and simulation much simpler.

The multiphase Clarke transformation matrix is shown in (3.31) [138], [139]

$$\mathbf{C}=\sqrt{\frac{2}{p}}\begin{bmatrix}
\frac{1}{\sqrt{2}} & \frac{1}{\sqrt{2}} & \frac{1}{\sqrt{2}} & \cdots & \frac{1}{\sqrt{2}} & \cdots & \frac{1}{\sqrt{2}} \\
1 & \cos\left(-\frac{2\pi}{p}\right) & \cos\left(-2\times\frac{2\pi}{p}\right) & \cdots & \cos\left(-m\times\frac{2\pi}{p}\right) & \cdots & \cos\left(-(p-1)\times\frac{2\pi}{p}\right) \\
0 & \sin\left(-\frac{2\pi}{p}\right) & \sin\left(-2\times\frac{2\pi}{p}\right) & \cdots & \sin\left(-m\times\frac{2\pi}{p}\right) & \cdots & \sin\left(-(p-1)\times\frac{2\pi}{p}\right) \\
\vdots & \vdots & \vdots & \vdots & \vdots & \vdots & \vdots \\
1 & \cos\left(-k\times\frac{2\pi}{p}\right) & \cos\left(-2\times k\times\frac{2\pi}{p}\right) & \cdots & \cos\left(-m\times k\times\frac{2\pi}{p}\right) & \cdots & \cos\left(-(p-1)\times k\times\frac{2\pi}{p}\right) \\
0 & \sin\left(-k\times\frac{2\pi}{p}\right) & \sin\left(-2\times k\times\frac{2\pi}{p}\right) & \cdots & \sin\left(-m\times k\times\frac{2\pi}{p}\right) & \cdots & \sin\left(-(p-1)\times k\times\frac{2\pi}{p}\right) \\
\vdots & \vdots & \vdots & \vdots & \vdots & \vdots & \vdots \\
1 & \cos\left(-\left(\frac{p-2}{2}\right)\times\frac{2\pi}{p}\right) & \cos\left(-2\times\left(\frac{p-2}{2}\right)\times\frac{2\pi}{p}\right) & \cdots & \cos\left(-m\times\left(\frac{p-2}{2}\right)\times\frac{2\pi}{p}\right) & \cdots & \cos\left(-(p-1)\times\left(\frac{p-2}{2}\right)\times\frac{2\pi}{p}\right) \\
0 & \sin\left(-\left(\frac{p-2}{2}\right)\times\frac{2\pi}{p}\right) & \sin\left(-2\times\left(\frac{p-2}{2}\right)\times\frac{2\pi}{p}\right) & \cdots & \sin\left(-m\times\left(\frac{p-2}{2}\right)\times\frac{2\pi}{p}\right) & \cdots & \sin\left(-(p-1)\times\left(\frac{p-2}{2}\right)\times\frac{2\pi}{p}\right) \\
\frac{1}{\sqrt{2}} & -\frac{1}{\sqrt{2}} & \frac{1}{\sqrt{2}} & \cdots & (-1)^m\frac{1}{\sqrt{2}} & \cdots & -\frac{1}{\sqrt{2}}
\end{bmatrix} \tag{3.31}$$

In (3.31), one assumption is made that the number of pole pairs is even. If the number of pole pairs is odd, then the last row in (3.31) should be deleted and all $(p-2)/2$ terms appeared in the last three rows should be replaced by $(p-1)/2$.

3.5 Simulation Results

Due to the limitation of voltage source excitation in the FE simulations, 3-phase balanced sinusoidal voltages are fed to the studied 3kW SPM machine to obtain rated torque before fault and its rotor mechanical speed is kept constant during the whole operation period. Then, different fault severities such as one-coil, half-a-coil and single-turn short-circuits have been investigated. Some representative results of the one coil, half-a-coil and single-turn faults have been provided in this section.

3.6 One Coil Short-Circuited

One coil short-circuit has been selected as the first example here to verify the proposed analytical model. Fig. 3.6 shows currents in the faulty coil A1 before and after the one-coil short-circuit fault, which are obtained from the linear FE model (a relative permeability $\mu_r = 10000$ is used for the stator and rotor core material) and simplified analytical model using branch currents (or phase currents) as state variables. A good agreement can be observed between the analytical and FE results. It is also found that after the one-coil short-circuit, the current in the short-circuited coil has been increased by almost 17 times (from 4.37A to 73.2A). In Fig. 3.7 and Fig. 3.8, simulation results of three phase currents and on-load torque are presented. In Fig. 3.7, only results from the analytical model are shown because results obtained from the FE and analytical models match well.

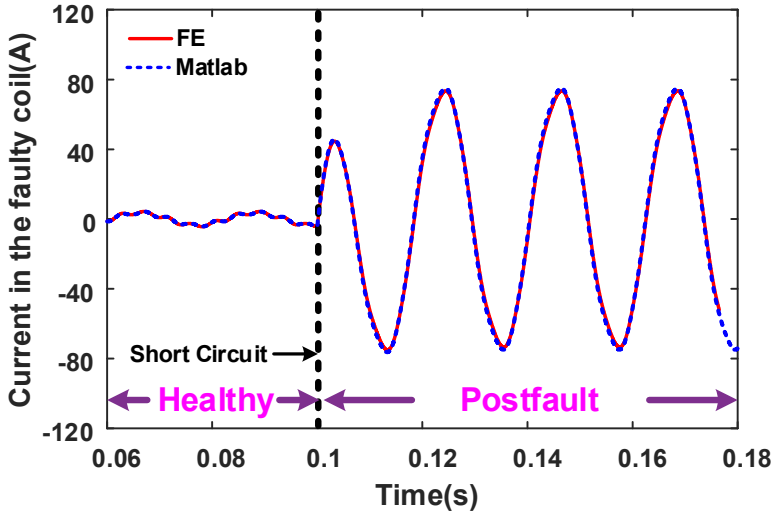

Fig. 3.6 Current in the faulty coil A1 before and after the one-coil short-circuit fault.

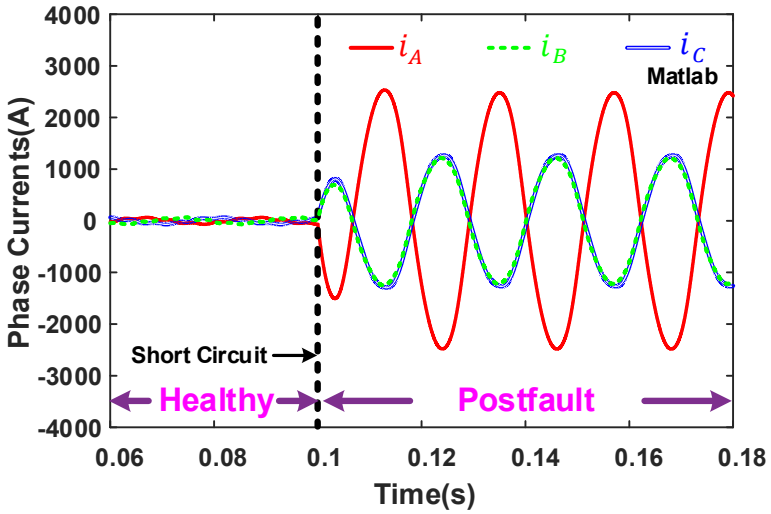

Fig. 3.7 3-phase currents before and after the one-coil short-circuit fault.

As the one-coil short-circuit for parallel-connected coils is equivalent to one phase short-circuit, the amplitude of current in phase A grows quite significantly, about 34.5 times that before the fault. In addition, the phase and amplitude of the currents in phases B and C are very much similar and the amplitude is 17.7 times higher than that before the fault. This change in three phase currents leads to significant change in the on-load torque in Fig. 3.8, i.e., the torque ripple significantly increases although the average torque has been maintained at a similar level as that before the fault. In Fig. 3.8, the developed electromagnetic torque has negative values at some rotor positions, meaning that the motor is changing from the motoring mode to the generating mode. This is mainly because the 3-phase currents are now dramatically unbalanced as shown in Fig. 3.7 and the developed electromagnetic torque, as the product of them and the corresponding 3-phase back EMFs, will yield the dc component and the fundamental component whose frequency is 2 times the electrical frequency. The appearance of some other higher even order harmonics in the torque profile can be analysed in a similar way if the currents and the corresponding back EMFs are approximated by the partial sum of their low-order harmonics such as the 1st, 3rd, 5th, and 7th harmonics. For example, the interaction between the fundamental component of the 3-phase back-EMFs and the third harmonic of 3-phase currents, typically will not appear before the fault, will yield the second and fourth harmonics in the torque waveform.

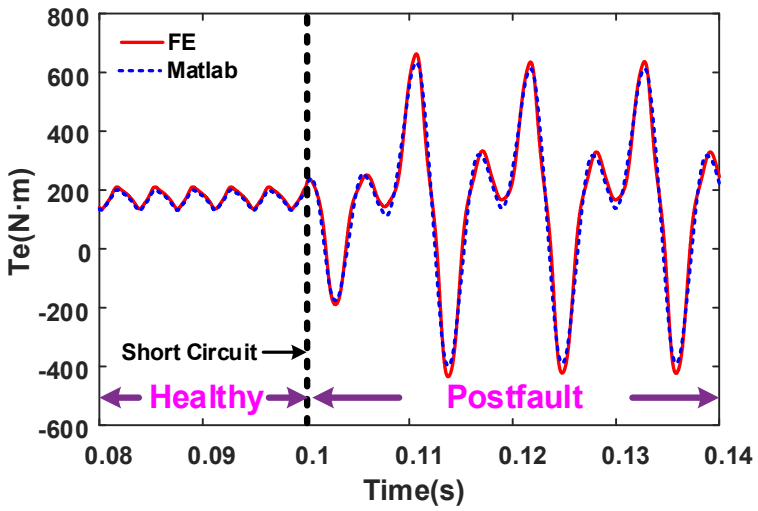

Fig. 3.8 On-load torque of the 3kW SPM machine before and after the one-coil short-circuit fault.

3.7 Half a Coil (50% Turns of a Coil) Short-Circuited

For the half-a-coil short-circuited case, $h_a = h_s/n_c$ and $h_b = (0.5n_c + 1)h_s/n_c$ are chosen. Fig. 3.9 shows the currents in the faulty coil A1 before and after the half-a-coil short-circuit fault.

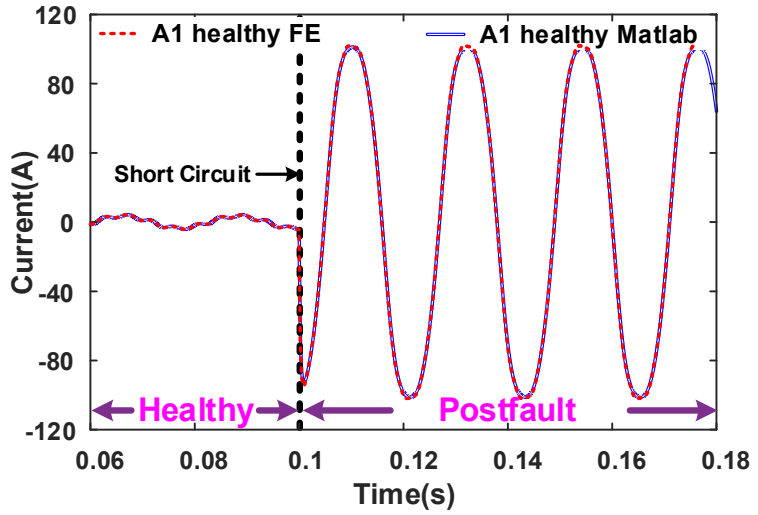

(a) Current in remaining healthy turns

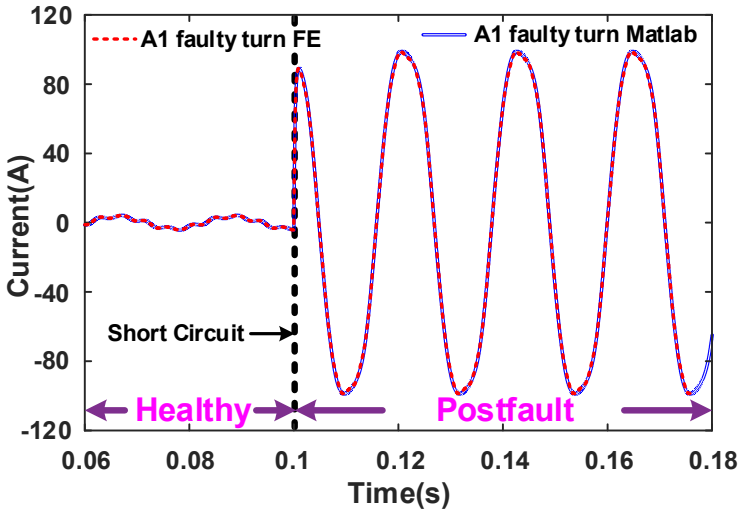

(b) Current in the short-circuited turns

Fig. 3.9 Current waveforms before and after the half-a-coil short-circuit fault.

It could be easily seen that there is a very small discrepancy in simulation results from the two models. Compared with the one-coil short-circuit fault case, the amplitude of the short-circuit current increased from 75A to 90A. This is mainly because the short-circuit current is almost inversely proportional to the number of short-circuited turns. When the number of short-circuited turns reduces, the amplitude of short-circuit current generally increases.

However, although the short-circuit current increases, lower number of turns being short-circuited means that the impact of fault on on-load torque is less significant, as shown in Fig. 3.10.

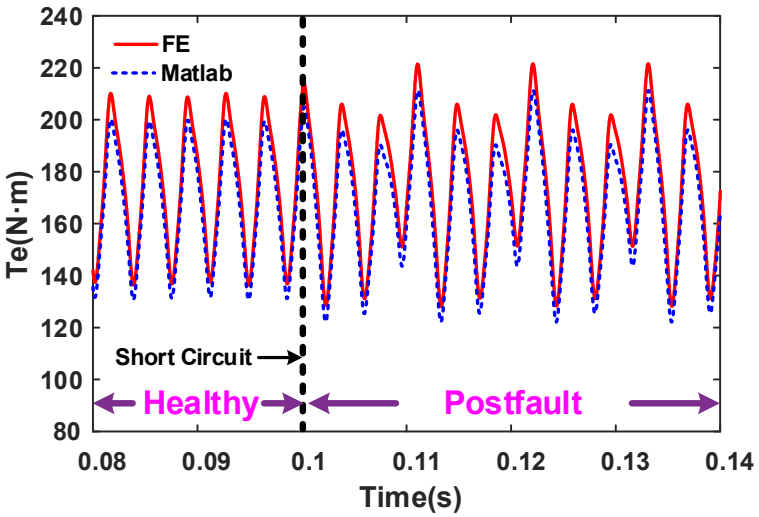

Fig. 3.10 On-load torque of the 3 kW SPM machine before and after the half-a-coil short-circuit fault.

On the other hand, some branch currents of phases B and C are shown in Fig. 3.11. It is found that not all branch currents in the remaining healthy phase windings are the same. In fact, the branch currents of phases B and C next to the faulty branch of phase A are significantly affected, meaning that the changes in i_{B1}, i_{B16}, i_{C1}, and i_{C16} are greater compared with other branch currents in phases B and C when the ITSC fault occurs in A1 branch.

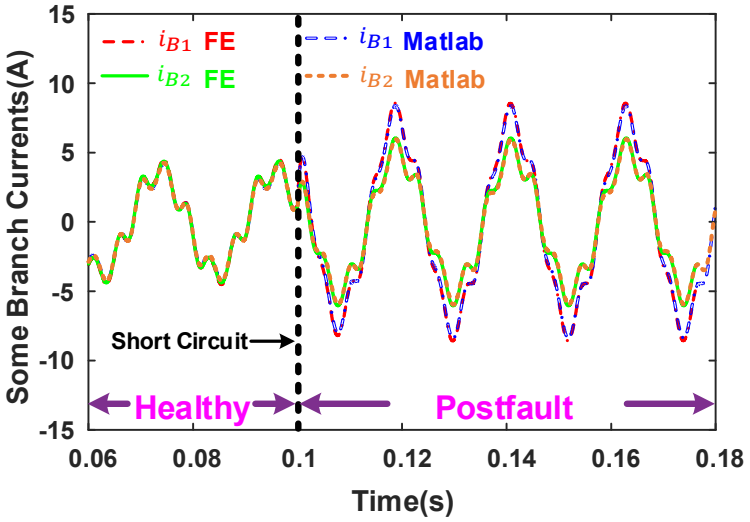

(a) Branch currents of phases B

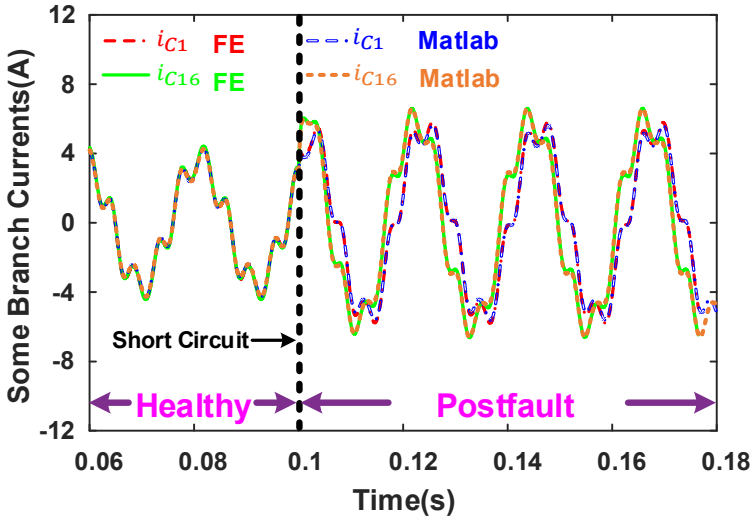

(b) Branch currents of phases C

Fig. 3.11 Some branch currents of phases B and C.

Although it is not shown here, the branch currents i_{B2} to i_{B15} in phase B (or i_{C2} to i_{C15} in phase C) are almost the same. In addition, it is found that the behaviour of branch currents of phase C is different from that of phase B. This is mainly because the mutual inductances $M_{A1B1} \neq M_{A1C1}$ and $M_{A1B16} \neq M_{A1C16}$. If both of them were equal, then the two branch

inductance matrices $\mathbf{M}_{AB} = \mathbf{M}_{AC}$ and $\mathbf{M}_{Bf} = \mathbf{M}_{Cf}$, leading to the same behaviour of branch currents in the two phases after the ITSC fault.

3.8 Single Turn Short-Circuited

As for the single-turn short-circuited case, it is assumed that the fault occurs at the bottom of the slot, and $h_a = h_s/n_c$ is chosen. Fig. 3.12 shows the currents in the faulty coil A1 before and after the single-turn short-circuit fault.

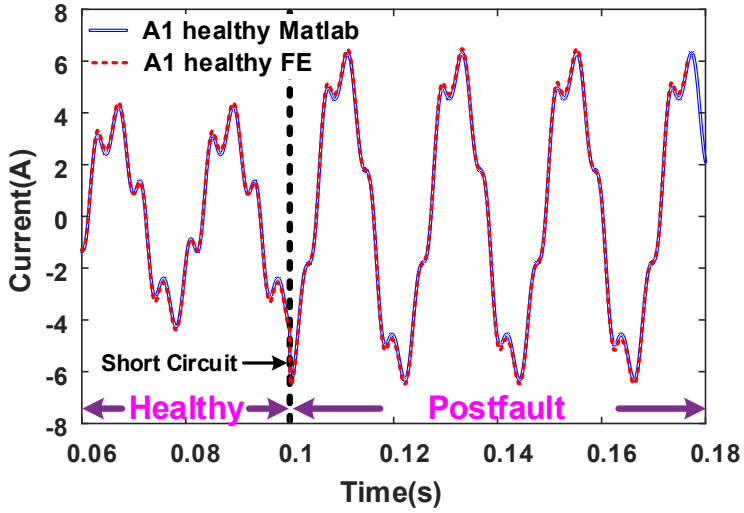

(a) Current in the remaining healthy turns

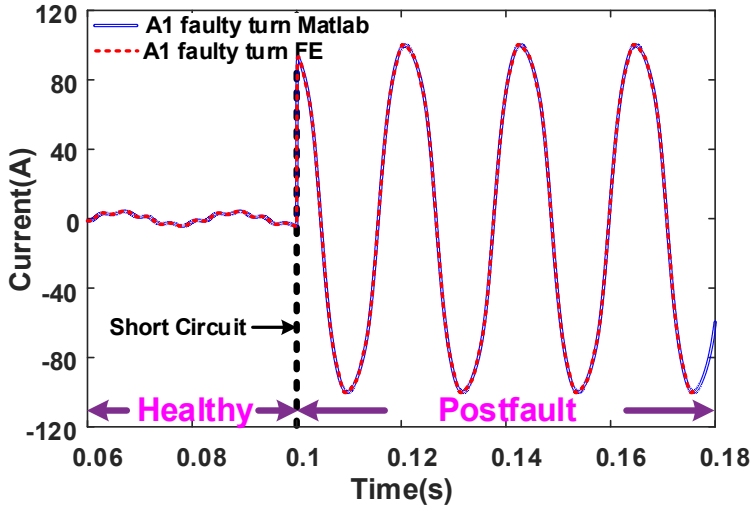

(b) Current in the short-circuited turn

Fig. 3.12 Current waveforms before and after the single-turn short-circuit fault.

As mentioned previously, the single-turn short-circuit current is the largest, up to 100A, about 28 times the rated current. However, it does not lead to great changes to the currents in the remaining healthy turns as shown in Fig. 3.12 (a). Although not shown, the currents in the

other healthy branches are almost unchanged. Therefore, considering that only 1 of 52 turns is short-circuited, the impact of fault on on-load torque is negligible, which is shown in Fig. 3.13.

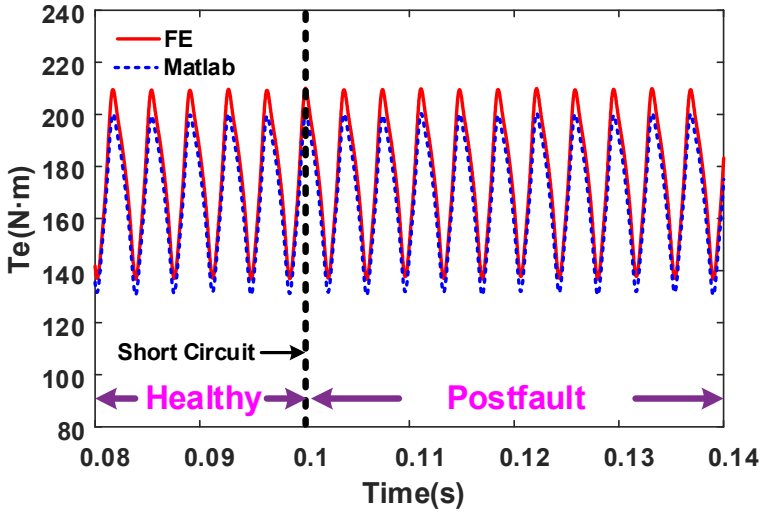

Fig. 3.13 On-load torque of the 3kW SPM machine before and after the single-turn short-circuit fault.

3.9 Currents at Different Speeds under Half-a-Coil Short-Circuit Fault

It is worth mentioning that the results in the previous section are obtained under the rated speed only. To further verify the accuracy of the proposed analytical model, simulations under half-a-coil short-circuit fault at different rotor speeds have been carried out. The amplitudes of the currents of phase A and faulty turns are shown in Fig. 3.14.

It is found that the ITSC current and postfault phase current increase almost linearly with the rotor speed. This is mainly due to the increase in back-EMF of the short-circuited turns. If the rotor speed keeps increasing, the fault current can be much higher than the rated current. This means that early fault detection is critical, otherwise, if the fault is left undetected and untreated, the affected coils could be overheated, leading to catastrophic damage to the entire machine.

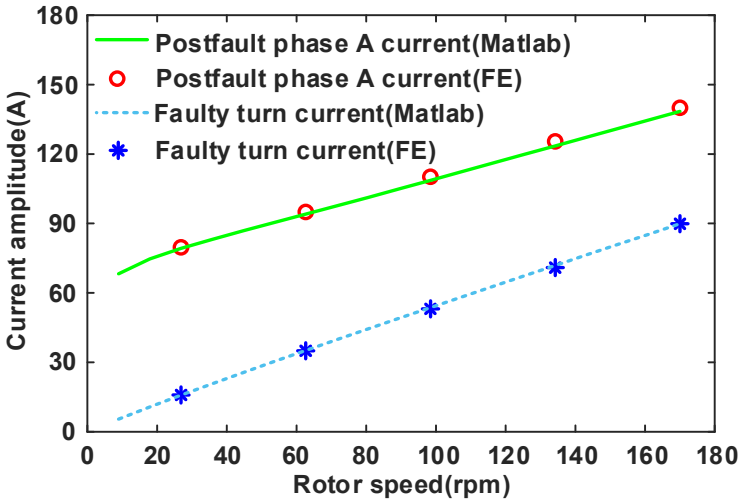

Fig. 3.14 Peak currents of phase A and faulty turns before and after half-a-coil short-circuit fault.

3.10 Conclusion

This chapter presents a general analytical model in a compact matrix form for PM wind generators with parallel-connected coils under ITSC fault. Inductance calculations using the developed analytical approach in chapter 2 for the SPM machines with parallel-connected coils have been carried out. Then the multiphase Clarke transformation has been proposed to simplify the fault model. Such model simplification method may be extended to other types of electrical machines with similar winding configurations, no matter how many phases the machines have.

For the sake of generality, different fault scenarios have been investigated using the proposed analytical model, in which the branch currents are used as state variables. First of all, the inductances in the fault model have been calculated by the proposed analytical approach, which have been compared against FE predictions when the core saturation is neglected. Overall good agreement has been observed except for the mutual inductances between two coils farther apart. However, these mutual inductances are very small. Then, these inductances have been used in the fault model built in Matlab/Simulink for a 3kW machine to predict the machine performance such as healthy and short-circuit currents and on-load torque before and after various short-circuit faults. The accuracy of the proposed analytical fault model has been validated by 2D time-stepping FE simulations. The analytical model developed in this chapter can be very useful for model-based fault detection and mitigation of large wind power generators, for which the FE or magnetic equivalent circuit modelling can be very time-consuming due to large number of slots and poles.

Chapter 4 In-depth Investigation of Inter-Turn Short-Circuit Faults of SPM Machines with Series-Parallel Coil Connections

Based on the developed general analytical fault model for SPM machines with parallel-connected coils in chapter 3, this chapter proposes the general analytical fault model for SPM machines with series-parallel coil connections. The inductances in the fault model are derived for SPM machines with series-parallel coil connections by the same analytical method as in the previous two chapters: winding function approach (WFA) together with slot permeance method. Based on the characteristics of the calculated inductances and the developed fault model, the multiphase Clarke transformation is found to be still useful for simplifying the fault model. In the process of model simplification, the healthy machine model using branch currents as state variables has been proven to be equivalent to that using 3-phase currents as state variables. The proposed fault models of a 3kW 96-slot 32-pole SPM machine with different series-parallel coil connections have been built in Matlab/Simulink and validated by time-stepping 2D FE simulations. Simulation results show that different series-parallel coil connections have little influence on the amplitude of the ITSC current.

Related Publications:

[Mei23c] Z. T. Mei, G. J. Li, Z. Q. Zhu, R. Clark, A. Thomas, and Z. Azar, "In-depth Investigation of Inter-Turn Short-Circuit Faults of PM Machines with Series-Parallel Coil Connections," *IET Electr. Power Appl.*, pp. 1–9, Apr. 2023.

4.1 Introduction

In chapter 3, the relatively simple and general analytical fault model for SPM machines with parallel-connected coils has been proposed. Based on that fault model, the general analytical fault model for SPM machines with series-parallel connected coils can be easily found. However, the fault model simplification using the multiphase Clark transformation matrix in that chapter is based on the analytical inductances derived for SPM machines with parallel-connected coils. Whether the fault model simplification method can be extended to SPM machines with series-parallel coil connections has not been proven.

This chapter continues to adapt the fault model proposed in chapter 3 so that it can be applied to SPM machines with series-parallel connected coils and calculate the inductances in the fault model by the same analytical method as in the previous two chapters. In addition, whether the fault model with analytical inductances can be simplified using the multiphase Clark transformation matrix will be explored. The winding of the analysed SPM machines is still single-layer, full-pitch and distributed [slot/pole/phase (SPP) is equal to 1], which is often the case for large PM generators used in wind power.

Due to this simple winding structure, inductances of the fault model can be calculated easily by analytical methods such as the winding function approach (WFA) together with slot permeance method. It is worth noting that the core saturation has been neglected during the analytical calculation of the inductances. Once the inductances are determined, it is found that the multiphase Clarke transformation can still be used to simplify the fault model based on the characteristics of the calculated inductances and the concise block matrix form of the developed fault model. As an example, fault models of a 3kW 96-slot 32-pole SPM machine with different series-parallel coil connections, have been built in Matlab/Simulink based on the proposed fault model and model simplification method, and they have been validated by time-stepping 2D FE simulations.

It should be mentioned that in this chapter, the core saturation has not been considered during the inductance calculations. However, in chapter 7, to validate the developed fault models, a small scale 24-slot 8-pole SPM machine has been built and tested, and nonlinear inductances obtained from both measurement and 3D FE models are employed. More simulated and measured results will be shown in Chapter 7.

4.2 Analytical Modelling Neglecting the Core Saturation

A schematic representation of series-parallel coil connections of a SPM machine is shown in Fig. 4.1, where the ITSC fault is assumed to be in the first branch (A1 branch) of phase A. Here it is also assumed that one parallel branch has r coils in series, and n parallel branches of one phase will therefore contain $p = r \times n$ coils in total, where p is the number of pole pairs. This is because the windings of the analyzed SPM machines shown in Fig. 4.2 are single-layer, integer-slot and distributed, thus the number of pole pairs p is the same as the number of coils in one phase winding. To simplify the analyses, in the following sections of this chapter, rS×nP will be used to represent the windings with r series coils (in each branch) and n parallel branches (in each phase).

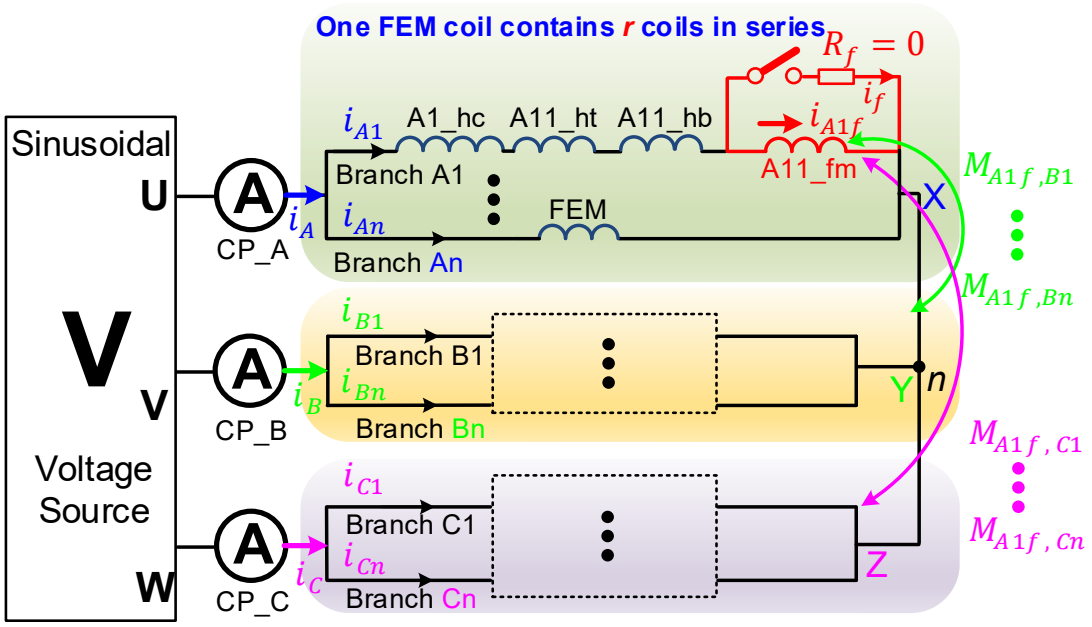

Fig. 4.1 Circuit schematic of the studied SPM machines under ITSC fault. One FEM coil contains r coils in series, and each phase has n parallel branches.

In addition, the short-circuited turns of the A11 faulty coil is named as A11_fm shown in Fig. 4.1. In the FE geometry model, assuming that the short-circuited turns A11_fm are somewhere in the middle of the affected slots, then A11_ht and A11_hb will represent the remaining healthy turns at the top and at the bottom of the affected slots, respectively. As for A1_hc, it represents the remaining healthy $r - 1$ coils of A1 branch. Some mutual inductances between the short-circuited turns and the other branches such as $M_{A1f,An}$, $M_{A1f,B1}$, $M_{A1f,Cn}$, etc are also illustrated in Fig. 4.1.

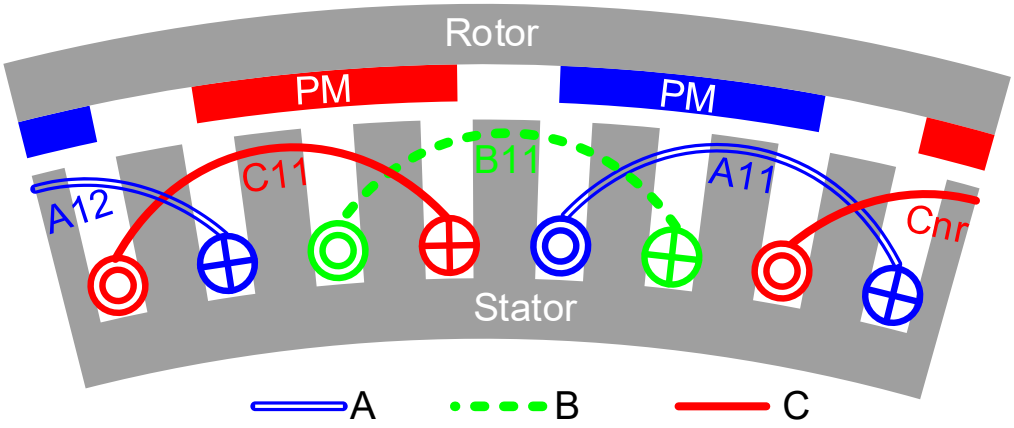

Fig. 4.2 The studied SPM machine with integer slot overlapping windings.

From Fig. 4.1, the voltage equations for every circuit branch can be easily derived from (3.1) in chapter 3 and expressed in a compact matrix form

$$\begin{bmatrix}\mathbf{v}_A\\ \mathbf{v}_B\\ \mathbf{v}_C\end{bmatrix}=\begin{bmatrix}\mathbf{L}_{AA} & \mathbf{M}_{AB} & \mathbf{M}_{AC}\\ \mathbf{M}_{BA} & \mathbf{L}_{BB} & \mathbf{M}_{BC}\\ \mathbf{M}_{CA} & \mathbf{M}_{CB} & \mathbf{L}_{CC}\end{bmatrix}\frac{\mathrm{d}}{\mathrm{d}t}\begin{bmatrix}\mathbf{i}_A\\ \mathbf{i}_B\\ \mathbf{i}_C\end{bmatrix}+R_{\mathrm{cb}}\begin{bmatrix}\mathbf{i}_A\\ \mathbf{i}_B\\ \mathbf{i}_C\end{bmatrix}+\begin{bmatrix}\mathbf{e}_A\\ \mathbf{e}_B\\ \mathbf{e}_C\end{bmatrix}-\begin{bmatrix}R_{A1f}\\ 0\\ \vdots\\ 0\end{bmatrix}i_f-\begin{bmatrix}\mathbf{M}_{Af}\\ \mathbf{M}_{Bf}\\ \mathbf{M}_{Cf}\end{bmatrix}\frac{\mathrm{d}i_f}{\mathrm{d}t} \tag{4.1}$$

where column vectors **v, i,** and **e** represents branch-to-neutral voltages (v), branch back-EMFs (e) or branch currents (i) for the phases A, B and C windings. For instance, $\mathbf{v}_A = [v_{A1} \quad v_{A2} \quad \cdots \quad v_{An}]^T$, and it has n entries, where n is the number of parallel branches defined earlier. Additionally, i_f is the current in the short-circuit path as shown in Fig. 4.1. As for $\mathbf{L}_{xx}$ and $\mathbf{M}_{xy}$ ("y" represents another phase winding different from x), they are branch inductance matrices introduced in chapter 3. Here they all have a size of $n \times n$. In addition, R_{cb} in (2.1) is the branch resistance, and R_{A1f} is the resistance of the short-circuited turns. The elements of three column vectors $\mathbf{M}_{Af}$, $\mathbf{M}_{Bf}$, and $\mathbf{M}_{Cf}$ represent the inductive couplings between the short-circuited turns and the branches in all three phases, and they have the same meanings except the dimensions as those explained in chapter 3.

As for the voltage equation of the short-circuited path, it is the same as (3.5). However, it is worth mentioning that $e_{A1f} = (\mu_1/r)e_A$ is the back EMF of the short-circuited turns, where the coil faulty turn ratio μ_1 is defined as $\mu_1 = n_f/n_c$ for the studied integer-slot SPM machines and e_A is the branch back-EMF of phase A.

For a wye-connected 3-phase windings having series-parallel coil connections, the branch currents need to obey the Kirchhoff's current law such as

$$\sum_{k=1}^{n} i_{Ak} + \sum_{k=1}^{n} i_{Bk} + \sum_{k=1}^{n} i_{Ck} = 0 \tag{4.2}$$

Additionally, if there are space harmonics in the branch back EMFs in (2.1) and the neutral point is not accessible, then the three branch-to-neutral (or phase) voltages v_A, v_B, and v_C cannot be determined directly from the line voltages v_{AB} and v_{BC} under the ITSC fault. However, if the "circulant" characteristic of branch inductance matrices and the constraint of branch currents are considered, adding all circuit branch voltage equations will give

$$v_A + v_B + v_C = (e_A + e_B + e_C) - \frac{1}{n}\left[R_{A1f} i_f + \left(\sum_{k=1}^{n} \left(\mathbf{M}_{Af} + \mathbf{M}_{Bf} + \mathbf{M}_{Cf}\right)_k\right)\frac{\mathrm{d}i_f}{\mathrm{d}t}\right] \tag{4.3}$$

where e_B and e_C are branch back-EMFs of phase B and C, respectively. $\left(\mathbf{M}_{Af} + \mathbf{M}_{Bf} + \mathbf{M}_{Cf}\right)_k$ indicates the k^{th} element of the sum of $\mathbf{M}_{Af}$, $\mathbf{M}_{Bf}$, and $\mathbf{M}_{Cf}$.

When the sum of the three branch-to-neutral voltages in (4.3) is known, the two line voltages v_{AB} and v_{BC} can be found using (3.9) and (3.10). In addition, the torque equation is the same as (3.11).

4.3 Inductance Calculation

This section will detail how to calculate all the elements in the nine branch inductance matrices and the three faulty inductance vectors.

4.3.1 Calculation of Inductances

It has been mentioned in the chapter 2 that there are three components in the phase self- and mutual- inductances. Based on the similar reasons as in the chapter 2, only the air-gap and slot-leakage inductance components will be calculated in the inductance calculations in this chapter.

If the branch A1 in Fig. 4.1 has an ITSC fault, the branch A1 will be separated into two parts: the faulty turns (A11_fm) and the remaining healthy turns (A11_hb, A11_ht, and A1_hc). The corresponding winding functions of the A1 branch with ITSC fault is depicted in Fig. 4.3, which can be used to obtain the air-gap components of inductances related to the short-circuited turns.

On the other hand, the corresponding winding function of a healthy branch Am (m=1, 2,⋯, n) in phase A is shown in Fig. 4.4, and it can be used to derive all the elements in the $\mathbf{L}_{AA}$ branch inductance matrix. The corresponding winding functions of a healthy branch of phases B and C can also be found in a similar way, and they can be used to find all the elements in the other branch inductance matrices.

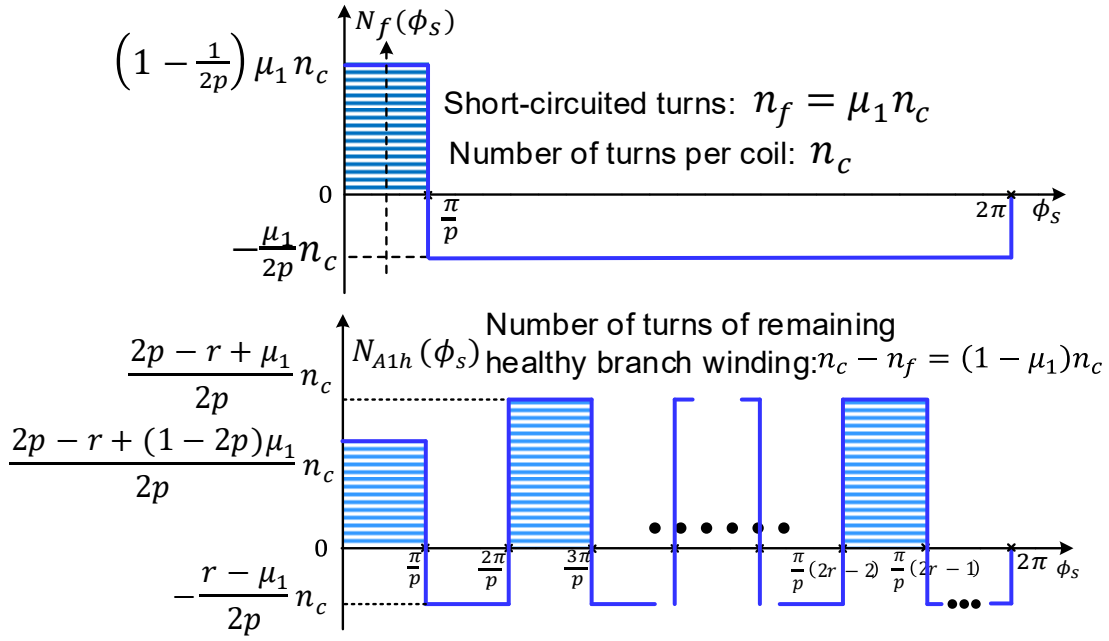

Fig. 4.3 Winding functions of faulty branch A1 in Phase A.

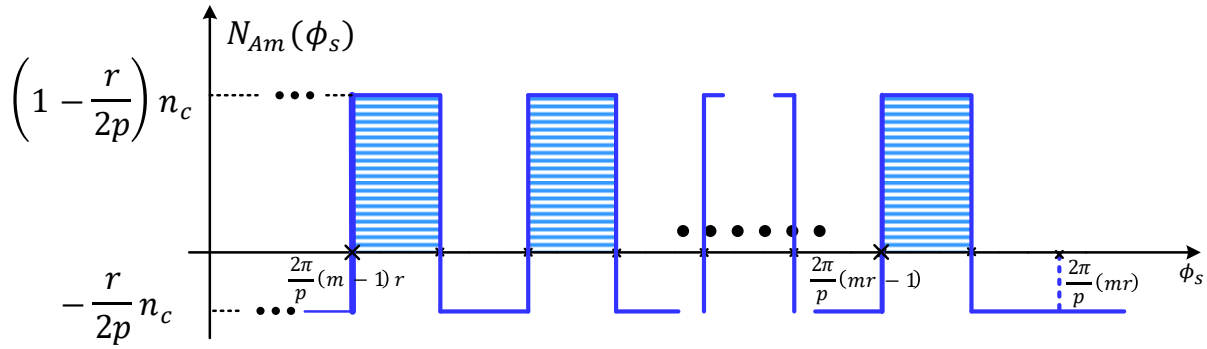

Fig. 4.4 The winding function of a healthy branch A*m* (m=1, 2,⋯, *n*) in Phase A.

After the winding functions of other branches are derived, all elements of the branch inductance matrices can be calculated using WFA together with the slot permeance method as detailed in [127]. It is found that all branch inductance matrices are still circulant matrices. According to the characteristic of the circulant matrices, once the elements in the first row are known, all the elements of the circulant matrices can be determined accordingly. As a result, all the inductances needed for the fault modelling can be obtained as

$$\begin{cases} L_{A1A1} = L_{B1B1} = L_{C1C1} = L_1 \\ M_{A1Aj} = M_{B1Bj} = M_{C1Cj} = M_1\ (j = 2,3,\cdots,n) \\ M_{A1B1} = M_{B1C1} = M_2 \\ M_{A1Bj} = M_{B1Cj} = M_1\ (j = 2,3,\cdots,n) \\ M_{A1Cj} = M_1\ (j = 2,3,\cdots,n-1) \\ M_{A1C1} = M_1 + M_\alpha \\ M_{A1Cn} = M_1 + M_\beta \end{cases} \tag{4.4}$$

with

$$\begin{cases} L_1 = \dfrac{\mu_0 r_e l_e}{g_e}\dfrac{r(2p-r)}{2p^2}\pi(n_c)^2 + 2r(n_c)^2\mu_0 l_e\left[\dfrac{h_s}{3S_\omega}\right] \\ M_1 = \dfrac{\mu_0 r_e l_e}{g_e}\left(-\dfrac{r^2}{2p^2}\right)\pi(n_c)^2 \text{ and } M_2 = -\dfrac{(2p-3r)}{3r}M_1 \\ M_\beta = \dfrac{\mu_0 r_e l_e}{g_e}\dfrac{1}{3p}\,\pi(n_c)^2 \text{ and } M_\alpha = (r-1)M_\beta \end{cases} \tag{4.5}$$

where the meanings of $\mu_0, r_e, l_e, g_e, h_s, S_\omega$ and p are the same as those in [140].

As for the elements in the fault inductance vectors, they are given as

$$\begin{cases} L_{A1f,A1f} + M_{A1h,A1f} = L_{11} \quad M_{Aj,A1f} = M_{Bj,A1f} = M_{11}\ (j = 2,3,\cdots,n) \\ M_{B1,A1f} = M_{Cn,A1f} = M_{22} \\ M_{Cj,A1f} = M_{11}\ (j = 1,2,\cdots,n-1) \end{cases} \tag{4.6}$$

Regarding $L_{A1f,A1f}$ and $M_{A1h,A1f}$, the air-gap and slot-leakage inductance components (indicated by subscripts "g" and "slot", respectively) will be also calculated separately, as those shown in chapter 3

$$\begin{aligned} L_{11} = L_{A1f,A1f} + M_{A1h,A1f} = \left(L_{A1f,A1f}\right)_g + \left(L_{A1f,A1f}\right)_{slot} \\ + \left(M_{A1h,A1f}\right)_g + \left(M_{A1h,A1f}\right)_{slot} \end{aligned} \tag{4.7}$$

with

$$\left(L_{A1f,A1f}\right)_g + \left(M_{A1h,A1f}\right)_g = \frac{\mu_0 r_e l_e}{g_e}\frac{(2p-r)}{2p^2}\mu_1\pi(n_c)^2 \tag{4.8}$$

In addition, the expressions for $\left(L_{A1f,A1f}\right)_{slot}$ and $\left(M_{A1h,A1f}\right)_{slot}$ are the same as (2.13) and (2.14).

As for M_{11} and M_{22} in (4.6), they can be expressed as

$$M_{11} = -\frac{\mu_0 r_e l_e}{g_e}\frac{r}{2p^2}\mu_1\pi(n_c)^2 \text{ and } M_{22} = \frac{(3r-2p)}{3r}M_{11} \tag{4.9}$$

Equations (4.5) to (4.9) show that the inductance elements in all branch inductance matrices and corresponding fault inductance vectors can be easily updated if the series-parallel coil connection rS×nP of a SPM machine is changed. This means that the developed fault model

in this thesis is generic and can be applicable to SPM machines with different series-parallel coil connections.

4.3.2 Results of Inductances

4.3.2.1 Elements of Branch Inductance Matrices

The key parameters of the studied 3kW SPM machine are listed in Table 4.1. This machine is the same as the one investigated in [140], [141], except this machine adopts different combinations of series-parallel-connected coils rather than series-connected or parallel-connected coils. By way of example, the 2D FE linear inductances of the 3kW machine with 2S×8P coil connection are shown in Fig. 4.5 (a). In Fig. 4.5 (b), the relative error of the inductances is the difference between the 2D analytical and FE inductances divided by the corresponding 2D FE inductances.

Table 4.1 Specifications of the studied 3kW SPM machine

	Series-parallel coil connections (rS×nP)		
	8S×2P	4S×4P	2S×8P
Rated power (kW)		3	
Rated speed (rpm)		170	
Rated voltage (Vrms)	345	172.5	86.3
Phase current (Arms)	5	10	20
Series turns/coil		52	
Numbers of slots/poles		96/32	
Rotor outer diameter (mm)		426.4	
Stack length (mm)		110	
Airgap length (mm)		2	

To be consistent with the conditions used by the analytical method, all permanent magnets in the FE model are treated as air, and the stator and rotor cores are assumed to be magnetically linear with a relative permeability $\mu_r = 10000$. After setting these conditions for materials, 1A DC current is then supplied to the A1 branch only, meaning all other branches in the three phases are open-circuited.

Due to the symmetrical 3-phase overlapping windings adopted by the studied SPM machine, the branch inductance matrices $\mathbf{L}_{AA} = \mathbf{L}_{BB} = \mathbf{L}_{CC}$ and $\mathbf{M}_{AB} = \mathbf{M}_{BC}$. As mentioned earlier, the determination of the elements in the first row of all these branch inductance matrices will be

enough to determine all the elements of these matrices. Hence showing the characteristics of inductances only related to A1 branch is sufficient.

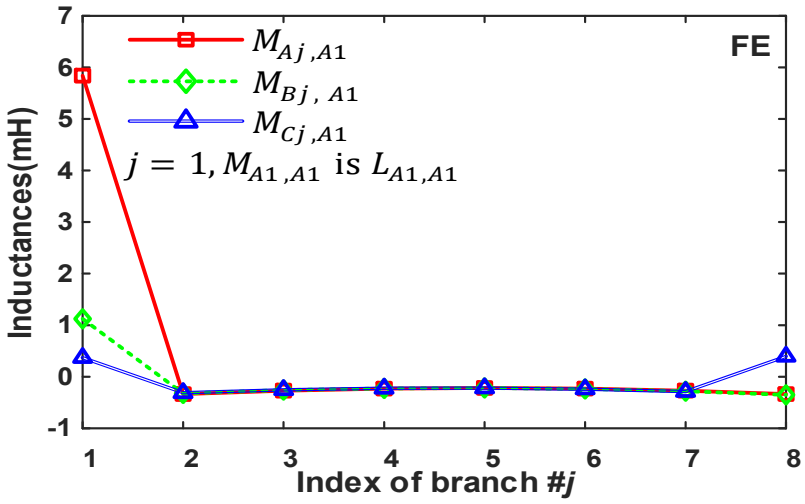

(a) 2D FE inductances

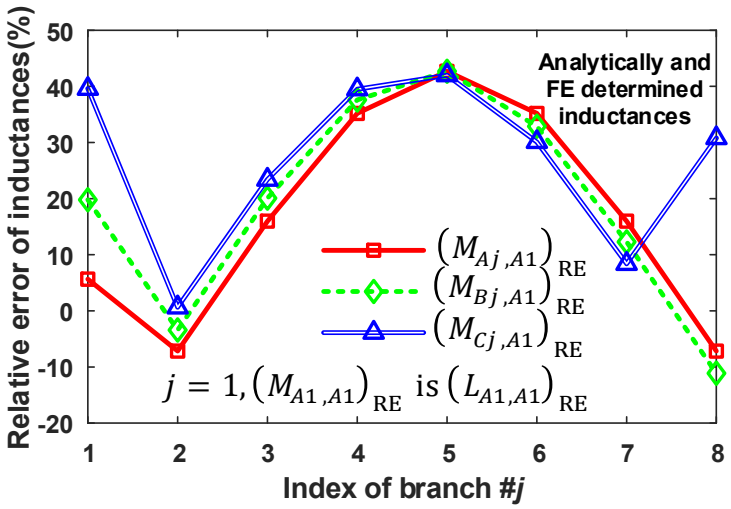

(b) Relative errors between analytical and FE inductances

Fig. 4.5 Characteristics of inductances between #A1 branch and other branches.

The relative errors between analytical and FE inductances are quite similar to those shown in chapter 3. Therefore, it can be concluded that although there are some large errors between analytical and FE inductances in Fig. 4.5 (b), due to the small values of these inductances, they may not have a significant impact on the accuracy of the developed fault model, as will be investigated in section 4.5.

4.3.2.2 Equivalent Phase Inductances

Further calculations of the equivalent phase self- and mutual inductances for the 2S×8P coil connection have been carried out, and the results are shown in Table 4.2. It is worth noting that how to calculate the equivalent phase self- and mutual- inductances for 3-phase windings with series-parallel coil connections will be left in section 4.4.

Table 4.2 Equivalent phase self- and mutual-inductances (mH)

Method	L_{AA}	M_{AB}	M_{AC}
2D FE	0.495	-0.0953	-0.0953
Analytical	0.499	-0.104	-0.104
Relative Error (%)	0.9	8.9	8.9

From Table 4.2, much smaller differences in the equivalent phase self- and mutual inductances can be observed. This means that the predicted phase currents of the healthy machines by the analytical and linear FE models would be very much similar. As for the inductance values and relative errors of inductances between the short-circuited turns and other branches, they are very much similar to those shown in Fig. 4.5 and hence are not presented here to avoid duplication.

4.4 Model Simplification

As mentioned in chapter 3, although the proposed fault model uses branch currents as state variables in the direct phase domain, it does not provide much meaningful physical insights because all the elements in the branch inductance matrices would not be zeros in theory, making the analyses very complicated. Meanwhile, it is difficult to construct a fault model in the Matlab/Simulink if the number of parallel branches n is large ($n \geq 10$), which is very often the case for large-power wind generators. To simplify the fault model, i.e., to make all the branch inductance matrices sparse ones, in this thesis, the original branch currents, voltages and back-EMFs are transformed into new variables using the multiphase Clarke transformation matrix $\mathbf{C}$ of [140] such as (4.10). More details can also be seen in equation (3.31) of chapter 3. The number of parallel branches n will replace the number of pole pairs p appearing in $\mathbf{C}$ of equation (3.31) of chapter 3 to keep matrix dimensions consistent.

$$\begin{bmatrix} \mathbf{f}'_A \\ \mathbf{f}'_B \\ \mathbf{f}'_C \end{bmatrix} = \begin{bmatrix} \mathbf{C} & \mathbf{0} & \mathbf{0} \\ \mathbf{0} & \mathbf{C} & \mathbf{0} \\ \mathbf{0} & \mathbf{0} & \mathbf{C} \end{bmatrix} \begin{bmatrix} \mathbf{f}_A \\ \mathbf{f}_B \\ \mathbf{f}_C \end{bmatrix} \tag{4.10}$$

where $\mathbf{f}'_A$, $\mathbf{f}'_B$ and $\mathbf{f}'_C$ are the corresponding transformed branch current, voltage, and back EMF vectors. In this thesis, $\mathbf{C}$ has the power invariant form, i.e., $\mathbf{C^{-1}} = \mathbf{C}^T$. Therefore, it is quite easy to obtain $\mathbf{f}_A$, $\mathbf{f}_B$ and $\mathbf{f}_C$ from $\mathbf{f}'_A$, $\mathbf{f}'_B$ and $\mathbf{f}'_C$ as shown in chapter 3.

After using the multiphase Clarke transformation, the new circuit-branch voltage equations can be expressed as

$$\begin{aligned}\begin{bmatrix}\mathbf{v}'_A\\ \mathbf{v}'_B\\ \mathbf{v}'_C\end{bmatrix} = &\begin{bmatrix}\mathbf{L}'_{AA} & \mathbf{M}'_{AB} & \mathbf{M}'_{AC}\\ \mathbf{M}'_{BA} & \mathbf{L}'_{BB} & \mathbf{M}'_{BC}\\ \mathbf{M}'_{CA} & \mathbf{M}'_{CB} & \mathbf{L}'_{CC}\end{bmatrix}\frac{\mathrm{d}}{\mathrm{d}t}\begin{bmatrix}\mathbf{i}'_A\\ \mathbf{i}'_B\\ \mathbf{i}'_C\end{bmatrix} + R_{\mathrm{cb}}\begin{bmatrix}\mathbf{i}'_A\\ \mathbf{i}'_B\\ \mathbf{i}'_C\end{bmatrix}\\ &+\begin{bmatrix}\boldsymbol{e}'_A\\ \boldsymbol{e}'_B\\ \boldsymbol{e}'_C\end{bmatrix} - \begin{bmatrix}\mathbf{C} & \mathbf{0} & \mathbf{0}\\ \mathbf{0} & \mathbf{C} & \mathbf{0}\\ \mathbf{0} & \mathbf{0} & \mathbf{C}\end{bmatrix}\left(\begin{bmatrix}R_{A1f}\\ 0\\ \vdots\\ 0\end{bmatrix} i_f + \begin{bmatrix}\mathbf{M}_{Af}\\ \mathbf{M}_{Bf}\\ \mathbf{M}_{Cf}\end{bmatrix}\frac{\mathrm{d}i_f}{\mathrm{d}t}\right)\end{aligned} \tag{4.11}$$

where $\mathbf{L}'_{xx} = \mathbf{C}\mathbf{L}_{xx}\mathbf{C}^{\boldsymbol{T}}$, $\mathbf{M}'_{xy} = \mathbf{C}\mathbf{M}_{xy}\mathbf{C}^{\boldsymbol{T}}$. "$x$" and "$y$" represent different phases amongst A, B, and C. If the inductances calculated by analytical method are employed in this analytical model, then $\mathbf{L}'_{xx}$, $\mathbf{M}'_{AB}$, and $\mathbf{M}'_{BC}$ are diagonal matrices and $\mathbf{M}'_{AC}$ is a block diagonal matrix. They can be expressed as

$$\mathbf{L}'_{xx} = \mathrm{diag}\big((L_1 + (n-1)M_1), (L_1 - M_1), (L_1 - M_1), \cdots, (L_1 - M_1)\big) \tag{4.12}$$

and

$$\mathbf{M}'_{AB} = \mathbf{M}'_{BC} = \mathrm{diag}\big((M_2 + (n-1)M_1), (M_2 - M_1), (M_2 - M_1), \cdots, (M_2 - M_1)\big) \tag{4.13}$$

and

$$(\mathbf{M}'_{AC})_{ij} = \begin{cases} M_\alpha + M_\beta + nM_1 & (i = j = 1)\\ M_\alpha + M_\beta \cos\left(\dfrac{2\pi k}{n}\right) & (i = j = 2k \text{ or } 2k+1)\\ M_\beta \sin\left(\dfrac{2\pi k}{n}\right) & (i = 2k, j = 2k+1)\\ -M_\beta \sin\left(\dfrac{2\pi k}{n}\right) & (i = 2k+1, j = 2k)\\ M_\alpha - M_\beta & (i = j = n)\end{cases} \tag{4.14}$$

In (4.14), the number of parallel branches n is assumed to be an even integer and the range of integer k is from 1 to $(n-2)/2$. Other elements of $\mathbf{M}'_{AC}$ are all zeros if their indices (i, j) do not satisfy the conditions listed in (4.14). When n is an odd integer, the range of integer k has to be changed to $[1, (n-1)/2]$ as $(n-2)/2$ is no longer an integer. In addition, the last element such as $M_\alpha - M_\beta$ when $i = j = n$ in (4.14) does not exist.

To sum up, after the transformation, the fault model is greatly reduced because the number of derivatives of state variables in every circuit branch voltage equation is reduced from $3n +$

1 to the minimum value. This means that there will only be 3 to 5 derivatives of state variables after the transformation.

The transformed voltage equation for the short-circuited path will be

$$\begin{aligned}\left(R_f + R_{A1f}\right)i_f + L_{A1f,A1f}\frac{\mathrm{d}i_f}{\mathrm{d}t} - e_{A1f} - R_{A1f}(\boldsymbol{C}^T\mathbf{i}'_A)_1 \\ = \left(\mathbf{CM}_{Af}\right)^T\frac{\mathrm{d}\mathbf{i}'_A}{\mathrm{d}t} + \left(\mathbf{CM}_{Bf}\right)^T\frac{\mathrm{d}\mathbf{i}'_B}{\mathrm{d}t} + \left(\mathbf{CM}_{Cf}\right)^T\frac{\mathrm{d}\mathbf{i}'_C}{\mathrm{d}t}\end{aligned} \tag{4.15}$$

where $(\mathbf{C}^T\mathbf{i}'_A)_1$ is the first element of the vector $\mathbf{C}^T\mathbf{i}'_A$. The torque equation now can be expressed as

$$T_e = \frac{\left(e_A i_A + e_B i_B + e_C i_C - e_{A1f} i_f\right)}{\omega_{rm}} + T_{cog} \tag{4.16}$$

It is worth mentioning that $i_A = i_{A1} + i_{A2} + \cdots + i_{An} = \sqrt{n}i'_{A1}$, similar relationships also exist between i_B and i'_{B1}, i_C and i'_{C1}. In addition, during the simplification process, the relationship between the phase self- and mutual- inductances for 3-phase windings having series-parallel-connected coils (L_{SP} and M_{SP}) and those having the series-connected coils (L_S and M_S) can be derived such as

$$\begin{cases}(L_{xx})_{SP} = \dfrac{1}{n}\displaystyle\sum_{j=1}^{n}(\mathbf{L}_{xx})_{1j} = \dfrac{1}{n^2}(L_{xx})_S \\ \left(M_{xy}\right)_{SP} = \dfrac{1}{n}\displaystyle\sum_{j=1}^{n}\left(\mathbf{M}_{xy}\right)_{1j} = \dfrac{1}{n^2}\left(M_{xy}\right)_S\end{cases} \tag{4.17}$$

4.5 Simulation Results

As can be seen from Fig. 4.1 in the FE simulations, the studied 3kW SPM machine is excited with 3-phase balanced sinusoidal voltages. In addition, the machine's rotor mechanical speed is kept constant during the whole operation period to shorten the simulation time. It is also worth mentioning that FE and Matlab/Simulink simulations for this 3kW SPM machine with different coil configurations such as 8S×2P, 4S×4P and 2S×8P have been carried out under different fault severities and different speeds. It is found that all the FE and analytical results generally have good agreements.

4.5.1 One Coil Short-Circuited

In this section some typical simulation results of the 96-slot 32-pole SPM machine with different coil configurations such as 8S×2P, 4S×4P and 2S×8P under the one-coil short-circuit fault are shown.

4.5.1.1 2S×8P

Fig. 4.6 shows some branch currents in all three phases before and after the one-coil short-circuit fault for the 2S×8P series-parallel winding configuration. It can be seen from Fig. 4.6 (a) that the branch currents obtained by these two models match well.

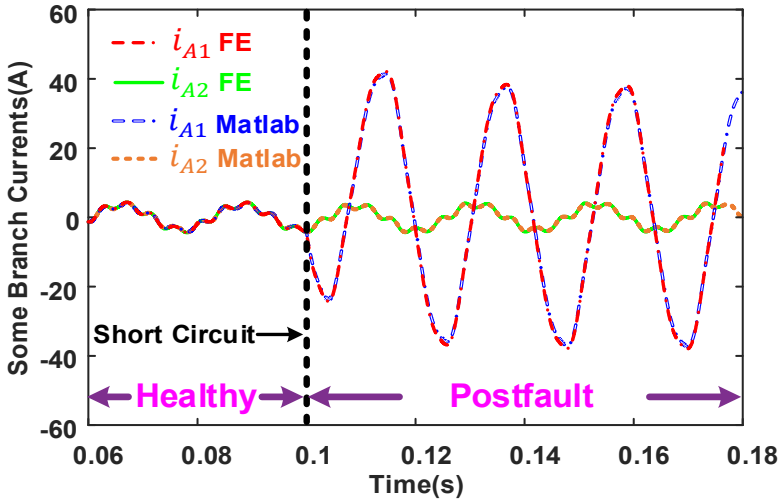

(a) Branch currents of phase A

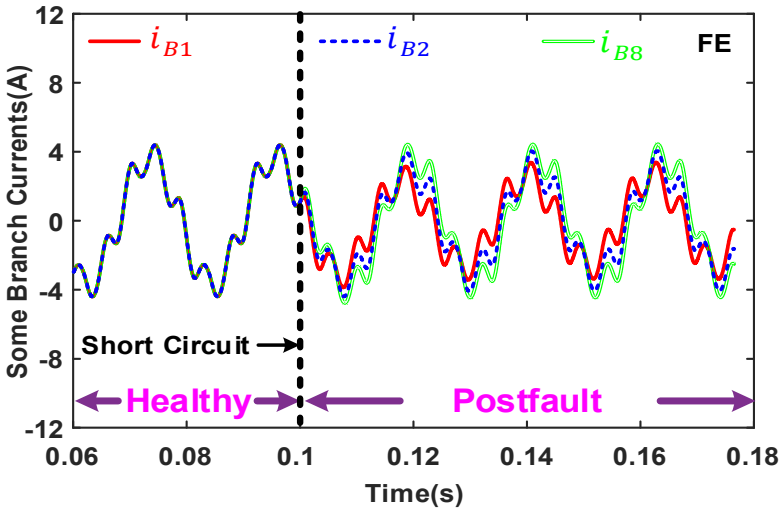

(b) Branch currents of phase B

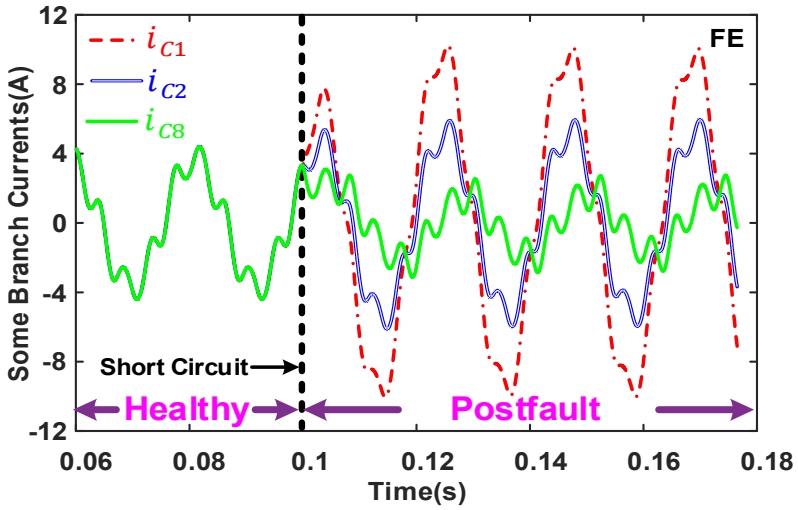

(c) Branch currents of phase C

Fig. 4.6 Some branch currents of three phases before and after one-coil short-circuit fault.

It is worth noting that i_{A3} to i_{A8} are very much similar to i_{A2}, i_{B3} to i_{B7} are very much similar to i_{B2}, and i_{C3} to i_{C7} are very much similar to i_{C2}. Hence they are not shown in these figures. Fig. 4.6 (b) and (c) show some branch currents of phases B and C. Here only the FE results are used, as they are very much the same as the analytical results. It is found that, different from the assumption made in [88], [89], the branch currents of the remaining healthy phases especially phase C are unequal for this integer-slot SPM machine after the ITSC fault. Meanwhile, the currents in the short-circuited coil predicted by the two models are shown in Fig. 4.7.

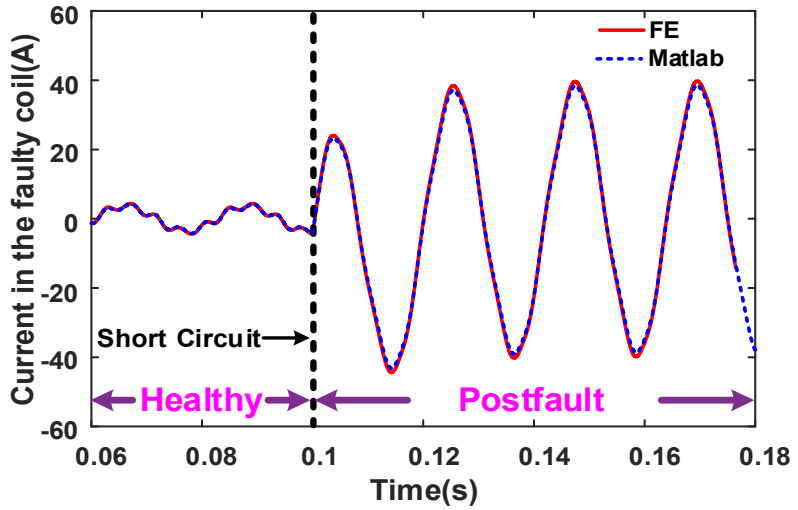

Fig. 4.7 Currents in the short-circuited coil under the one-coil short-circuit fault.

It can be seen that there is a significant increase in the current of the short-circuited coil. For example, the amplitude of current in the short-circuited coil increases from 4.25A to 38.6A after the ITSC fault. This will lead to changes in the phase current, and hence changes in the developed electromagnetic torque, as shown in Fig. 4.8.

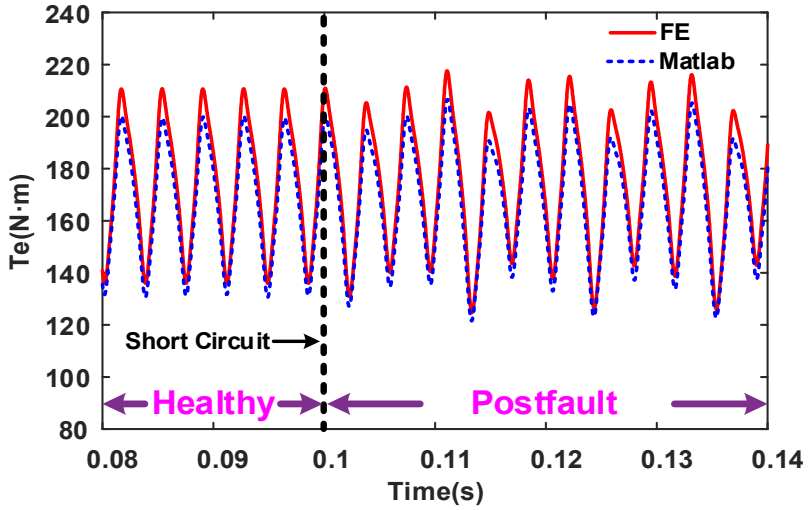

Fig. 4.8 Change in on-load torque of the 3kW SPM machine before and after the one coil short-circuit fault.

It is worth noting that, in Fig. 4.8, the cogging torque has already been included in the analytical model according to (4.16) to give more accurate prediction of torque ripple under the ITSC fault. It can be seen that after the ITSC fault, the torque ripple increases only slightly. This is mainly because each phase current is the sum of 8 individual branch currents. As a result, although some branch currents change significantly, the phase current is only slightly affected.

4.5.1.2 4S×4P

Considering that the FE results are very much the same as the analytical results, in Fig. 4.9 all branch currents from the FE model in all three phases before and after the one-coil short-circuit fault for the 4S×4P series-parallel winding configuration are shown. It can be easily seen that i_{A3} to i_{A4} are very much similar to i_{A2}, i_{B3} are very much similar to i_{B2}, and i_{C2}, i_{C3} are very much similar. Compared with the 2S×8P winding configuration, the current in the remaining healthy turns of A1 branch of the 4S×4P winding configuration decreases significantly (from 38A to 13A), meaning that the local overheating due to the one- coil short-circuit fault in the 4S×4P winding configuration is not worse than that in the 2S×8P winding configuration.

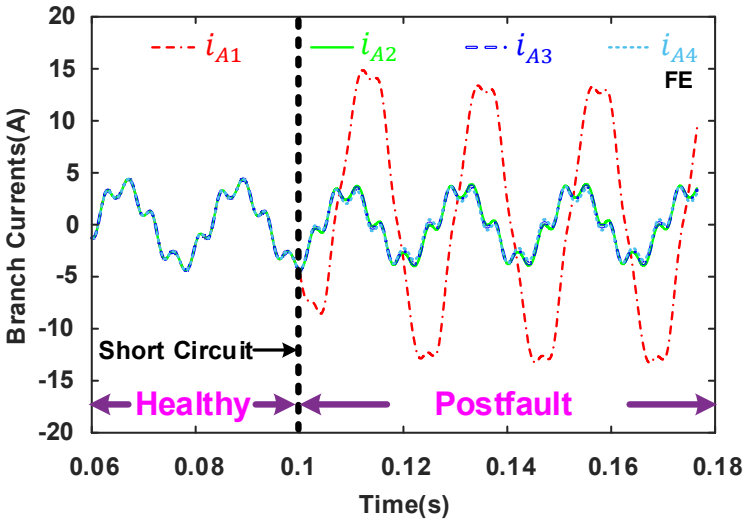

(a) Branch currents of phase A

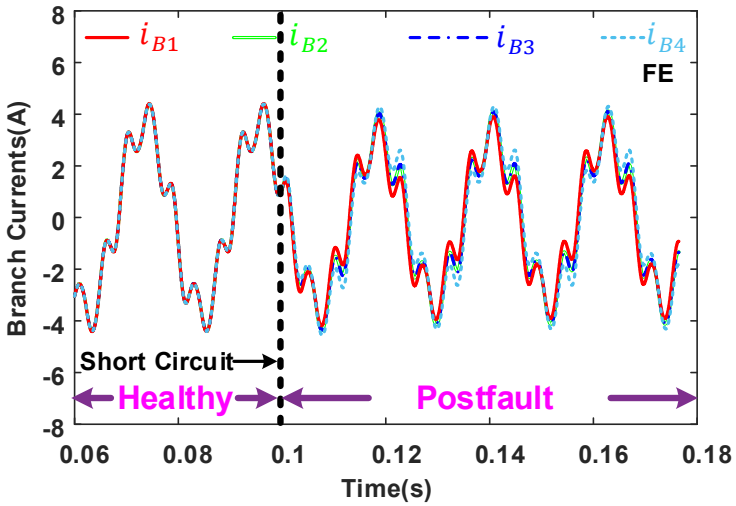

(b) Branch currents of phase B

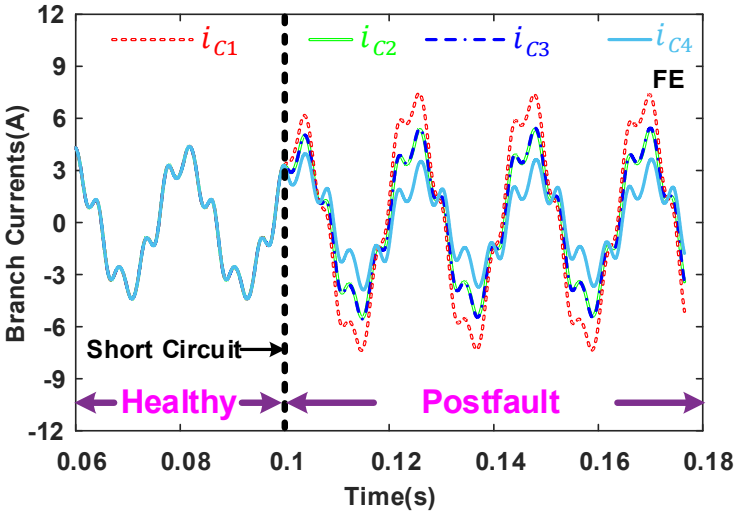

(c) Branch currents of phase C

Fig. 4.9 Branch currents of three phases before and after one-coil short-circuit fault.

In addition, different from the assumption made in [88], [89], the branch currents in the remaining healthy phases are not all equal for this integer-slot SPM machine after the one- coil short-circuit fault. As for the current in the short-circuited coil and on-load torque of the 3kW SPM machine before and after the one coil short-circuit fault, they are very much similar to those shown in Fig. 4.7 and Fig. 4.8, thus they are not provided here.

4.5.1.3 8S×2P

The special case of series-parallel winding configuration is that each phase winding only has 2 parallel branches. For this case, all branch currents in all three phases before and after the one-coil short-circuit fault are shown in Fig. 4.10.

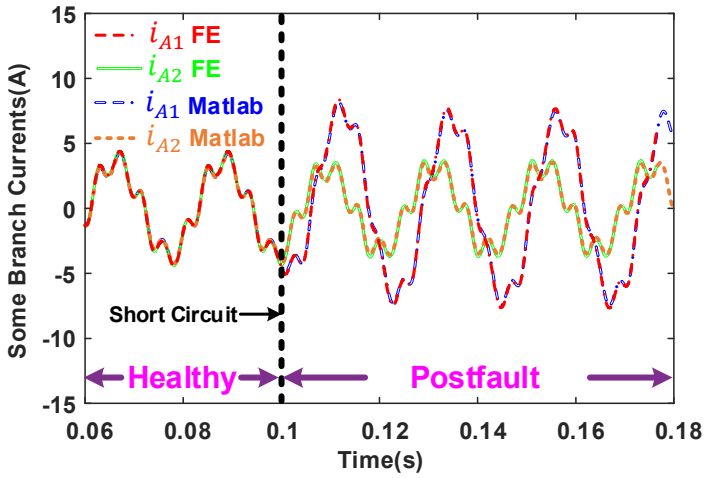

(a) Branch currents of phase A

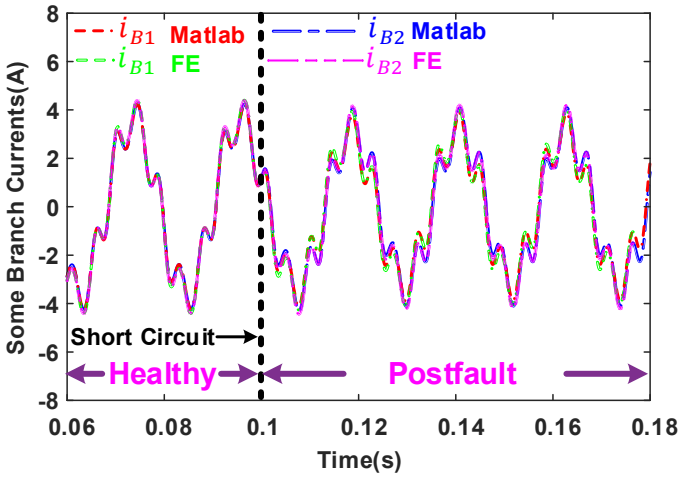

(b) Branch currents of phase B

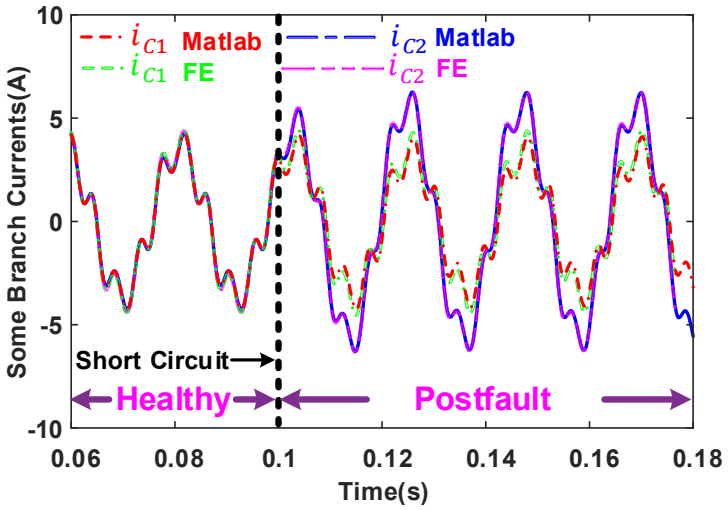

(c) Branch currents of phase C

Fig. 4.10 Branch currents of three phases before and after one-coil short-circuit fault.

The good agreements between the FE and analytical results can be observed in Fig. 4.10. In addition, it is evident that the assumption made in [88], [89], i.e., the branch currents in the remaining healthy phases are all equal is not valid for this integer-slot SPM machine after the one- coil short-circuit fault. For the same reasons as those for the 4S×4P winding configuration, the current in the short-circuited coil and on-load torque of the 3kW SPM machine before and after the one coil short-circuit fault are not shown here.

4.5.2 Different Fault Severities

The amplitudes of inter-turn short-circuit currents obtained by FE and Matlab/Simulink simulations for the 3kW SPM machine with different coil connections such as 8S×2P, 4S×4P, and 2S×8P and under different fault severities are shown in Fig. 4.11. Here, the fault location is at the bottom of the slot, i.e., $h_a = h_s/n_c$. A generally good agreement between the FE and analytical results can also be observed. The slightly larger difference between FE and Matlab/Simulink results for 8S×2P and 4S×4P coil connections is mainly because the relative errors between the inductances obtained by linear 2D FE and analytical approaches are larger when the number of branches is smaller.

It is also found that when the coil faulty turns ratio increases, the ITSC current reduces. This is the case for all series-parallel coil connections. The reason for this is that the ITSC current is mainly determined by the ratio of open-circuit flux linkage of the short-circuited turns to their self-inductance. When the faulty turns ratio increases, the self-inductance of the short-circuited turns (proportional to number of turns squared) increases faster than its open-circuit flux linkage (proportional to number of turns). In addition, if the coil faulty turns ratio is the

same, different series-parallel coil connections will have negligible influence on the amplitude of the ITSC current. This is mainly because for all the series-parallel coil connections, the number of turns per coil is the same. As a result, when the coil faulty turns ratio is the same, the number of short-circuited turns is also identical, leading to the same ITSC current.

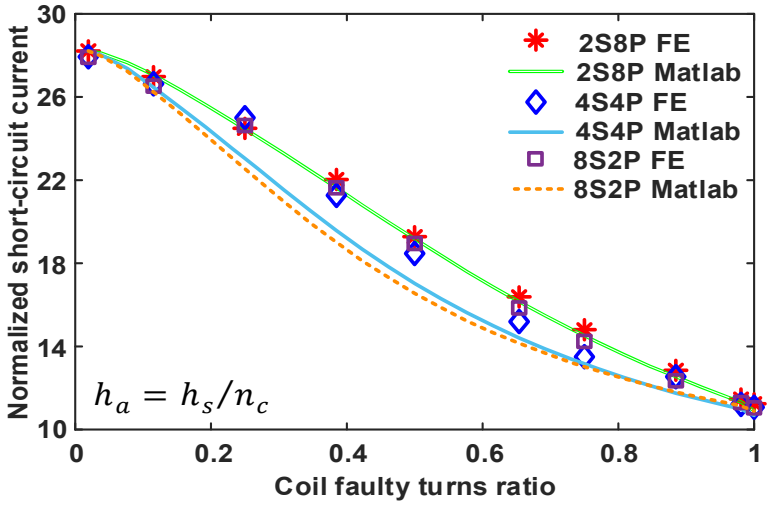

Fig. 4.11 Amplitudes of ITSC current *vs* coil faulty turns ratio for different series-parallel coil connections.

4.6 Conclusion

This chapter develops a general and simple analytical model for PM wind generators with different series-parallel coil connections under inter-turn short-circuit (ITSC) faults. In the fault model, branch currents are used as state variables and inductances for different series-parallel coil connections are calculated by an analytical method such as winding function approach (WFA) together with slot permeance method. Based on the characteristics of the calculated inductances and the concise block matrix form of the developed fault model, the multiphase Clarke transformation has been proposed to simplify the fault model. In the process of model simplification, the healthy machine model using branch currents as state variables has been proven to be equivalent to that using 3-phase currents as state variables. The proposed fault model and model simplification method are generic and may be extended to other types of non-PM machines and also their multiphase counterparts. Simulation results from 2D FE and analytical models generally match well for different fault scenarios and different coil connections. This validates the accuracy of the proposed fault model. The analytical fault model proposed in this chapter can be very useful for developing model-based fault detection and mitigation strategies for large wind power generators. For these machines, the modelling methods like FE or magnetic equivalent circuit can be very time-consuming. In addition, it can

also be used to evaluate the fault-tolerant abilities of SPM machines with different winding configurations. From the developed fault model, it is found that the branch currents of the remaining healthy phases under ITSC fault are not always equal and different series-parallel coil connections have negligible influence on the amplitude of ITSC current at the same torque and speed.

Chapter 5 Modelling and Analysis of Inter-Turn Short-Circuit Fault for Large-Power SPM Wind Generators

Based on the developed general analytical fault model in chapter 4, this chapter focuses on the fault model simplification for large-power surface-mounted permanent magnet (SPM) wind generators. It is found that the multiphase Clarke transformation can be used to simplify the proposed fault model with FE linear or nonlinear inductances. Thus the accuracy of the fault model with analytical inductances can be easily validated by the fault model with FE linear inductances when some relative errors between analytical and FE linear inductances having large values in the fault model are large. If more accurate predictions are required, nonlinear FE inductances can be used in the simplified fault model. Studies of scaling effect and influence of fault location considering series-parallel coil connections of PM machines with different power ratings (3kW, 500kW, 3MW) have been carried out. Simulation results show that large-power SPM wind generators are vulnerable to ITSC faults when relatively small number of turns are short-circuited and the single turn short-circuit fault at the top of the slot is the worst case.

Related Publications:

[Mei23d] Z. T. Mei, G. J. Li, Z. Q. Zhu, R. Clark, A. Thomas, and Z. Azar, "Modelling and Analysis of Inter-Turn Short-Circuit Fault for Large-Power SPM Wind Generators" *Energies*, vol. 16, no. 12, 2023.

5.1 Introduction

In chapter 4, the relatively simple and general analytical fault model for SPM machines with series-parallel coil connections has been proposed. However, the fault model simplification using the multiphase Clark transformation matrix in chapter 4 is based on the analytical inductances derived for SPM machines. Whether the fault model with analytical inductances and model simplification method can be extended to large-power surface-mounted permanent magnet (SPM) wind generators have not been investigated.

This chapter continues to study whether the model simplification method can be extended to the fault models for SPM machines with FE linear or nonlinear inductances. It is found that the model simplification method using the multiphase Clarke transformation can be applied to the fault models of large-power surface-mounted permanent magnet (SPM) wind generators. In fact, the model simplification method will be still valid for SPM machines with other winding configurations only if the branch inductance matrices are all circulant matrices.

5.2 Inductance Calculation by FEM

In chapter 4 the general analytical fault model has been proposed for SPM machines with series-parallel coil connections. The inductances in the fault model are derived for SPM machines with series-parallel coil connections by the same analytical method: winding function approach (WFA) together with slot permeance method. This section will detail the characteristics of inductance calculation for large-power SPM wind generators.

Although direct FE simulation of large-power SPM wind generators under ITSC fault using voltage sources is quite time-consuming, inductance calculation using FEM can often obtain accurate results in a short time. For the studied 3MW SPM wind generator, it will only take about several seconds to obtain all linear inductances, and several hours to obtain all the nonlinear inductances using the flux linkage subtraction method when the core saturation is not heavy. These FE inductances can then be used in the fault model for predicting the performance of machines under ITSC faults. It is worth mentioning that under ITSC faults, the machine becomes asymmetric and therefore full FE model shown in Fig. 2.4 is necessary to calculate all the inductances needed in the fault model.

In Fig. 2.4, the fault locations h_a and h_b related to the number of short-circuited turns (marked in red color) are highlighted. The coil having short-circuited turns shown in Fig. 2.4 is divided into three FEM coils with different numbers of turns, shown in Fig. 2.4. The A1_hc FEM coil in Fig. 5.1 represents the remaining $r-1$ healthy coils of A1 branch. With regard to

A11_hb and A11_ht FEM coils in Fig. 5.1, they are the remaining healthy turns at the bottom and top of the two affected slots having short-circuited turns. The last FEM coil A11_fm in A1 branch of Fig. 5.1 represents the short-circuited turns in the middle of the two affected slots. In addition, one FEM coil in every other healthy branch of the three phase windings is used to indicate it has r healthy coils connected in series.

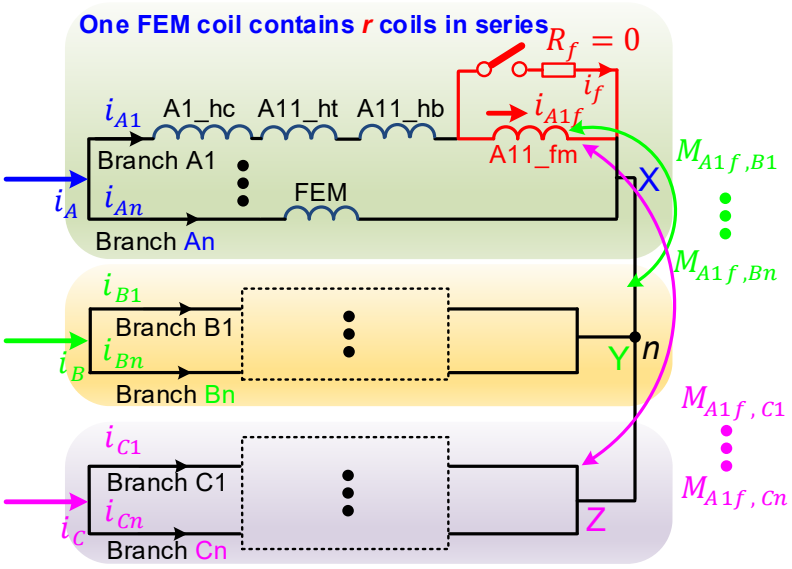

Fig. 5.1 Circuit schematic of the studied SPM wind generators under ITSC fault.

5.3 Results of Inductances

The main parameters of the studied SPM machines are shown in Table 5.1. The initial design dimensions can be found in [142], thus it is very easy to obtain them. Some analytical and direct FE inductance results of the 500kW machine are shown in Fig. 5.2 (a) and (b) as examples. In Fig. 5.2 (c), the relative error of the inductances is the difference between the 2D analytical and FE inductances divided by the corresponding 2D FE inductances. On the other hand, some analytical and direct FE inductance results of the 3MW machine are shown in Fig. 5.3. As for the inductance results of the 3kW SPM machine with series-connected coils, they have been shown in chapter 2. It can be seen from Fig. 5.2 (c) that some relative errors of the elements in the branch inductance matrices for the 500kW SPM machine are relatively large for some inductances having larger values such as about 100% for M_{A1B1} and M_{A1C1}. As for the large difference such as 500% for some very small inductance values, they might not affect too much the accuracy of the fault model. In Fig. 5.3, the inductances of the 3MW SPM machine also have similar characteristics.

Table 5.1 Key parameters of the studied SPM machines [142]

Rated power	3kW	500kW	3MW
Rated speed (rpm)	170	32	15
Rated voltage (Vrms)	690	690	690
Phase current (Arms)	2.5	438.2	2790
Series-parallel winding	16S1P*	7S7P*	4S20P*
Series turns/coil	52	23	14
Numbers of slots/poles	96/32	294/98	480/160
Rotor outer diameter (mm)	426.4	2195.5	5000
Stack length (mm)	110	550	1200
Airgap length (mm)	2	2.15	5

*: *r*S*n*P such as 16S1P is used to represent the series-parallel winding configuration of the studied machines. It means *r* coils in series, *n* parallel branches.

Considering that the fault modelling using direct FE simulations for the 500kW and 3MW SPM machines are very time-consuming due to their large number of slots and poles as well as numerous parallel branches, it seems that the validation of the fault model using analytical inductances by direct FE simulations becomes difficult. In addition, if the validation of the fault model with the analytical inductances is carried out by using the fault model with FE linear inductances, then first-order systems of a large number of differential equations with mostly non-zero coefficients have to be built, which are quite complex.

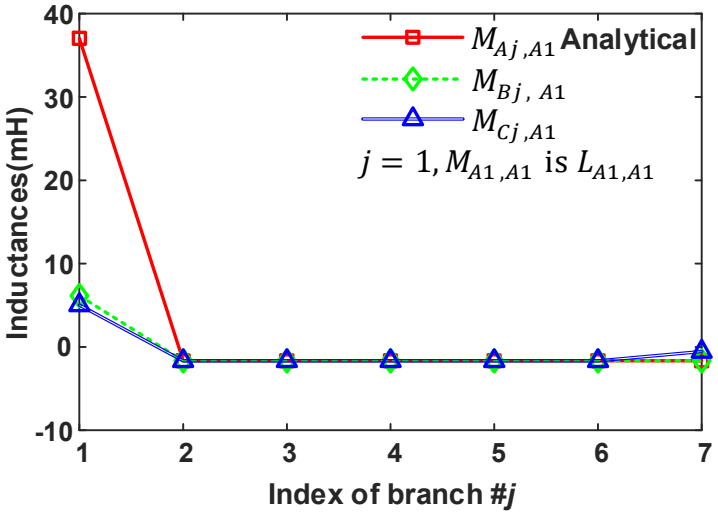

(a) Analytical inductances

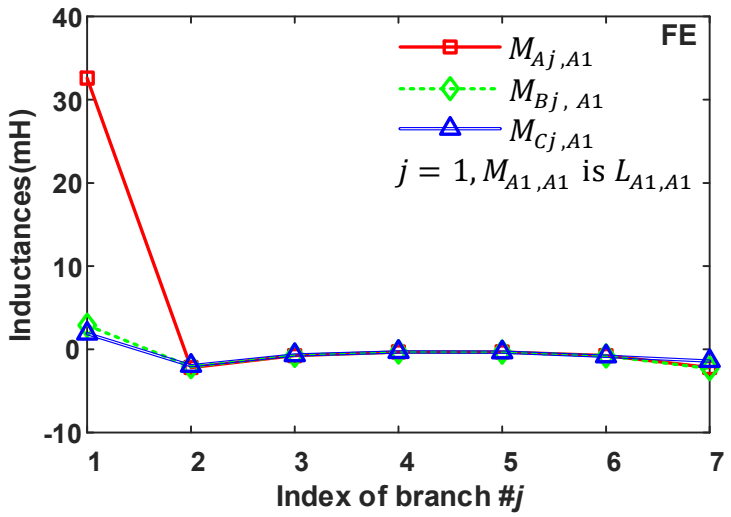

(b) 2D FE inductances

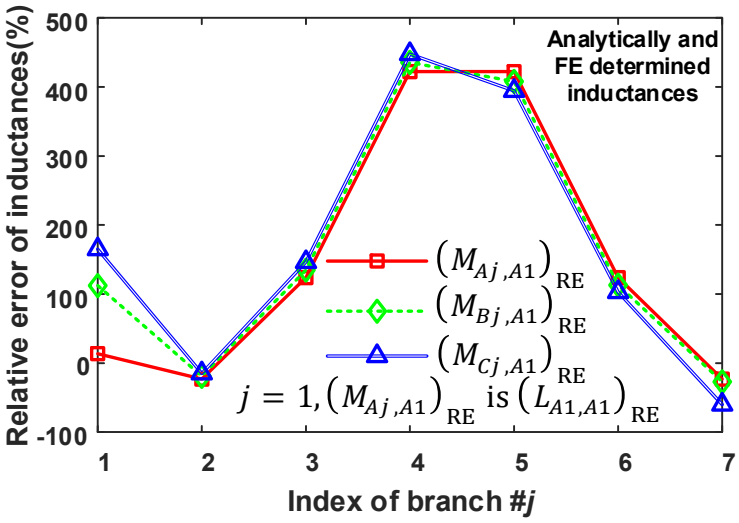

(c) Relative errors between analytical and FE inductances

Fig. 5.2 Characteristics of inductances between #A1 branch and other branches for the 500kW SPM machine.

However, it is found that the multiphase Clarke transformation developed in chapter 3 can be used to simplify the fault model with FE inductances only if the circulant property of all branch inductance matrices is retained. Therefore, the validation of the fault model with analytical inductances can be carried out by using the fault model with FE linear inductances in a simpler manner and the prediction of fault performance using inductances obtained by both analytical and FE methods is feasible. It is worth noting that the fault simulations using analytical inductances will be the fastest, but with nonlinear FE inductances it will be much more accurate.

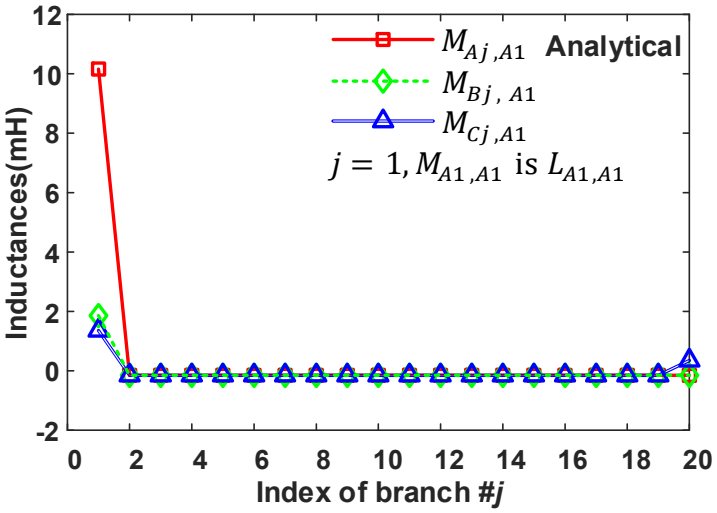

(a) Analytical inductances

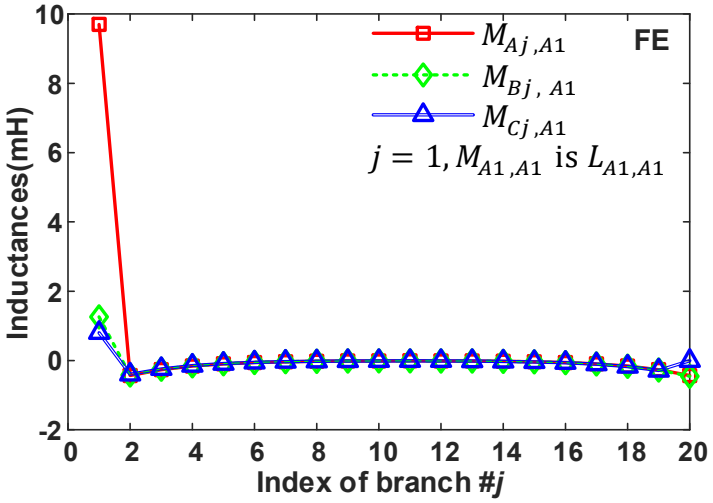

(b) 2D FE inductances

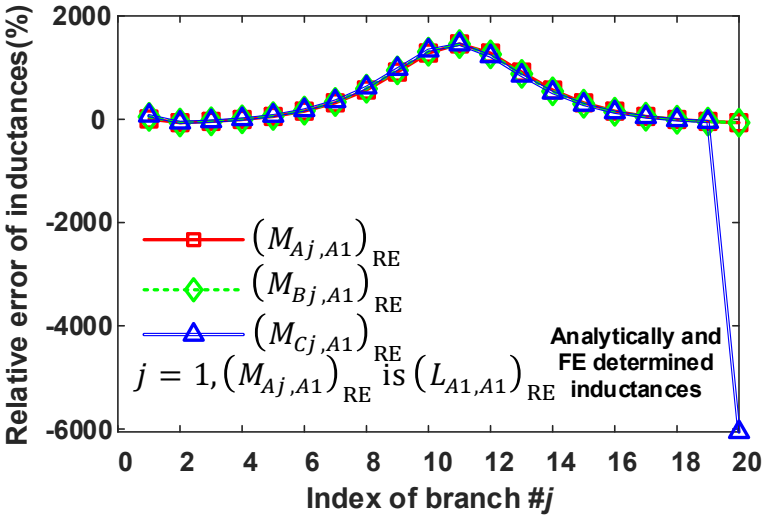

(c) Relative errors between analytical and FE inductances

Fig. 5.3 Characteristics of inductances between #A1 branch and other branches for the 3MW SPM machine.

5.4 Model Simplification

As mentioned in chapter 4, the developed multiphase Clarke transformation matrix can be used to simplify the fault model using analytical inductances. The transformed branch inductance matrices are $\mathbf{L}'_{xx} = \mathbf{C}\mathbf{L}_{xx}\mathbf{C}^{\boldsymbol{T}}$, $\mathbf{M}'_{xy} = \mathbf{C}\mathbf{M}_{xy}\mathbf{C}^{\boldsymbol{T}}$. If these transformed branch inductance matrices are sparse ones, then the fault model is greatly simplified. The general case would be that the branch inductance matrices such as $\mathbf{L}_{xx}$ and $\mathbf{M}_{xy}$ are circulant matrices with elements different to each other, which can be written as

$$\mathrm{circ}(L_0, L_1, \cdots, L_{n-1}) = \begin{bmatrix} L_0 & L_1 & L_2 & \cdots & L_{n-1} \\ L_{n-1} & L_0 & L_1 & \cdots & L_{n-2} \\ L_{n-2} & L_{n-1} & L_0 & \cdots & L_{n-3} \\ \vdots & \vdots & \vdots & \ddots & \vdots \\ L_1 & L_2 & L_3 & \cdots & L_0 \end{bmatrix} \tag{5.1}$$

For brevity, $\mathbf{L}_{\mathrm{circ}} = \mathrm{circ}(L_0, L_1, \cdots, L_{n-1})$ is defined. In this case if the multiphase Clarke transformation matrix is used, then the transformed branch inductance matrices will become block diagonal matrices, the elements of which are expressed as

$$(\mathbf{C}\mathbf{L}_{\mathrm{circ}}\mathbf{C}^T)_{i,j} = \begin{cases} (\mathbf{C}\mathbf{L}_{\mathrm{circ}}\mathbf{C}^T)_{1,1} = \sum_{h=0}^{n-1} L_h \\ (\mathbf{C}\mathbf{L}_{\mathrm{circ}}\mathbf{C}^T)_{2k,2k} = (\mathbf{C}\mathbf{L}_{\mathrm{circ}}\mathbf{C}^T)_{2k+1,2k+1} = \sum_{h=0}^{n-1} L_h \cos\left(\frac{2\pi h}{n}\right) \quad k = 1, 2, \cdots, \frac{n-2}{2} \\ (\mathbf{C}\mathbf{L}_{\mathrm{circ}}\mathbf{C}^T)_{2k,2k+1} = -(\mathbf{C}\mathbf{L}_{\mathrm{circ}}\mathbf{C}^T)_{2k+1,2k} = -\sum_{h=0}^{n-1} L_h \sin\left(\frac{2\pi h}{n}\right) \; k = 1, 2, \cdots, \frac{n-2}{2} \\ (\mathbf{C}\mathbf{L}_{\mathrm{circ}}\mathbf{C}^T)_{n,n} = (-1)^h \sum_{h=0}^{n-1} L_h \end{cases} \tag{5.2}$$

In addition, the relationship between the equivalent phase self- and mutual-inductances for 3-phase windings having series-parallel-connected coils (L_{SP} and M_{SP}) and those having series-connected coils (L_S and M_S) can be also established as (4.17) even when nonlinear inductances are used.

5.5 Model Construction Using Matlab/Simulink

In this section how to build a general fault model in the Matlab/Simulink environment will be detailed using the developed fault model and model simplification method. To illustrate the

model structure clearly, the fault model for the 500kW SPM machine will be used here as an example. Based on the fault model for the 500kW SPM machine, the fault models for SPM machines with other power ratings can be easily developed in a similar way.

In Fig. 5.4, the whole system in the uppermost layer of the developed Simulink model is shown. It can be easily seen that the whole system is divided into two parts: the electrical model will contain all the voltage equations and the developed electromagnetic torque equation, and the mechanical model will represent the two common mechanical equations. The names of the input and output variables of all the subsystems are explained as follows. For example, Vab and Vbc represent the two line voltages v_{AB} and v_{BC}. theta_r and w_r represent the rotor electrical position θ_r and speed ω_r, respectively.

It is worth mentioning that the electrical model contains much information. Generally, there are three major parts in the electrical model shown in Fig. 5.4: the parameter initialization part includes the assignment of inductance values to the branch inductance matrices and three faulty inductance vectors as shown in Fig. 5.5 and Fig. 5.6, calculation of back-EMFs and phase voltages. The transformed branch current state-variable model part as shown in Fig. 5.7 will represent all the branch voltage equations, and the current output part outputs all the transformed and original branch currents, as shown in Fig. 5.8.

In addition, it can be seen that many signal routing "**From**" and "**Goto**" blocks are frequently used inside of the electrical model, as shown in Fig. 5.6 to Fig. 5.8. The tag visibility parameter of the **Goto** signal routing blocks are all set to be "global", thus **From** and **Goto** blocks using the same tag can be anywhere inside the electrical model to avoid unnecessary crossing of signal lines. For example, the M_A1B1p **From** block used inside the "Phase_A" subsystem of Fig. 5.7 corresponds to the M_A1B1p **Goto** block in Fig. 5.5. This kind of representation will make the model easier to read and build.

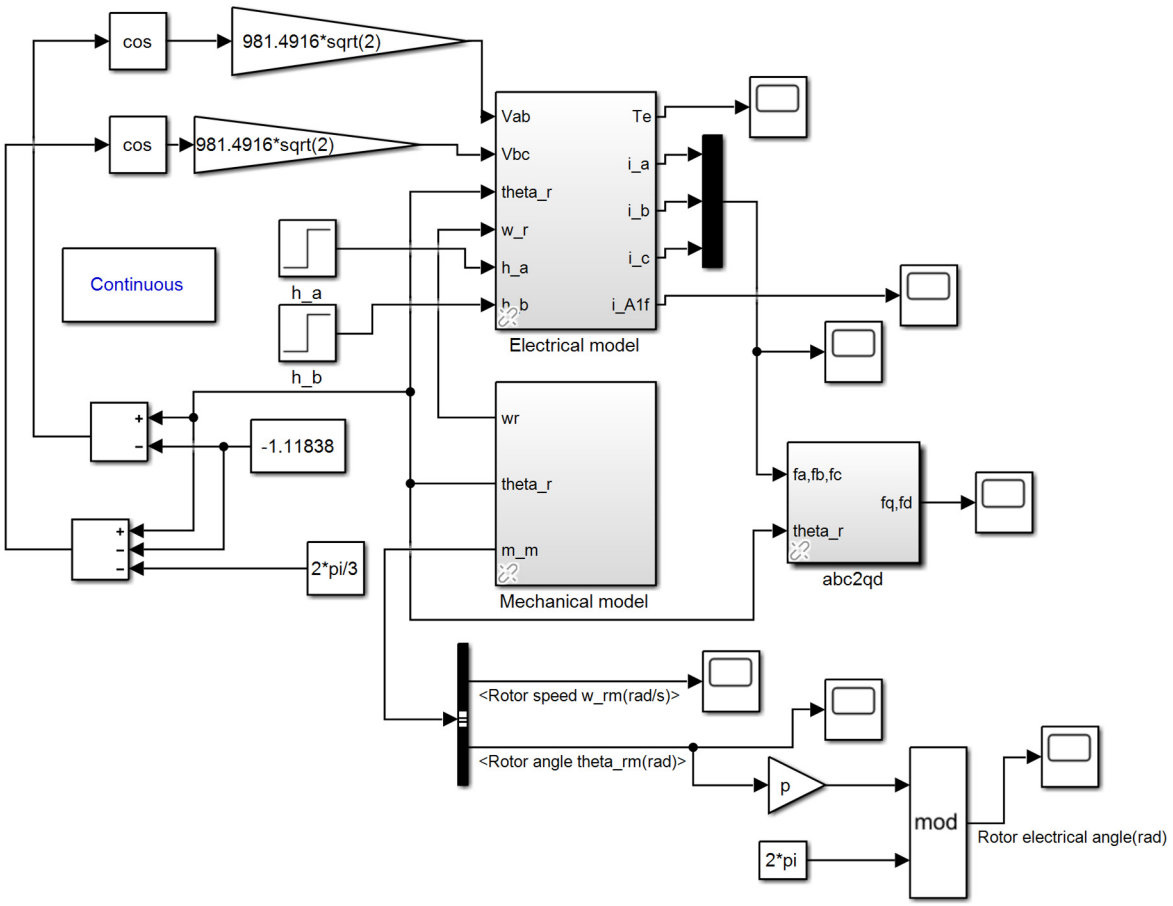

Fig. 5.4 Representation of the whole system in the uppermost layer in the Matlab/Simulink environment.

On the other hand, Fig. 5.5 shows how to transform the elements of $\mathbf{M}_{AB}$ into the elements of $\mathbf{M}'_{AB}$ using (5.2). The elements of $\mathbf{M}'_{AB}$ can be represented as follows

$$\mathbf{M}'_{AB} = \begin{bmatrix} M'_{A1B1} & 0 & 0 & \cdots & \cdots & 0 & 0 & 0 \\ 0 & M'_{A2B2} & M'_{A2B3} & \cdots & \cdots & 0 & 0 & 0 \\ 0 & M'_{A3B2} & M'_{A3B3} & \cdots & \cdots & 0 & 0 & 0 \\ \vdots & \vdots & \vdots & \ddots & \vdots & \vdots & \vdots & \vdots \\ \vdots & \vdots & \vdots & \vdots & \ddots & \vdots & \vdots & \vdots \\ 0 & 0 & 0 & \cdots & \cdots & M'_{A(n-2),B(n-2)} & M'_{An-2,B(n-1)} & 0 \\ 0 & 0 & 0 & \cdots & \cdots & M'_{A(n-1),B(n-2)} & M'_{A(n-1),B(n-1)} & 0 \\ 0 & 0 & 0 & \cdots & \cdots & 0 & 0 & M'_{AnBn} \end{bmatrix} \tag{5.3}$$

As for the elements of $\mathbf{M}_{AB}$, they can be represented as

$$\mathbf{M}_{AB} = \begin{bmatrix} M_{AB1} & M_{AB2} & M_{AB3} & \cdots & \cdots & M_{AB,n-2} & M_{AB,n-1} & M_{ABn} \\ M_{ABn} & M_{AB1} & M_{AB2} & \cdots & \cdots & M_{AB,n-3} & M_{AB,n-2} & M_{AB,n-1} \\ M_{AB,n-1} & M_{ABn} & M_{AB1} & \cdots & \cdots & M_{AB,n-4} & M_{AB,n-3} & M_{AB,n-2} \\ \vdots & \vdots & \vdots & \ddots & \vdots & \vdots & \vdots & \vdots \\ \vdots & \vdots & \vdots & \vdots & \ddots & \vdots & \vdots & \vdots \\ M_{AB4} & M_{AB5} & M_{AB6} & \cdots & \cdots & M_{AB1} & M_{AB2} & M_{AB3} \\ M_{AB3} & M_{AB4} & M_{AB5} & \cdots & \cdots & M_{ABn} & M_{AB1} & M_{AB2} \\ M_{AB2} & M_{AB3} & M_{AB4} & \cdots & \cdots & M_{AB,n-1} & M_{ABn} & M_{AB1} \end{bmatrix} \tag{5.4}$$

This kind of representation corresponds to all the names of the "**Goto**" blocks. In addition, if the elements of $\mathbf{M}_{AB}$ are obtained by different methods such as the analytical approach or FEM, they can be loaded to the Simulink model easily to see the difference of fault performances.

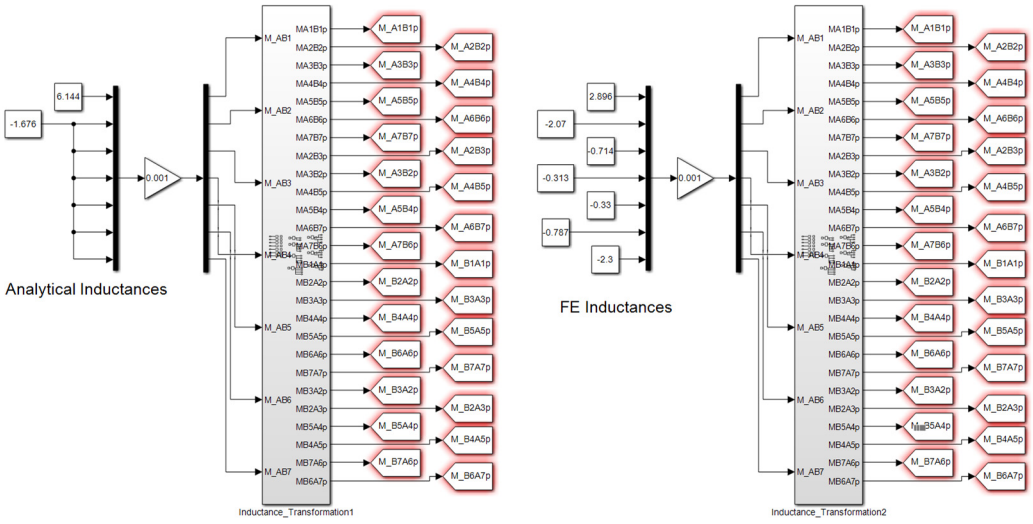

Fig. 5.5 Transforming $\mathbf{M}_{AB}$ with analytical or FE inductances to $\mathbf{M}'_{AB}$.

As for the elements of the transformed three faulty inductance vectors $\mathbf{M}'_{Af}$, $\mathbf{M}'_{Bf}$ and $\mathbf{M}'_{Cf}$, they are shown in Fig. 5.6. The elements of the three original faulty inductance vectors $\mathbf{M}_{Af}$, $\mathbf{M}_{Bf}$ and $\mathbf{M}_{Cf}$ will relate to the two fault locations h_a and h_b by using the Matlab function block. This will also leave us some flexibility if the elements of the three original faulty inductance vectors are calculated by one of the two different approaches.

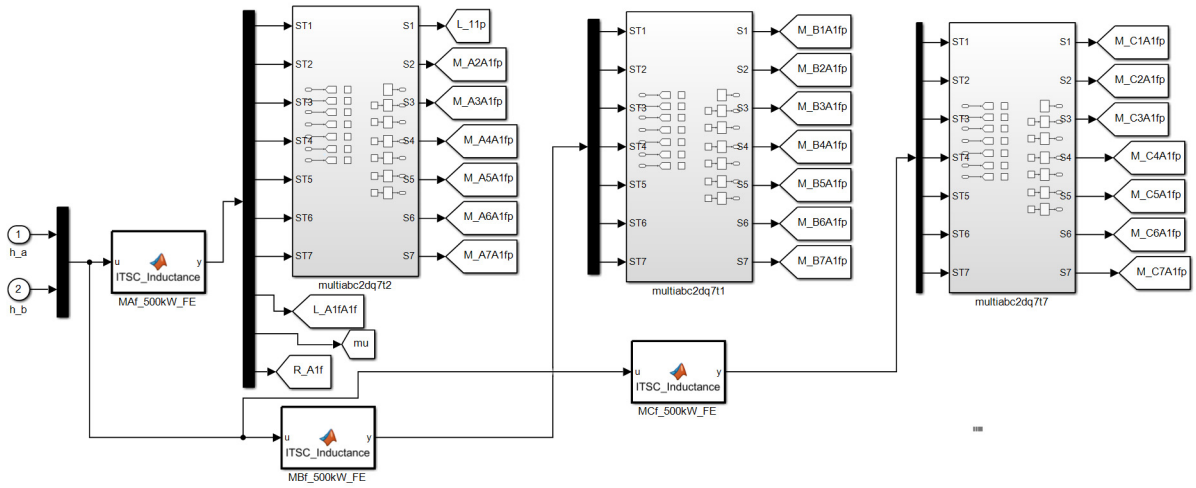

Fig. 5.6 Transforming the inductances and resistances relating to the two fault locations h_a and h_b.

After parameter initialization, next is to build all the voltage equations in the form of first-order differential equations. The construction of all the transformed branch voltage equations in the Simulink model is shown in Fig. 5.7. The Phase_A, Phase_B and Phase_C subsystems in Fig. 5.7 will contain all the transformed branch voltage equations belonging to Phase A, B and C windings, respectively. All the branch current variables together with their derivatives will have the corresponding **Goto** blocks, thus they can be used inside the Phase_A, Phase_B and Phase_C subsystems to build the transformed branch voltage equations.

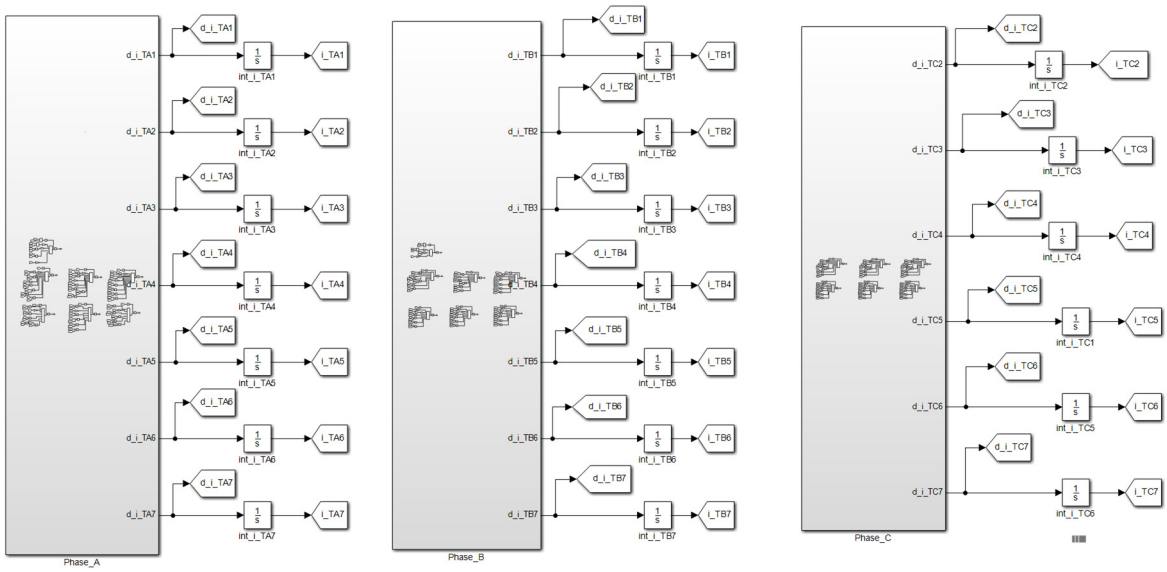

Fig. 5.7 Mathematical representation of all the transformed branch voltage equations.

Finally, all the necessary current variables will be monitored by the scope blocks. Some of the currents related to A phase are shown in Fig. 5.8.

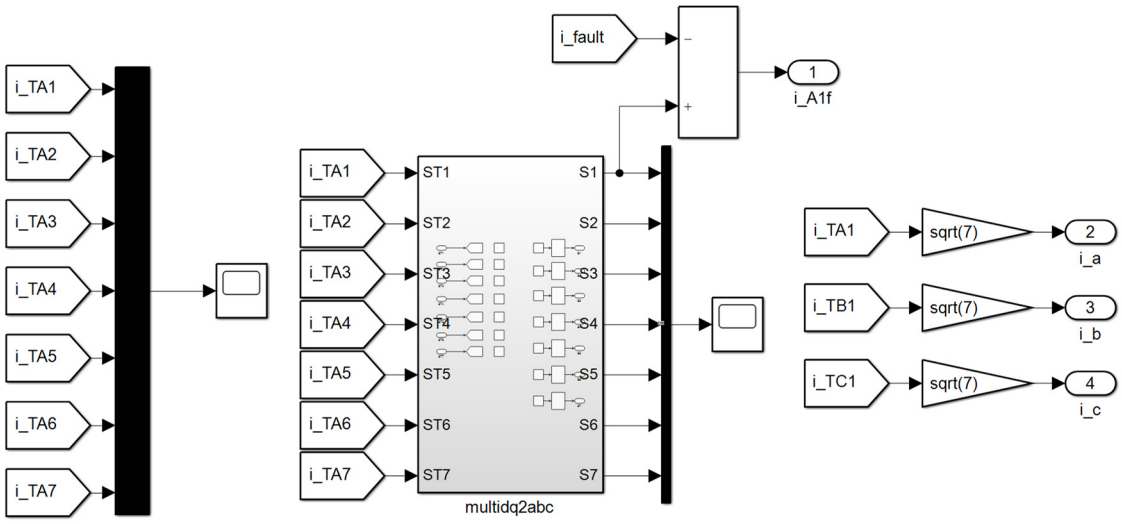

Fig. 5.8 Transformed branch currents $\mathbf{i}'_A$, branch currents $\mathbf{i}_A$ and 3-phase currents.

5.6 Simulation Results

A series of Matlab/Simulink simulations using analytical, FE linear and nonlinear inductances have been carried out for the 3kW, 500kW, 3MW SPM faulty machines with distributed overlapping windings. As the main purpose of this chapter is to validate the fault model and model simplification method, for simplicity, the rotor speeds are kept constant and balanced 3-phase sinewave voltages are fed to the fault model to shorten the simulation time. The inter-turn short-circuit faults are introduced when the machines operate under the rated condition, i.e., rated speed and torque with i_d = 0A control. It is also worth mentioning that a system of 23 first-order differential equations is required to simulate the 500kW faulty machine, and for the 3MW machine, a system of 62 first-order differential equations needs to be built. Such large-scale systems of first-order differential equations are very complex and much more computationally demanding than that for a healthy machine (only 4 to 6 first-order differential equations are required).

5.6.1 Fault Simulations with Linear Inductances

In this section, simulation results of the one-coil short-circuit and single-turn short-circuit faults for the 500kW and 3MW machine are shown. It is worth noting that the results for half-a-coil are quite similar to those for one coil short-circuit fault, therefore they are not shown here to avoid duplication.

5.6.1.1 One-coil short-circuit fault (500kW)

In Fig. 5.9, the currents of the faulty coil before and after one-coil short circuit fault are shown. A small discrepancy between the results from the two models by using FE linear and analytical inductances can be observed. In addition, it can be seen that the fault current under the one-coil short-circuit fault increases slightly, meaning that there would be sufficient time to detect this fault. It is worth noting that the steady-state current waveforms before (1.92 to 2s) and after the one coil short-circuit fault (3.84 to 4s) have been put together because the current transients last for a quite long time. By doing so, it is much easier to see the variation of current before and after the short-circuit fault. Furthermore, since the results from the two models by using analytical and FE linear inductances are very much similar, in Fig. 5.10, only the results using the FE linear inductances are shown.

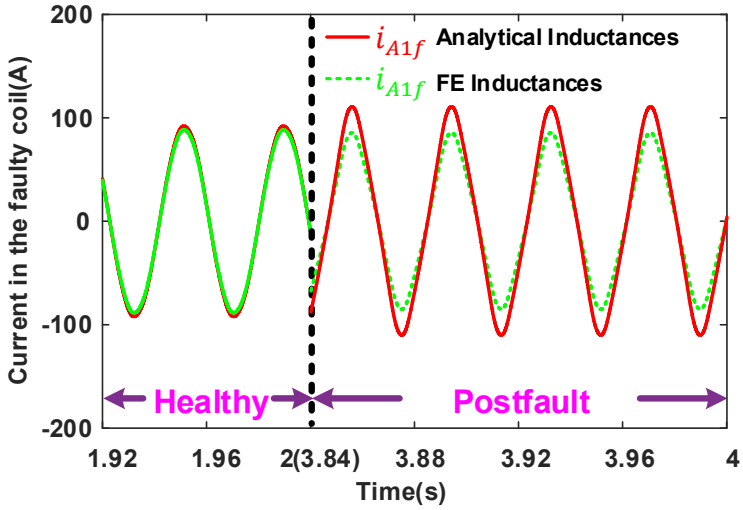

Fig. 5.9 Steady state currents in the faulty coil before and after one-coil short circuit fault in the 500kW machine with linear inductances.

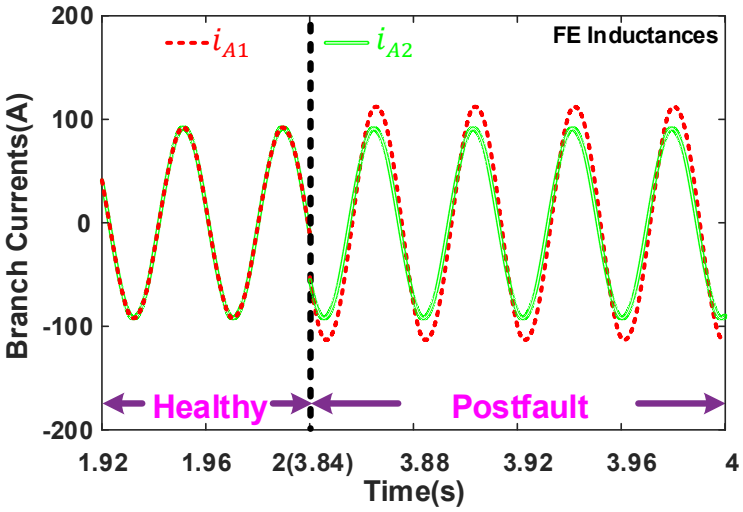

(a) Branch currents of phase A

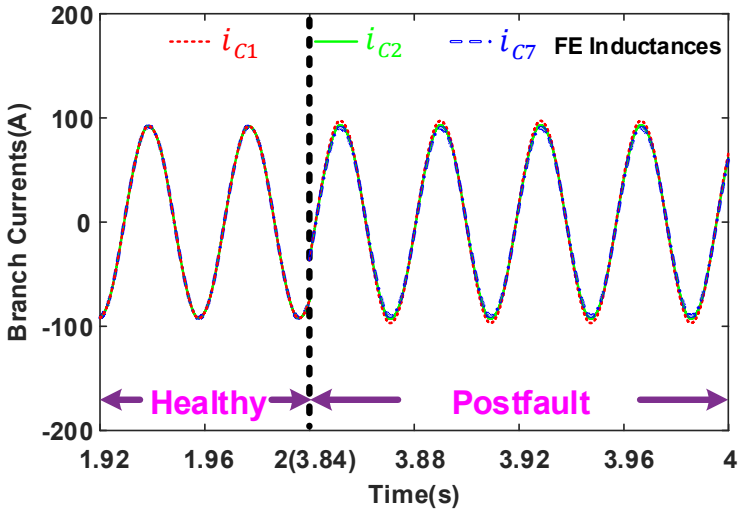

(b) Branch currents of phase C

Fig. 5.10 Steady-state branch currents before and after the one-coil short-circuit fault in the 500kW machine with linear inductances.

It should be mentioned that the branch currents i_{A3} to i_{A7} are very much similar to i_{A2}, and i_{C3} to i_{C6} are very much similar to i_{C2}. Although not shown, the changes in the branch currents of phase B are negligible. Since the changes of branch currents and short-circuit current caused by the one coil short-circuit fault is quite small, the change of developed electromagnetic torque will be negligible, as shown in Fig. 5.11.

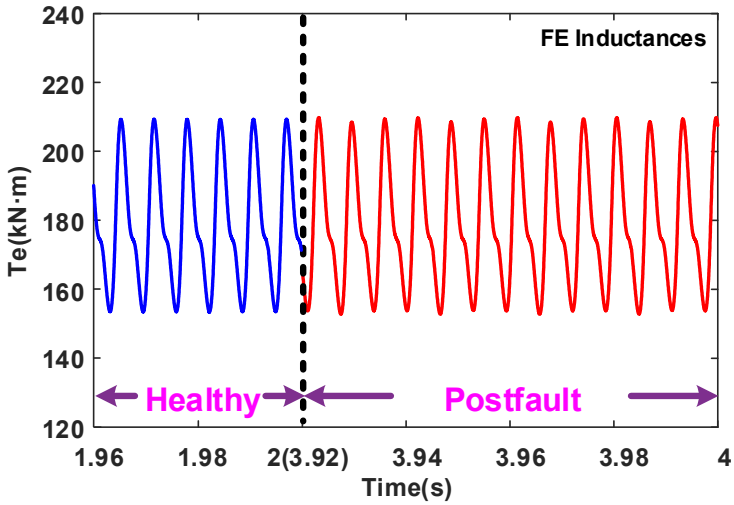

Fig. 5.11 On-load torque before and after the one-coil short-circuit fault in the 500kW machine with linear inductances.

5.6.1.2 Single-turn short-circuit fault (500kW)

In contrast to the one coil short-circuit fault, the currents will reach steady state very soon after the fault. In Fig. 5.12, the currents in the short-circuited turn from two Simulink models before and after the single-turn short-circuit fault are shown. It can be seen that the difference between the simulation results is still very small.

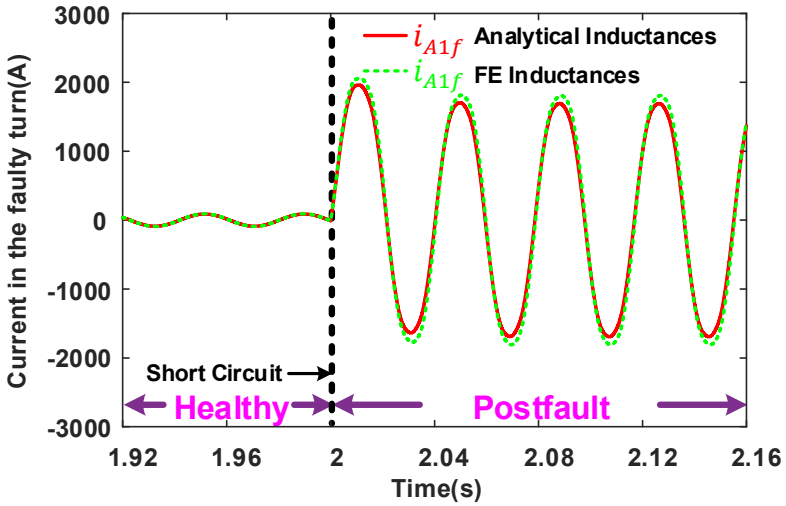

Fig. 5.12 Currents in the short-circuited turn before and after the single-turn short-circuit fault in the 500kW machine with linear inductances.

However, unlike the one-coil short-circuit fault, the current in the short-circuited turn is about 20 times the rated current, meaning that the local overheating is serious. In addition, this fault causes very little changes in branch currents as shown in Fig. 5.13. The little changes in

currents will have imperceptible influence on the developed electromagnetic torque, as shown in Fig. 5.14. Due to these two reasons, detecting this fault by utilizing the currents as a fault signature might be difficult.

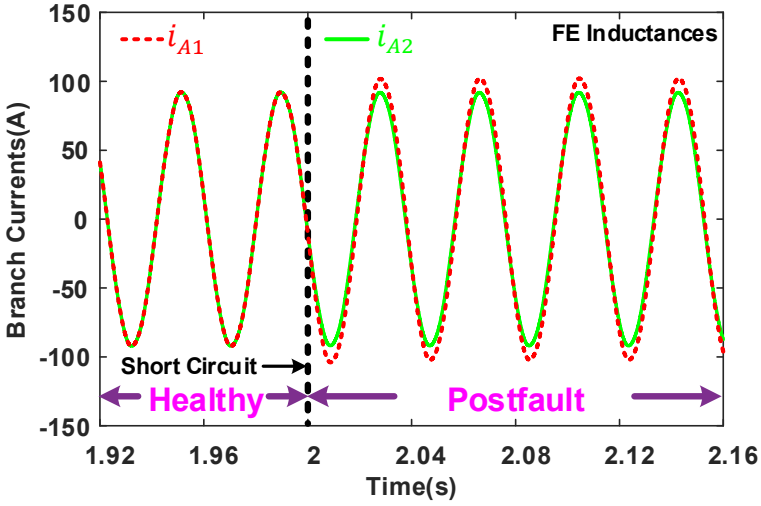

(a) Branch currents of phase A

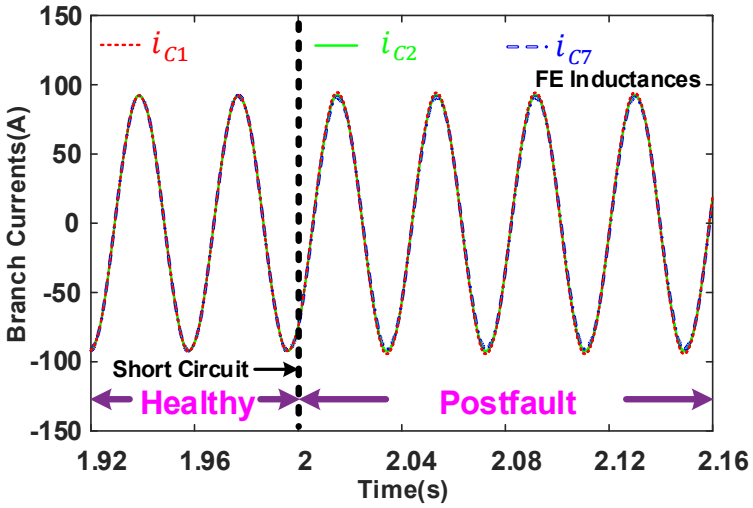

(b) Branch currents of phase C

Fig. 5.13 Branch currents before and after the single-turn short-circuit fault in the 500kW machine with linear inductances.

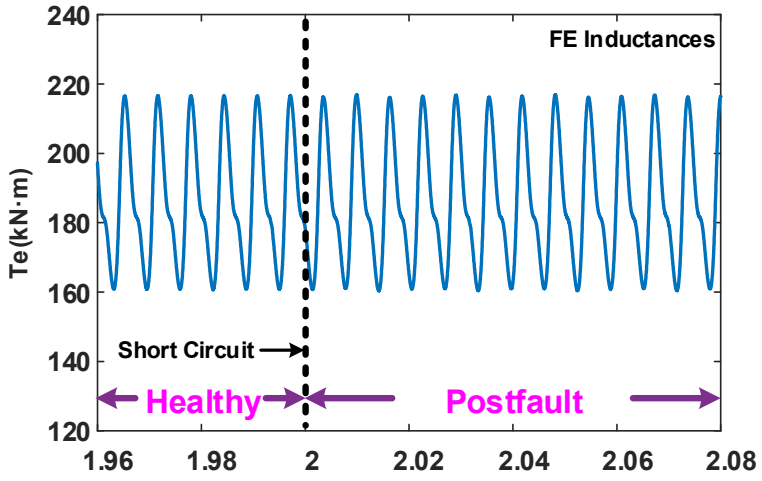

Fig. 5.14 On-load torque before and after the single-turn short-circuit fault in the 500kW machine with linear inductances.

5.6.1.3 One-coil short-circuit fault (3MW)

Compared with other fault scenarios, the one-coil short-circuit fault will generally lead to the greatest imbalance in branch currents. In Fig. 5.15, the currents of the faulty coil before and after the one-coil short circuit fault are shown.

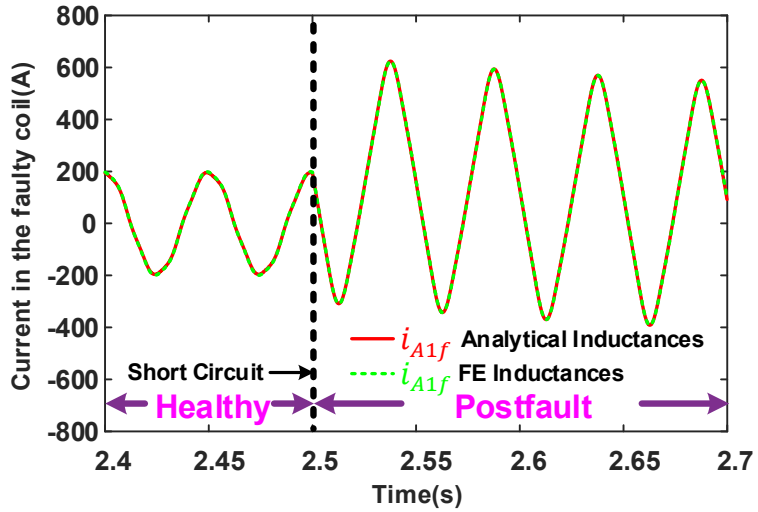

Fig. 5.15 Current in the faulty coil before and after the one-coil short circuit fault in the 3MW machine with linear inductances.

A good match between the results from the two models by using FE linear and analytical inductances can be observed. In addition, it can be observed that the fault current under the one-coil short circuit fault increases significantly, about 2 to 3 times the current in the faulty coil before fault.

Some steady-state branch currents in phases A and C before and after the one-coil short circuit fault are illustrated in Fig. 5.16. It is worth noting that the steady-state current waveforms before (2.4 to 2.5s) and after the one coil short-circuit fault (3.8 to 4s) have been put together because the current transients last for quite a long time. By doing so, it is much easier to see the variation of current before and after the short-circuit fault.

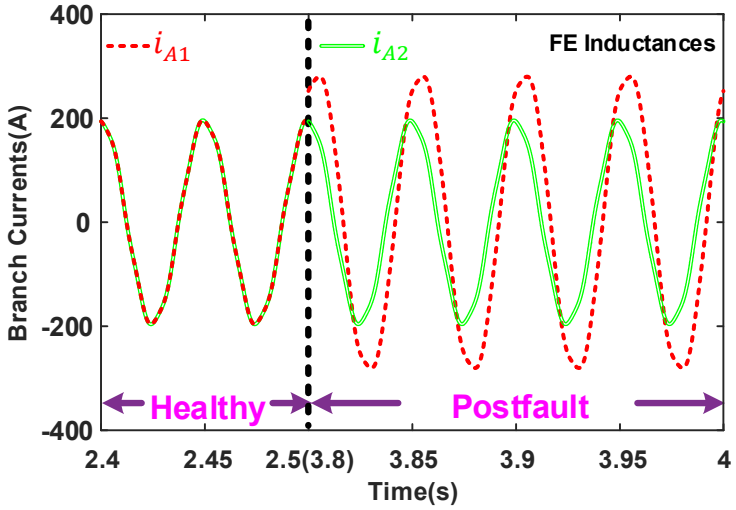

(a) Branch currents of phase A

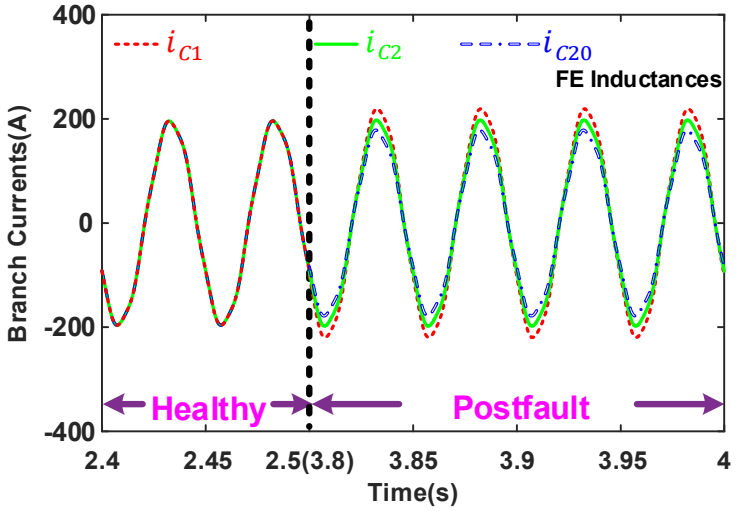

(b) Branch currents of phase C

Fig. 5.16 Steady-state branch currents before and after the the one-coil short-circuit fault in the 3MW machine with linear inductances.

In addition, since the results from the two models by using analytical and FE linear inductances are very much similar, in Fig. 5.16, only the results using the FE linear inductances are shown. It is also worth noting that the branch currents i_{A3} to i_{A20} are very much similar to i_{A2}, and i_{C3} to i_{C19} are very much similar to i_{C2}. Although not shown, the changes in the branch

currents of phase B are negligible. These changes in currents will affect the developed torque slightly, as shown in Fig. 5.17.

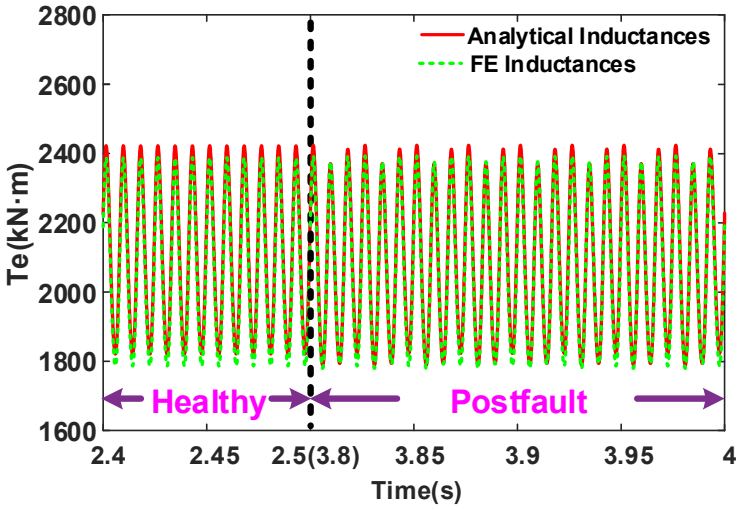

Fig. 5.17 On-load torque before and after the one-coil short-circuit fault in the 3MW machine with linear inductances.

Unsurprisingly, as the 3MW SPM machine has large number of parallel branches (n=20) and in each parallel branch, it has 4 coils connected in series, the three phase currents only change slightly before and after the one coil short-circuit fault. However, lower order harmonics can still be observed in d-axis and q-axis currents, as shown in Fig. 5.18, and they may be used as a fault signature[143], [144].

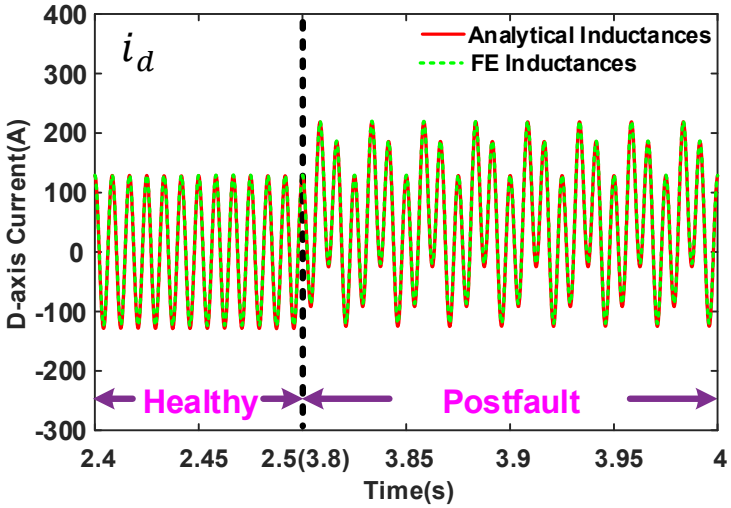

(a) d-axis current

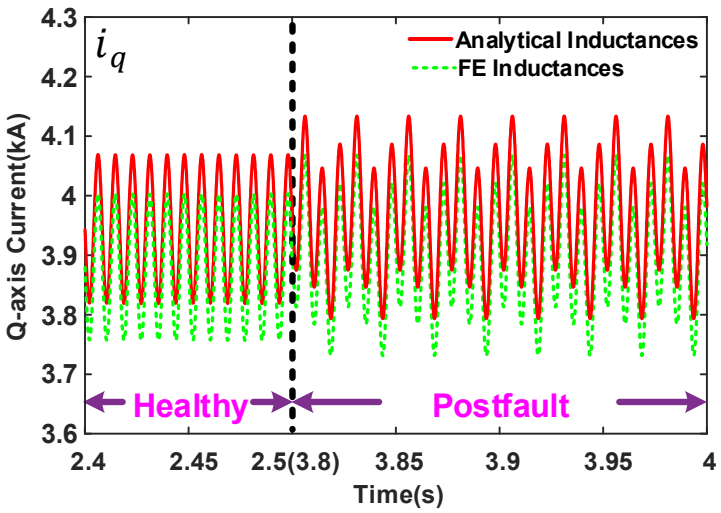

(b) q-axis current

Fig. 5.18 Steady-state dq-axis currents before and after the one-coil short-circuit fault in the 3MW machine with linear inductances.

5.6.1.4 Single-turn short-circuit fault (3MW)

The currents in the short-circuited turn of the 3MW SPM machine from two Simulink models before and after the single-turn short-circuit fault are shown in Fig. 5.19.

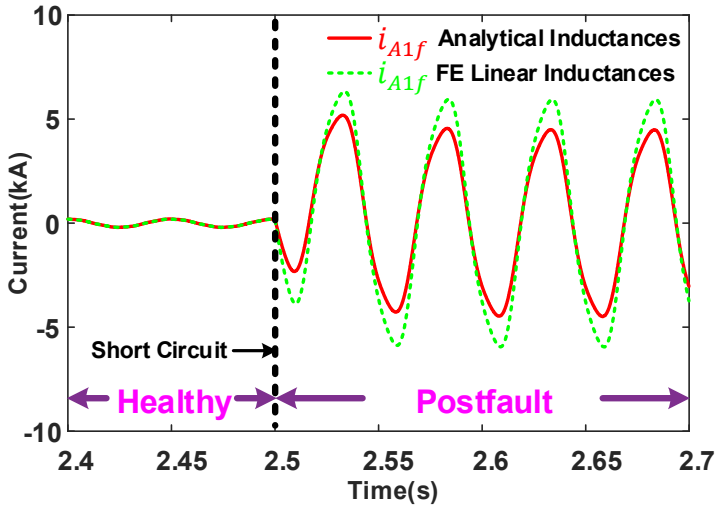

Fig. 5.19 Currents in the short-circuited turn before and after the single-turn short-circuit fault in the 3MW machine with linear inductances.

Now the difference between the simulation results is a little bigger, up to 25%. This difference is due to the inaccurate prediction of the inductances in the fault model by the proposed analytical method. In addition, unlike the same case of the 500kW SPM machine, this fault causes more significant changes in branch currents, as shown in Fig. 5.20.

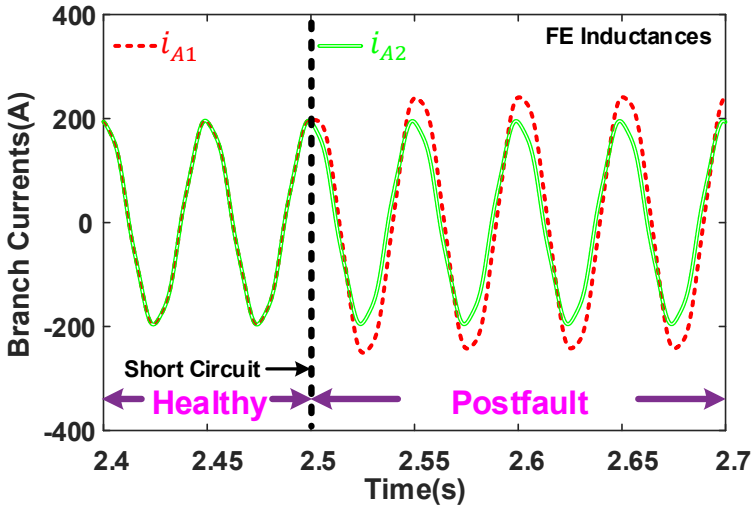

(a) Branch currents of phase A

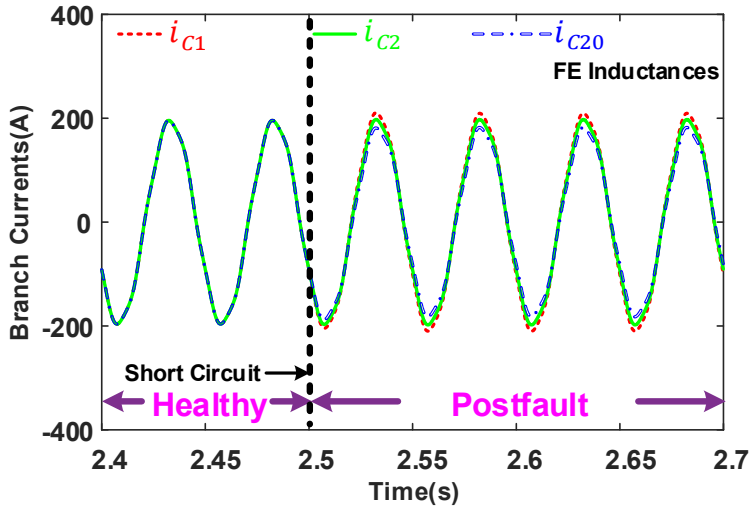

(b) Branch currents of phase C

Fig. 5.20 Branch currents before and after the single-turn short-circuit fault in the 3MW machine with linear inductances.

These changes in branch currents are also reflected in the *dq*-axis currents, which are shown in Fig. 5.21. Interestingly, under the single-turn short-circuit fault, the developed torque for this 3MW SPM machine will be affected slightly, which is in contrast to the 500kW SPM machine, as shown in Fig. 5.22. This is mainly because the 3MW machine have fewer number of turns per coil and fewer number of coils connected in series than those of the 500kW machine.

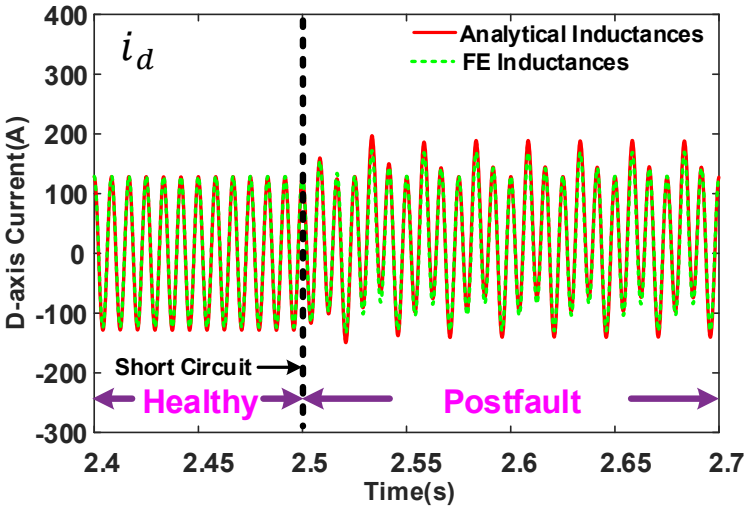

(a) *d*-axis current

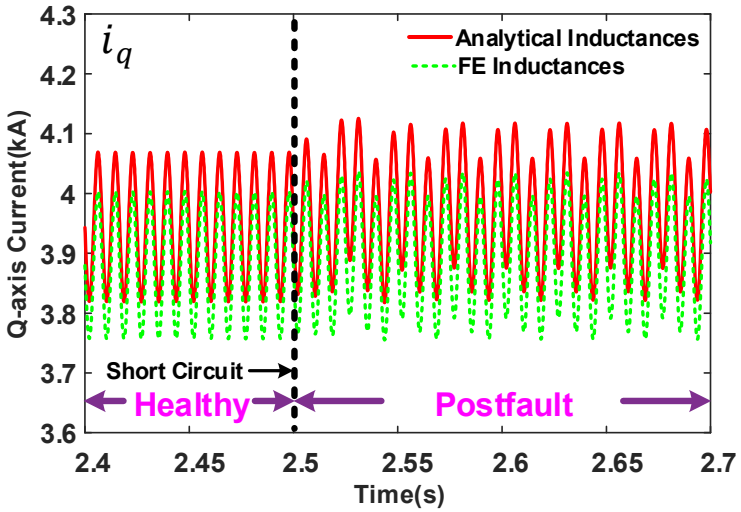

(b) *q*-axis current

Fig. 5.21 *dq*-axis currents before and after the single-turn short-circuit fault in the 3MW machine with linear inductances.

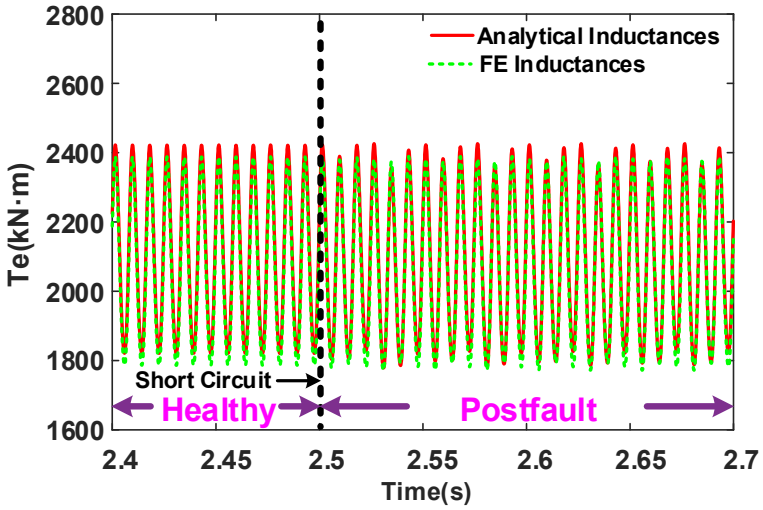

Fig. 5.22 On-load torque before and after the single-turn short-circuit fault in the 3MW machine with linear inductances.

5.6.2 Fault Simulations with Nonlinear Inductances

As described earlier, the multiphase Clarke transformation developed in section 4.4 can still be used to simplify the fault model with nonlinear inductances. Thus, some simulations can be carried out in Matlab/Simulink in a more realistic way if FE nonlinear inductances can be easily obtained.

5.6.2.1 One-coil short-circuit fault (500kW)

In Fig. 5.23, the currents of the faulty coil before and after one-coil short circuit fault are shown. It can be seen that before the one coil short-circuit fault the current amplitude predicted by using nonlinear inductances is slightly higher than that using analytical inductances. This is because the core saturation will reduce the inductance values to some extent. However, the difference between the currents with analytical inductances and nonlinear inductances becomes much smaller after the short-circuit fault. This is mainly because the one-coil short-circuit current is mainly determined by the voltage inputs and inductances such as $\sum_{k=1}^{n}(\mathbf{M}_{Af})_k$, $\sum_{k=1}^{n}(\mathbf{M}_{Bf})_k$, $\sum_{k=1}^{n}(\mathbf{M}_{Cf})_k$ and $L_{A1f,A1f}$ if one more assumption that after the fault, all branch currents of the remaining healthy phases are equal is made. However, $\sum_{k=1}^{n}(\mathbf{M}_{Af})_k$, $\sum_{k=1}^{n}(\mathbf{M}_{Bf})_k$, $\sum_{k=1}^{n}(\mathbf{M}_{Cf})_k$ and $L_{A1f,A1f}$ have different inaccuracies.

In addition, some branch currents predicted by using the nonlinear inductances are shown in Fig. 5.24. Like the corresponding linear case, the branch currents i_{A3} to i_{A7} are very much similar to i_{A2}, and the branch currents of phase C are very much similar, although they

increased slightly compared with those before the fault. Although not shown, the changes in the branch currents of phase B are also negligible. Contrary to the changes of branch currents, the changes of lower order harmonics of d-axis and q-axis currents are apparent, which are shown in Fig. 5.25.

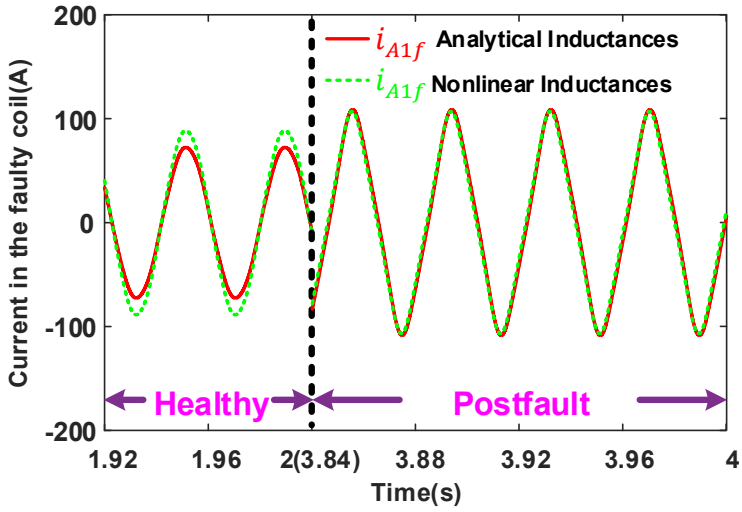

Fig. 5.23 Steady state currents in the faulty coil before and after the one-coil short circuit fault in the 500kW machine.

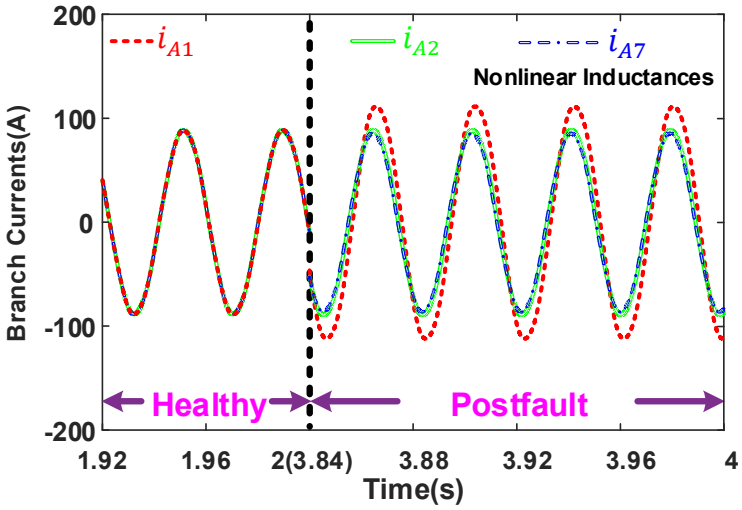

(a) Branch currents of phase A

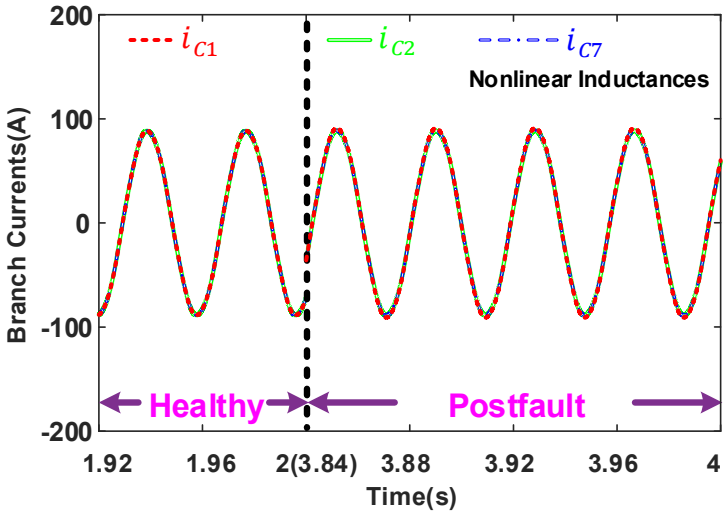

(b) Branch currents of phase C

Fig. 5.24 Steady-state branch currents before and after the one-coil short-circuit fault in the 500kW machine with nonlinear inductances.

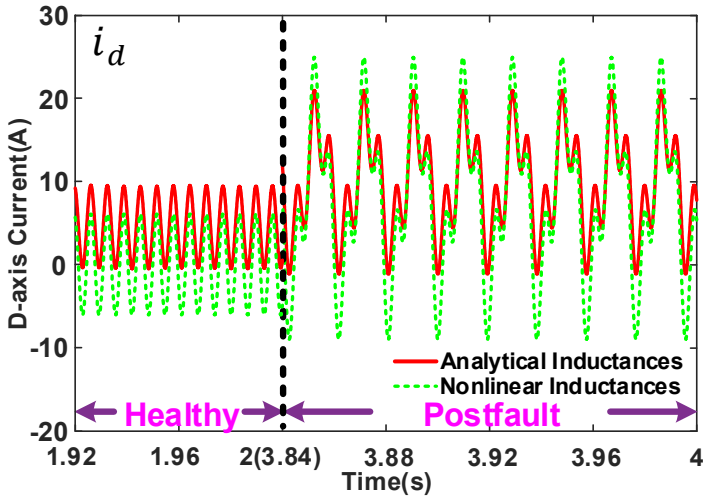

(a) *d*-axis current

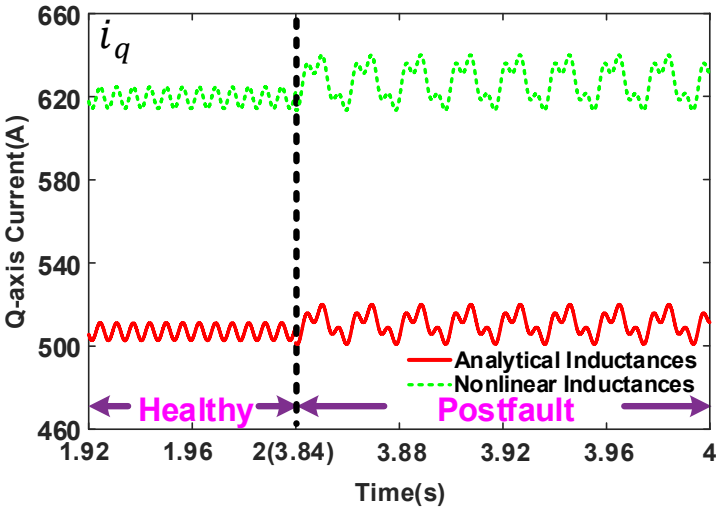

(b) q-axis current

Fig. 5.25 Steady-state dq-axis currents before and after the one-coil short-circuit fault in the 500kW machine.

On the other hand, the developed torque is shown in Fig. 5.26. It can be seen that the developed torque by using nonlinear inductances experiences a slight change before and after the fault. However, this slight change cannot be observed when the analytical inductances are used in the fault model.

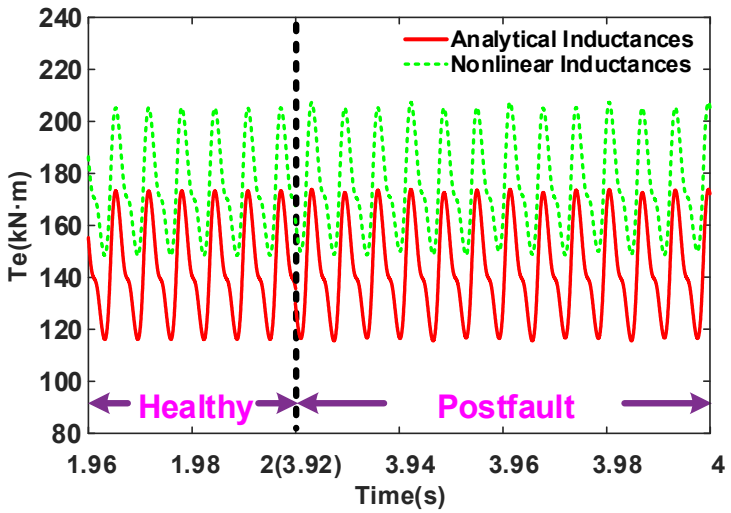

Fig. 5.26 On-load torque before and after the one-coil short-circuit fault in the 500kW machine.

5.6.2.2 Single-turn short-circuit fault (500kW)

As for the currents in the short-circuited turn of the 500kW SPM machine before and after the single-turn short-circuit fault, they are shown in Fig. 5.27. A significant difference in the

amplitudes of short-circuit current after the single-turn short-circuit fault has been observed, which is now about 22%. In addition, a very small phase shift between the currents can be observed. This is again due to the impact of core saturation on the inductance values.

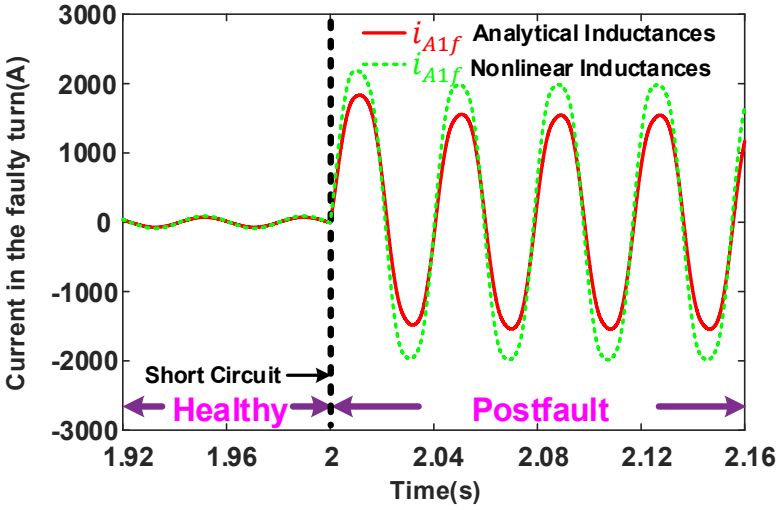

Fig. 5.27 Currents in the short-circuited turn before and after the single-turn short-circuit fault in the 500kW machine.

The single-turn short-circuit fault will also have some slight influence on the branch currents, as shown in Fig. 5.28. These slight changes in the branch currents are then amplified by the *dq*-axis currents, as shown in Fig. 5.29. It is worth noting that the proportions of the low-order harmonics in the *d*-axis current are very different from those after the one-coil short-circuit fault. However, considering that only 1 of 161(=7×23) turns in one branch is short-circuited, it will have negligible influence on the developed electromagnetic torque, as shown in Fig. 5.30.

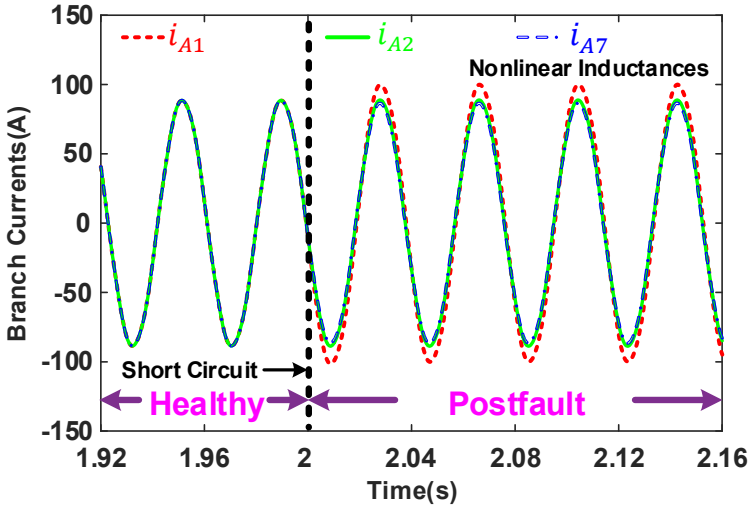

(a) Branch currents of phase A

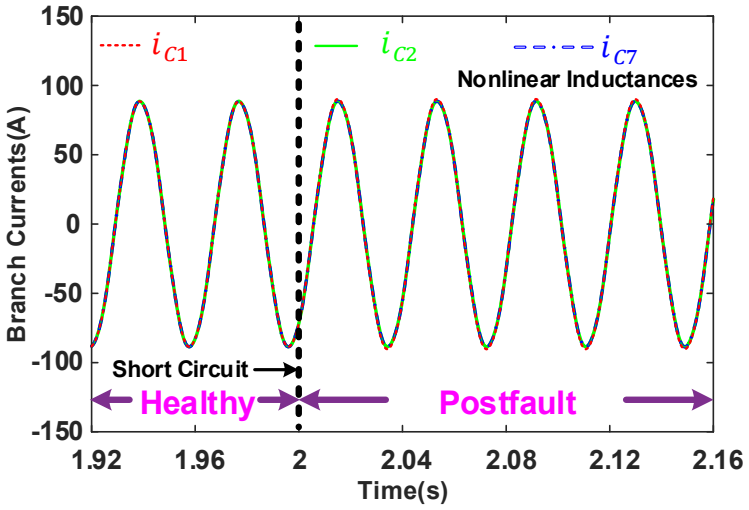

(b) Branch currents of phase C

Fig. 5.28 Branch currents before and after the single-turn short-circuit fault in the 500kW machine with nonlinear inductances.

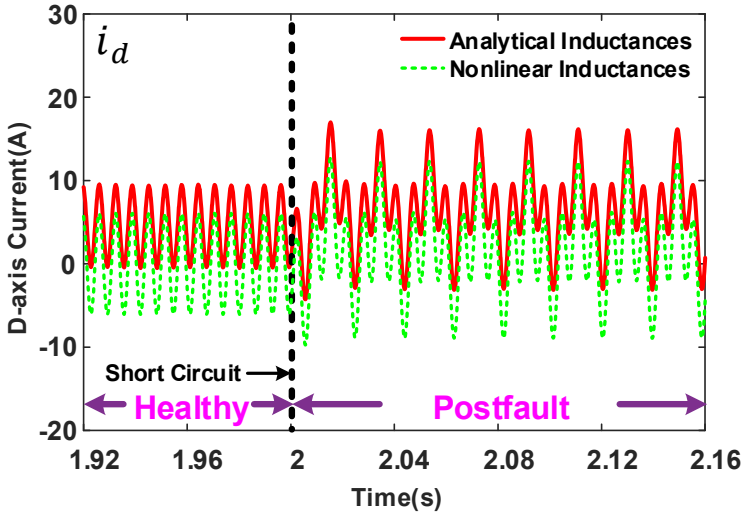

(a) d-axis current

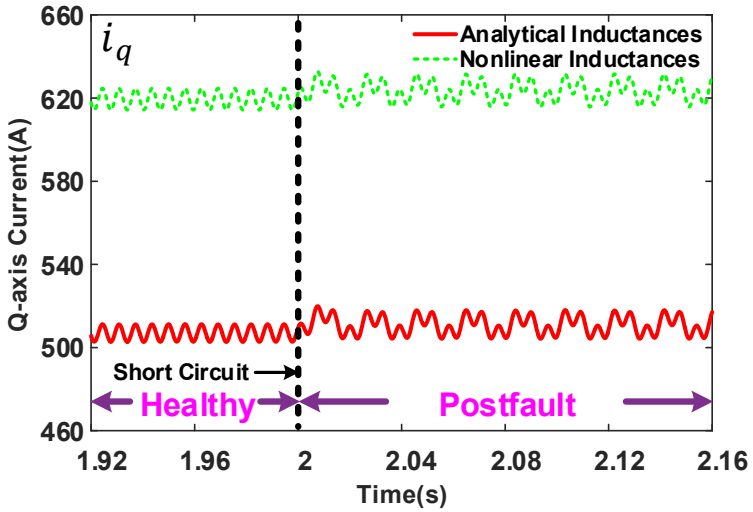

(b) q-axis current

Fig. 5.29 dq-axis currents before and after the single-turn short-circuit fault in the 500kW machine.

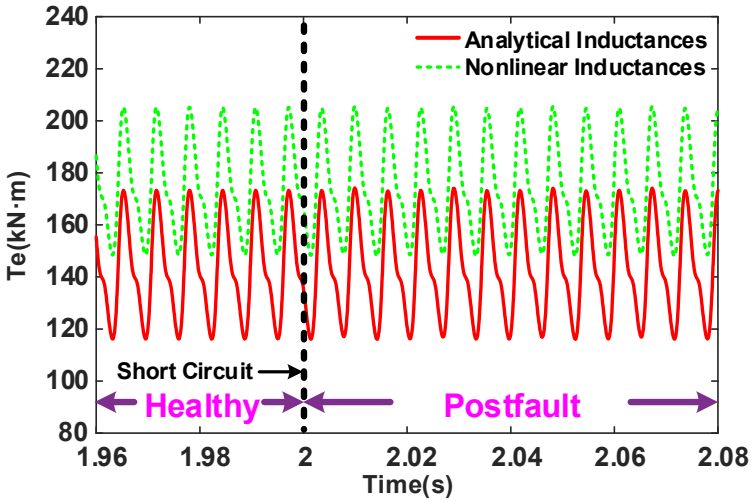

Fig. 5.30 On-load torque before and after the single-turn short-circuit fault in the 500kW machine.

5.6.2.3 One-coil short-circuit fault (3MW)

When the nonlinear FE inductances are used, the currents in the faulty coil of the 3MW SPM machine before and after the one-coil short circuit fault are shown in Fig. 5.31. It can be seen that before and after the one-coil short circuit fault, there is some slight difference between the results obtained with analytical and nonlinear inductances.

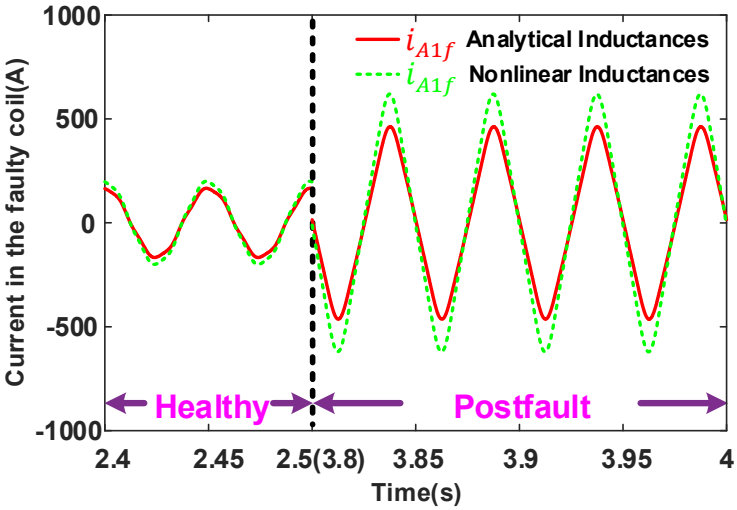

Fig. 5.31 Currents in the faulty coil before and after the one-coil short circuit fault in the 3MW machine.

However, regardless of which inductance values are used, it is found that after the fault, the fault current in the short-circuited coil is about 3 times the rated current. This means that, for the 3MW machine, the detection of the one-coil short-circuit fault is still necessary. In addition, the changes of some branch currents caused by the fault are shown in Fig. 5.32.

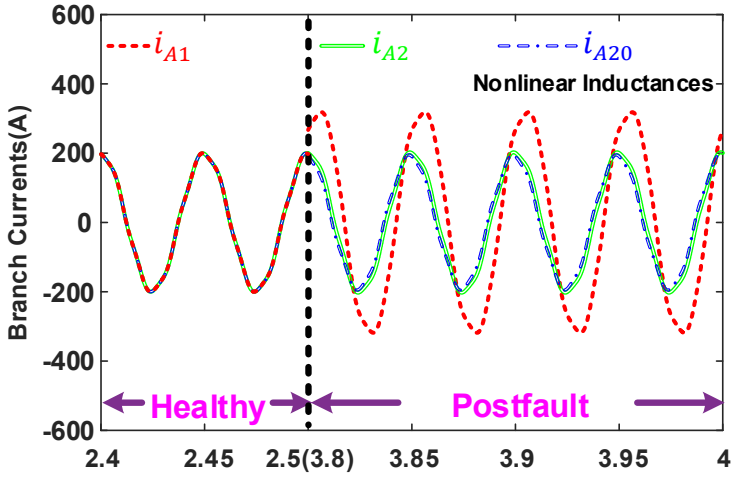

(a) Branch currents of phase A

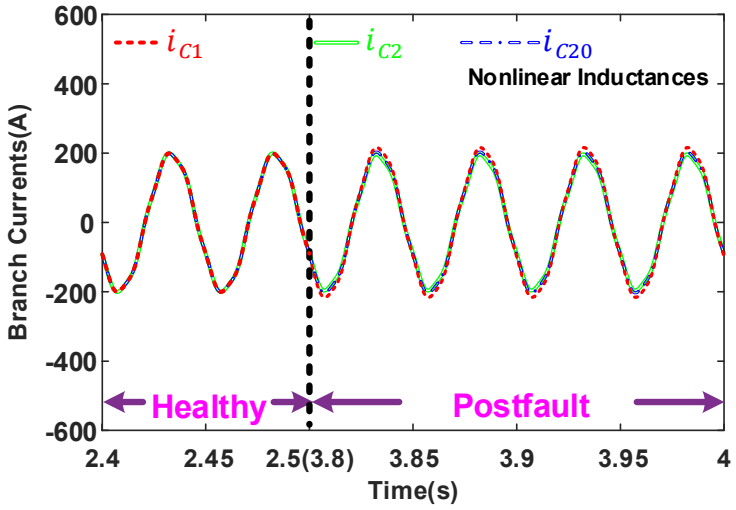

(b) Branch currents of phase C

Fig. 5.32 Steady-state branch currents before and after the the one-coil short-circuit fault in the 3MW machine with nonlinear inductances.

It should be mentioned that the branch currents i_{A3} to i_{A20} are very much similar to i_{A2}, and i_{C1} to i_{C20} are quite similar. Although not shown, all the branch currents of phase B are almost the same. Without question, there would be minor changes in 3-phase currents. However, the changes in *dq*-axis current seem to be more obvious, as shown in Fig. 5.33. Considering that there are 20 parallel branches and 4 coils connected in series in every branch, the influence of the one-coil short-circuit fault on the developed torque is still very minor, as shown in Fig. 5.34.

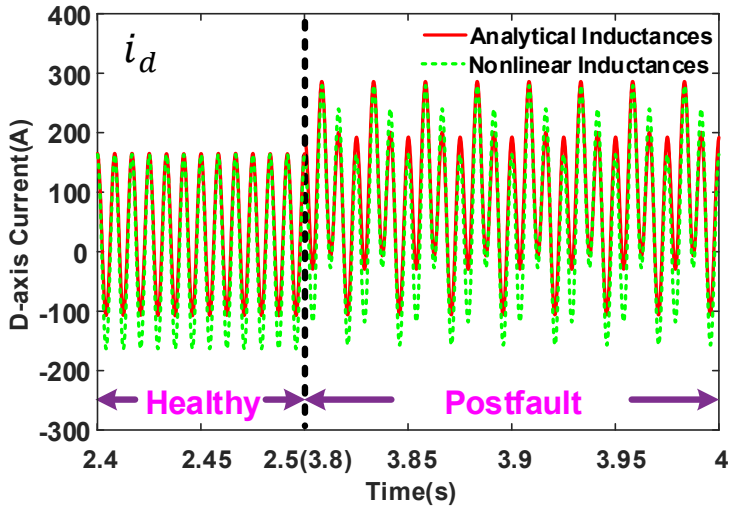

(a) *d*-axis current

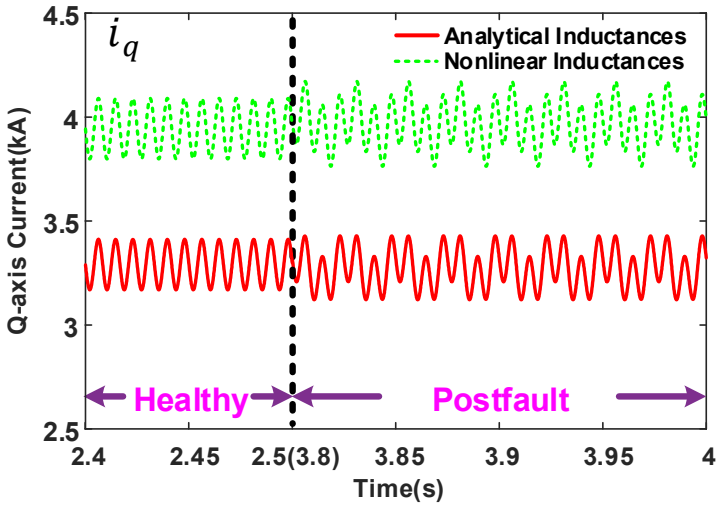

(b) q-axis current

Fig. 5.33 Steady-state dq-axis currents before and after the one-coil short-circuit fault in the 3MW machine.

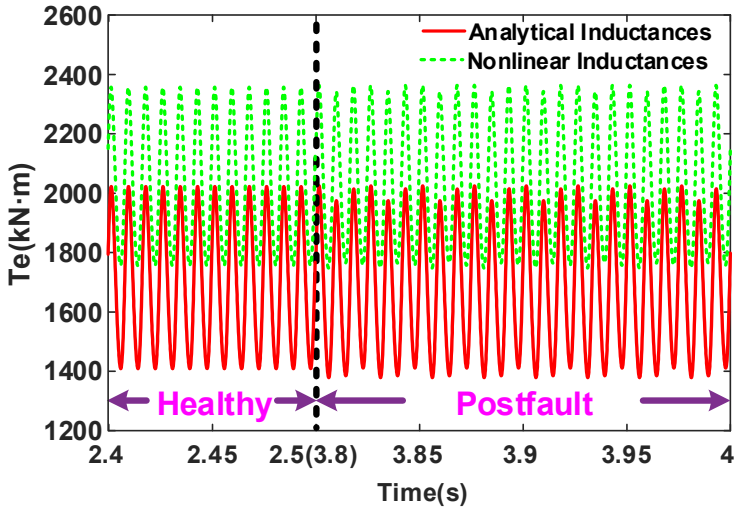

Fig. 5.34 On-load torque before and after the one-coil short-circuit fault in the 3MW machine.

In addition, it should be mentioned that in our case studies the voltage inputs to the two models with analytical or nonlinear inductances obtained by the analytical approach or FEM are assumed to be the same, thus the model with smaller nonlinear inductance values will inherently yield more torque. This phenomenon does not imply that the saturated machine will have better electromagnetic performance. In practice, the 3-phase currents are regulated by PI current controllers in the synchronously rotating dq-axis reference frame, indicating that the two models will develop the same torque under closed-loop control. Therefore, the results presented here could be unrepresentative of what will be found in a wind turbine.

5.6.2.4 Single-turn short-circuit fault (3MW)

When the nonlinear inductances are used, the amplitude of the single-turn short-circuit current is much higher than that predicted by using analytical inductances. In addition, the fault current is around 35 times the rated current. The corresponding current waveforms are shown in Fig. 5.35. This large short-circuit current will cause local overheating of the windings in a very short time and may also lead to demagnetization of the permanent magnets. It is therefore important to detect this fault.

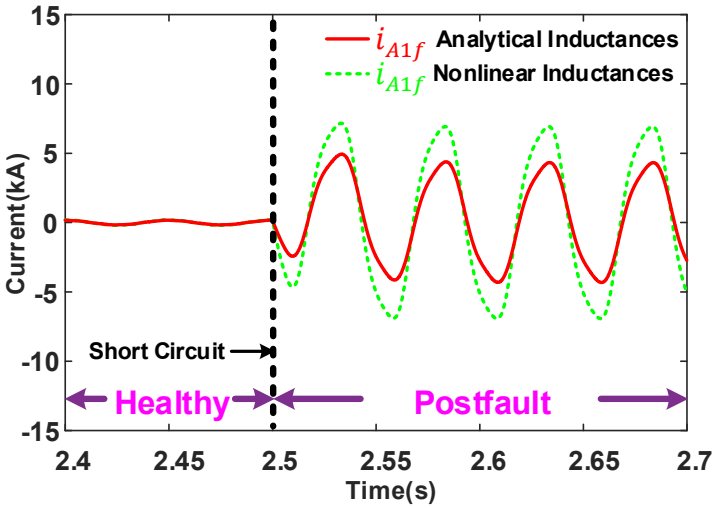

Fig. 5.35 Currents in the short-circuited turn before and after the single-turn short-circuit fault in the 3MW machine.

However, the changes of branch currents caused by this fault are very small, which are shown in Fig. 5.36. When the *dq*-axis currents are used, the changes seem to be a bit more obvious, as shown in Fig. 5.37. However, these changes are still limited, which does not provide meaningful indication when a single-turn short-circuit fault occurs, and therefore might not be used for fault detection. Again, the minor changes of branch currents will also lead to negligible impact on the developed torque waveform, as shown in Fig. 5.38.

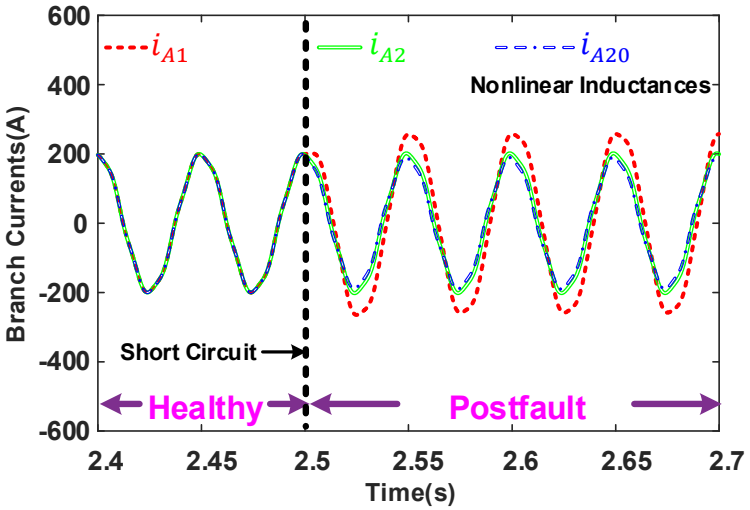

(a) Branch currents of phase A

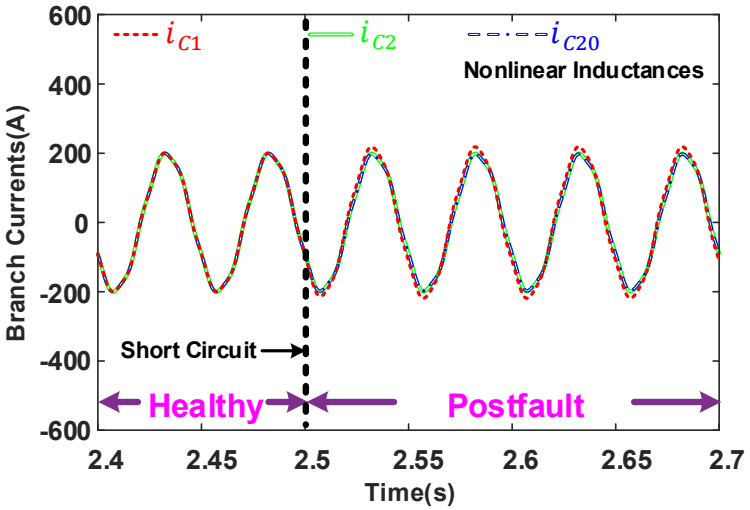

(b) Branch currents of phase C

Fig. 5.36 Branch currents before and after the single-turn short-circuit fault in the 3MW machine with nonlinear inductances.

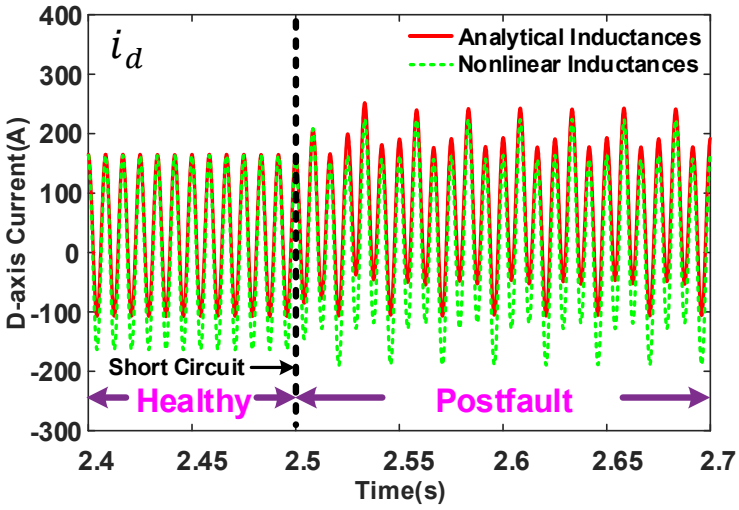

(a) *d*-axis current

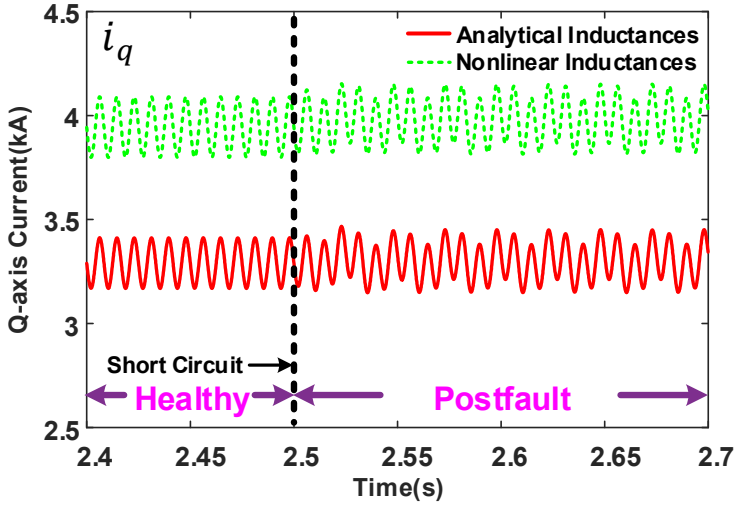

(b) *q*-axis current

Fig. 5.37 *dq*-axis currents before and after the single-turn short-circuit fault in the 3MW machine.

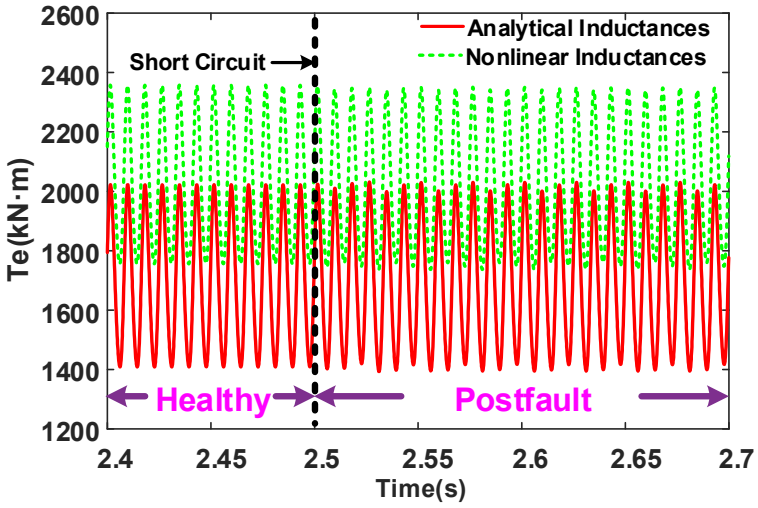

Fig. 5.38 On-load torque before and after the single-turn short-circuit fault in the 3MW machine.

5.6.2.5 Scaling Effect

Although the scaling effect study has been investigated in [141], the large-power SPM machines are assumed to have series-connected windings, which is often not the case in a real wind power generator. According to the previous analysis, the large-power SPM machines now will have series-parallel winding configurations so that a more practical study can be made. The normalized ITSC currents of PM machines with different power ratings (3kW, 0.5MW and 3MW) versus coil faulty turns ratio are shown in Fig. 5.39.

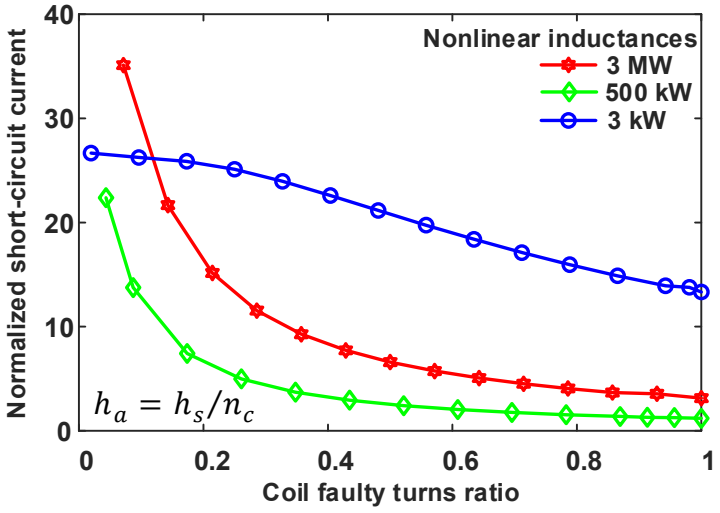

Fig. 5.39 Normalized short-circuit current *vs* coil faulty turns ratio using nonlinear inductances.

The reference current values of these PM machines are their corresponding rated coil currents. In addition, the ITSC faults for this scaling effect study are located at the bottom of

the slot, i.e., $h_a = h_s/n_c$. The same conclusion as those in [141] can be reached even when practical series-parallel coil connections are considered: large-power SPM machines are generally more fault-tolerant to the ITSC fault, but they are still vulnerable to ITSC faults when a relatively small number of turns are short-circuited. This is because different series-parallel coil connections have negligible influence on the amplitude of ITSC current at the same torque and speed, which has been studied in chapter 4.

5.6.2.6 Influence of Fault Location

Although in the scaling effect study the fault locations were chosen to be at the bottom of the slot, it is worth noting that the amplitude of the ITSC current actually depends on the locations of the fault. This is because all the elements of the three faulty inductance vectors $\mathbf{M}_{Af}$, $\mathbf{M}_{Bf}$, and $\mathbf{M}_{Cf}$ are fault location dependent. It has been reported that the worst-case scenario for the fractional-slot SPM machines under single turn short-circuit fault is a short circuit close to the slot opening [113], [117], [118]. However, to the best of our knowledge, there is no similar report on large-power SPM machines with series-parallel coil connections. Based on the proposed fault model and model simplification method, the influence of fault location on the amplitude of the ITSC current under the single turn short-circuit fault can be studied. The results are shown in Fig. 5.40. For large-power SPM machines (500kW and 3MW), the worst-case scenario of the single turn short-circuit fault is also a short circuit close to the slot opening. However, for low-power SPM machines (3kW), the influence of fault location on the amplitude of the ITSC current is negligible. It is worth mentioning that for the 3kW machine, the ITSC current amplitude can be approximated as the ratio of back EMF to the impedance of the short-circuited single turn. Thus the fault location has negligible influence on the ITSC current amplitude. However, for large-power machines such as the 500kW and 3MW ones, the ITSC current amplitude will be affected by the voltage inputs and inductances such as $\sum_{k=1}^{n}\left(\mathbf{M}_{Af}\right)_k$, $\sum_{k=1}^{n}\left(\mathbf{M}_{Bf}\right)_k$, $\sum_{k=1}^{n}\left(\mathbf{M}_{Cf}\right)_k$ and $L_{A1f,A1f}$. All these inductances are fault location dependent and the complex interaction between them leads to the variations of ITSC current with respect to fault locations shown in Fig. 5.40. This conclusion is reached by analysing the reduced-order fault model to approximately predict the amplitude of the ITSC current, which is based on one more assumption that after the fault, all branch currents of the remaining healthy phases are equal.

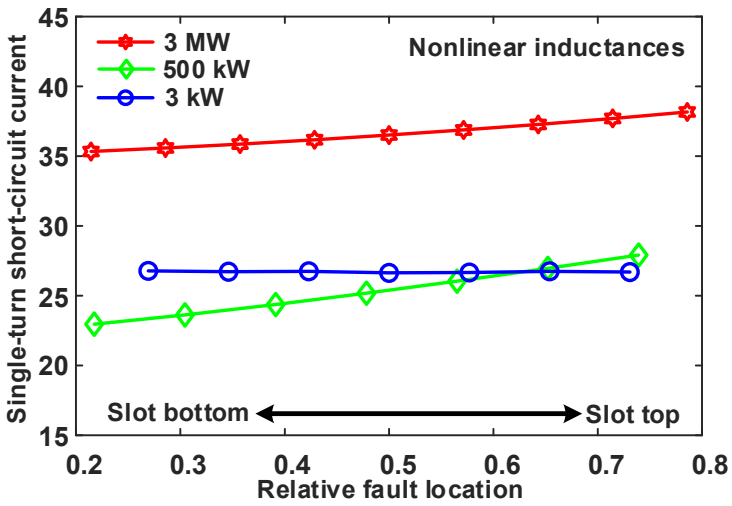

Fig. 5.40 Normalized single-turn short-circuit current at different fault locations.

5.7 Conclusion

This chapter extends the model simplification method using multiphase Clarke transformation to large-power SPM wind generators under inter-turn short-circuit (ITSC) fault. Calculation of inductances in the fault model using FEM has been presented. It is found that the multiphase Clarke transformation can be used to simplify the fault model with FE linear and nonlinear inductances because all branch inductance matrices are circulant matrices. As a result, simulations for large-power SPM wind generators under ITSC fault can be carried out directly in an easier and more time-saving way while keeping adequate accuracy using the simplified fault model with FE inductances. Meanwhile, the accuracy of fault model with analytical inductances can be easily validated by the fault model with FE linear inductances when some relative errors between analytical and FE linear inductances having large values in the fault model are large. It is worth mentioning that the proposed fault model and model simplification method are general and may be applied to other types of non-PM machines and also their multiphase counterparts. In addition, based on the simplified fault model, studies of scaling effect and influence of fault location on the amplitude of ITSC current of PM machines with different power ratings (3kW, 500kW, 3MW) have been carried out. Simulation results show that large-power SPM wind generators are vulnerable to ITSC faults when relatively small number of turns are short-circuited and the single-turn short-circuit fault at the slot top is the worst-case scenario.

Chapter 6 Analysis of SPM Machines with Different Winding Configurations Under Inter-Turn Short-Circuit Fault

Based on the developed general analytical fault model in chapter 4 and general model simplification method using the multiphase Clarke transformation in chapter 5, this chapter compares the performance of SPM machines with two different winding configurations under ITSC faults. The two different winding configurations are the non-modular and modular overlapping windings. It is found that the elements of some branch inductance matrices and faulty inductance vectors in the fault model for these two different winding configurations are not exactly the same although the equivalent phase self- and mutual-inductances are the same, meaning that the healthy machine performances for a SPM machine with the non-modular or modular overlapping windings are the same, but their fault performances may be different. Simulation results of the 96-slot 32-pole SPM machine under ITSC faults have confirmed this conclusion. In addition, fault performances of the same fault occurring in different phases have been studied when these two winding configurations are considered. It is found that for the non-modular windings, the same fault in different phases will lead to different changes in the branch currents. In addition, compared with the modular windings, the same fault in the non-modular windings will lead to greater imbalance in branch currents. Thus, compared with the non-modular windings, the modular windings generally are more fault-tolerant. However, these differences in the large-power SPM machines could be negligible because the ITSC faults cause very little imbalance in the branch currents of large-power SPM machines. Finally, fault simulations using the 500kW SPM machine with the modular windings have been carried out to support this conclusion. No further investigations have been carried out for the 3MW SPM machine as it has the same conclusion as that for the 500kW SPM machine.

Related Publications:

Z. T Mei, G. J. Li, Z. Q. Zhu, R. Clark, A. Thomas, and Z. Azar, "Analysis of SPM Machines with Different Winding Configurations Under Inter-Turn Short-Circuit Fault" *Energies*. (To be submitted)

6.1 Introduction

In chapters 2 to 5, the relatively simple and general analytical fault models of the SPM machines with series, parallel and series-parallel coil connections have been proposed. In addition, the general model simplification method using the multiphase Clarke transformation has been well developed. However, the analysed windings are the commonly used non-modular overlapping windings. In practice, the modular overlapping windings are adopted for wind turbine generator systems from the point of view of increasing the fault-tolerant capability of wind turbines [145]. It is therefore necessary to analyse and simulate the fault performance of SPM machines with the modular windings and compare it against their counterparts with the non-modular windings. It should be mentioned that the analytical fault model proposed in chapter 4 is general and can be extended to SPM machines with other winding configurations including the modular windings. However, whether the general model simplification method using the multiphase Clarke transformation can be extended to the SPM machines with other winding configurations will depend on whether there is a circulating current flowing in any two branches of one certain phase winding of the studied SPM machines when they are under no-load condition. For most of the machine design schemes, circulating current flowing in any two branches of one phase winding should be avoided to reduce unnecessary copper losses. This action will also lead to symmetrical windings. Therefore, it can be inferred that the general model simplification method using the multiphase Clarke transformation can be extended to most of the symmetrical SPM machines.

6.2 Inductance Calculation

A comparison of the modular and non-modular overlapping windings of the studied SPM machines has been shown in Fig. 6.1. In Fig. 6.1, the windings of the analysed SPM machines are still single-layer, full-pitch and distributed [slot/pole/phase (SPP) is equal to 1], which is often the case for large SPM generators used in wind power. In addition, it is easier to calculate inductances used in the fault model by the proposed analytical method in chapters 2 to 5 based on this winding layout. In Fig. 6.1 (a), two modular segments are put together to form one large segment. However, this is different for the non-modular overlapping windings shown in Fig. 6.1 (b). It can be seen that, in Fig. 6.1 (b), one coil side of a certain coil in the adjacent segment is contained in this segment, meaning that the two coil sides have to be welded together later. Although this is very common for some large-power hydro or turbo generators [82], [146], from the point of view of modularity, the non-modular windings is not as good as the modular

windings. On the other hand, the numberings of the coils in Fig. 6.1 are in such a way that the numberings of the coils in one phase winding will increase in the counter-clockwise direction.

Like the assumptions made in chapter 4, here it is also assumed that one parallel branch has r coils in series, and n parallel branches of one phase will therefore contain $p = r \times n$ coils in total, where p is the number of pole pairs.

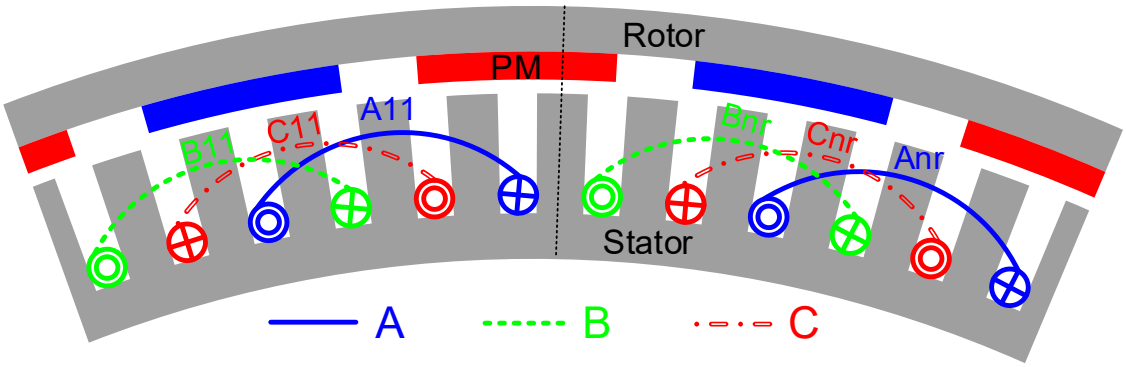

(a) Modular windings

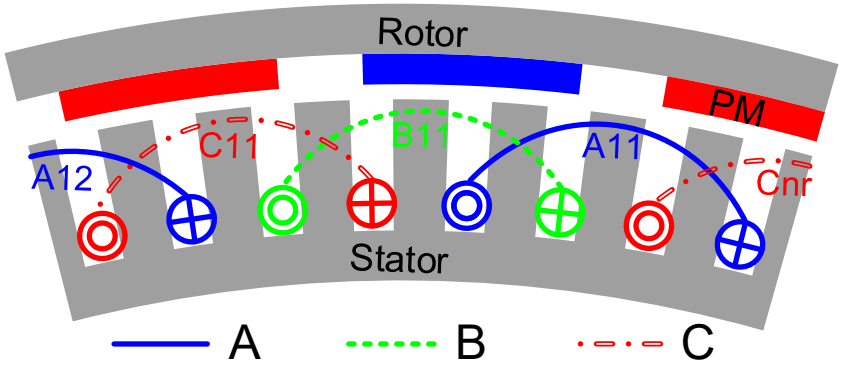

(b) Non-modular windings

Fig. 6.1 The studied SPM machines with integer-slot modular and non-modular windings.

6.2.1 Calculation of Inductances

It has been mentioned in the chapter 2 that there are three components in the phase self- and mutual- inductances. Similarly, in this chapter, only the air-gap and slot-leakage inductance components for the modular windings will be calculated.

It can be also seen from Fig. 6.1 that the current distribution of all the conductors making up the coils for both winding configurations are exactly the same, the only difference is the end connection of coils belonging to the phase C winding. This slight change of end connections leads to the difference of the winding functions of the parallel branches of phase C winding. As an example, winding functions of the first parallel branch of phase C winding for the modular and non-modular windings are shown in Fig. 6.2.

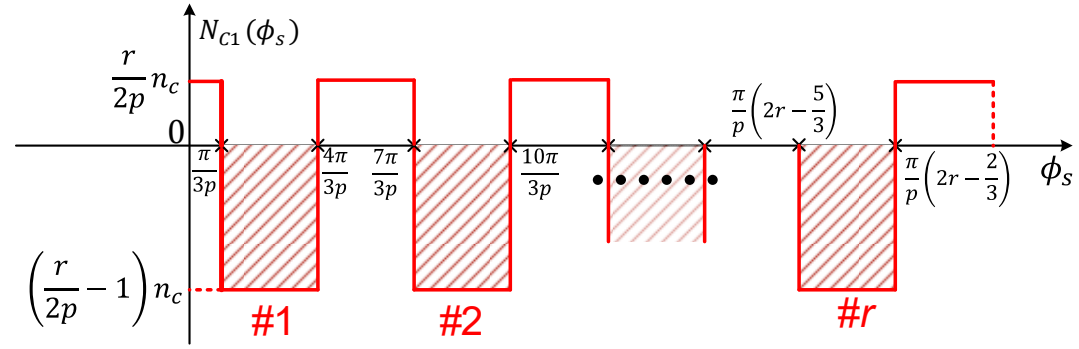

(a) Winding function for modular windings

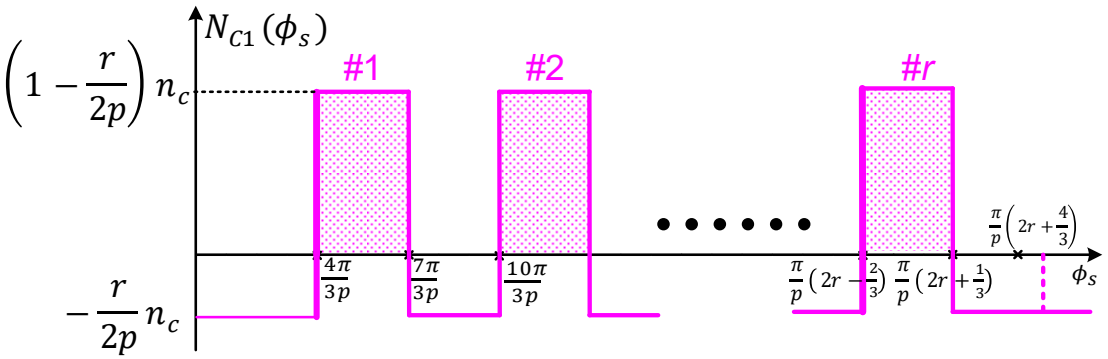

(b) Winding function for non-modular windings

Fig. 6.2 Winding functions of the first parallel branch of phase C winding for the modular and non-modular windings.

Due to the difference of the winding functions of the parallel branches of phase C winding for both winding configurations, the elements in the branch inductance matrices $\mathbf{M}_{AC}$ and $\mathbf{M}_{BC}$ are different. As the inductance calculations for the non-modular windings have been carried out in chapter 4, here only the inductance calculations for the modular windings will be presented. In addition, it is found that all the branch inductance matrices of the modular windings are still circulant matrices. After the winding functions of all parallel branches are derived, all the elements of the branch inductance matrices can be calculated by using WFA together with the slot permeance method as detailed in [127]

$$\begin{cases} L_{A1A1} = L_{B1B1} = L_{C1C1} = L_1 \\ M_{A1Aj} = M_{B1Bj} = M_{C1Cj} = M_1 \ (j = 2,3,\cdots,n) \\ M_{A1B1} = M_2 \\ M_{A1Bj} = M_1 \ (j = 2,3,\cdots,n) \\ M_{A1Cj} = M_{B1Cj} = -M_1 \ (j = 2,3,\cdots,n) \\ M_{A1C1} = M_{B1C1} = M_3 \end{cases} \tag{6.1}$$

with

$$\begin{cases} L_1 = \dfrac{\mu_0 r_e l_e}{g_e}\dfrac{r(2p-r)}{2p^2}\pi(n_c)^2 + 2r(n_c)^2\mu_0 l_e\left[\dfrac{h_s}{3S_\omega}\right] \\ M_1 = \dfrac{\mu_0 r_e l_e}{g_e}\left(-\dfrac{r^2}{2p^2}\right)\pi(n_c)^2 \text{ and } M_2 = -\dfrac{(2p-3r)}{3r}M_1 \\ M_3 = \dfrac{\mu_0 r_e l_e}{g_e}\left(\dfrac{r(3r-4p)}{6p^2}\right)\pi(n_c)^2 \end{cases} \tag{6.2}$$

where the meanings of μ_0, r_e , l_e, g_e, h_s, S_ω and p are the same as those in [140].

As for the elements in the fault inductance vectors, they are also given as

$$\begin{cases} L_{A1f,A1f} + M_{A1h,A1f} = L_{11} \quad M_{B1,A1f} = M_{22} \\ M_{Aj,A1f} = M_{Bj,A1f} = M_{11}\ (j = 2,3,\cdots,n) \\ M_{C1,A1f} = M_{33} \\ M_{Cj,A1f} = -M_{11}\ (j = 2,3,\cdots,n) \end{cases} \tag{6.3}$$

Regarding $L_{A1f,A1f}$ and $M_{A1h,A1f}$, the same equations as those shown in chapters 2 and 4 can be used to calculate them.

As for M_{11}, M_{22} and M_{33} in (4.6), they are expressed as

$$\begin{cases} M_{11} = -\dfrac{\mu_0 r_e l_e}{g_e}\dfrac{r}{2p^2}\mu_1\pi(n_c)^2 \\ M_{22} = \dfrac{\mu_0 r_e l_e}{g_e}\dfrac{(2p-3r)}{6p^2}\mu_1\pi(n_c)^2 \\ M_{33} = \dfrac{\mu_0 r_e l_e}{g_e}\dfrac{(3r-4p)}{6p^2}\mu_1\pi(n_c)^2 \end{cases} \tag{6.4}$$

Equations from (6.1) to (6.4) clearly show that the inductances in the fault model of the modular windings are not exactly the same as those of the non-modular windings. As a result, for the SPM machines with modular windings, it can be expected that their fault performance will be different from those with non-modular windings.

6.2.2 Results of Inductances

The key parameters of the studied 3kW SPM machine have been shown in Table 4.1 of chapter 4. Taking the 2S×8P coil connection as an example, the calculated results of the inductance elements of $\mathbf{M}_{AC}$ and $\mathbf{M}_{BC}$ are shown in Fig. 6.3. During the inductance calculation, the core saturation has also been neglected. It can be seen from Fig. 6.3 that the inductance elements of $\mathbf{M}_{AC}$ and $\mathbf{M}_{BC}$ predicted by the proposed analytical approach in chapters 2 to 4 generally match well with those calculated by FEM. In Fig. 6.3 (a), for the non-modular windings, the values of M_{C1A1} and M_{C8A1} are both positive, and other inductance elements from M_{C2A1} to M_{C7A1} are all negative. However, for the modular windings, only M_{C1A1} is negative. In Fig. 6.3 (b), the signs of M_{C1B1} to M_{C1B8} for the non-modular windings are

opposite to those for the modular windings. As for the details of inductance calculation by the FEM, they have been described in chapter 4, thus they will not be duplicated here.

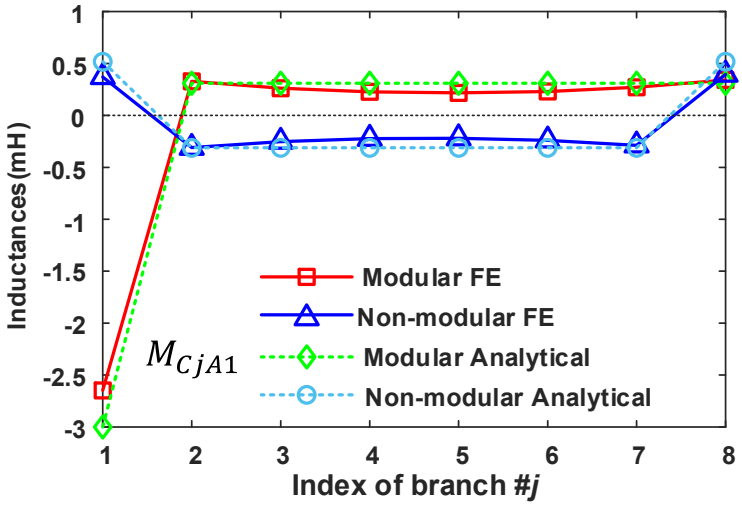

(a) Inductance elements of $\mathbf{M}_{AC}$

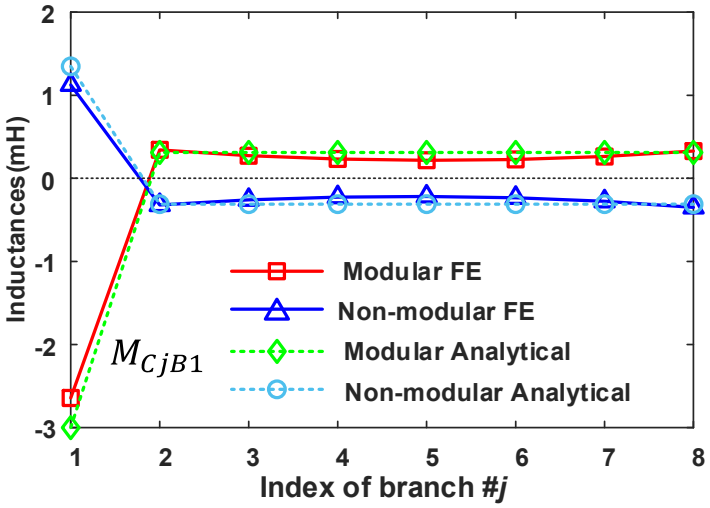

(b) Inductance elements of $\mathbf{M}_{BC}$

Fig. 6.3 Inductance elements of $\mathbf{M}_{AC}$ and $\mathbf{M}_{BC}$ by the analytical approach and FEM.

It is worth mentioning that although the inductance elements of $\mathbf{M}_{AC}$ and $\mathbf{M}_{BC}$ for the non-modular and modular windings are different, the sum of the elements in the first row of $\mathbf{M}_{AC}$ for both windings are the same. This is also the case for $\mathbf{M}_{BC}$ for the non-modular and modular windings. Therefore, for these two winding configurations, they will have the same equivalent phase self- and mutual-inductances. This means that the healthy machine performance for these two windings will be the same according to the derivations shown in chapters 4 and 5.

6.3 Simulation Results

As can be seen in the previous chapters, the one-coil short-circuit fault will lead to the greatest imbalance in the branch currents compared with other ITSC faults. Therefore, the fault performance of the 3kW SPM machine with the modular and non-modular windings under the one-coil short-circuit fault has been simulated. The series-parallel coil connections considered are 2S×8P, 4S×4P, and 8S×2P, respectively. Although there is some difference in the simulated results for both windings with all series-parallel coil connections, the difference for these two windings with 2S×8P coil connection is the most significant. In addition, to shorten the simulation time, the studied 3kW SPM machine has been supplied with 3-phase balanced sinusoidal voltages and the machine's rotor mechanical speed has been kept constant during the whole operation period. In addition, considering that the three faulty inductance vectors $\mathbf{M}_{Af}$, $\mathbf{M}_{Bf}$, and $\mathbf{M}_{Cf}$ are different when the ITSC faults happen in different phases, the influence of the one-coil short-circuit fault in different phases on the fault performance of the 3kW SPM machine has also been considered. Finally, simulations for the 500kW SPM machine with the modular windings under the one-coil short-circuit fault have also been carried out to see the scaling effect on the difference of the fault performance from those with the non-modular windings.

6.3.1 Results for the 3kW SPM Machine

It is worth mentioning that the simulated results from direct 2D FE linear simulations are almost the same as those from the proposed fault models with the corresponding FE linear inductances. However, the direct 2D FE linear simulations are much more time-consuming than the corresponding fault models with FE linear inductances. In addition, the core saturation will have almost the same influence on the fault performance for both windings. Therefore, for simplicity, only the results from the proposed fault models with FE linear inductances have been provided in this section.

6.3.1.1 One-Coil Short-Circuit Fault in Phase A (2S×8P)

When the one-coil short-circuit fault occurs in phase A, the short-circuit currents of the faulty coil for the non-modular and modular windings are shown in Fig. 6.4. It can be seen that there is negligible difference in the currents of the faulty coil for both windings. This is mainly because the short-circuit current in the faulty coil is approximated by the ratio of the back-EMF of the short-circuited coil to the impedance of the short-circuited coil, meaning that the winding configurations will have negligible influence on the short-circuit current.

The branch currents of 3-phase windings of the 3kW SPM machine with non-modular and modular windings are shown in Fig. 6.5, Fig. 6.6, and Fig. 6.7, respectively. When the one-coil short-circuit fault occurs in the first branch of phase A, the changes of branch currents of phase A in the non-modular and modular windings are almost the same. In Fig. 6.5, i_{A2} to i_{A8} are very similar.

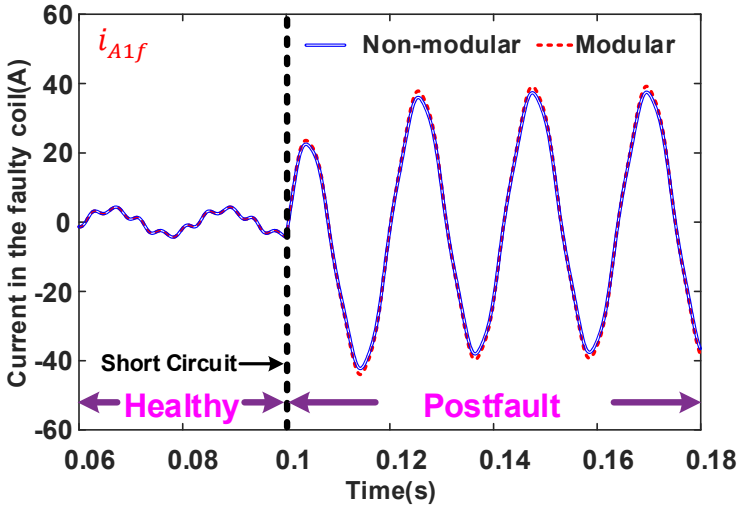

Fig. 6.4 Currents in the faulty coil of the 3kW SPM machine with non-modular and modular windings before and after the one-coil short circuit fault.

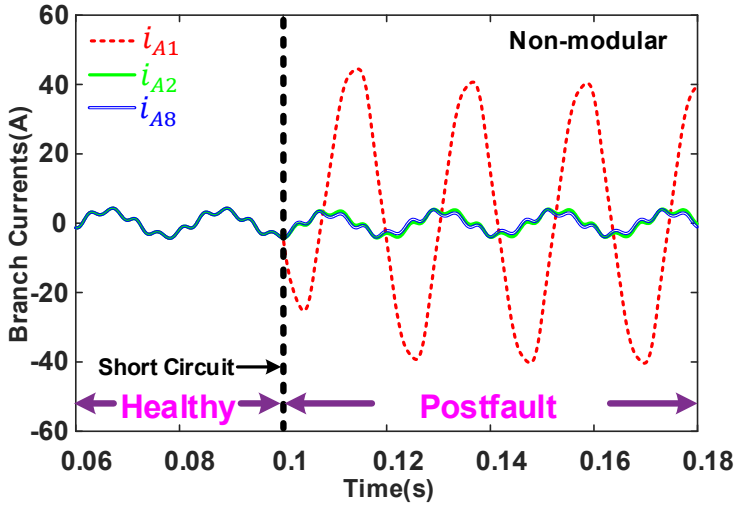

(a) Branch currents of phase A for the non-modular windings

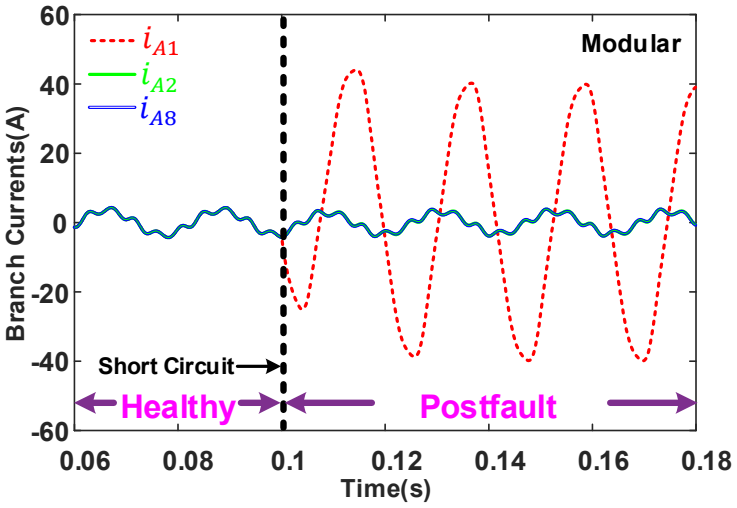

(b) Branch currents of phase A for the modular windings

Fig. 6.5 Branch currents of phase A of the 3kW SPM machine with non-modular and modular windings before and after the the one-coil short-circuit fault.

For the non-modular windings, although in Fig. 6.6 there are some changes in the branch currents of phase B, the difference between them is small. However, when the one-coil short-circuit fault occurs, there are negligible changes in the branch currents of phase B for the modular windings.

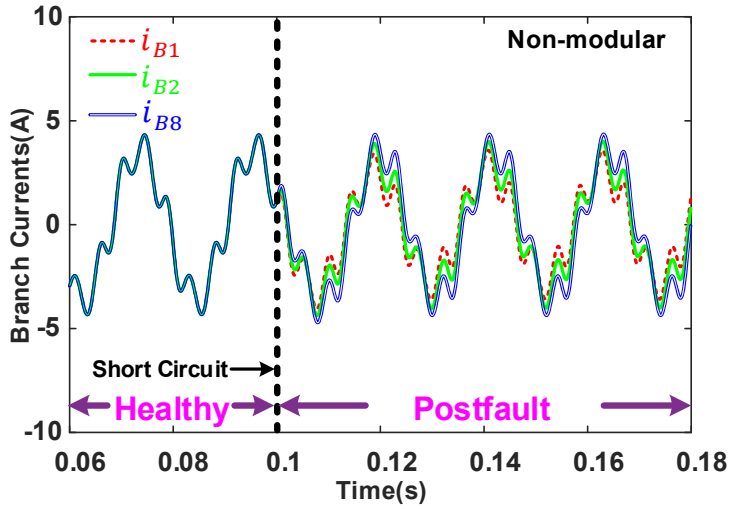

(a) Branch currents of phase B for the non-modular windings

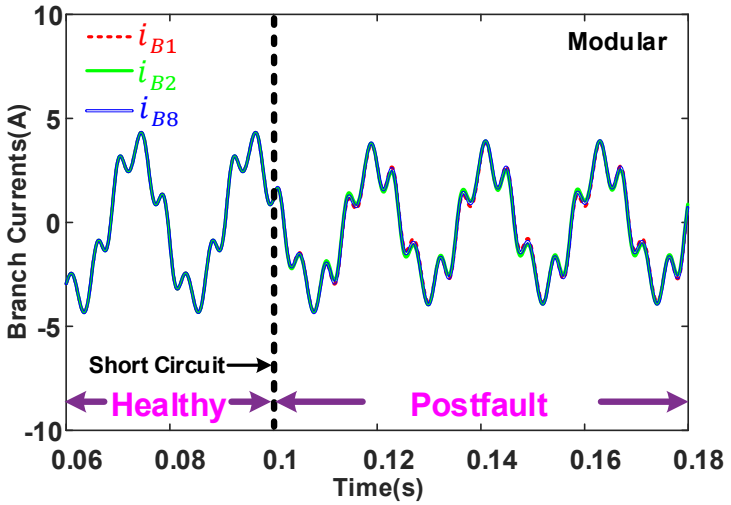

(b) Branch currents of phase B for the modular windings

Fig. 6.6 Branch currents of phase B of the 3kW SPM machine with non-modular and modular windings before and after the one-coil short-circuit fault.

Compared with the changes in the branch currents of phases A and B, the changes in the branch currents of phase C are much more significant for the non-modular windings. It can be seen from Fig. 6.7 (a) that when the one-coil short-circuit fault occurs in the A1 branch, the currents in the branches of phase C adjacent to the A1 branch, namely i_{C1} and i_{C8}, are significantly affected. The amplitude of i_{C1} increases from 4.3A to 10.1 A, although i_{C8} becomes much smaller, the amplitude of which decreases from 4.3A to 2.6A. It has also been noticed that for the non-modular windings the sum of i_{C1} and i_{C8} is almost two times as large as i_{C2}, and i_{C2} to i_{C7} are almost the same.

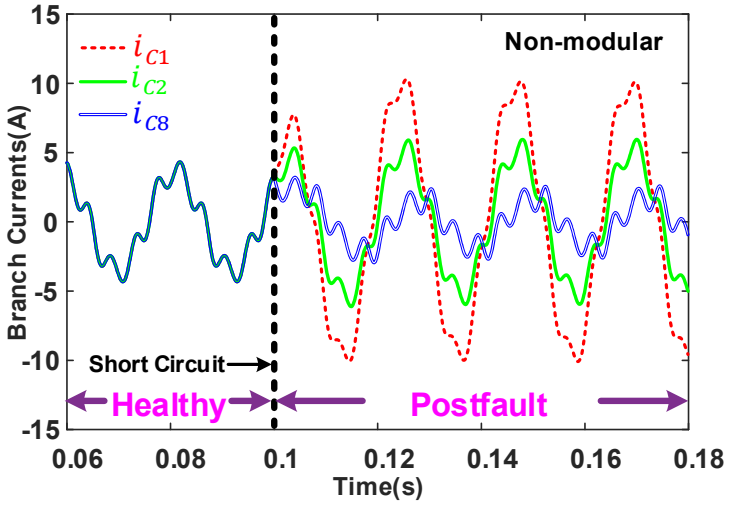

(a) Branch currents of phase C for the non-modular windings

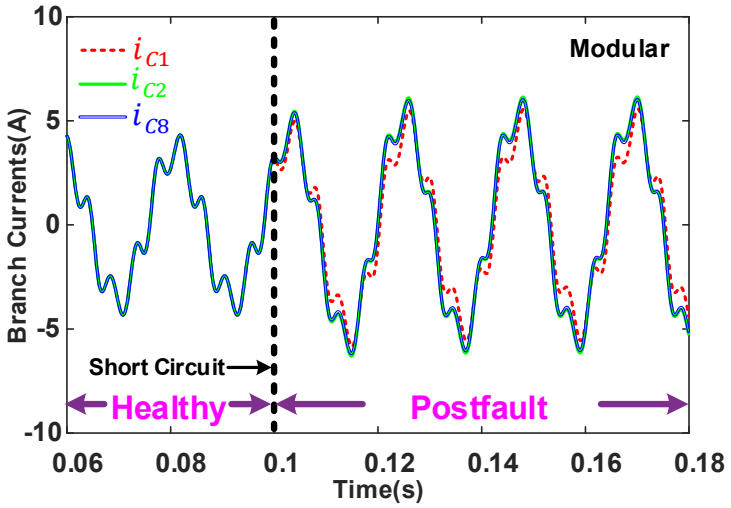

(b) Branch currents of phase C for the modular windings

Fig. 6.7 Branch currents of phase C of the 3kW SPM machine with non-modular and modular windings before and after the one-coil short-circuit fault.

However, the changes of branch currents of phase C are almost the same for the modular windings, as shown in Fig. 6.7 (b). In Fig. 6.7 (b), the amplitude of the branch currents only increases from 4.3A to 5.8A. Thus, the one-coil short-circuit fault will cause greater imbalance in branch currents of the 3kW machine with the non-modular windings. In addition, the *dq*-axis currents of the 3kW SPM machine with non-modular and modular windings before and after the one-coil short-circuit fault are shown in Fig. 6.8. It is worth noting that there are harmonic components in the *d*- and *q*-axis currents under healthy and faulty conditions, and this is mainly due to the harmonics in the back-EMFs.

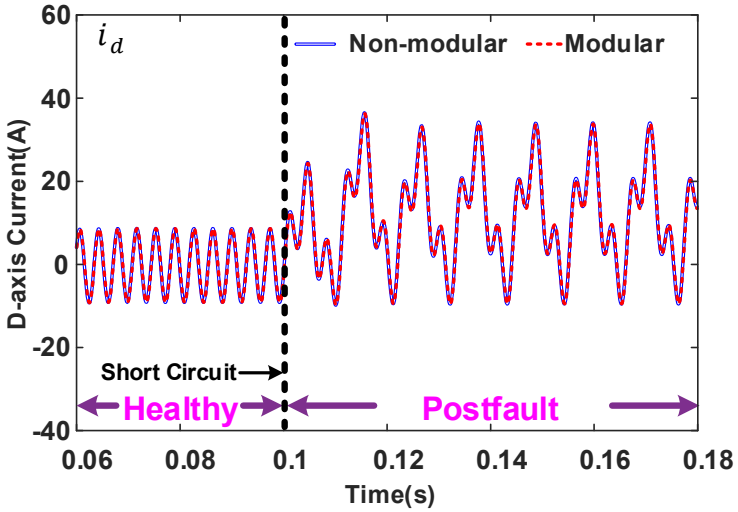

(a) *d*-axis currents

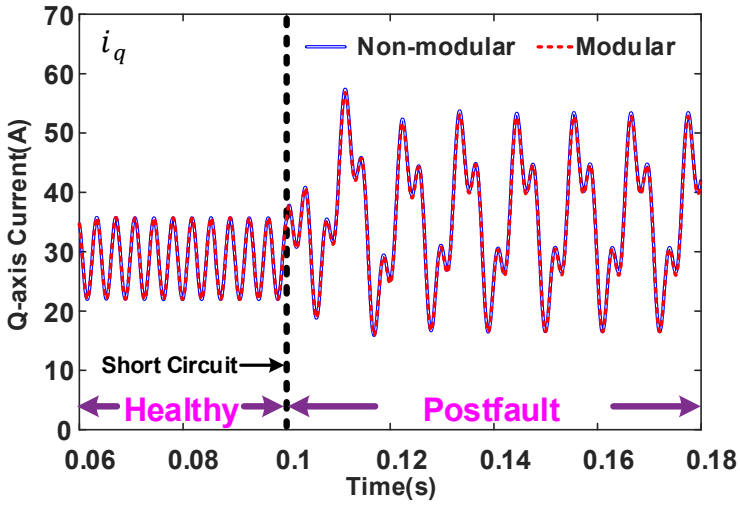

(b) q-axis currents

Fig. 6.8 dq-axis currents of the 3kW SPM machine with non-modular and modular windings before and after the one-coil short-circuit fault.

Interestingly, the dq-axis currents of the 3kW SPM machine with non-modular and modular windings are very similar before and after the one-coil short-circuit fault, meaning that from the 3-phase currents before and after the fault it would be impossible to tell the difference between these two winding configurations. Although it is easy to find that the changes in the currents in phases A and B are the same for the non-modular and modular windings from Fig. 6.5 and Fig. 6.6, it is a little difficult to tell why the changes in phase C currents have no difference. When this phenomenon is carefully analysed, it is found that for the non-modular windings, although i_{C1} and i_{C8} are greatly affected, the sum of i_{C1} and i_{C8} is almost two times as large as i_{C2}. Furthermore, for both winding configurations, i_{C2} to i_{C7} are very similar. These changes in branch currents finally lead to the same variations of phase C currents for both winding configurations. In addition, the same changes in the 3-phase currents and current in the faulty coil also result in the same changes in the developed torque for both winding configurations, as shown in Fig. 6.9.

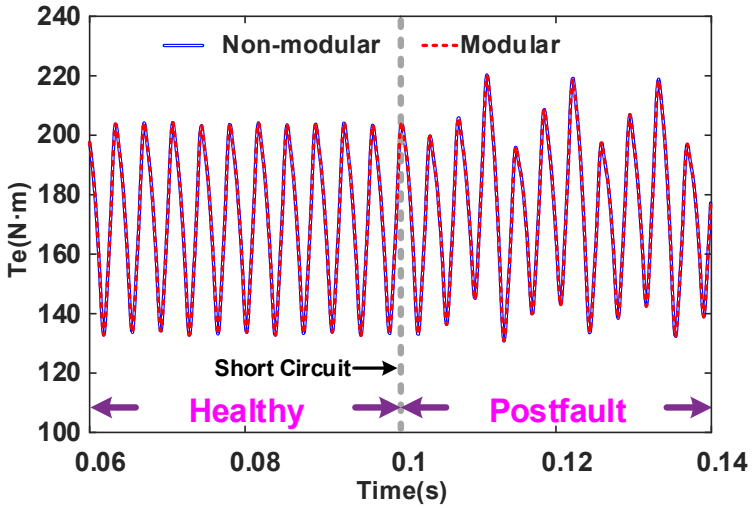

Fig. 6.9 Change in on-load torque of the 3kW SPM machine with non-modular and modular windings before and after the one coil short-circuit fault.

6.3.1.2 One-Coil Short-Circuit Fault in Phase B (2S×8P)

When the one-coil short-circuit fault happens in the first branch of phase B, the currents in the faulty coil of the 3kW SPM machine with non-modular and modular windings are shown in Fig. 6.10. A very slight difference between the currents of the faulty coil for both windings can be observed. This slight difference may be caused by numerical errors introduced during the inductance calculation and FFT analysis of no-load flux linkages.

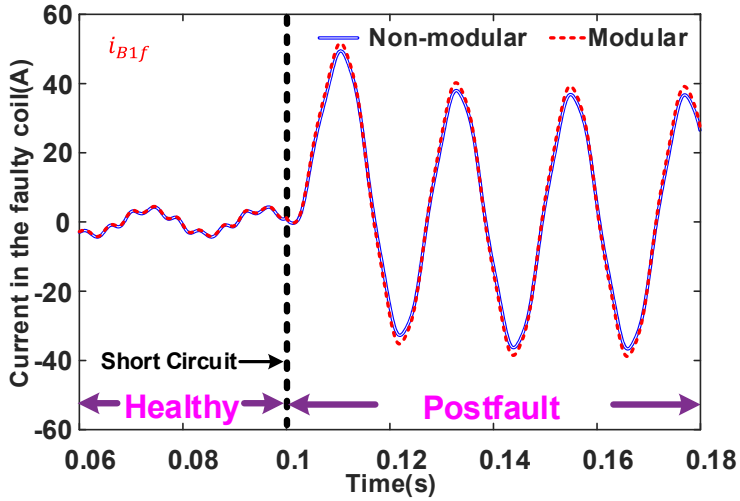

Fig. 6.10 Currents in the faulty coil of the 3kW SPM machine with non-modular and modular windings when the one coil short-circuit fault occurs in the first branch of phase B.

The branch currents of the 3-phase windings of the 3kW SPM machine with non-modular and modular windings are shown in Fig. 6.11, Fig. 6.12, and Fig. 6.13 , respectively, when the one-coil short-circuit fault happens in the first branch of phase B. It can be seen that there is

almost no difference in the branch currents of 3-phase windings for both winding configurations. In addition, there is no difference for the modular windings whether the one-coil short-circuit fault occurs in phase A or B. However, for the non-modular windings, when the one-coil short-circuit fault occurs in phase B rather than in phase A, it will cause less imbalance in branch currents.

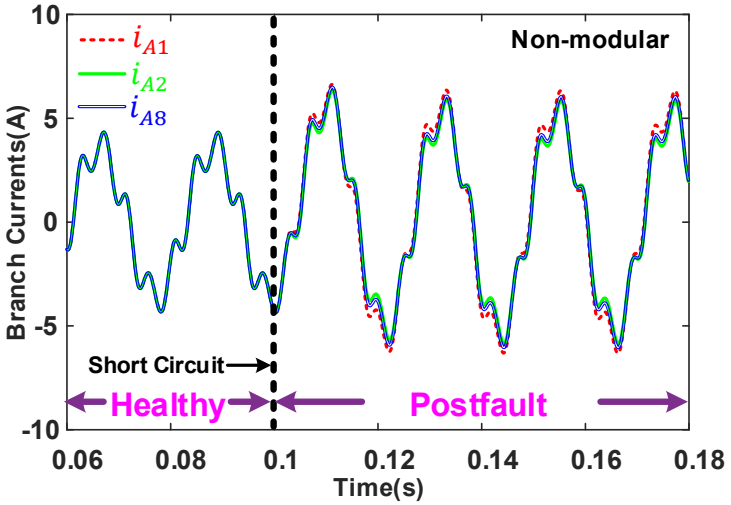

(a) Branch currents of phase A for the non-modular windings

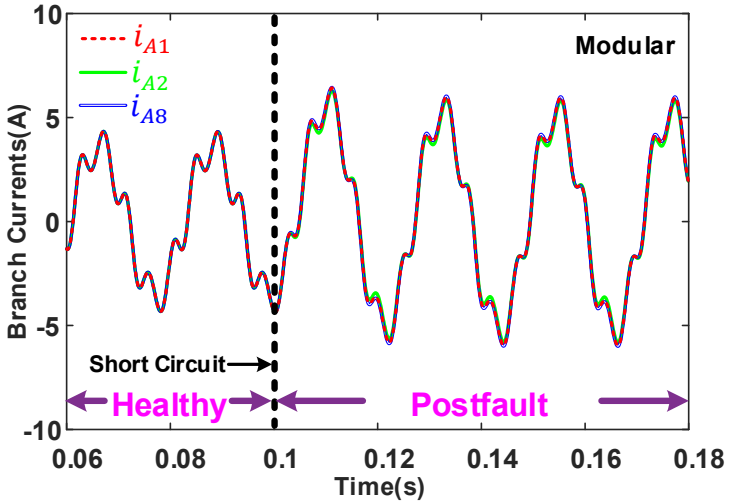

(b) Branch currents of phase A for the modular windings

Fig. 6.11 Branch currents of phase A of the 3kW SPM machine with non-modular and modular windings when the one coil short-circuit fault occurs in the first branch of phase B.

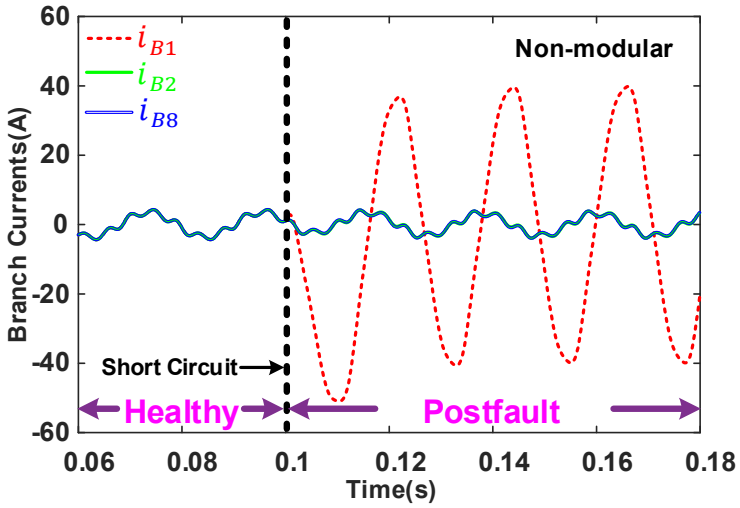

(a) Branch currents of phase B for the non-modular windings

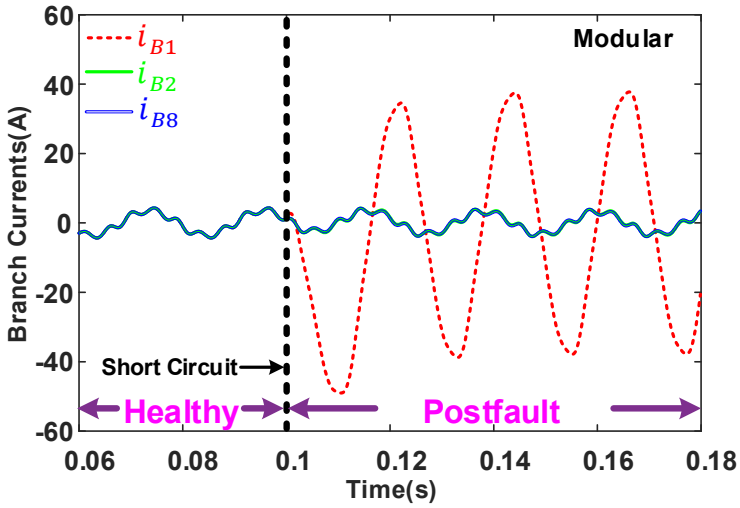

(b) Branch currents of phase B for the modular windings

Fig. 6.12 Branch currents of phase B of the 3kW SPM machine with non-modular and modular windings when the one coil short-circuit fault occurs in the first branch of phase B.

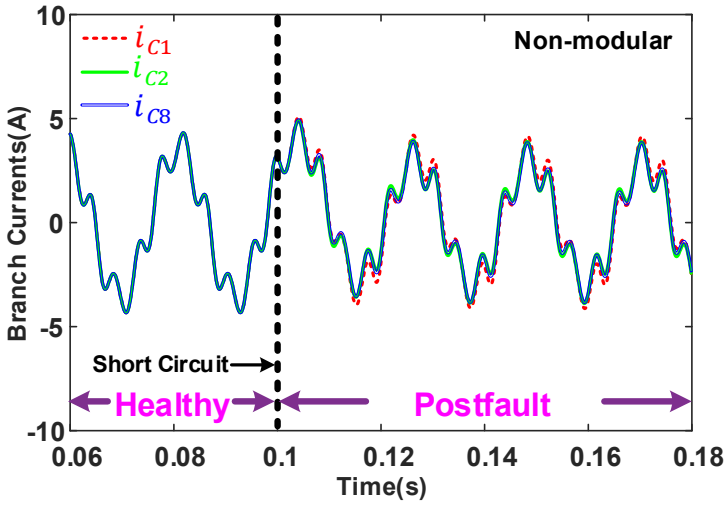

(a) Branch currents of phase C for the non-modular windings

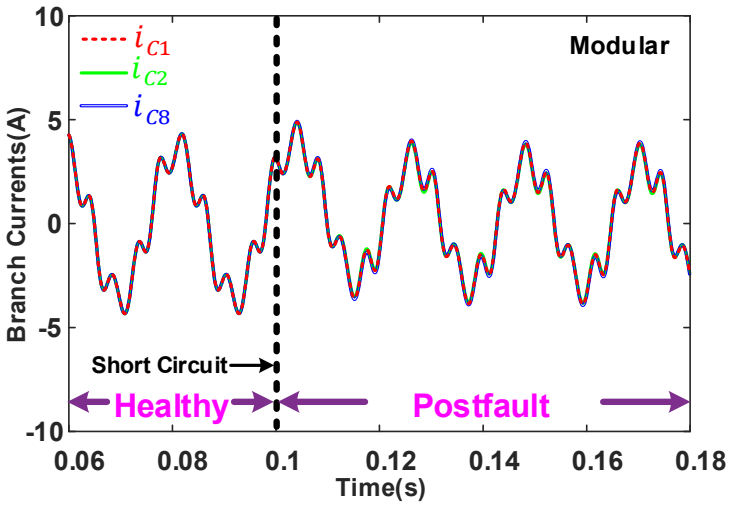

(b) Branch currents of phase C for the modular windings

Fig. 6.13 Branch currents of phase C of the 3kW SPM machine with non-modular and modular windings when the one coil short-circuit fault occurs in the first branch of phase B.

The *dq*-axis currents of the 3kW SPM machine with non-modular and modular windings are also shown in Fig. 6.14. Again, there is very little difference of *dq*-axis currents for these two windings.

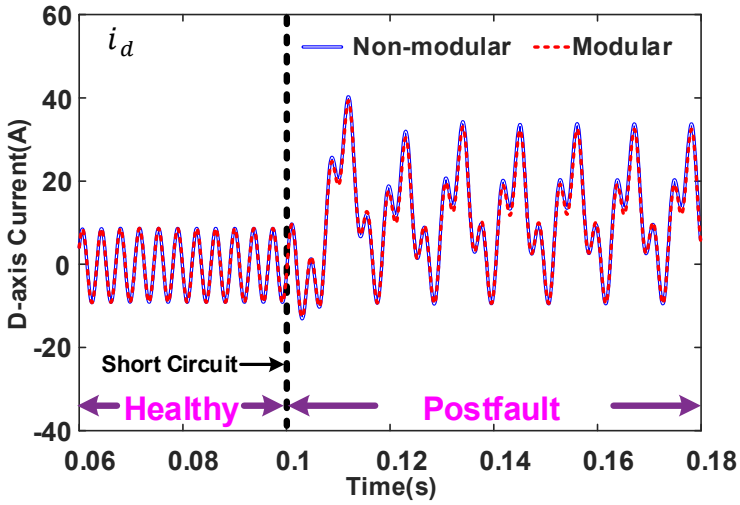

(a) d-axis currents

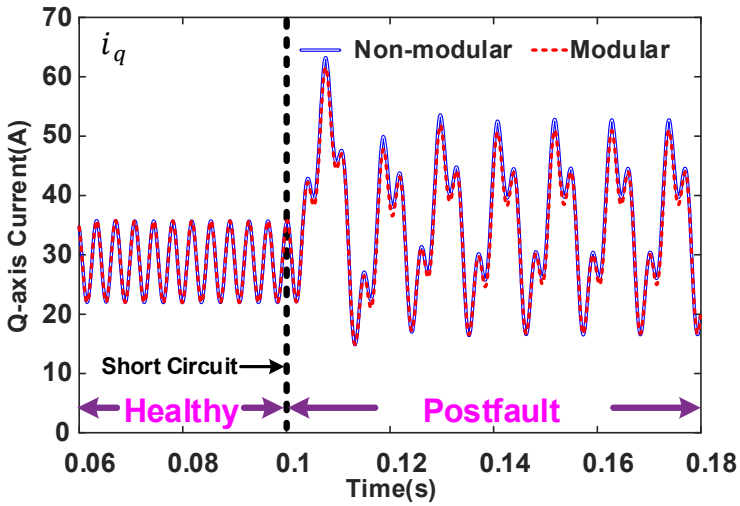

(b) q-axis currents

Fig. 6.14 dq-axis currents of the 3kW SPM machine with non-modular and modular windings when the one coil short-circuit fault occurs in the first branch of phase B.

6.3.1.3 One-Coil Short-Circuit Fault in Phase C (2S×8P)

When the one-coil short-circuit fault occurs in the first branch of phase C winding, the currents in the faulty coil for both windings are shown in Fig. 6.15. Again, there is negligible difference in the currents of the faulty coil for both windings. The branch currents of the 3-phase windings of the 3kW SPM machine with non-modular and modular windings are also shown in Fig. 6.16, Fig. 6.17 and Fig. 6.18, respectively. It is obvious from Fig. 6.16 that the branch currents of phase A are different for both windings. For the non-modular windings, the amplitude of i_{A2} is the greatest amongst all the branch currents of phase A, around 7.12A. The amplitude of i_{A1} also increases from 4.3A to 5.5A. Other branch currents are very similar and

the amplitude of i_{A8} actually drops a little, from 4.3A to 3.9A. It is worth mentioning that the two branches of phase A next to C1 where the fault occurs now are A1 and A2. This is why the changes in the currents of these two branches are more significant than those of the other branches.

In addition, although the branch currents of phase B are almost the same for both windings, the amplitudes of them actually increase from 4.3A to 6A after the fault. As for the branch currents of phase C, they are almost the same as the branch currents of phase A if the fault is introduced in phase A, or the branch currents of phase B when the fault is introduced in phase B.

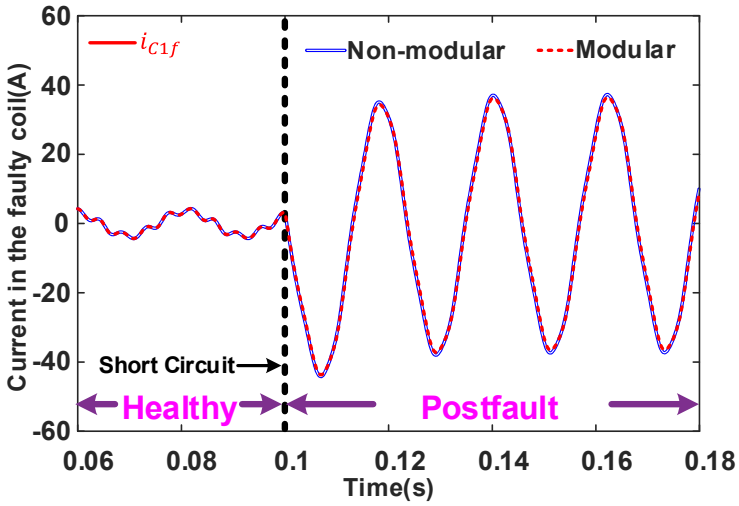

Fig. 6.15 Currents in the faulty coil of the 3kW SPM machine with non-modular and modular windings when the one coil short-circuit fault occurs in the first branch of phase C.

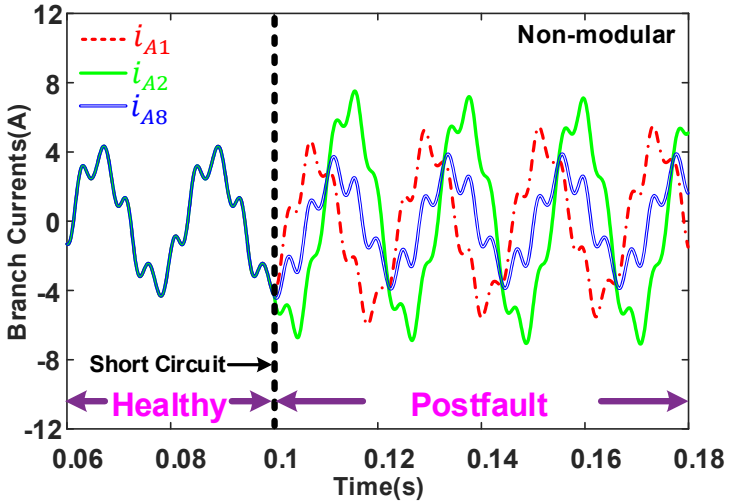

(a) Branch currents of phase A for the non-modular windings

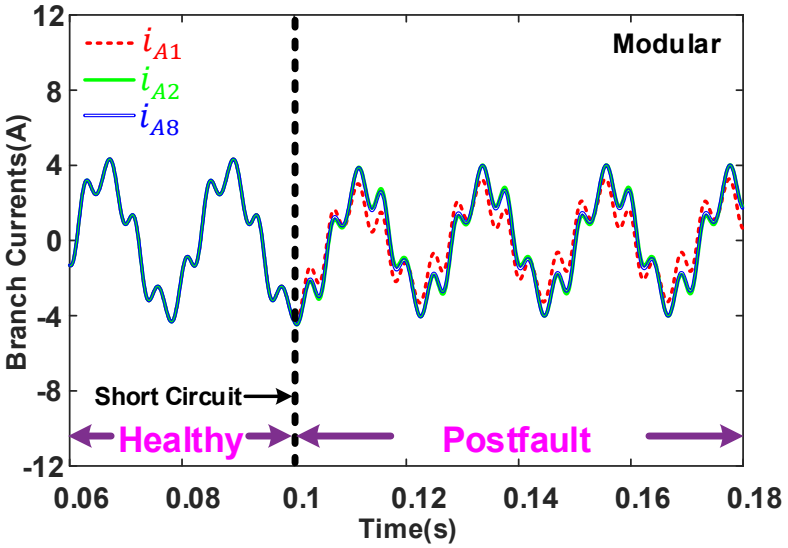

(b) Branch currents of phase A for the modular windings

Fig. 6.16 Branch currents of phase A of the 3kW SPM machine with non-modular and modular windings when the one coil short-circuit fault occurs in the first branch of phase C.

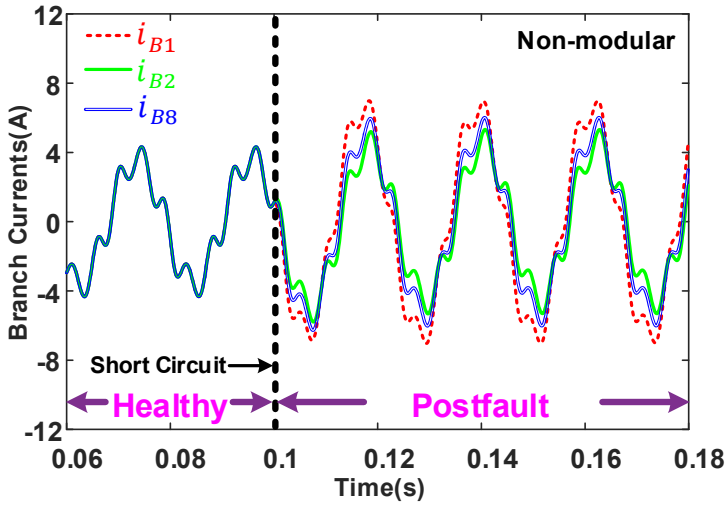

(a) Branch currents of phase B for the non-modular windings

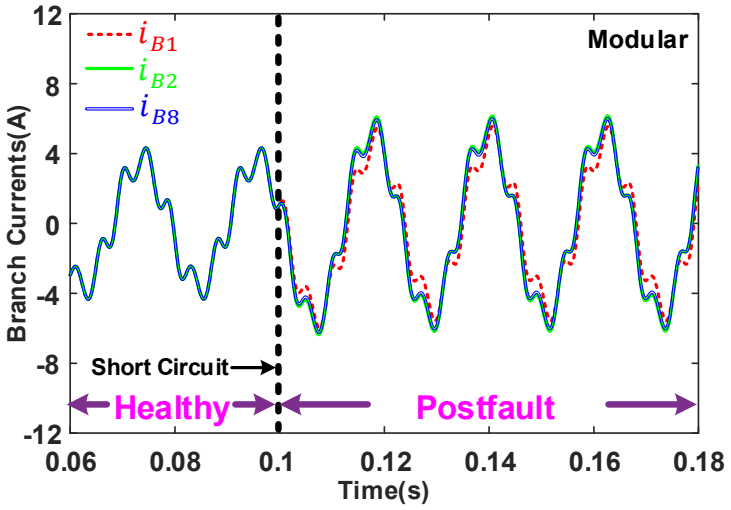

(b) Branch currents of phase B for the modular windings

Fig. 6.17 Branch currents of phase B of the 3kW SPM machine with non-modular and modular windings when the one coil short-circuit fault occurs in the first branch of phase C.

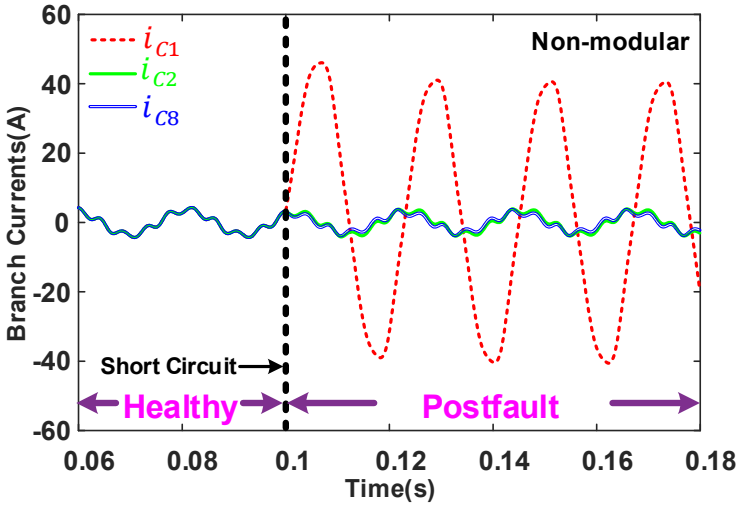

(a) Branch currents of phase C for the non-modular windings

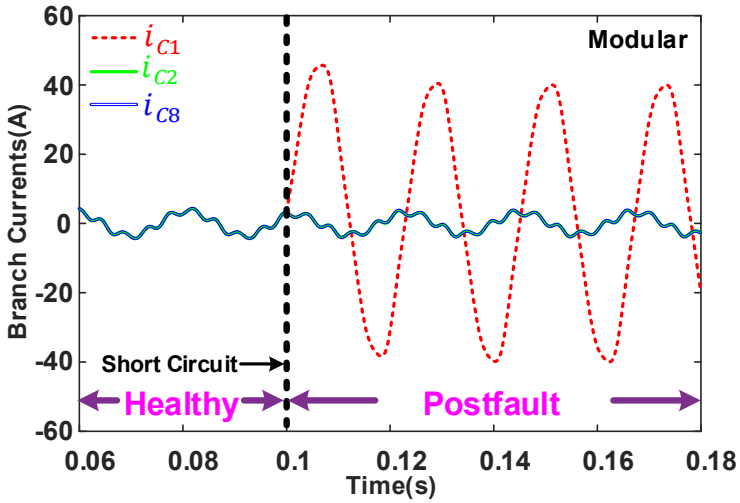

(b) Branch currents of phase C for the modular windings

Fig. 6.18 Branch currents of phase C of the 3kW SPM machine with non-modular and modular windings when the one coil short-circuit fault occurs in the first branch of phase C.

Although the branch currents for both windings are not totally the same, the changes in 3-phase currents are very similar. These changes in turn are reflected in the *dq*-axis currents. To avoid duplication, they are not shown here. However, a comparison of the *dq*-axis currents when the one coil short-circuit fault occurs in different phases has also been carried out, as shown in Fig. 6.19. It can also be seen that the steady state *d*-axis current or *q*-axis current are quite similar except there is a time shift between them when the fault occurs in different phases. This also means that it is really difficult to tell the one-coil short-circuit fault occurs in which phase timely by analysing the current waveforms only.

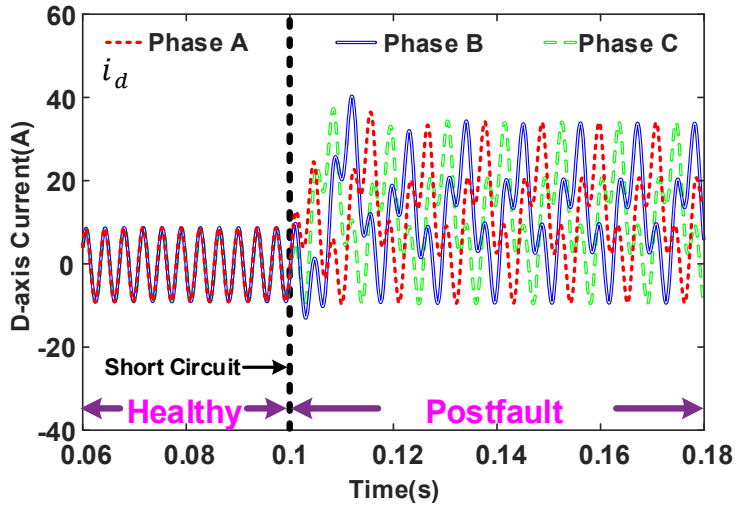

(a) *d*-axis currents

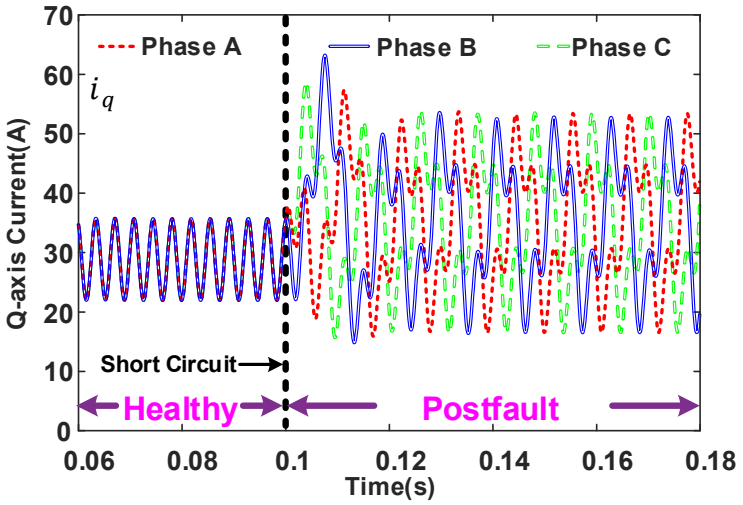

(b) q-axis currents

Fig. 6.19 dq-axis currents of the 3kW SPM machine when the one coil short-circuit fault occurs in the first branch of different phases.

6.3.1.4 One-Coil Short-Circuit Fault in Phase A (4S×4P)

When the coil connections are changed from 2S×8P to 4S×4P, the short-circuit currents of the faulty coil for the non-modular and modular windings are shown in Fig. 6.20. Now the one coil short-circuit fault is also assumed to occur in the first branch of phase A.

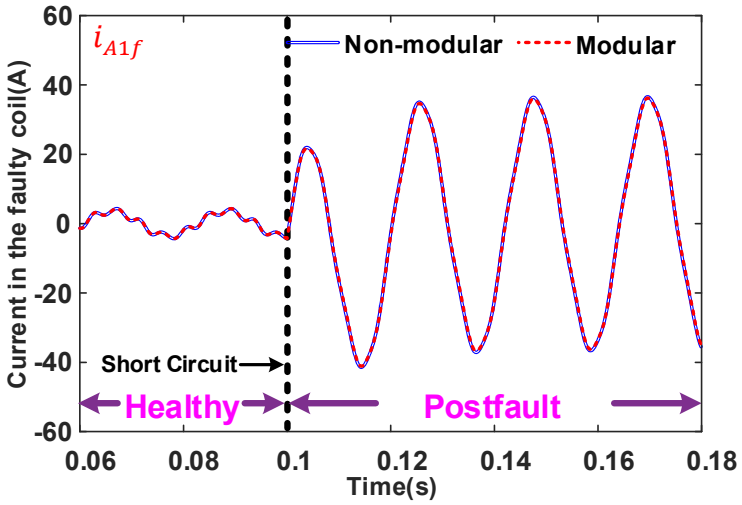

Fig. 6.20 Currents in the faulty coil of the 3kW SPM machine with 4S×4P coil connections and two winding configurations when the one coil short-circuit fault occurs in the first branch of phase A.

The amplitudes of the short-circuit currents for both windings in Fig. 6.20 are about 36.3A, similar to those for 2S×8P coil connection. This is also because the short-circuit current in the

faulty coil can be approximated by the ratio of the back-EMF of the short-circuited coil to the impedance of the short-circuited coil.

The branch currents of 3-phase windings of the 3kW SPM machine with 4S×4P coil connections and two winding configurations are shown in Fig. 6.21, Fig. 6.22, and Fig. 6.23 respectively. It can be seen that although the branch currents of phases A and B for the two winding configurations are quite similar, the branch currents of phase C are different.

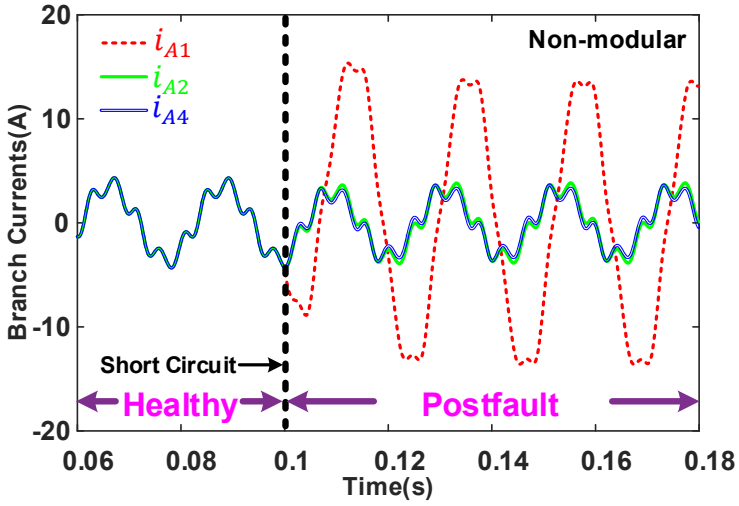

(a) Branch currents of phase A for the non-modular windings

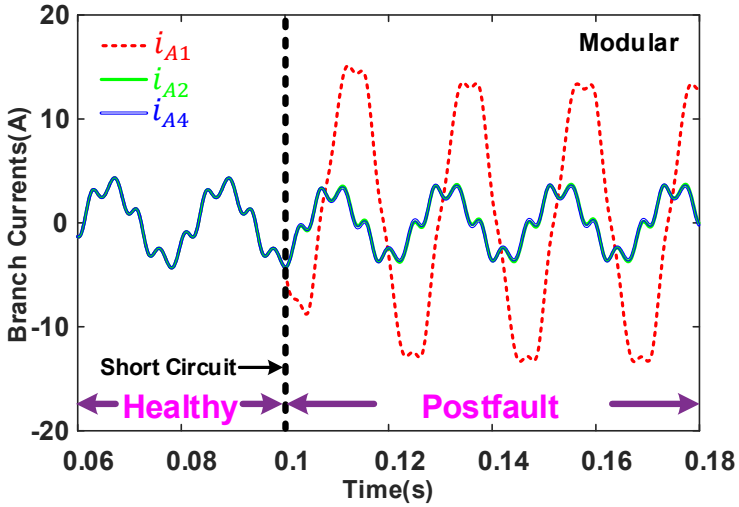

(b) Branch currents of phase A for the modular windings

Fig. 6.21 Branch currents of phase A of the 3kW SPM machine with 4S×4P coil connections and two winding configurations when the one coil short-circuit fault occurs in the first branch of phase A.

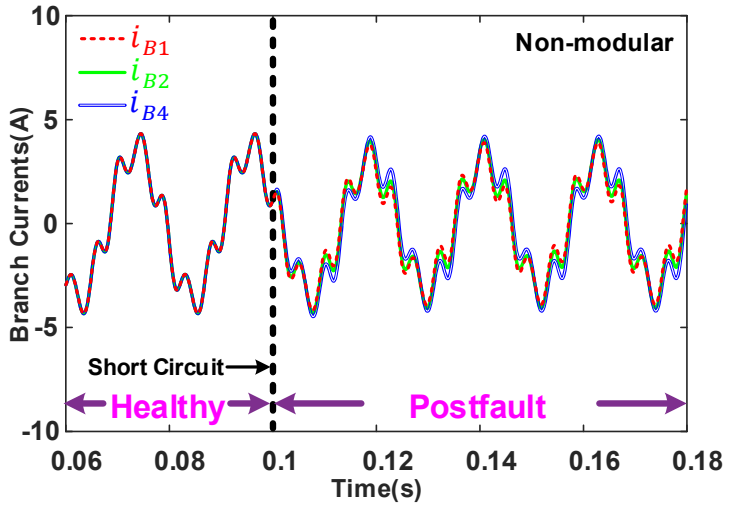

(a) Branch currents of phase B for the non-modular windings

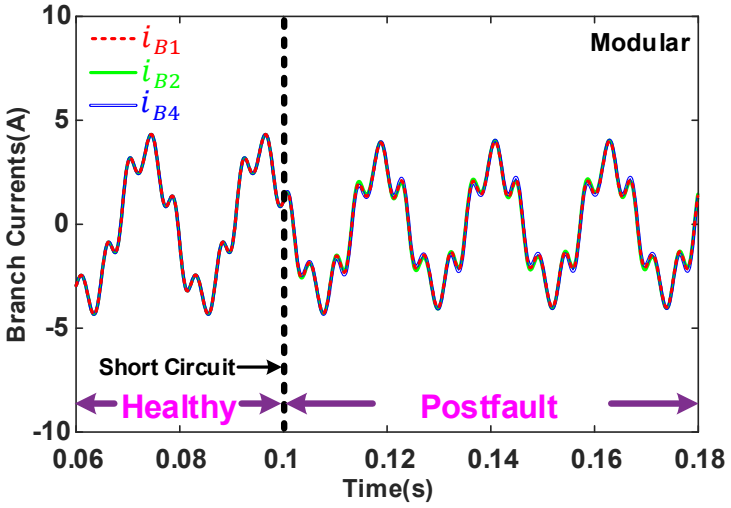

(b) Branch currents of phase B for the modular windings

Fig. 6.22 Branch currents of phase B of the 3kW SPM machine with 4S×4P coil connections and two winding configurations when the one coil short-circuit fault occurs in the first branch of phase A.

In Fig. 6.23 (a), when the one-coil short-circuit fault occurs in the A1 branch, for the non-modular windings the branch currents i_{C1} and i_{C4} of phase C, adjacent to the A1 branch, are significantly affected. The amplitude of i_{C1} increases from 4.3A to 7.4 A, and i_{C4} becomes a little smaller, the amplitude of which decreases from 4.3A to 3.7A. It has also been noticed that the sum of i_{C1} and i_{C4} in Fig. 6.23 (a) is almost two times as large as i_{C2}, and i_{C2} and i_{C3} are almost the same. However, all the branch currents of phase C are almost the same for the modular windings, as shown in Fig. 6.23 (b), the amplitudes of which increase from 4.3A to 5.4A after the fault.

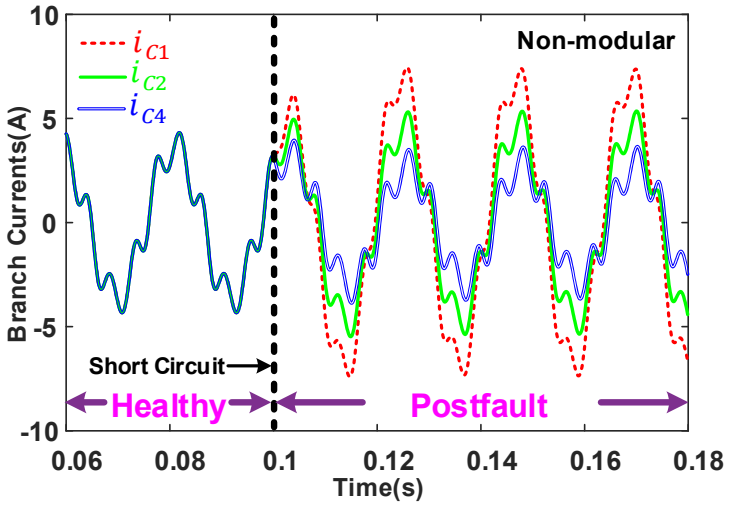

(a) Branch currents of phase C for the non-modular windings

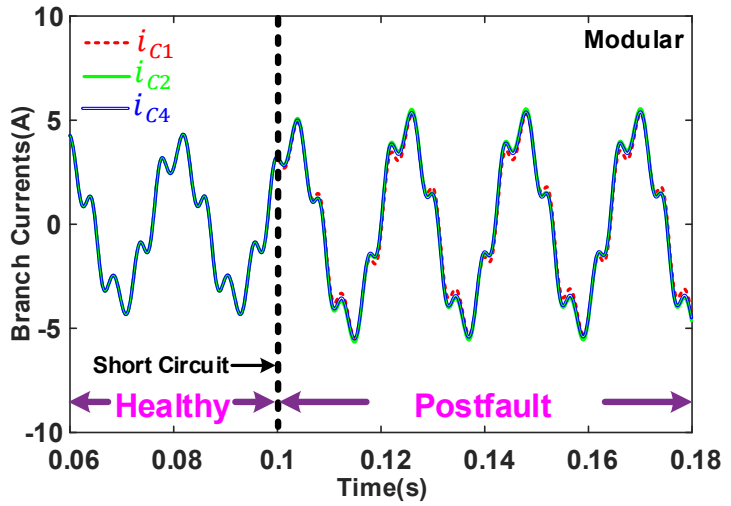

(b) Branch currents of phase C for the modular windings

Fig. 6.23 Branch currents of phase C of the 3kW SPM machine with 4S×4P coil connections and two winding configurations when the one coil short-circuit fault occurs in the first branch of phase A.

A comparison of the *dq*-axis currents of the 3kW SPM machine with 4S×4P coil connections and two winding configurations before and after the one-coil short-circuit fault are shown in Fig. 6.24. It can be seen that the *dq*-axis currents for both windings are almost the same before and after the one-coil short-circuit fault. These negligible differences in the *dq*-axis currents and current in the faulty coil will also lead to the negligible difference in the generated electromagnetic torque, as shown in Fig. 6.25. Compared with the torque ripple for 2S×8P coil connections, the torque ripple for the 4S×4P coil connections becomes a little smaller.

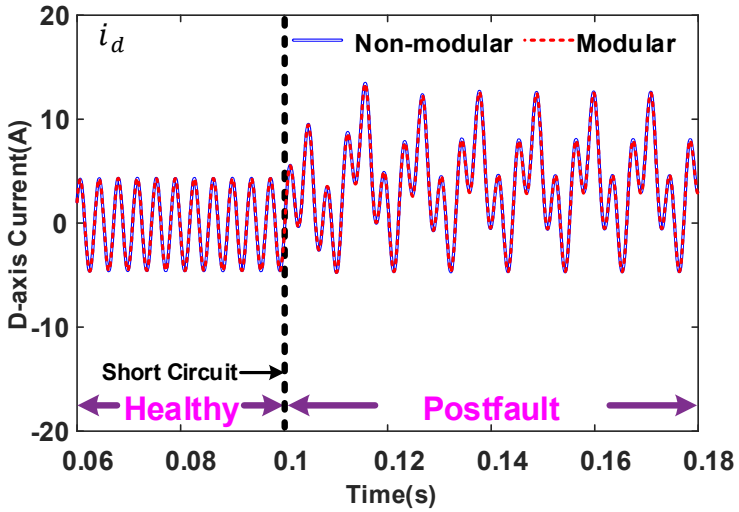

(a) *d*-axis currents

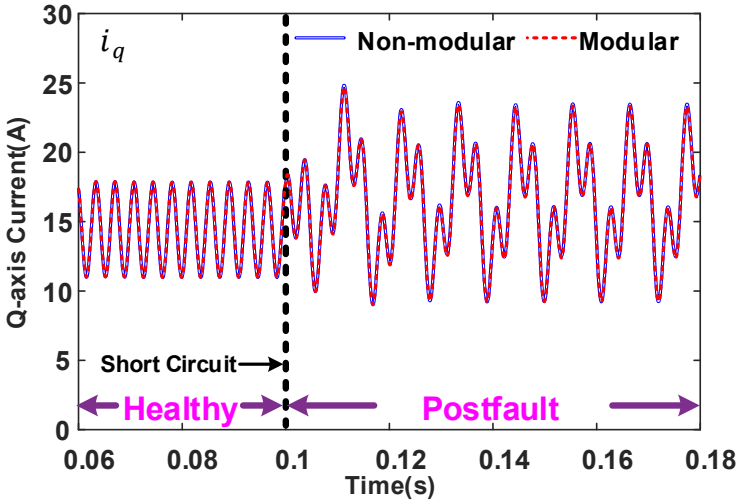

(b) *q*-axis currents

Fig. 6.24 *dq*-axis currents of the 3kW SPM machine with 4S×4P coil connections and two winding configurations when the one coil short-circuit fault occurs in the first branch of phase A.

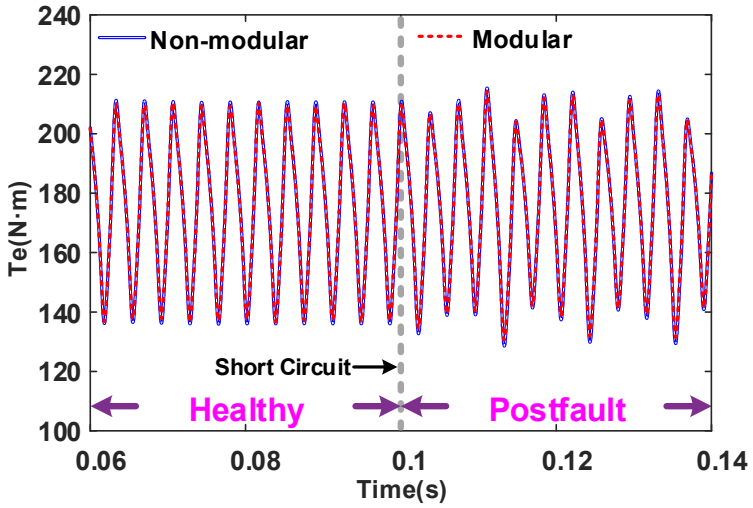

Fig. 6.25 Change in on-load torque of the 3kW SPM machine with 4S×4P coil connections and two winding configurations before and after the one coil short-circuit fault.

6.3.1.5 One-Coil Short-Circuit Fault in Phase A (8S×2P)

In this section, the one coil short-circuit fault is also assumed to occur in the first branch of phase A. When the coil connections are changed to 8S×2P, the short-circuit currents of the faulty coil for the non-modular and modular windings are shown in Fig. 6.26.

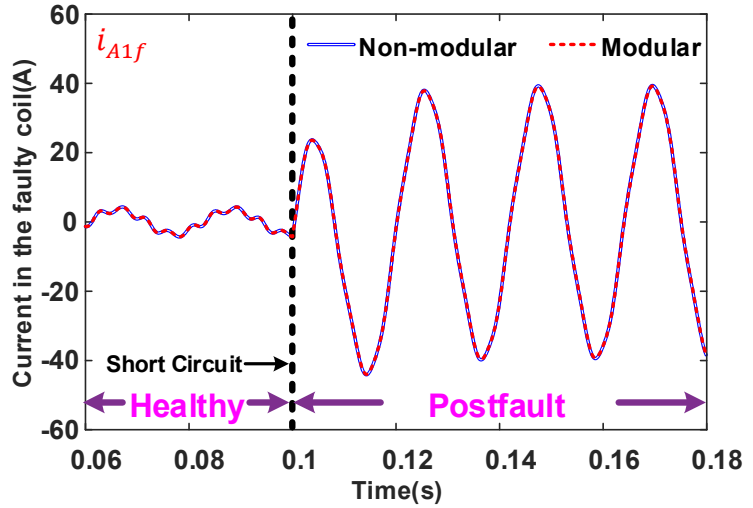

Fig. 6.26 Currents in the faulty coil of the 3kW SPM machine with 8S×2P coil connections and two winding configurations when the one coil short-circuit fault occurs in the first branch of phase A.

Since it has been shown in chapter 4 that different series-parallel coil connections have little influence on the amplitude of the ITSC current at the same torque and speed, it can be expected that the amplitudes of the short-circuit current in the faulty coil for the non-modular overlapping windings are the same as those for 2S×8P and 4S×4P coil connections. Again, for

the modular windings, the short-circuit current in the faulty coil is almost the same as that for the non-modular windings.

The branch currents of 3-phase windings of the 3kW SPM machine with 8S×2P coil connections and two winding configurations are shown in Fig. 6.27, Fig. 6.28 and Fig. 6.29.

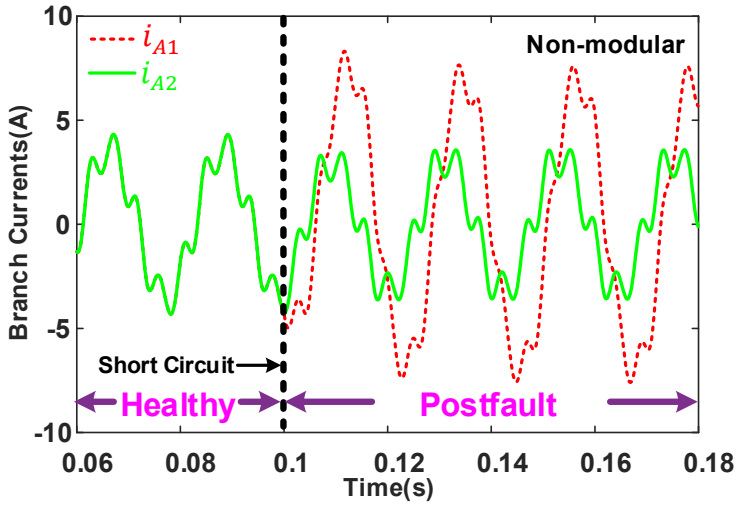

(a) Branch currents of phase A for the non-modular windings

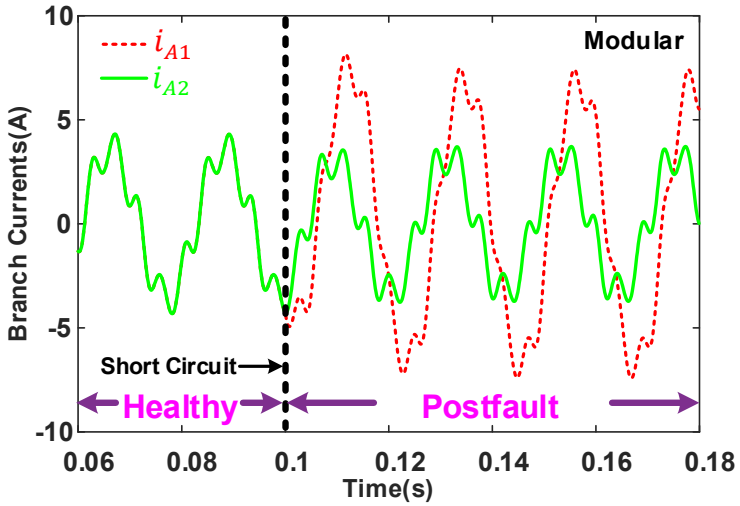

(b) Branch currents of phase A for the modular windings

Fig. 6.27 Branch currents of phase A of the 3kW SPM machine with 8S×2P coil connections and two winding configurations when the one coil short-circuit fault occurs in the first branch of phase A.

It can be seen from Fig. 6.27 that the branch currents of phase A for these two winding configurations are almost the same. The amplitude of i_{A1} increases from 4.3A to 7.6A, and the amplitude of i_{A2} decreases from 4.3A to 3.6A, much smaller than the short-circuit current in the faulty coil, around 39.4A. Regarding the branch currents of phase B for these two winding

configurations, they are also very much the same, as shown in Fig. 6.28. Actually, after the one-coil short-circuit fault, they become a little smaller, the amplitude of which are about 4A.

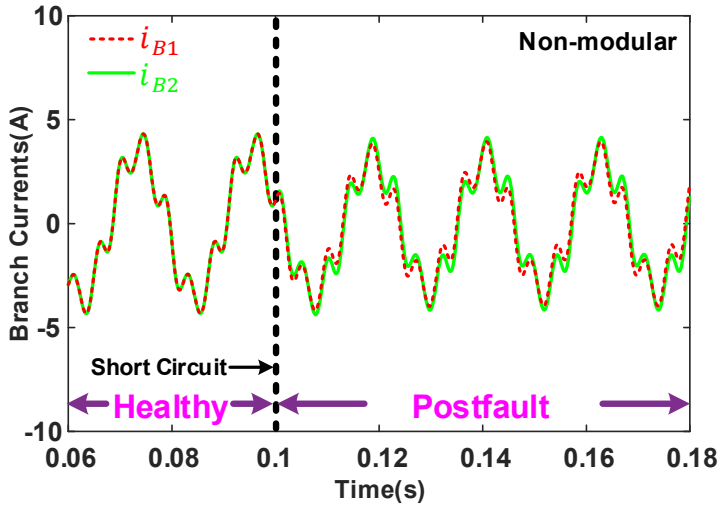

(a) Branch currents of phase B for the non-modular windings

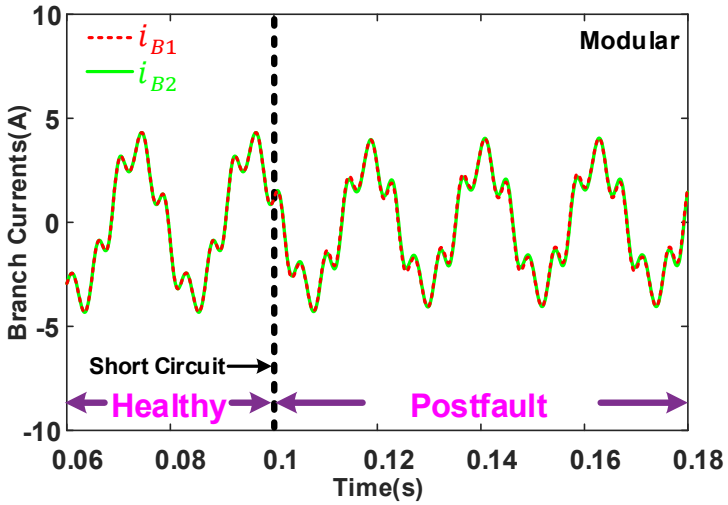

(b) Branch currents of phase B for the modular windings

Fig. 6.28 Branch currents of phase B of the 3kW SPM machine with 8S×2P coil connections and two winding configurations when the one coil short-circuit fault occurs in the first branch of phase A.

However, the difference of changes in the branch currents of phase C for the non-modular and modular windings can still be observed in Fig. 6.29 for the 3kW SPM machine with the 8S×2P coil connections. For the non-modular windings in Fig. 6.29 (a), the amplitude of i_{C1} increases from 4.3A to 6.2A, and i_{C2} is almost unchanged. However, for the modular windings in Fig. 6.29 (b), there is negligible difference between i_{C1} and i_{C2}. The amplitudes of them are about 5.2A.

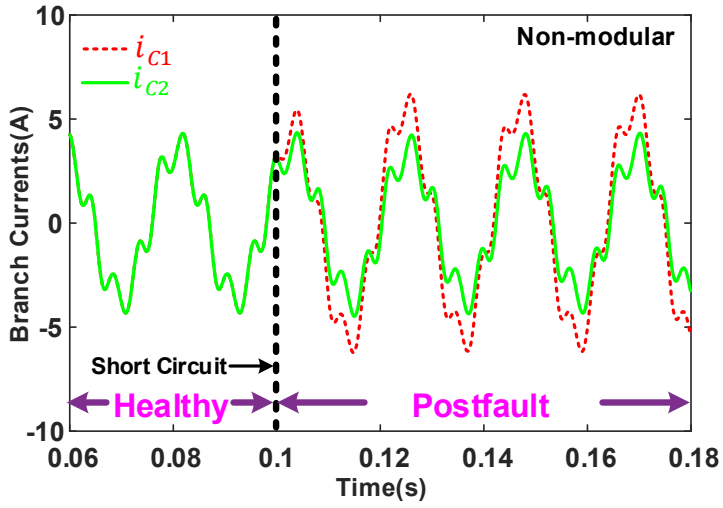

(a) Branch currents of phase C for the non-modular windings

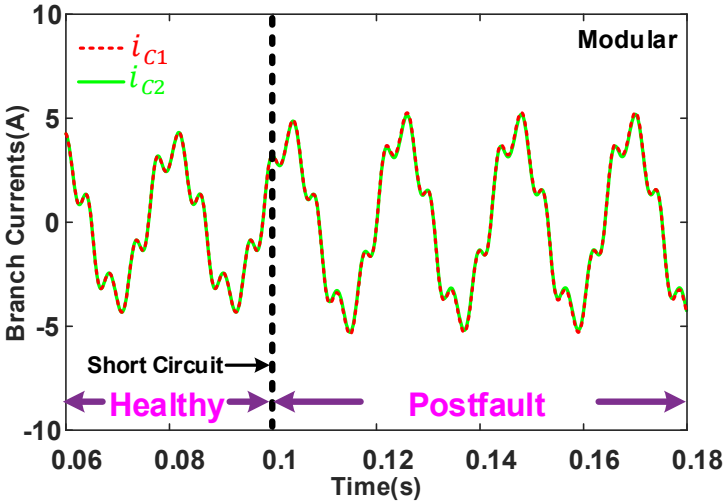

(b) Branch currents of phase C for the modular windings

Fig. 6.29 Branch currents of phase C of the 3kW SPM machine with 8S×2P coil connections and two winding configurations when the one coil short-circuit fault occurs in the first branch of phase A.

As for the *dq*-axis currents of the 3kW SPM machine with 8S×2P coil connections and two winding configurations before and after the one-coil short-circuit fault, they are shown in Fig. 6.30. It can be seen that there is a negligible difference in the *dq*-axis currents for both windings before and after the one-coil short-circuit fault. Because the *dq*-axis currents and current in the faulty coil are almost the same for these two windings, the generated electromagnetic torques as shown in Fig. 6.30 will have no difference.

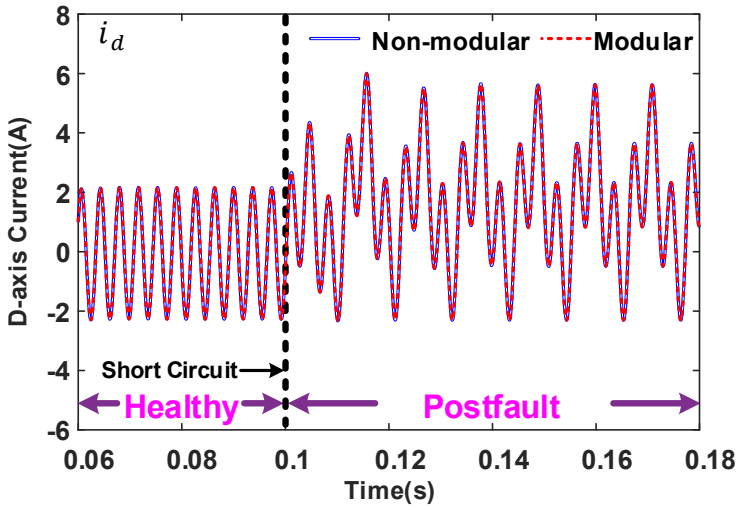

(a) *d*-axis currents

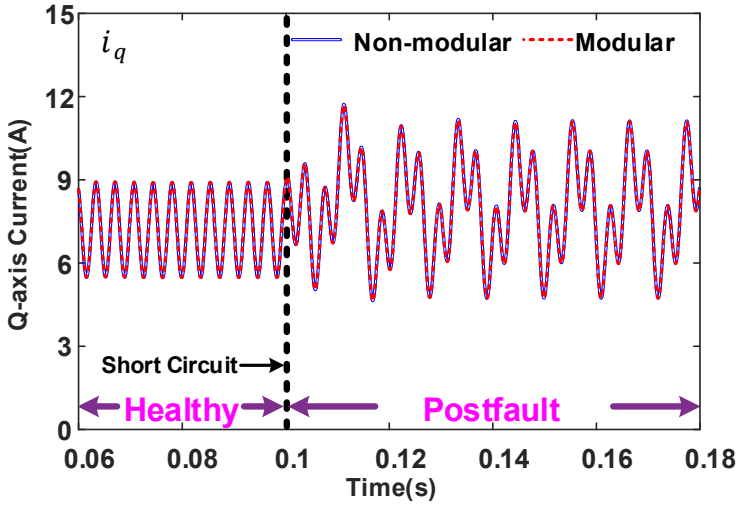

(b) *q*-axis currents

Fig. 6.30 *dq*-axis currents of the 3kW SPM machine with 8S×2P coil connections and two winding configurations when the one coil short-circuit fault occurs in the first branch of phase A.

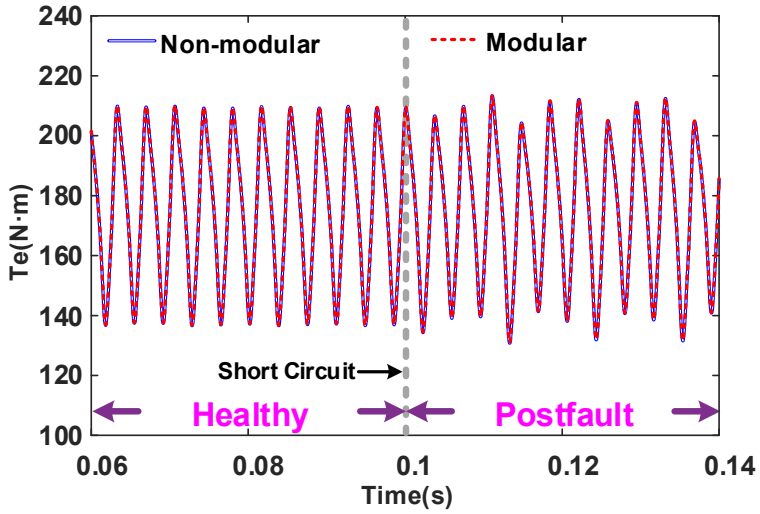

Fig. 6.31 Change in on-load torque of the 3kW SPM machine with 8S×2P coil connections and two winding configurations before and after the one coil short-circuit fault.

6.3.2 Results for the 500kW SPM Machine

Although there is some difference in branch currents of the 3kW SPM machine with non-modular and modular windings, this is not the case for the 500kW SPM machine. It is worth mentioning that the branch currents of different phases of the 500kW SPM machine with non-modular windings under the one-coil short-circuit fault have been shown in chapter 5, and it can be seen from those results that there are negligible changes in the branch currents of different phases for the non-modular windings when the one-coil short-circuit fault occurs. These phenomena are very much the same for the modular windings, as shown in Fig. 6.32. Considering that the branch currents of phases B and C are hardly changed before and after the one-coil short-circuit fault, the waveforms of which are not shown here. It can be seen from Fig. 6.32 that there is almost no difference in the branch currents of phase A for both windings, and this is also the same for the branch currents of phase B or C. This is because the one-coil short-circuit fault will often do very little harm to large-power SPM machines with many parallel branches and many coils connected in series for one branch. Therefore, it can be concluded that for large-power SPM machines with non-modular and modular windings, the difference in the fault performance would be negligible. In this case, in this chapter, it has been deemed unnecessary to carry out further studies for the 3MW generators or beyond.

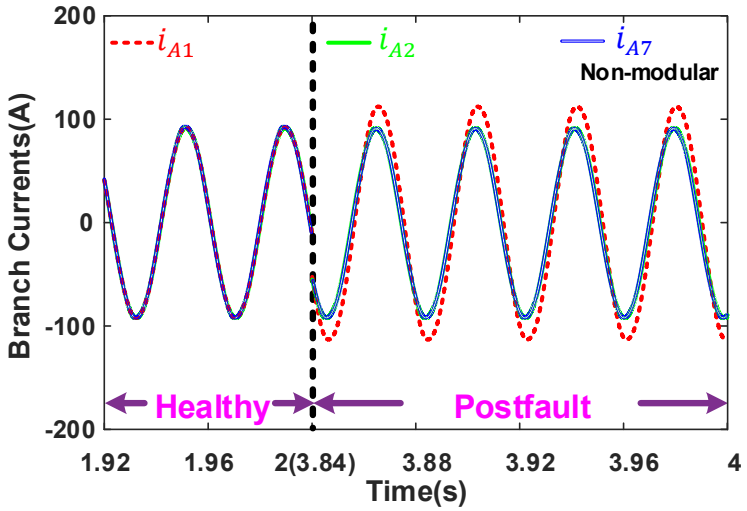

(a) Branch currents of phase A for the non-modular windings

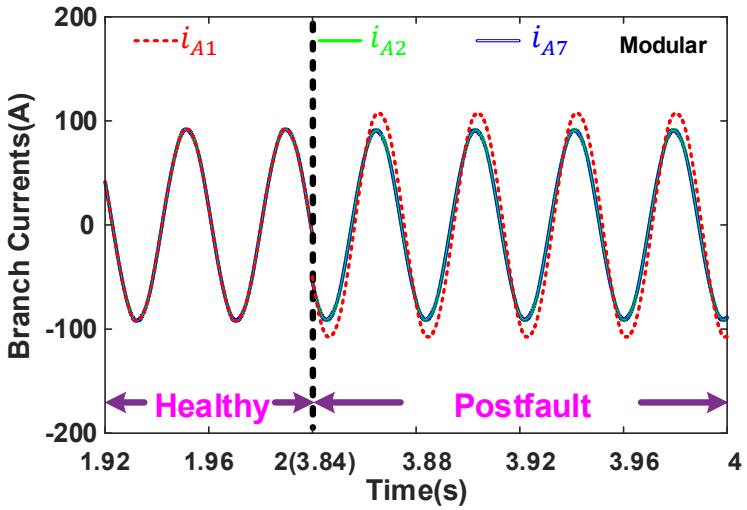

(b) Branch currents of phase A for the modular windings

Fig. 6.32 Branch currents of phase A of the 500kW SPM machine with non-modular and modular windings when the one coil short-circuit fault occurs in the first branch of phase A.

6.4 Conclusion

This chapter compares the performance of SPM machines with non-modular and modular windings under ITSC faults. It is found that the elements of branch inductance matrices $\mathbf{M}_{AC}$ and $\mathbf{M}_{BC}$ and three faulty inductance vectors $\mathbf{M}_{Af}$, $\mathbf{M}_{Bf}$, and $\mathbf{M}_{Cf}$ in the fault model for these two different winding configurations are different although the equivalent phase self- and mutual-inductances are the same, meaning that the healthy machine performances for a SPM machine with non-modular or modular windings are the same, but their fault performances are different. Simulation results of the 96-slot 32-pole SPM machine under inter-turn short-circuit

faults have confirmed this conclusion. In addition, machine performances of the same fault occurring in different phases have been simulated when these two winding configurations are considered. It is found that for the non-modular windings, the same fault in different phases will lead to different changes in branch currents. In addition, compared with the modular windings, the same fault in the non-modular windings will lead to greater imbalance in the branch currents of certain phases. However, the changes in three phase currents are almost the same. Thus, compared with the non-modular windings, the modular windings are generally more fault tolerant. However, these differences in the large-power (500kW and beyond) SPM machines become negligible because ITSC faults often cause very little imbalance in branch currents for large-power SPM machines with many parallel branches and many coils connected in series for one branch.

Chapter 7 Experimental Validation

Previous chapters from 2 to 4 have shown good agreements between the analytical and 2D FE simulation results for the 96-slot 32-pole 3kW SPM machine with different series-parallel coil connections. This chapter will validate the fault models of the SPM machines with series-connected coils, parallel-connected coils, and series-parallel connected coils by a series of experiments on two different small-scale machine prototypes.

Related Publications:

[Mei23a] Z. T. Mei, G.J. Li, Z. Q. Zhu, R. Clark, A. Thomas, and Z. Azar, "Scaling Effect On Inter-Turn Short-Circuit Fault of PM Machines for Wind Power Application," *IEEE Trans. Ind. Appl.*, vol. 59, no. 1, pp. 789–800, Jan.-Feb. 2023.

[MEI23b] Z. T. Mei, G. J. Li, Z. Q. Zhu, R. Clark, A. Thomas, and Z. Azar, "Modelling and Analysis of Inter-Turn Short-Circuit Fault of PM Machines with Parallel-Connected Coils," *IEEE Trans. Energy Convers.*, vol. 38, no. 2, pp. 1268-1279, Jun. 2023.

[Mei23c] Z. T. Mei, G. J. Li, Z. Q. Zhu, R. Clark, A. Thomas, and Z. Azar, "In-depth Investigation of Inter-Turn Short-Circuit Faults of PM Machines with Series-Parallel Coil Connections," *IET Electr. Power Appl.*, pp. 1–9, Apr. 2023.

7.1 Model Validation for Series-Connected Coils

To validate the fault models of the SPM machines with series-connected and parallel connected coils, a 12-slot 4-pole SPM machine has been built.

7.1.1 Machine Prototype and Experimental Setup

A 12-slot 4-pole SPM machine prototype with internal rotor has been built by our group member from a previous project [142] and refitted by us to introduce the ITSC faults to validate the proposed fault model. It should be mentioned that whether the rotor is internal or external will have no influence on the validation of the proposed fault model. The main machine specifications are listed in Table 7.1 and the stator and rotor are shown in Fig. 7.1 (a) and Fig. 7.1 (b), respectively.

Table 7.1 Specifications of the12-slot 4-pole SPM machine [142]

Rated speed (rpm)	400	Stator outer diameter (mm)	100
Rated current rms (A)	2.5	Rotor outer diameter (mm)	49
Series turns/coil	40	Airgap length (mm)	1
Slots/poles	12/4	Stack length (mm)	50

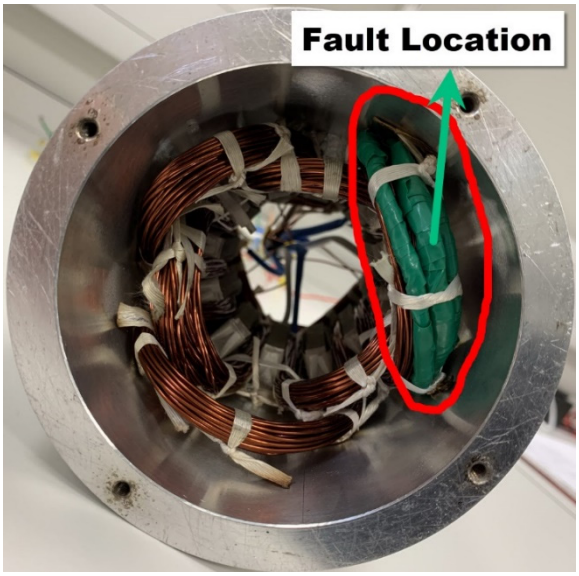

(a) Stator

(b) Rotor

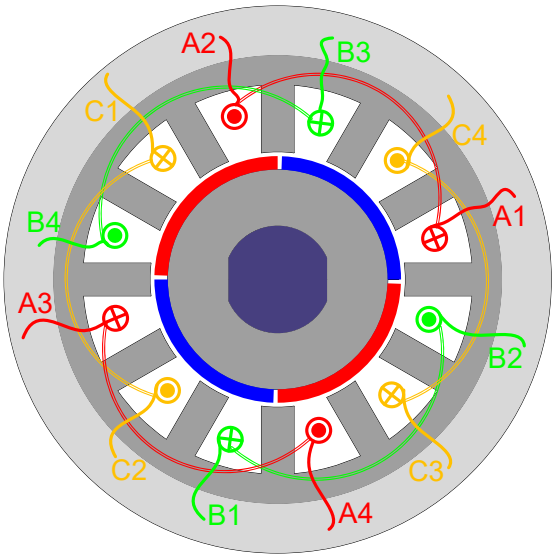

(c) Winding layout

Fig. 7.1 The 12-slot 4-pole SPM machine with ITSC faults.

Three fault scenarios can be introduced, i.e., single-turn, half-a-coil, and one-coil short-circuit faults. Because the main purpose of the experiments is to validate the proposed fault model, the SPM machine is used as a generator driven by a dc machine. In this way, no sophisticated control algorithm is needed, and the experimental setup can be simplified, as shown in Fig. 7.2. Because the validation of the fault model requires rotor speed as an input, the position encoder together with dSPACE shown in Fig. 7.2 are used to accurately capture the speed information (DC and ripple components).

The winding layout of this 12-slot 4-pole SPM machine is shown in Fig. 7.1 (c). All the coil ends (labelled as A1 to A4, B1 to B4 and C1 to C4) will be connected outside of the machine housing. On the other hand, the associated circuit schematic is illustrated in Fig. 7.3, in which each phase has two coils connected in series. The ITSC faults to be implemented will occur in A1A2 coil of the phase A. It is worth mentioning that no extra current limiting resistor is added to R_f in the external short-circuited path. However, $R_f \neq 0$ because the resistive effect caused by the extension wires and the electrical contact have to be included, particularly when fewer turns are short-circuited. The value of R_f can be obtained by subtracting R_{Af} from $R_f + R_{Af}$. It should be mentioned that both R_{Af} and $R_f + R_{Af}$ can be measured by using a low resistance instrument like the Rhopoint Milli-Ohmmeter M210 or Hioki IM3570 Impedance Analyzer before the ITSC is introduced. For the single-turn, half-a-coil, and one-coil short circuit faults, the measured values of R_f are 0.036Ω, 0.031Ω, and 0.033Ω, respectively. As for R_{Af}, they are 0.007Ω, 0.145Ω, and 0.323Ω, respectively.

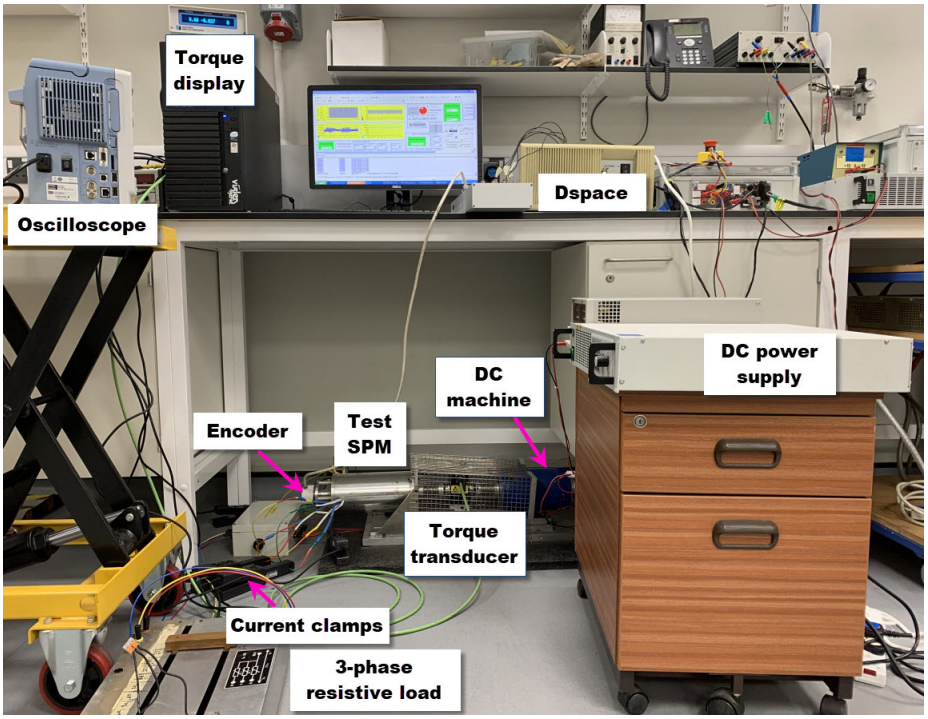

Fig. 7.2 Experimental setup.

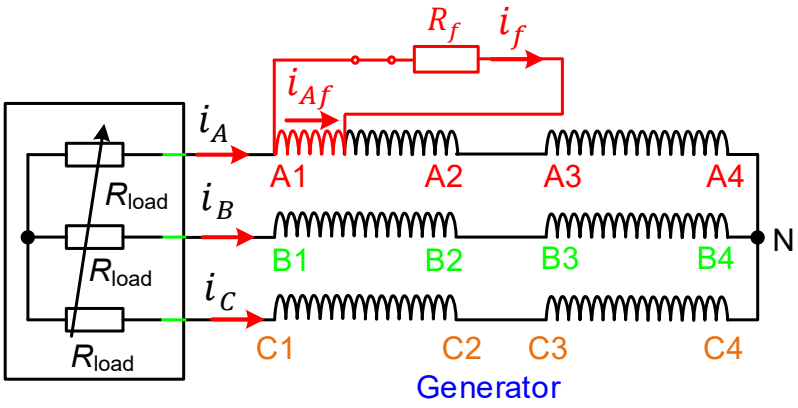

Fig. 7.3 Circuit schematic showing the introduced ITSC fault.

7.1.2 Cogging Torque and Back EMFs

As mentioned previously, the cogging torque needs to be included in the analytical model built in Matlab/Simulink to predict the torque ripple more accurately. The cogging torque obtained from the 2D FE model and experimental measurement using the method in [147] is shown in Fig. 7.4 and the corresponding test setup for the measurement is shown in Fig. 7.5 [142]. The rotor is kept stationary on the lathe, which is fixed by an aluminium beam of a certain length such as 300 mm, and a preload is put onto one end of the beam to measure the applied force on the digital scale. The preload is needed because the cogging torque can be positive or negative, depending on rotor positions. The torque can be simply calculated by

using the measured force multiplied by the length of the beam (300 mm). To measure the force (and torque) at different rotor positions, the stator is rotated, which leads to a relative angular motion between the stator and the rotor.

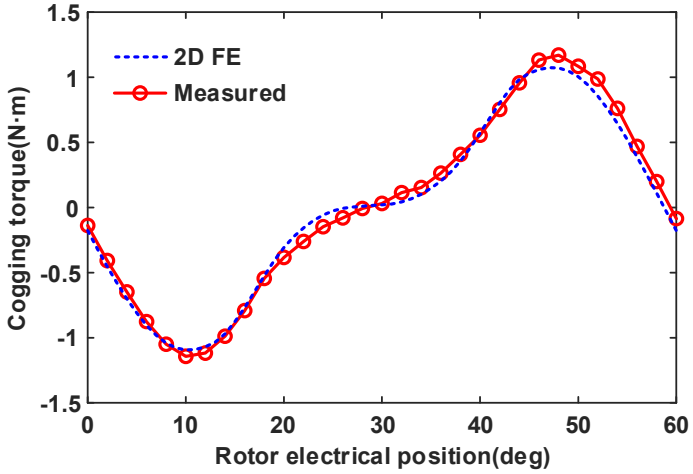

Fig. 7.4 Cogging torque obtained from the 2D FE model and measurement.

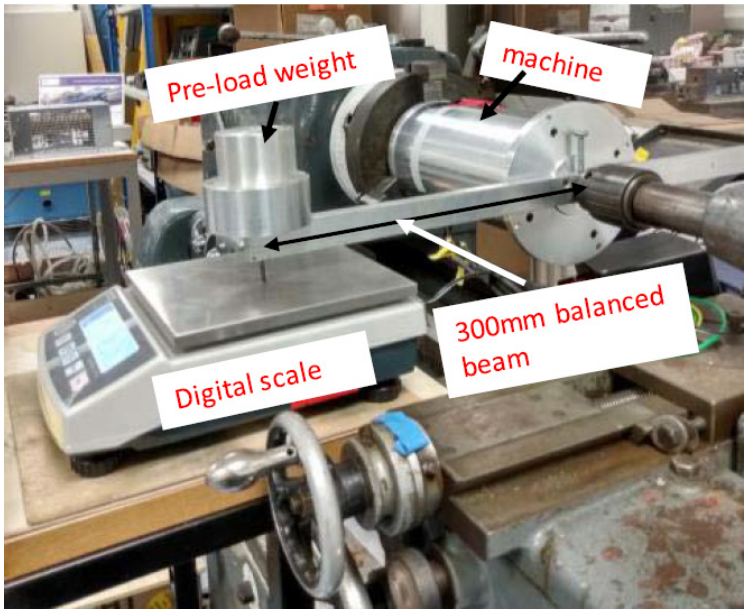

Fig. 7.5 Test setup for measuring the cogging torque [142].

It is noticed that the cogging torque of the test machine is quite large relative to the torque output capability of the driving dc machine. At low speed, it could not be overcome by the developed torque of the dc machine, and thus it prevents the test motor from spinning. The cogging torque also acts as a torque disturbance to the dc machine to cause speed variations, especially at low speed, as will be investigated in section 7.1.4.

On the other hand, to avoid the negative impact of relatively large speed variations on the back EMFs measurement, a rotor speed of 900rpm has been adopted for the simulated and measured back EMFs of A1A2 coil as shown in Fig. 7.6.

As mentioned earlier, the harmonics of the phase back EMFs, as shown in Fig. 7.6 (b), can be included into the proposed model to predict currents more accurately.

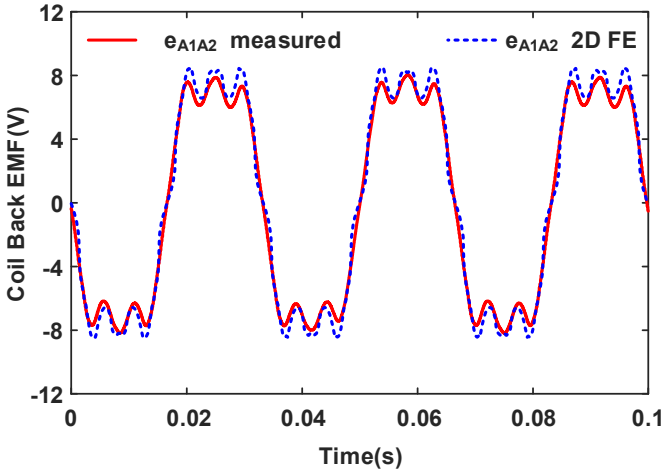

(a) Waveforms

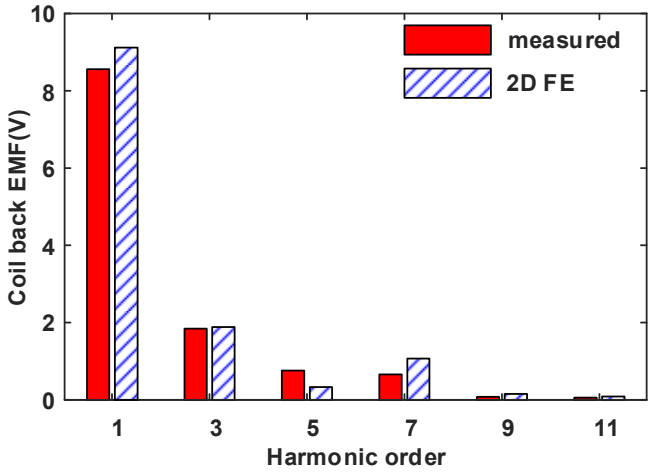

(b) Spectra

Fig. 7.6 Measured and 2D FE predicted back EMFs of A1A2 coil.

7.1.3 2D and 3D FE Inductances

The analytical method proposed in this thesis to calculate the 2D linear FE inductances under ITSC faults is applied to this 12-slot 4-pole SPM machine. To simplify the calculation of the slot-leakage inductances, the trapezoidal slot shown in Fig. 7.1 (c) is approximated to a rectangular slot with equal height and area. With this approximation, the inductances have been

calculated and results are shown in Table 7.2. It should be mentioned that all the FE inductances are average values over one electrical period. From Table 7.2, a generally good agreement between the analytical and FE results can be observed.

In addition, the effect of the core saturation on inductance values can also be observed based on the results shown in Table 7.2. It can be seen that when the core saturation is considered, the inductance values drop significantly, therefore the core saturation cannot be neglected. It is also worth noting that as the length of end-winding at each side of this small prototype is almost equal to the stack length, the end-windings cannot be neglected during the inductance calculations either. To make a direct comparison against the measured inductances using the Hioki IM3570 Impedance Analyzer, as shown in Fig. 7.7, a 3D FE model has been built (see Fig. 7.8) and the 3D FE and measured inductances are also shown in Table 7.2.

From Table 7.2, it is found that the discrepancies between the measured and 3D FE phase self- and mutual-inductances are relatively small, both of them can therefore be used in the simulations for the prediction of healthy and faulty machine performance in the following sections.

Table 7.2 Inductances in mH of the machine prototype under one coil short-circuit fault

Method	$L_{AA}/L_{BB}/L_{CC}$	$M_{AB}/M_{BC}/M_{AC}$	M_{Bf}/M_{Cf}	$M_{Ah,f}$
Analytical	1.148	-0.328	-0.164	-0.246
2D FE (Linear)	1.116	-0.3	-0.15	-0.223
Error (%)	2.9	9.3	9.3	10.3
2D FE (Nonlinear)	0.85	-0.21	-0.105	-0.08
Difference (%)	31.3	42.9	42.9	178.8
3D FE (Nonlinear)	1.323/1.321/1.319	-0.264/-0.266/-0.265	-0.126 /-0.127	-0.095
Measurement	1.418/1.461/1.419	-0.283/-0.294/-0.296	-0.153 /-0.158	-0.125
Error(%)	-6.7/-9.6/-7	-6.7/-9.5/-10.5	-17.6/ -19.6	-24

Note: the difference (%) in the fourth-from-last row is between the 2D FE (linear) and 2D FE (nonlinear)

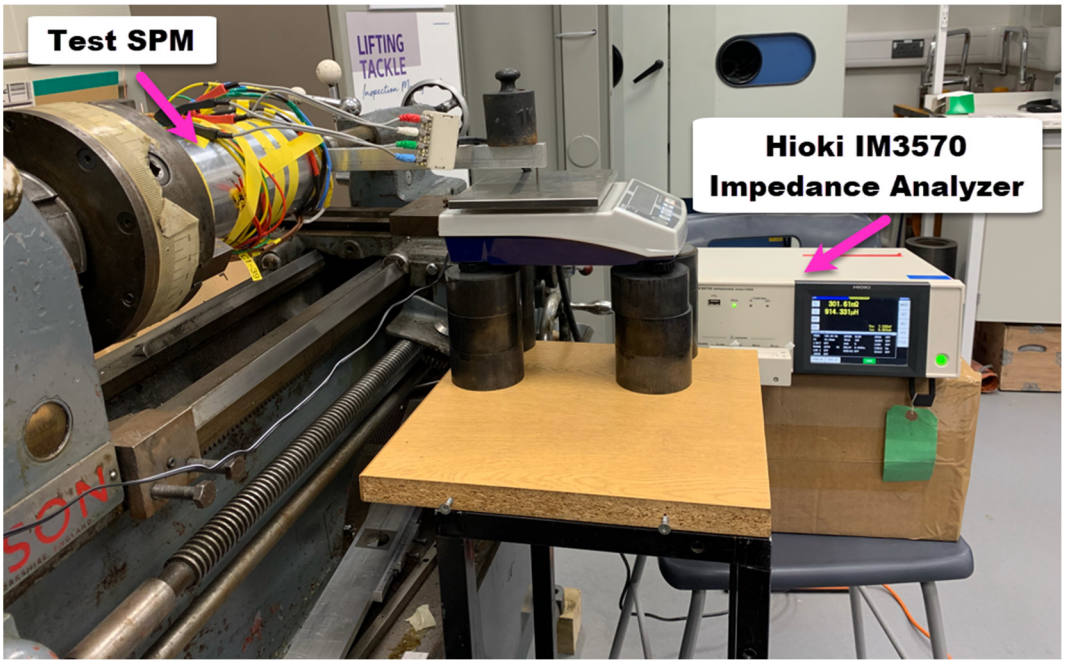

Fig. 7.7 Inductance measurement by the Hioki IM3570 Impedance Analyzer.

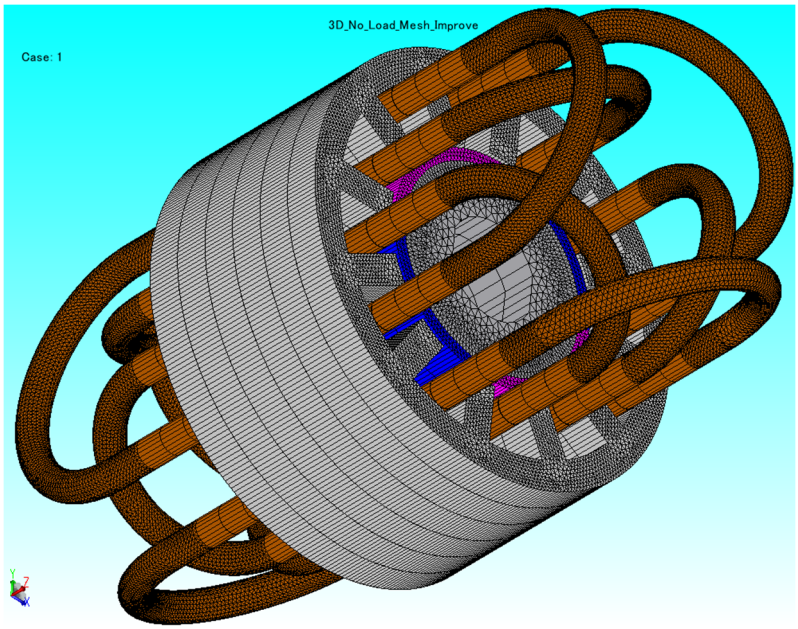

Fig. 7.8 A 3D FE model of the 12-slot 4-pole SPM machine.

In addition, it is worth mentioning that 36 data points in one electrical cycle have been recorded during the inductance measurements by the Hioki IM3570 Impedance Analyzer. The waveforms of some measured and 3D FE nonlinear inductances are shown in Fig. 7.9 and Fig. 7.10, respectively.

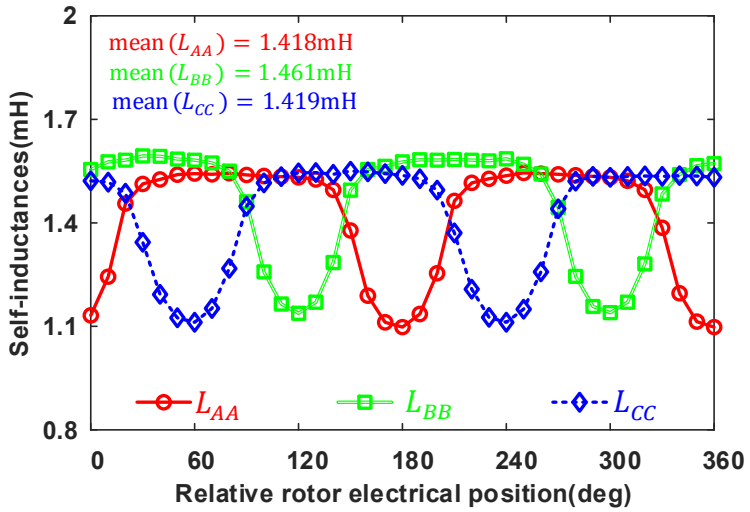

(a) Self-inductances

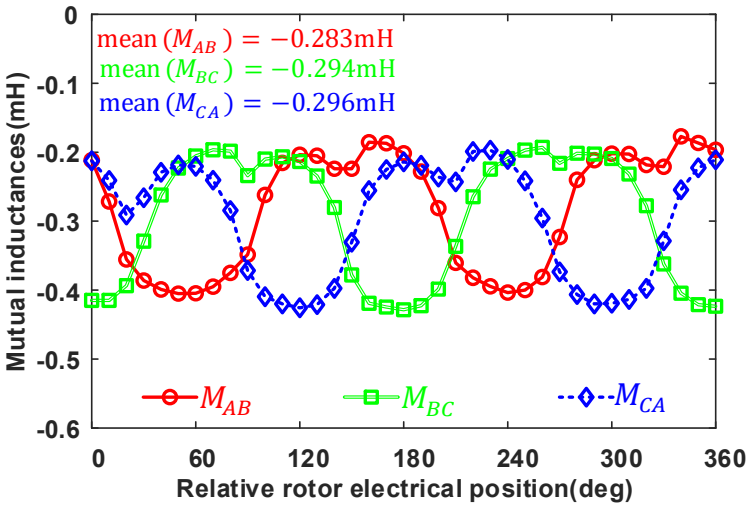

(b) Mutual inductances

Fig. 7.9 Waveforms of some measured inducances.

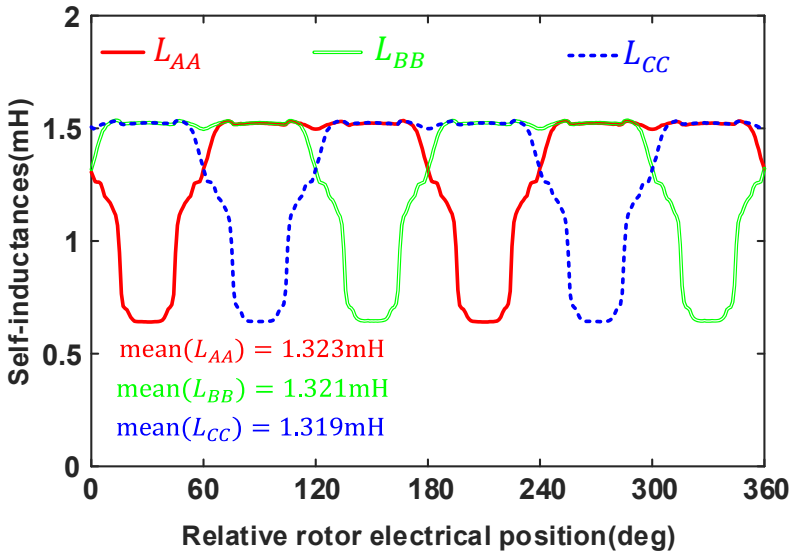

(a) Self-inductances

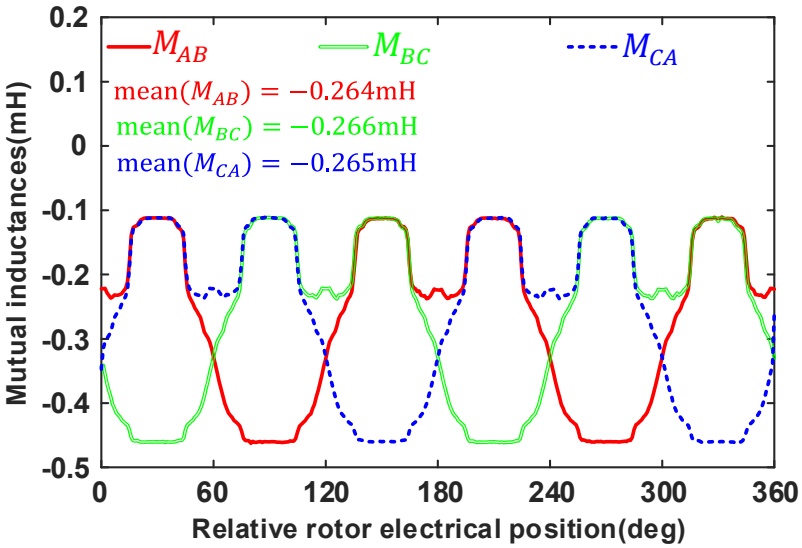

(b) Mutual inductances

Fig. 7.10 Waveforms of some 3D FE nonlinear inducances.

In Fig. 7.9 and Fig. 7.10, large fluctuations in phase self- and mutual-inductances with respect to rotor position can be observed. This is because the core saturation caused by permanent magnets is rotor position dependent, as can be seen from the inductance results shown in Fig. 7.11. Although the 2D linear inductances are rotor position independent, the 2D nonlinear inductances in Fig. 7.11 have the same variations as those shown in Fig. 7.10 (a). This is because the end-turn inductances are rotor position independent and thus can be neglected. The contour and flux line plots of the open-circuit magnetic flux density at two different rotor electrical positions $\theta_r = 30°$ and $\theta_r = 90°$ are also shown in Fig. 7.12 and Fig.

7.13. It can be easily seen that the saturations of the stator teeth and yoke are rotor position dependent.

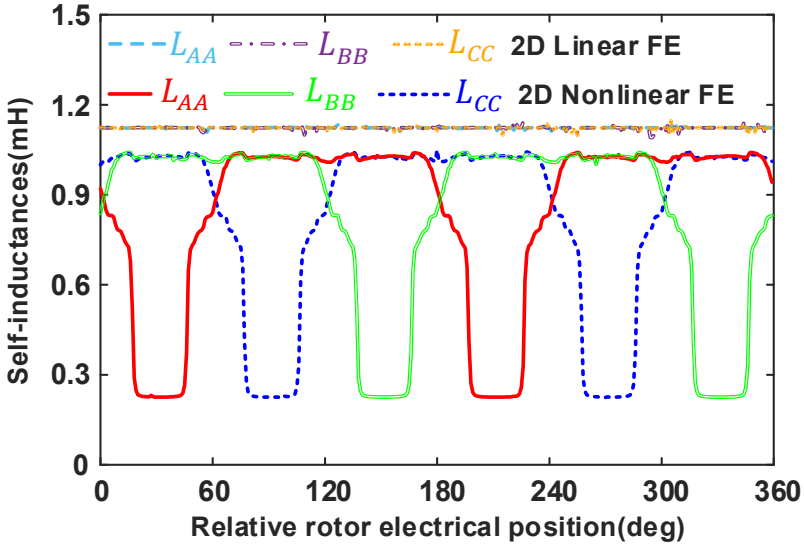

Fig. 7.11 Phase self-inductances obtained by 2D linear and nonlinear FE models.

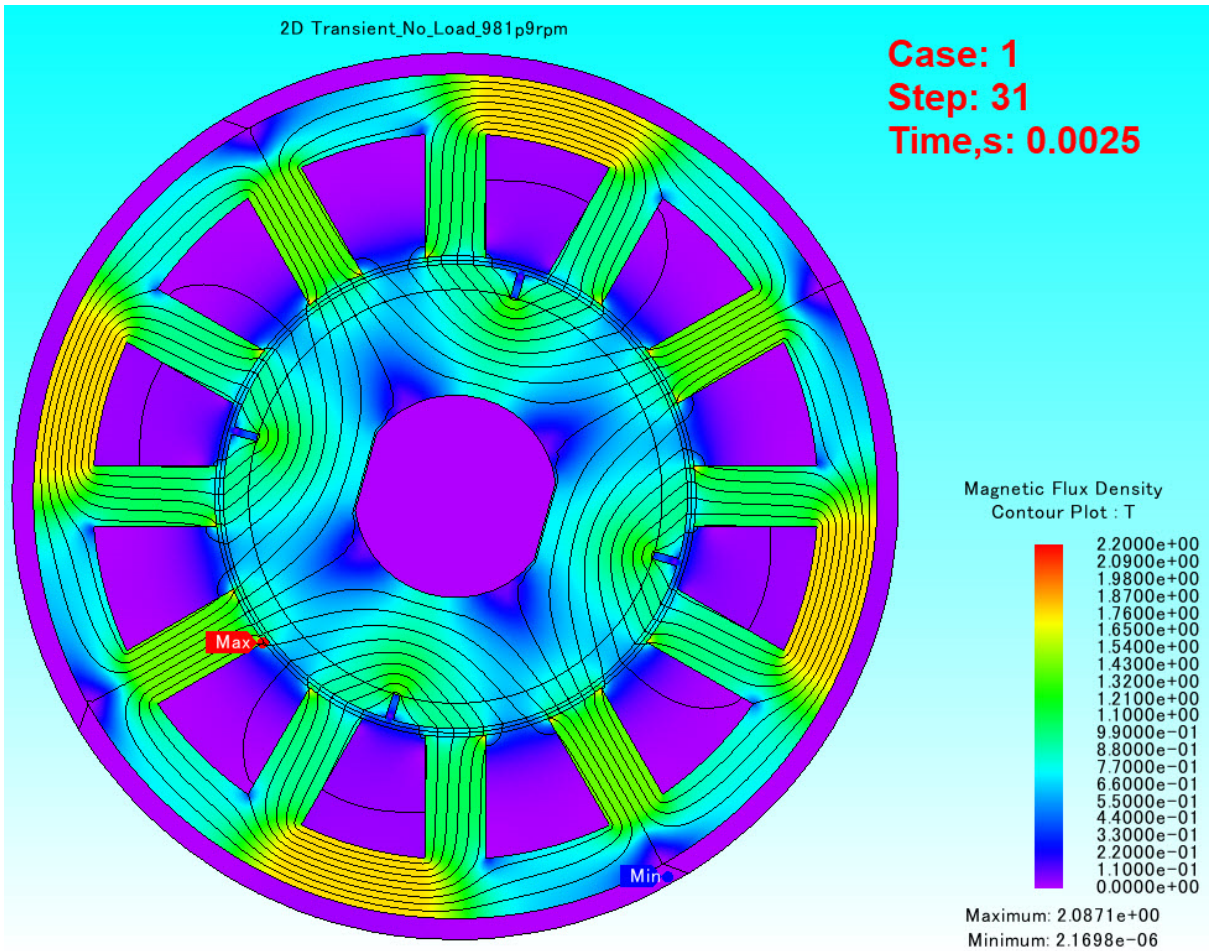

Fig. 7.12 Magnetic flux density distribution at $\theta_r = 30°$.

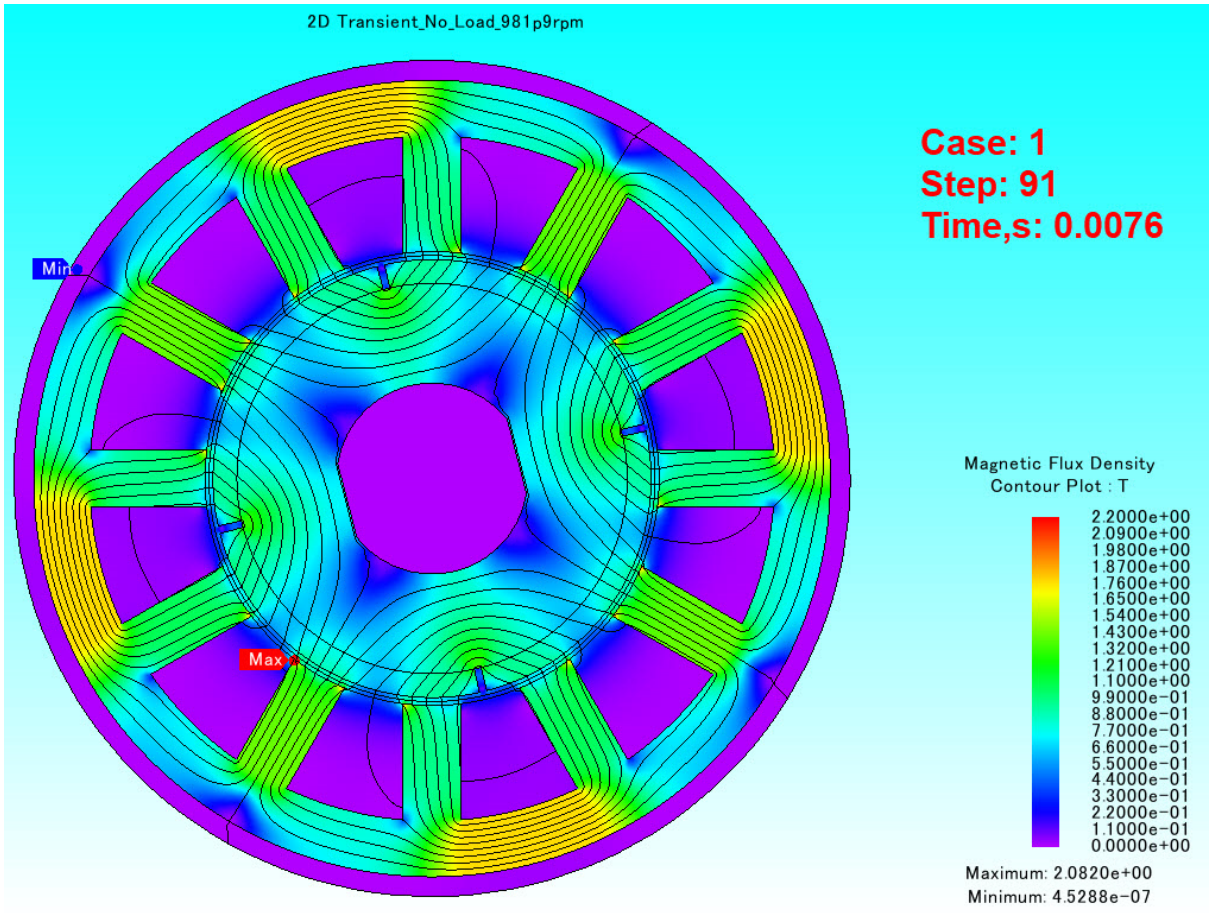

Fig. 7.13 Magnetic flux density distribution at $\theta_r = 90°$.

7.1.4 Phase and Faulty Currents

In this section, all the three fault cases including the one-coil, half-a-coil, and single-turn short-circuits have been investigated, and the measured and simulated currents have been provided and analysed.

7.1.4.1 One-Coil Short-Circuit Fault

When the one-coil short-circuit fault is introduced, a 3-phase resistive load (see Fig. 7.3) of $R_{load} = 5\Omega$ is used to limit the amplitude of the phase currents. The measured speed is obtained from the encoder, as shown in Fig. 7.14. This speed is used in the simulation to fully consider the impact of speed ripple on the predicted current waveforms. The measured and predicted phase currents and the fault current (i_{Af}) in the short-circuited coil are shown in Fig. 7.15. In Fig. 7.15 (a), it is worth noting that, as the predicted phase currents obtained by using the measured inductances and the 3D FE inductances are very much the same, to make the comparison between the measured and predicted phase currents clearer, only the predicted

phase currents using the 3D FE inductances are shown. The relative errors between the amplitudes of predicted and measured phase currents are less than 5%. However, there is a 15% relative error of the amplitudes of the predicted and measured fault currents (i_{Af}) in the short-circuited coil, as shown in Fig. 7.15 (b), where the predicted fault currents (i_{Af}) both obtained by using 3D FE inductances and measured inductances have been presented. This is mainly due to the potential measurement errors in the fault current and R_{Af}. For example, if the resistance R_{Af} is increased from 0.356Ω to 0.406Ω (a 0.05Ω increase), the relative error in the fault current will decrease from 15% to less than 5%.

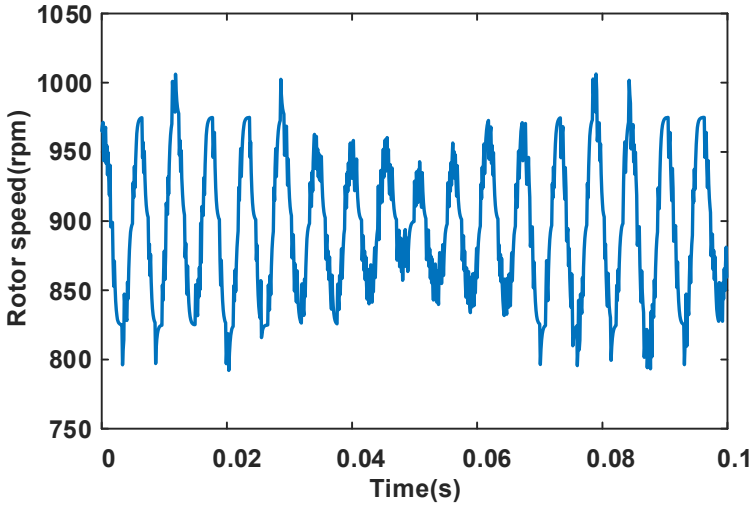

Fig. 7.14 Rotor speed under one-coil short-circuit fault.

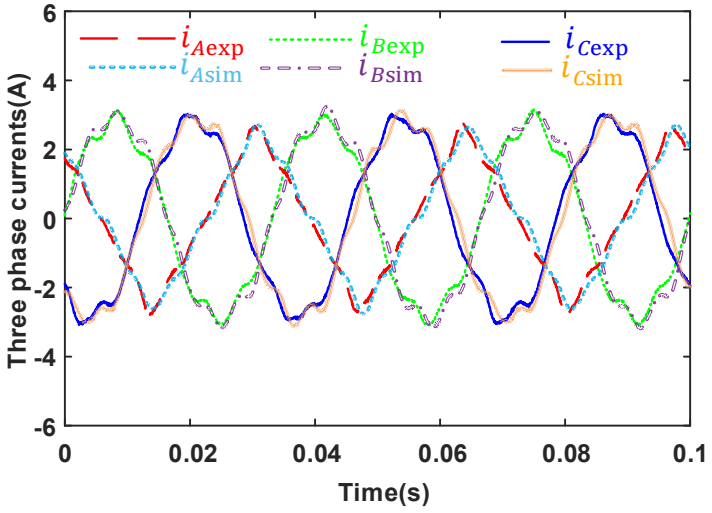

(a) Phase currents

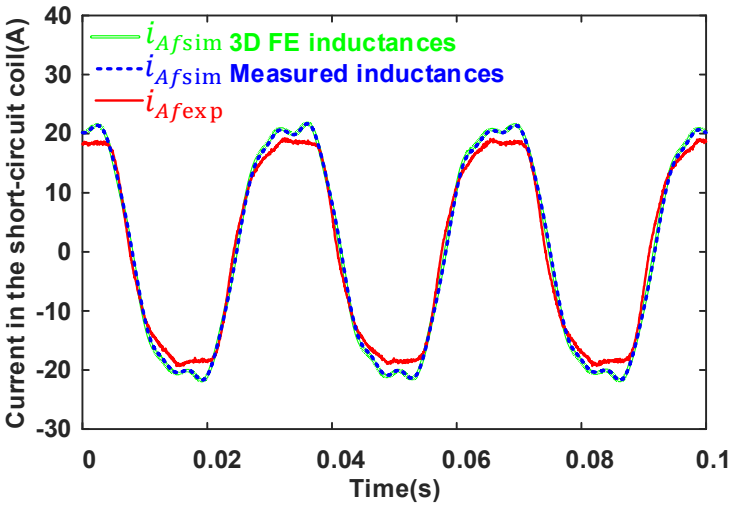

(b) Fault current (i_{Af})

Fig. 7.15 Currents under the one coil short-circuit fault.

7.1.4.2 Half-a-Coil Short-Circuit Fault

The 3-phase currents and current in the short-circuited turns are shown in Fig. 7.16. The 3-phase resistive load R_{load} (see Fig. 7.3) is also set to be 5Ω to limit the amplitude of 3-phase currents, and the tested motor starts under the half-a-coil short-circuit fault directly.

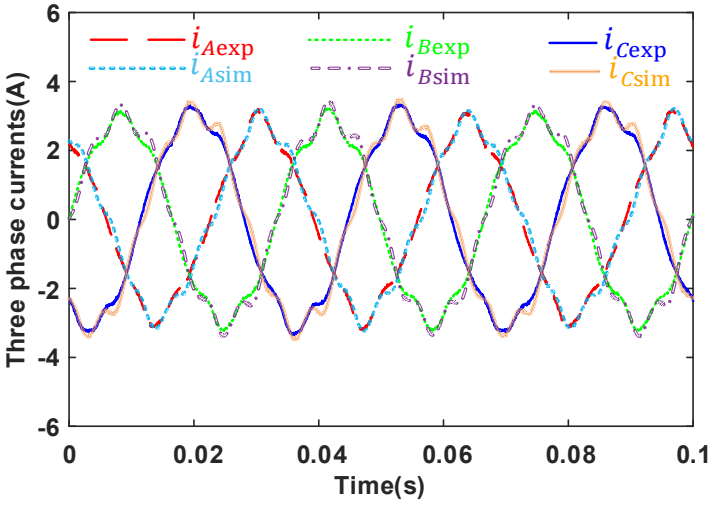

(a) Phase currents

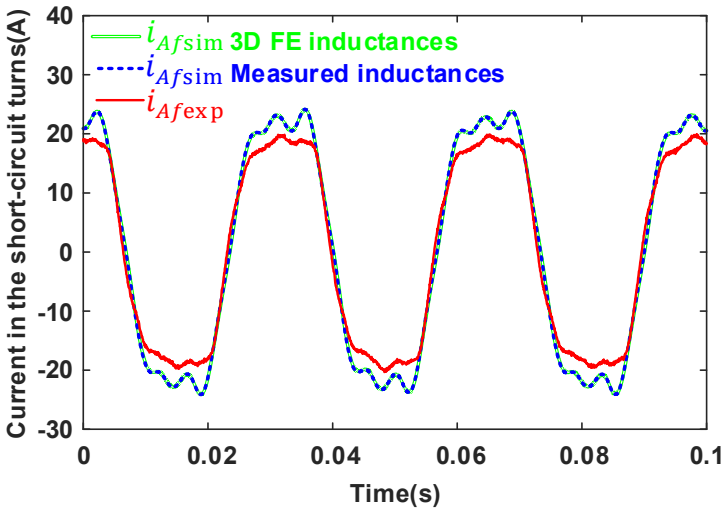

(b) Fault current (i_{Af})

Fig. 7.16 Currents under the half-a-coil short-circuit fault.

Like the one-coil short-circuit fault, the speed information is captured and loaded in the simulation to fully consider the impact of the speed ripple on the predicted current waveforms. It can be observed that the relative errors between the amplitudes of the predicted and measured phase currents are also less than 5% and the relative error of the current in the short-circuited turns is about 25%. The reason leading to this relatively large relative error of the current in the short-circuited turns is the same as those of the one-coil short-circuit current.

7.1.4.3 Single-Turn Short-Circuit Fault

In this case, the 3-phase resistive load R_{load} (see Fig. 7.3) is also set to be 5Ω, and the tested motor starts under a single-turn short-circuit fault directly. The speed profile obtained from the encoder is similar to that shown in Fig. 7.14. The corresponding phase currents and current in the short-circuited turn are shown in Fig. 7.17.

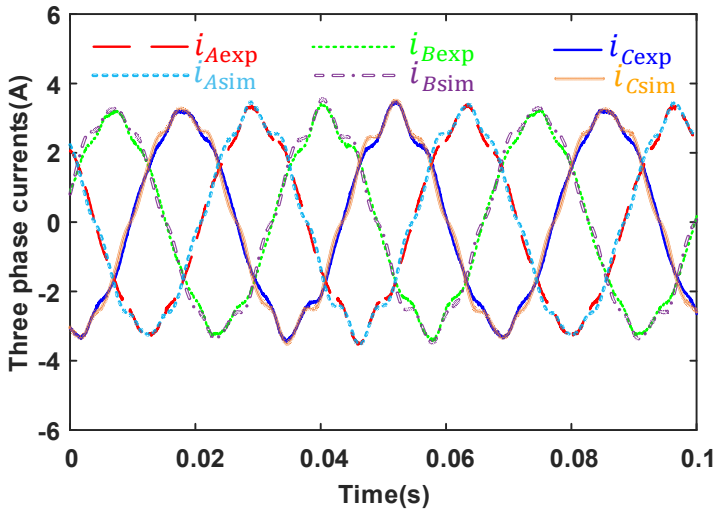

(a) Phase currents

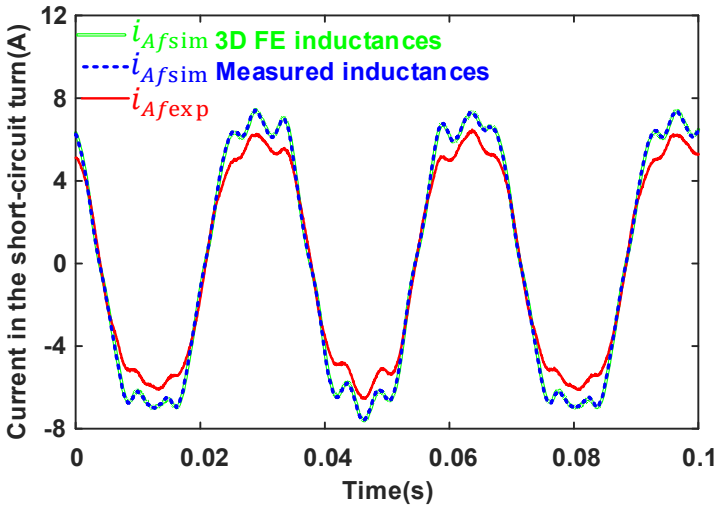

(b) Fault current (i_{Af})

Fig. 7.17 Currents under the single turn short-circuit fault.

In Fig. 7.17 (a), there is a very small difference (less than 5% difference in the current amplitudes) between the predicted and measured phase currents. However, in Fig. 7.17 (b), the difference between the fault current (i_{Af}) of the short-circuited turn is relatively larger. This difference is mainly caused by the not very accurate measurement of the single-turn resistance and by the neglected contact resistance between the connection points of the single turn when introducing the short-circuit fault. It is worth mentioning that the single turn resistance ($R_{Af} + R_f$) is only 43mΩ. Such a small value is very sensitive to any disturbance and it can be altered after introducing the short-circuit fault. For example, if R_f is increased from 35.6 mΩ to 50

mΩ (a change about 15 mΩ), then the relative error of the current in the short-circuited turn can be limited to less than 5%.

In addition, compared with the one-coil short-circuit current in Fig. 7.15 (b), the single-turn short-circuit current shown in Fig. 7.17 (b) for this machine prototype is much lower, which is opposite to those observed for the 3kW one shown in Fig. 2.11 and Fig. 2.12. This is mainly because for this 12-slot 4-pole machine, not a perfect full single-turn short-circuit fault is introduced, i.e., $R_f = 0.036\Omega \neq 0\Omega$, which is about 5 times the resistance of short-circuited turns ($R_{Af} = 0.007\Omega$). In addition, for this tested machine operating at 900rpm, the resistances are at least 2.5 times the corresponding inductive impedances. As a result, the inductive impedance in (2.15) could be neglected for simplification. This allows for an estimate of the amplitude of the fundamental component of i_f by using

$$I_f \approx \frac{\mu \omega_r \lambda_m}{\left(R_f + R_{Af}\right)} \tag{7.1}$$

For the one-coil short circuit fault, the estimated I_f is 25.6A. However, for the single-turn short circuit fault, I_f is only 5.23A. It is noticed that both the estimated I_f are slightly higher than the corresponding measured results. This is due to the slightly lower measured resistances, which cannot take the contact resistance into consideration when the two terminals are connected to introduce the ITSC fault.

7.1.4.4 Different Loads and Speeds

Further validation of the proposed model has been carried out for different load conditions (different currents and rotor speeds). The currents (peak value) in the short-circuited coil A1A2 under two different resistive loads and different rotor speeds have been measured, as shown in Fig. 7.18. Again, the measured results generally match well with the simulated ones using the measured inductances, further proving the accuracy of the proposed fault model under various operating conditions.

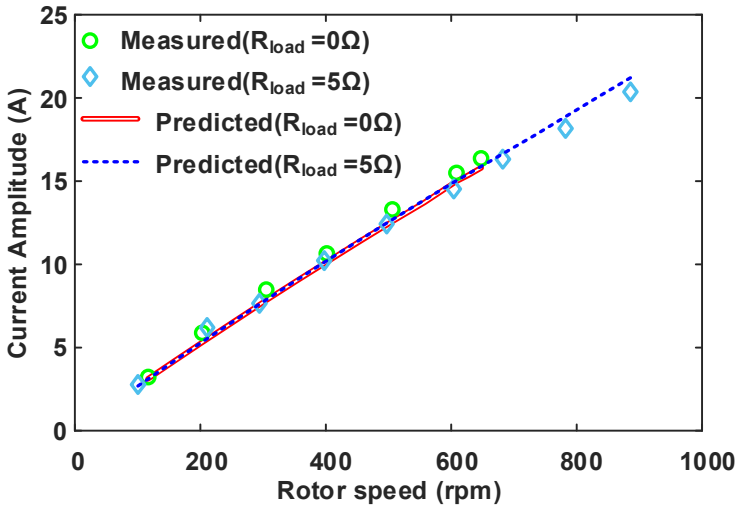

Fig. 7.18 Amplitudes of currents of the short-circuited coil under different resistive loads and speeds.

7.2 Model Validation for Parallel-Connected Coils

7.2.1 Prototype and Test Rig

Considering that the 12-slot 4-pole SPM machine only has two parallel branches in each phase and all the coils of the prototype machine can be connected outside of the machine housing, it can also be used for model validation for parallel-connected coils. In addition, the branch currents in all phases can be measured outside of the machine housing. The test rig shown in Fig. 7.19 is similar to that shown in Fig. 7.2, except that the number of current probes now is increased from 3 to 6 to measure 5 branch currents and the current (i_f) in the external short-circuit path, shown in Fig. 7.20. Similarly, using this prototype machine, three fault scenarios can be carried out: one-coil, half-a-coil, and single-turn short-circuit faults. In addition, all the faults are introduced in the A1 coil. As the main purpose of the experiments is to validate the proposed fault model, the SPM machine will also be used as a generator driven by a dc machine, and its 3-phase terminals are connected to an adjustable 3-phase resistive load bank, as shown in Fig. 7.20. In this way, no inverter is required to drive the SPM machine, avoiding the necessity of complicated control schemes.

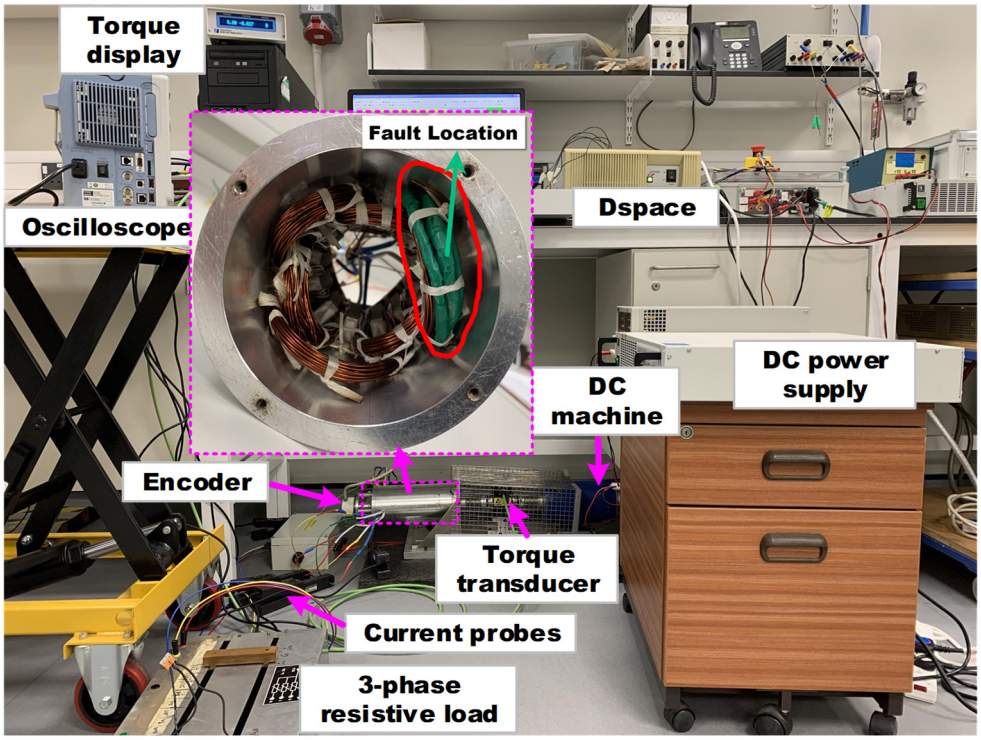

Fig. 7.19 Test rig.

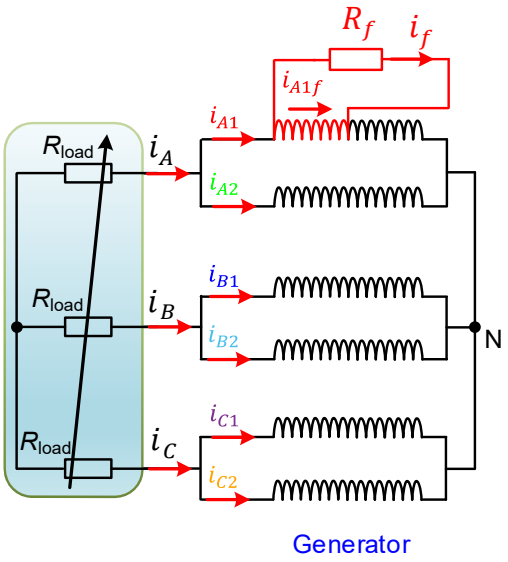

Fig. 7.20 Circuit schematic with the introduced ITSC fault.

7.2.2 Inductances

The analytical method for inductance calculation developed in chapter 3 has also been applied to this 12-slot 4-pole SPM machine. Some representative results have been provided

in Table 7.3, where all the FE inductances in Table 7.3 are average values over one electrical period.

Table 7.3 Inductances related to the A1 coil in mH

Method	L_{A1A1}	M_{A1A2}	M_{A1B1}	M_{A1B2}
Analytical	0.82	-0.246	0.082	-0.246
2D FE (Linear)	0.78	-0.224	0.074	-0.224
Difference (%)	5.1	9.8	10.8	9.8
2D FE (Nonlinear)	0.508	-0.08	0.0075	-0.112
Difference (%)	53.5	180	886.7	100
Method	L_{A1A1}	L_{C1C1}	M_{A1B1}	M_{A1C2}
3D FE (Nonlinear)	0.821	0.823	0.0063	0.0063
Measured	0.857	0.856	0.0192	0.0237
Difference (%)	-4.2	-3.8	-67.2	-73.4

Note: the difference (%) in the fifth-from-last row is between the 2D FE (linear) and 2D FE (nonlinear).

A generally good agreement can be observed between the analytical and 2D linear FE results. However, it is found that the length of the end windings at each side of this small prototype machine is almost equal to the stack length. This means that the influence of the end windings on inductance values cannot be neglected. Meanwhile, the core saturation also has a significant impact on the inductance values, which has been shown in Table 7.3, making the inductances much smaller.

In order to obtain more accurate inductance results, a 3D FE model shown in Fig. 7.8 can be utilized. The obtained 3D FE nonlinear inductances are compared against the measured ones by using the Hioki IM3570 Impedance Analyzer, and some of the values are also shown in Table 7.3. The corresponding waveforms are shown in Fig. 7.21 and Fig. 7.22, respectively.

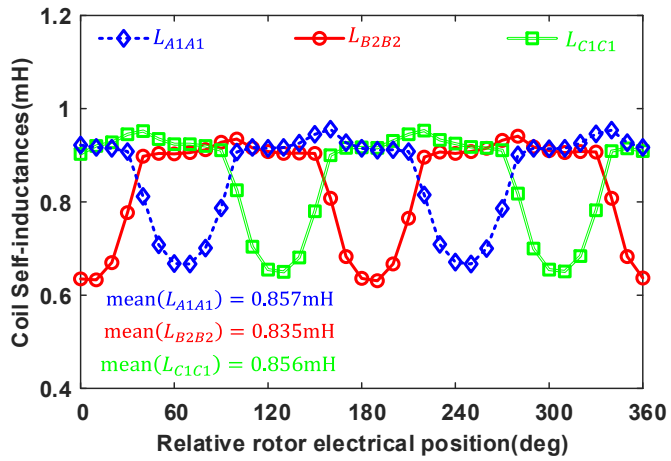

(a) Self-inductances

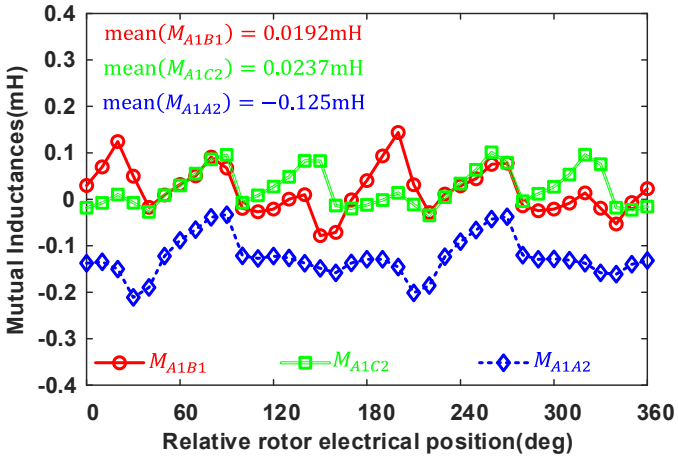

(b) Mutual inductances

Fig. 7.21 Waveforms of some measured inductances.

It can be observed from Table 7.3 that most of the relative errors between the 3D FE nonlinear and measured inductances are generally within an acceptable range. However, the relative error of M_{A1B1} exceeds 50%. This is mainly because the absolute value of M_{A1B1} is very small, so the measured value may not be reliable due to potential measurement errors.

In addition, due to its very small value, its impact on machine performance prediction can be negligible, as will be investigated in the following section. As for the 3D FE nonlinear inductances related to the short-circuited turns, they can be estimated by using the inductances related to the coil A1.

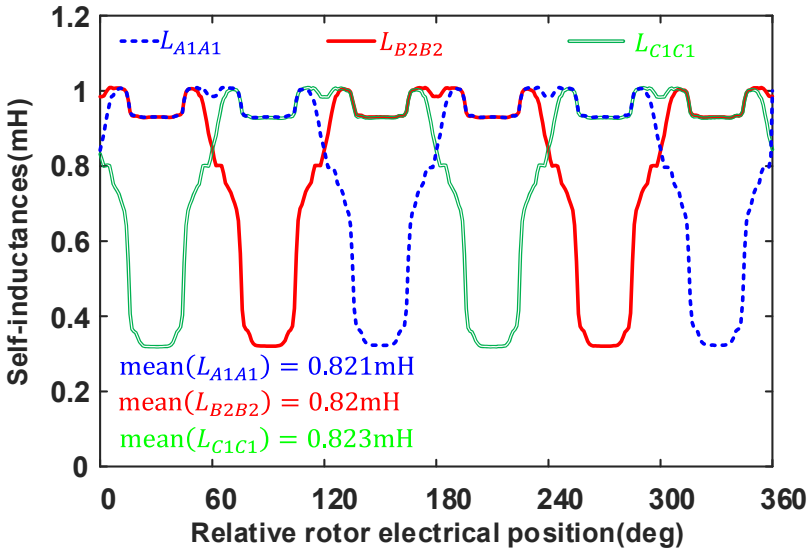

(a) Self-inductances

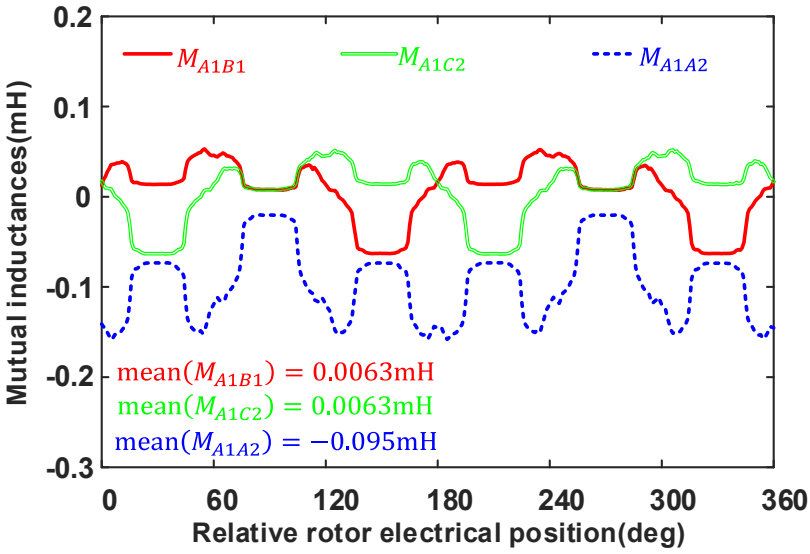

(b) Mutual inductances

Fig. 7.22 Waveforms of some 3D FE nonlinear inductances.

7.2.3 Branch and Faulty Currents

In this section, all the three fault cases including the single-turn, half-a-coil, and one-coil short-circuit faults have been investigated, and the measured and simulated currents have been provided and analysed. It should be mentioned that all the three fault scenarios have been carried out under different speeds and loads to validate the proposed fault model, and the measured and simulated results generally match well.

In addition, it is worth mentioning that for this machine, the cogging torque is quite large and its amplitude is comparable to the rated torque. As a result, the cogging torque causes large speed ripples and could prevent the machine from spinning at low speed. One example is that when the machine is rotating at 900rpm, the maximum speed ripple is about 200rpm (22%). This is why the position encoder (see Fig. 7.19) is required to capture the speed ripples accurately so that the predicted current profiles will be closer to the measured ones.

7.2.3.1 One-Coil Short-Circuit Fault

Under the one-coil short-circuit fault, due to the relatively low load capability of the dc machine, limited power rating of the dc power supply, and large cogging torque of the tested machine prototype, the average rotor speed cannot reach 900rpm to reduce the influence of the speed ripple on the current profiles. The speed information captured by the position encoder is shown as Fig. 7.23 when the voltage applied to the armature winding of the dc machine reaches the maximum value (60V). The recorded speed information will then be loaded into the Simulink model to obtain the simulated current waveforms. In addition, the 3-phase resistive load R_{load} (see Fig. 7.20) is set to be 1.2Ω to limit the amplitude of branch currents to safe values.

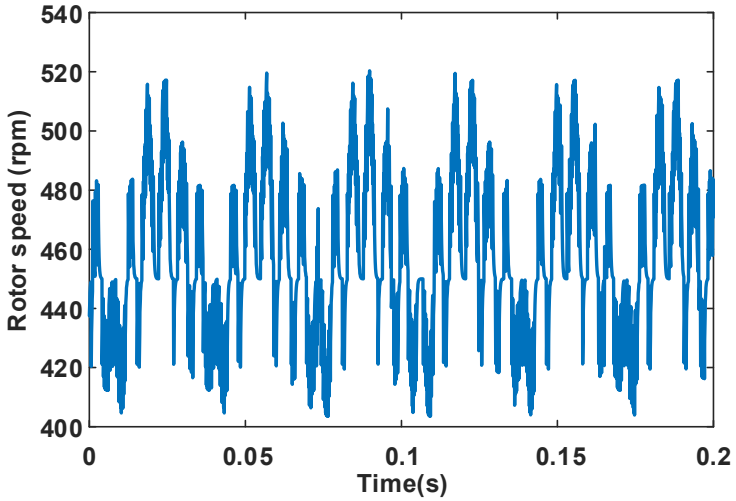

Fig. 7.23 Rotor speed under the one-coil short-circuit fault.

The measured and simulated branch currents are shown in Fig. 7.24. Generally, the relative errors of the amplitudes of measured and simulated branch currents are less than 10%. It is worth mentioning that the predicted branch and phase currents by using the 3D FE and measured inductances in the fault model are almost the same. Therefore, only the predicted results using the measured inductances have been provided in Fig. 7.24 and Fig. 7.25.

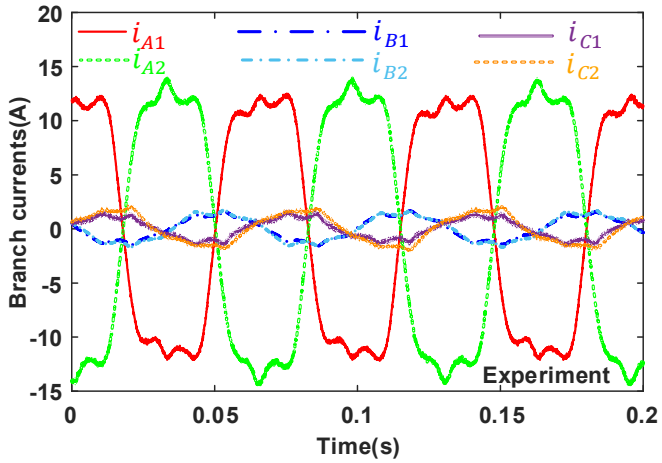

(a) Measured branch currents

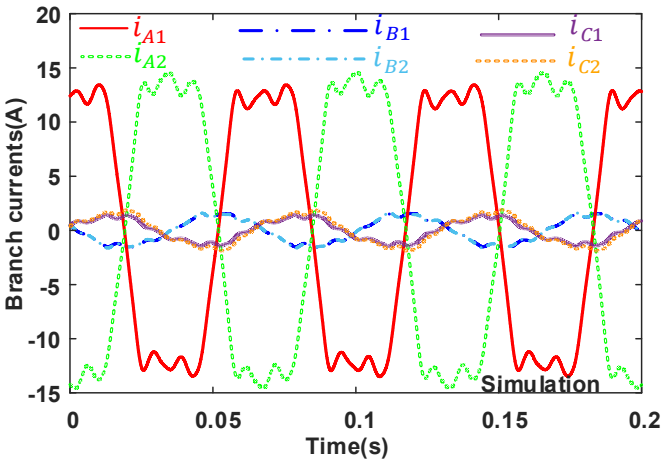

(b) Predicted branch currents

Fig. 7.24 Branch currents under the one-coil short-circuit fault.

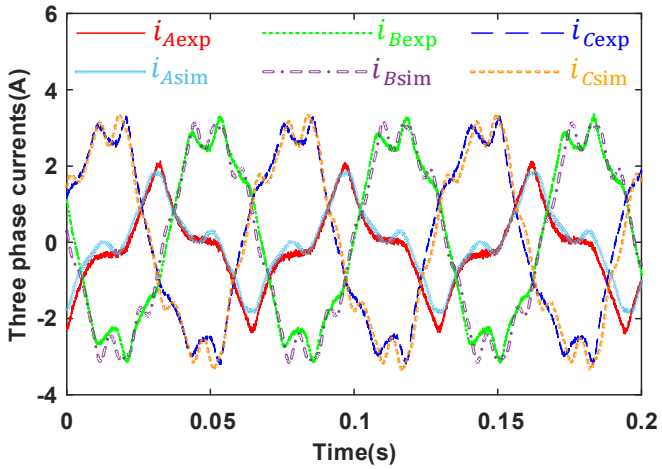

Fig. 7.25 Measured and predicted 3-phase currents under the one-coil short-circuit fault.

As the one-coil short-circuit fault is equivalent to the one-phase short-circuit fault for this SPM machine, the increase in the amplitudes of the branch currents in the shorted branches A1 and A2 are almost the same, if the influence of asymmetric windings on the model parameters such as resistances and inductances is neglected. In addition, it seems that the branch currents in other remaining healthy phases are not greatly affected.

Furthermore, the predicted fault current i_{A1f} in the short-circuited coil (using both 3D FE and measured inductances) has also been shown in Fig. 7.26 together with the measured i_{A1f}. It can be seen that even at this low speed, the fault current i_{A1f} in the short-circuited coil is still about 3 times the rated current, meaning that the windings may be burnt out in a very short time if timely detection is not adopted.

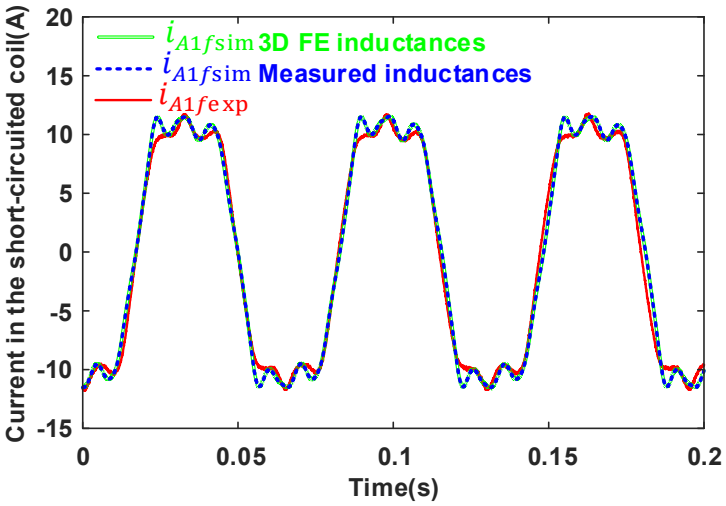

Fig. 7.26 Predicted and measured fault currents (i_{A1f}) in the short-circuited coil.

7.2.3.2 Half-a-Coil Short-Circuit Fault

A 3-phase resistive load of $R_{load} = 1.2\Omega$ is connected to the 3-phase terminals of this prototype machine to limit the amplitude of the branch and phase currents when the half-a-coil short-circuit fault is introduced. The speed and current data have been collected when the average speed of the prototype machine is about 900rpm. This relatively high speed is chosen in order to reduce the impact of speed ripple on the current predictions. At the same time, the branch currents and phase currents are shown in Fig. 7.27 and Fig. 7.28, respectively.

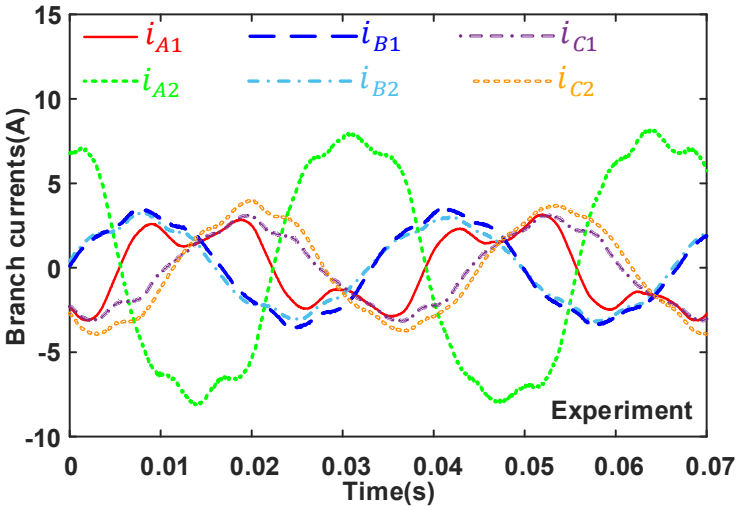

(a) Measured branch currents

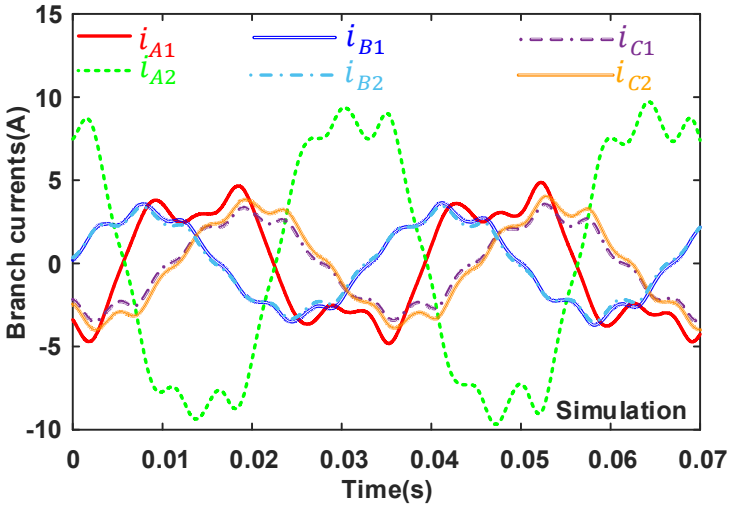

(b) Predicted branch currents

Fig. 7.27 Branch currents under the half-a-coil short-circuit fault.

It is also worth mentioning that the predicted branch and phase currents by using the 3D FE and measured inductances in the fault model are almost the same. Therefore, only the predicted results using the measured inductances have been provided in Fig. 7.27 and Fig. 7.28. It can be seen from Fig. 7.27 that the measured and predicted branch currents match well (the relative errors of the corresponding amplitudes are less than 10%), this is the same for the measured and predicted three phase currents as shown in Fig. 7.28.

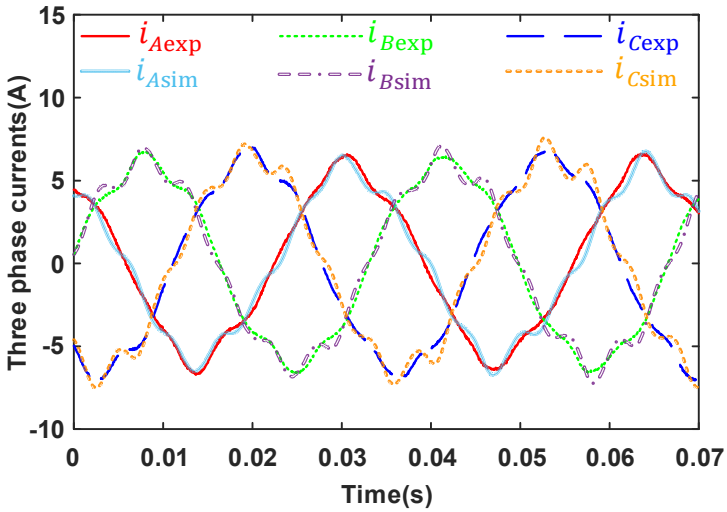

Fig. 7.28 Measured and predicted 3-phase currents under half-a-coil short-circuit fault.

Unlike the one-coil short-circuit fault, the detection of the fault by making full use of 3-phase currents is not easy. The amplitude of the phase A current (6.6A) is only slightly smaller than those of the other two remaining healthy phases (7A for phase B and 7.4A for phase C respectively), as shown in Fig. 7.28. In addition, the fault current i_{A1f} in the short-circuited turns as shown in Fig. 7.29 is about 5.6 times the rated current, meaning that the windings may be burnt out in a very short time if timely detection is not adopted. Again, the predicted i_{A1f} using the 3D FE and measured inductances in Fig. 7.29 match very well, although both are slightly larger than the measured i_{A1f}, which may be due to measurement errors as explained for series-connected windings.

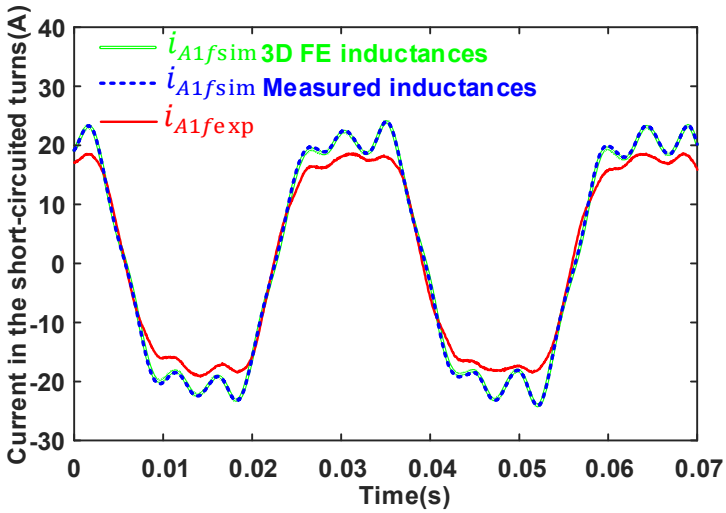

Fig. 7.29 Predicted and measured fault currents (i_{A1f}) in the short-circuited turns.

7.2.3.3 Single-turn Short-Circuit Fault

The single-turn short-circuit fault with a 3-phase resistive load of $R_{load} = 1.2\Omega$ has also been carried out using the same test rig. The speed and current data have been collected when the average speed of the prototype machine is also about 900rpm. As mentioned earlier, this relatively high speed is chosen in order to reduce the impact of speed ripple on the current predictions. Meanwhile, a relatively large short-circuit current will be generated. It should be mentioned that the measured values of some very small inductances are not reliable, and they are estimated based on the measured inductances related to one coil. In this way, the predicted branch and phase currents by using the 3D FE and measured inductances in the fault model are almost the same. The corresponding branch currents and phase currents are shown in Fig. 7.30 and Fig. 7.31, respectively.

Although 1 out of 40 turns has been short-circuited, the changes in the branch currents and phase currents are very minor, making it difficult to detect this fault. In addition, compared with the half-a-coil short-circuit current in Fig. 7.29, the single-turn short-circuit current shown in Fig. 7.32 is much smaller. This is mainly because for this 12-slot 4-pole machine, not a perfect full single-turn short-circuit fault is introduced, i.e., $R_f = 0.036\Omega \neq 0\Omega$, which is about 5 times the resistance of the short-circuited turns ($R_{Af} = 0.007\Omega$).

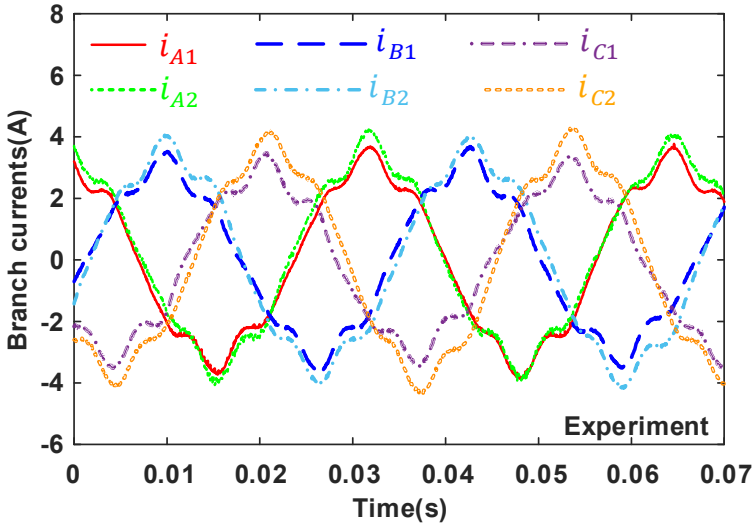

(a) Measured branch currents

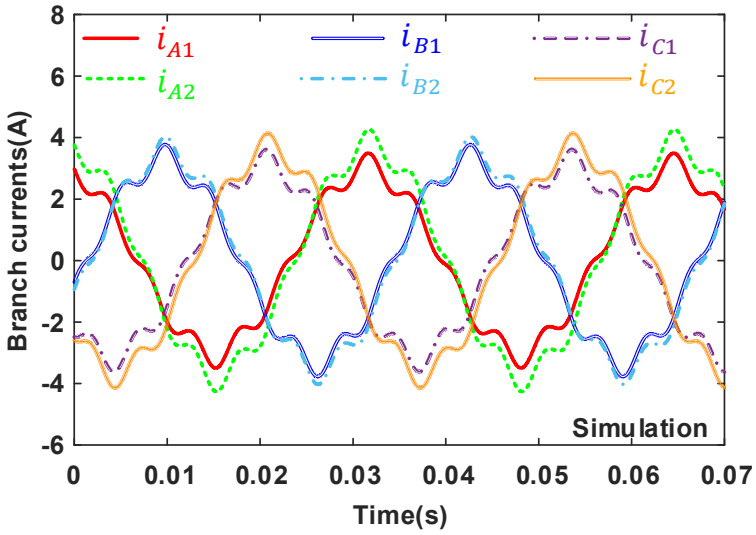

(b) Predicted branch currents

Fig. 7.30 Branch currents under the single-turn short-circuit fault.

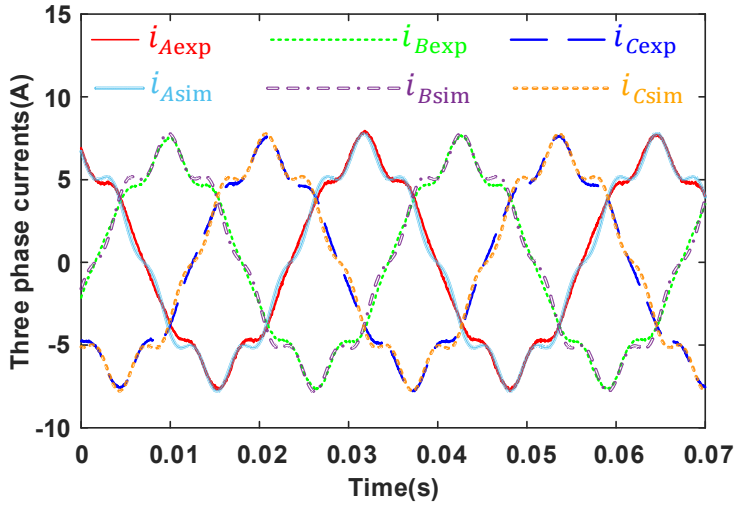

Fig. 7.31 Measured and predicted 3-phase currents under the single-turn short-circuit fault.

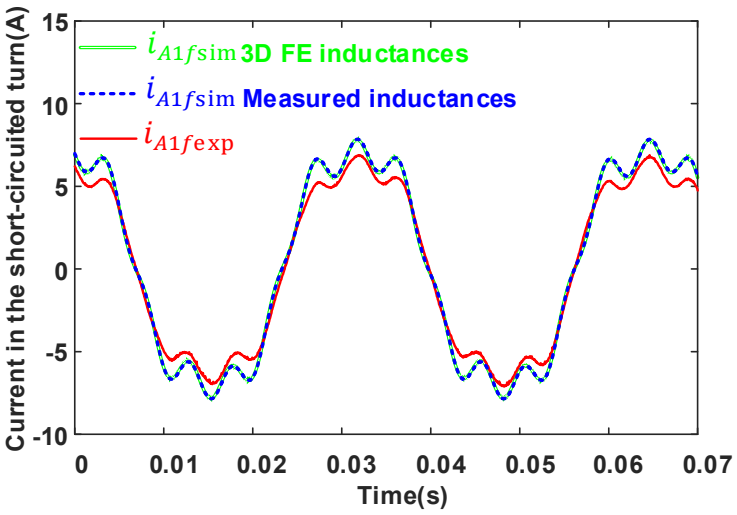

Fig. 7.32 Predicted and measured fault currents (i_{A1f}) in the short-circuited single turn.

7.2.3.4 Different Loads and Speeds

For completeness of the model verification, further tests with different loads and speeds under the one-coil short-circuited fault have also been carried out, the results of which are shown in Fig. 7.33. It can be seen that the currents (peak value) in the short-circuited coil A1 and faulty phase A with two different resistive loads and different rotor speeds from the measurement and simulation match well. Therefore, it can be concluded that the developed fault model is accurate in predicting the ITSC fault behaviours of the SPM machines.

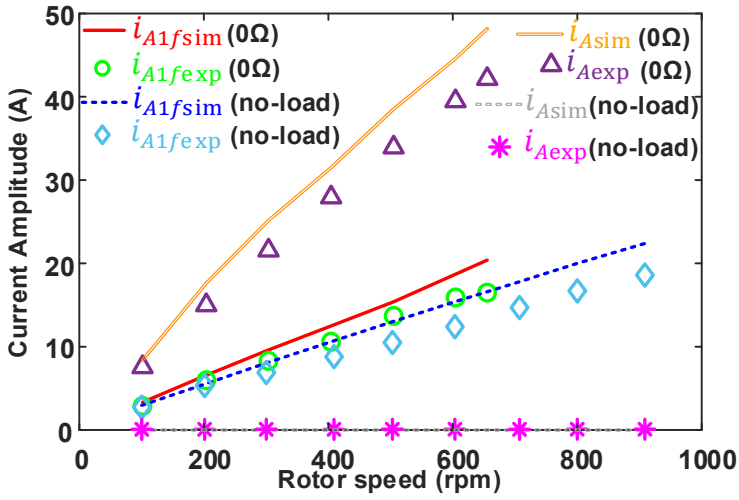

Fig. 7.33 Amplitudes of current of short-circuited coil and faulty phase under different resistive loads and speeds.

7.3 Model Validation for Series-Parallel-Connected Coils

As the 12-slot 4-pole prototype only has 2 coils per phase, it is impossible to realise a machine with a series-parallel coil connection, which requires at least 4 coils per phase. In this case, a second prototype, a small-scale 24-slot 8-pole SPM machine, has been manufactured to validate the proposed fault model for the SPM machines with series-parallel connected coils. A series of experiments on this machine prototype have been carried out.

7.3.1 Test rig setup

The main parameters of this machine prototype are listed in Table 7.4. This prototype has a single-layer, full-pitch, and distributed winding structure, as shown in Fig. 7.34. Each phase will have 4 coils in total. To achieve a series-parallel coil connection, each phase winding will have 2 parallel branches and each branch has 2 coils connected in series. In addition, Fig. 7.35 shows the coil where the ITSC faults are introduced and Fig. 7.36 shows the stator and rotor of the 24-slot 8-pole SPM prototype machine.

Table 7.4 Specifications of the 24-slot 8-pole SPM prototype machine

Rated torque (Nm)	1.09	Stator outer diameter (mm)	100
Rated current rms (A)	2.5	Rotor outer diameter (mm)	49
Series turns/coil	20	Air gap length (mm)	1
Slots/poles	24/8	Stack length (mm)	50

It is worth mentioning that three fault scenarios (single-turn, half-a-coil, and one-coil short-circuit faults) have been designed and can be carried out outside of the machine housing. All these faults have been introduced in the A11 coil shown in Fig. 7.34.

On the other hand, the associated circuit schematic is illustrated in Fig. 7.37, in which each branch has two coils connected in series. As for the any two integers below a coil symbol in Fig. 7.37, they indicate the numbering of the two slots where the two coil sides of that coil are lodged.

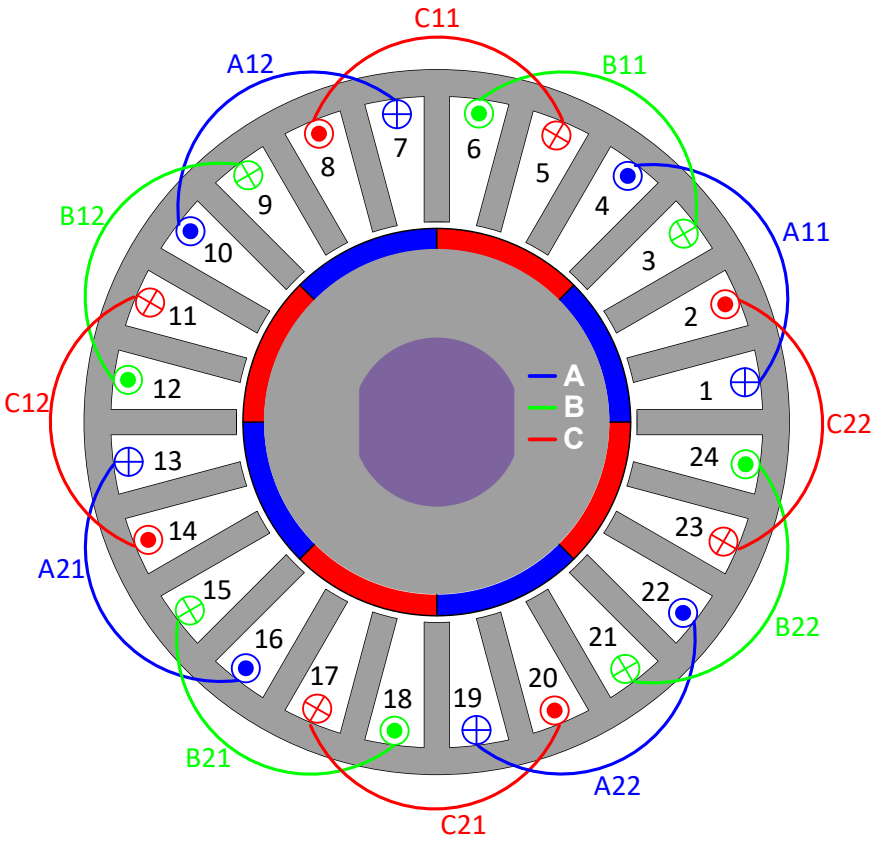

Fig. 7.34 The winding layout of the 24-slot 8-pole SPM machine.

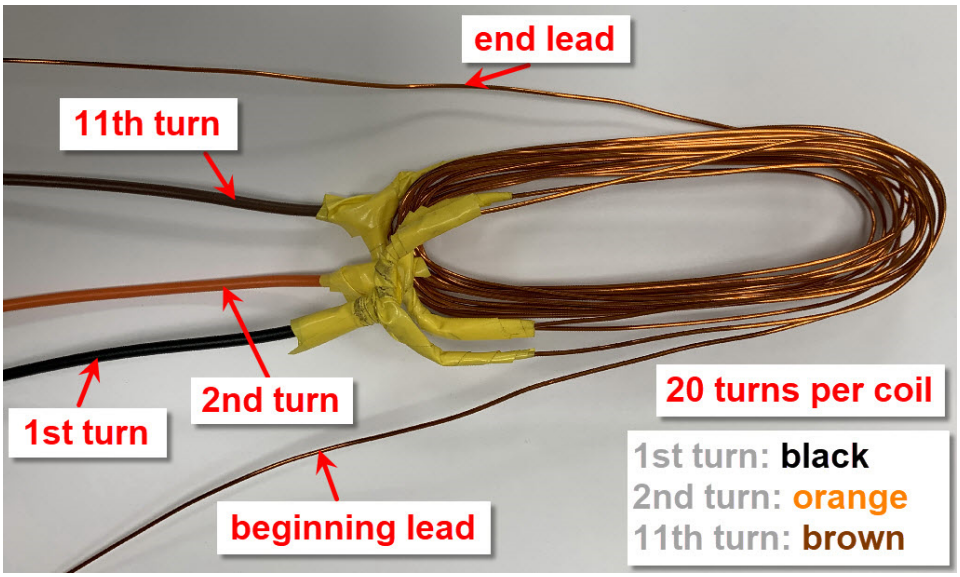

Fig. 7.35 The coil where the ITSC faults are introduced.

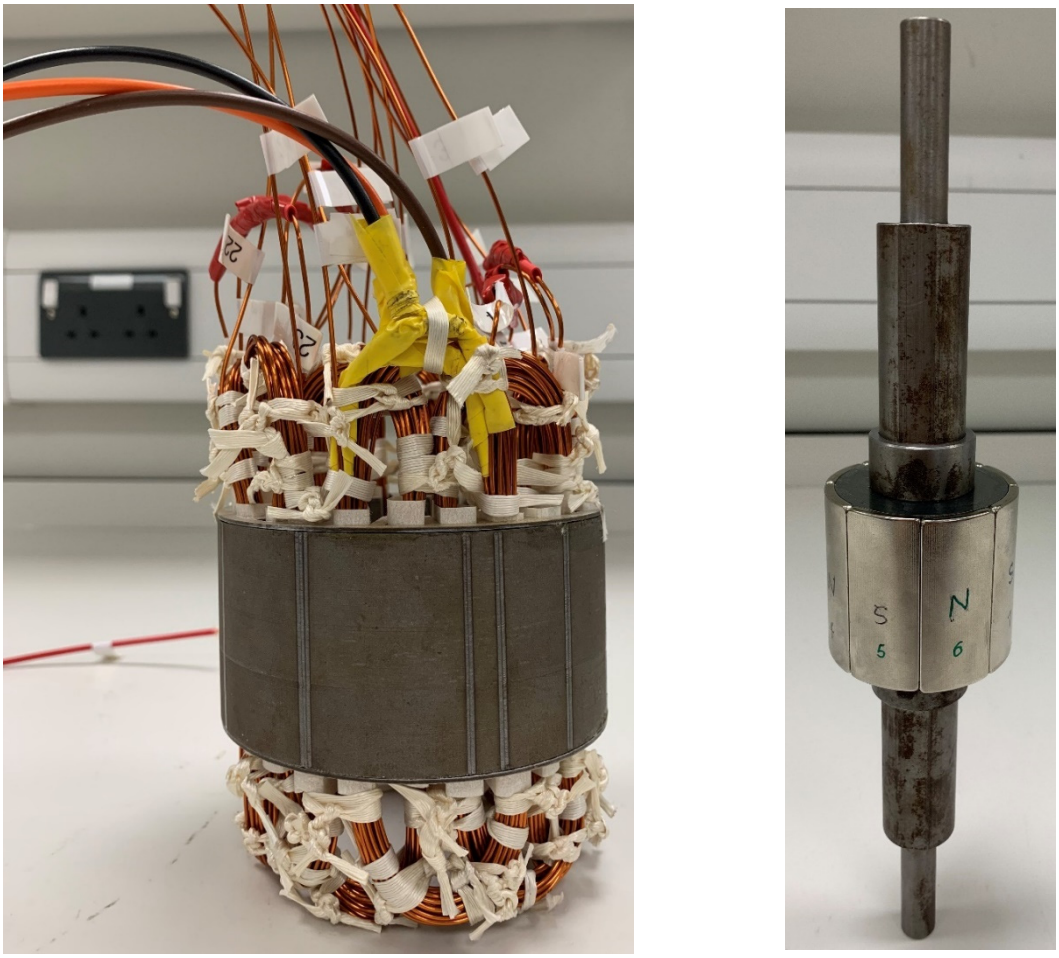

(a) Stator (b) Rotor

Fig. 7.36 Stator and rotor of the 24-slot 8-pole SPM machine.

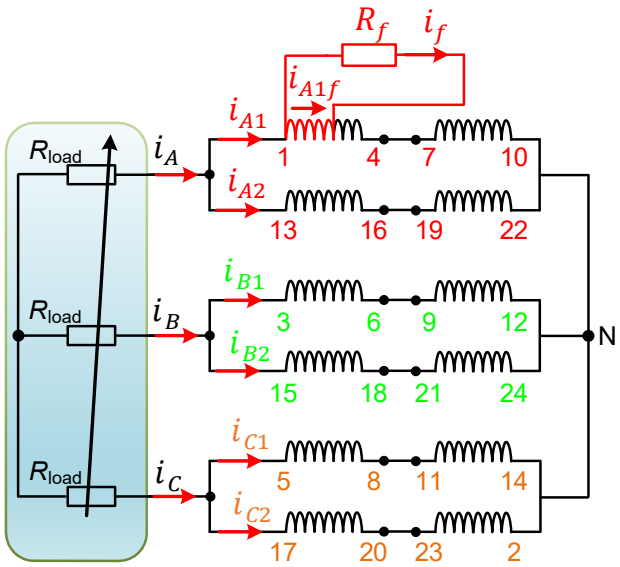

Fig. 7.37 Circuit schematic showing the introduced ITSC fault.

After the machine is assembled, it is put on the test rig shown in Fig. 7.38. Because the main purpose of the experiments is to validate the proposed fault model, the SPM machine is also used as a generator driven by a dc machine and its 3-phase terminals are connected to a 3-phase rheostat. In this way, the hardware implementation of the fault experiments becomes much simpler and the main purpose of fault model validation by experimentation can still be achieved.

On the other hand, it is found that it is sufficient to use the Magtrol Model 3411 torque display instead of a position encoder to record the speed information, which is an input to the analytical model built in Matlab/Simulink. This is because the 2.2kW dc machine has a good torque-speed characteristic to reduce the speed ripple caused by the 150W 24-slot 8-pole SPM machine prototype, which acts as its load.

It is also worth mentioning that, to measure the branch currents and current i_f in the external short-circuit path using current probes outside of the machine, the lead wires of the prototype have been made a little longer on purpose and thus the series-parallel coil connections can be easily accomplished outside of the machine housing.

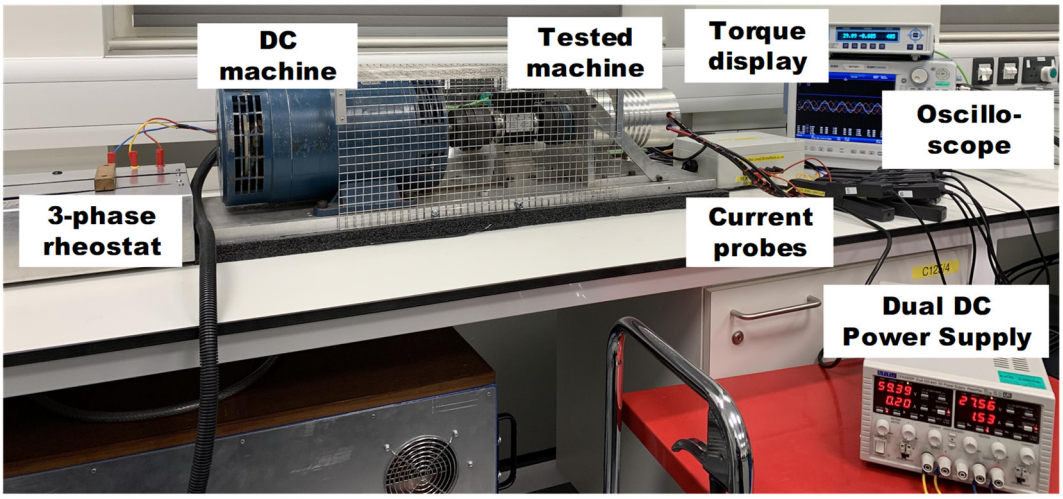

Fig. 7.38 Test rig setup on the desk.

7.3.2 Cogging Torque and Back-EMFs

Although cogging torque needs to be included in the analytical model built in Matlab/Simulink to predict the torque ripple more accurately, the measured values using the same method in [147] were not accurate and thus the results were not used for the simulations. This is because this method assumes that the rotor is stationary when rotating the stator to a fixed angle to measure the cogging torque. However, an imperceptible rotation of the rotor will make the measured values not reliable when the fastening of the rotor shaft outside of the

machine housing by a specially designed bolt shown in Fig. 7.7 cannot be secured. As a result, the cogging torque predicted by the 2D FE model as shown in Fig. 7.39 will be used in the Matlab/Simulink model.

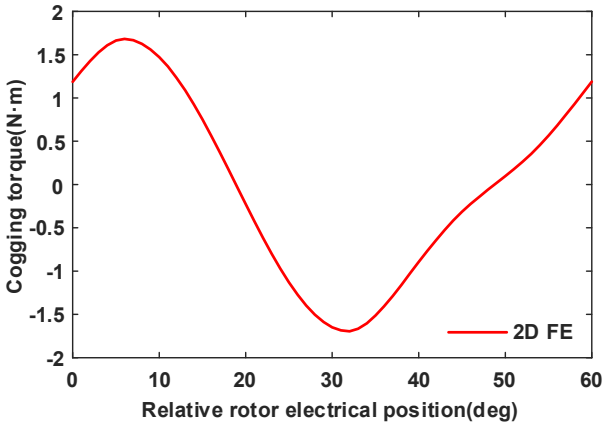

Fig. 7.39 Cogging torque obtained from the 2D FE model.

It can be seen that the amplitude of the cogging torque reaches about 1.6Nm, 1.5 times the rated torque. This large cogging torque prevents the test motor from spinning at low speed. In addition, the cogging torque also acts as a torque disturbance to the dc machine to cause speed variations. However, the 2.2kW dc machine has a good torque-speed characteristic to overcome this cogging torque and can reduce the speed ripple caused by the 150W 24-slot 8-pole SPM machine prototype.

The back-EMFs of different circuit branches (A1, A2, B2, C2) have been measured first to check whether the number of turns per branch are the same and the corresponding two branches of the same phase such as A1 and A2 are in phase with each other. The measured results of back-EMFs of different circuit branches are shown in Fig. 7.40. It should be mentioned that these measured results are obtained by using the Keysight DSOX2024A oscilloscope with the averaging acquisition mode at about 900rpm. This acquisition mode will automatically filter some measurement noise. From Fig. 7.40, it can be seen that the number of turns per branch of the wound machine are exactly the same and the corresponding two branches of the same phase are in phase with each other.

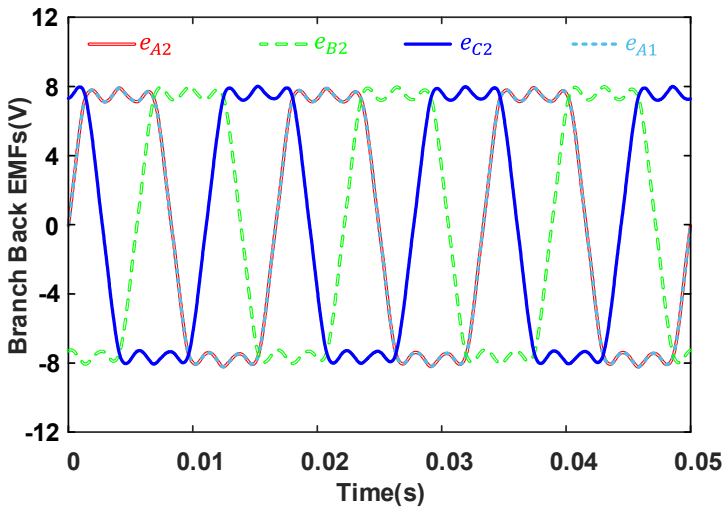

Fig. 7.40 Measured back-EMFs of different circuit branches.

On the other hand, to avoid the negative impact of relatively large speed variations on the back-EMFs measurement, a rotor speed of 900rpm has also been adopted for the simulated and measured back-EMFs of the A1 branch, as shown in Fig. 7.41. A good agreement between the measured and simulated results can be observed. The harmonics of the phase back EMFs as shown in Fig. 7.41 (a) can be easily found in Fig. 7.41 (b) using the FFT technique and then they will be loaded into the developed fault model to predict the healthy and fault currents more accurately.

In addition, to check if the ITSC faults are introduced correctly, for example, if the one-coil short-circuit, half-a-coil short-circuit, single-turn short-circuit faults can be correctly carried out, the relevant back-EMFs have been measured and are shown in Fig. 7.42, Fig. 7.43, and Fig. 7.44, respectively.

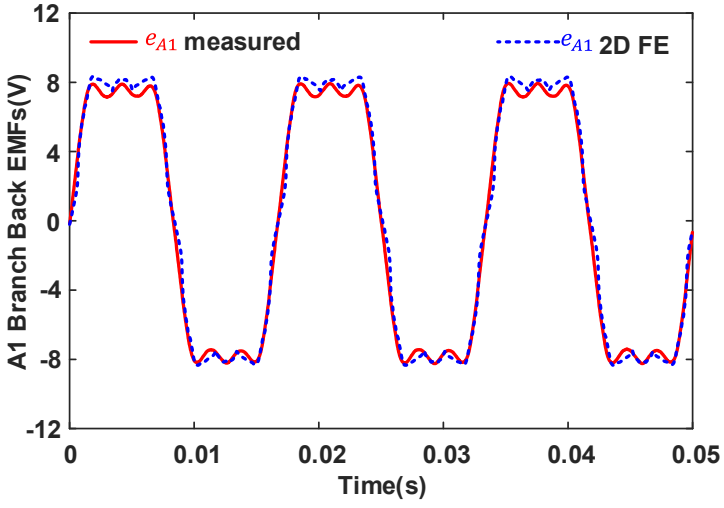

(a) Waveforms

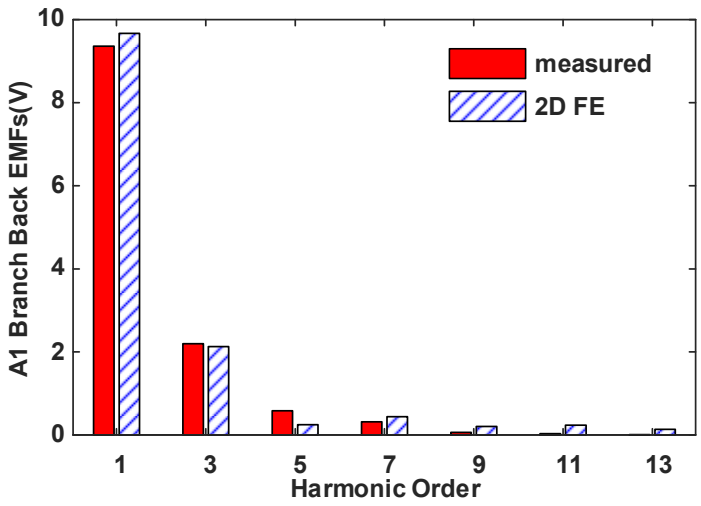

(b) Spectra

Fig. 7.41 Measured and 2D FE predicted back-EMFs of the A1 branch.

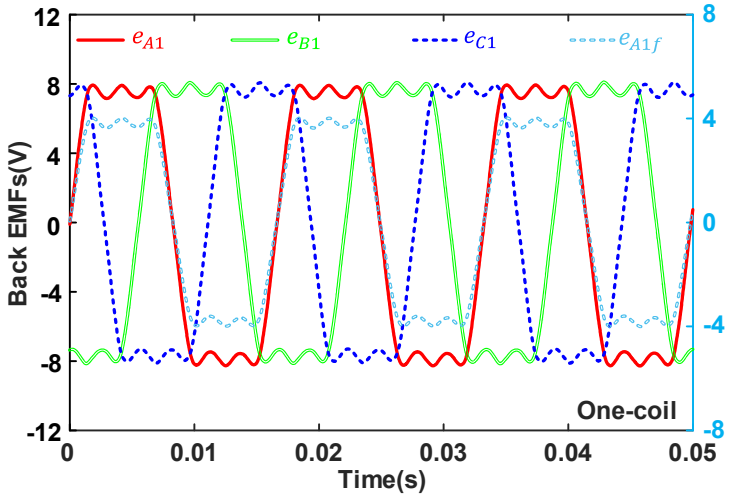

Fig. 7.42 Back-EMFs related to the one-coil short-circuit fault.

It is worth mentioning that the back-EMF is proportional to the number of turns, thus it would be easy to identify some short-circuit or open-circuit faults by back-EMF tests before doing any other loading tests. In addition, it is easy to check the number of turns per coil is 20 before inserting the coils into the slots because the number of turns per coil is not large.

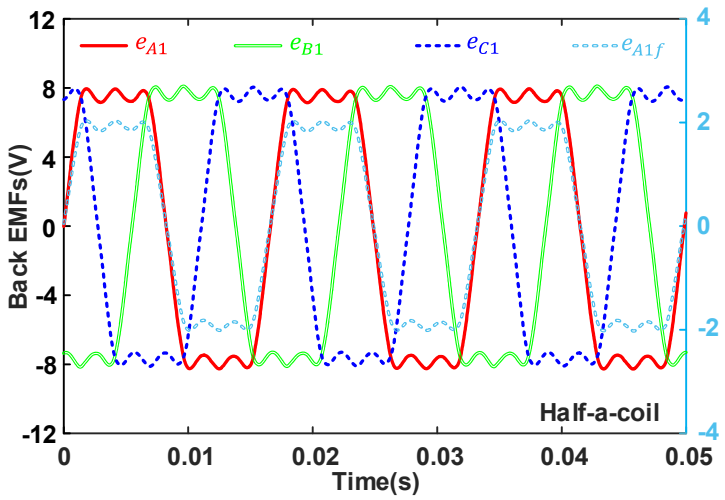

Fig. 7.43 Back-EMFs related to the half-a-coil short-circuit fault.

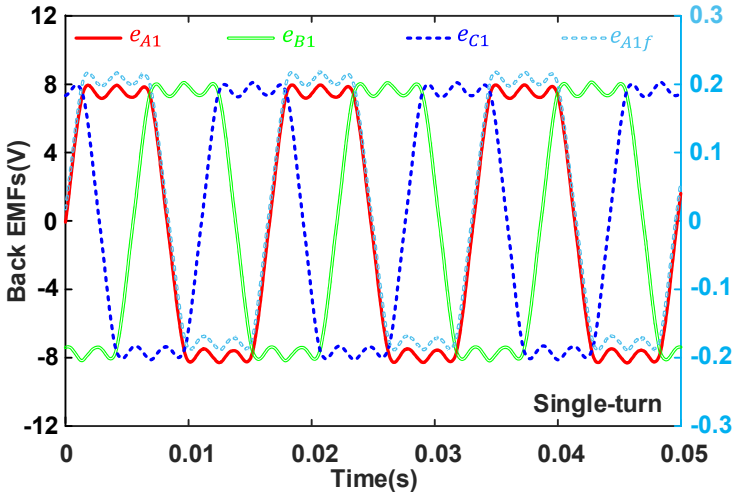

Fig. 7.44 Back-EMFs related to the single-turn short-circuit fault.

7.3.3 Inductances

The analytical method proposed in chapter 4 to calculate the 2D linear FE inductances under the ITSC faults is also applied to this 24-slot 8-pole SPM machine. The trapezoidal slot shown in Fig. 7.34 is also approximated to a rectangular slot with equal height and area to simplify the calculation of the slot-leakage inductances. The results of calculated inductances are shown in Table 7.5. A good agreement between them can be observed. Like the 12-slot 4-pole SPM machine, to consider the influence of the core saturation and long end windings on the inductance values, a nonlinear 3D FE model of this prototype has also been built using JMAG, as shown in Fig. 7.45. The 3D FE nonlinear inductance results are then compared against the measured ones by using the Hioki IM3533-01 LCR Meter, and the corresponding results are

also shown in Table 7.5. It can be seen from Table 7.5 that all the relative errors between the nonlinear 3D FE and measured inductances are generally acceptable.

Table 7.5 2D FE and analytical inductances (μH) of the machine prototype

Method	L_{A1A1}	M_{A1A2}	M_{A1B1}	M_{A1B2}
2D FE (Linear)	331.7	-59.4	19.3	-59.5
2D Analytical	283.5	-63.1	21	-63.1
Difference (%)	14.53	-6.23	-8.81	-6.05
3D FE (Nonlinear)	316.8	-25.8	-14.5	-34.1
Measured	317.5	-27.45	-13.68	-35.3
Difference (%)	-0.22	-6.4	5.65	-3.52

As for the nonlinear 3D FE and measured inductances related to the short-circuited turns, especially those associated with the single turn short-circuit fault, they can be estimated by using the inductances related to coil A11. For example, the self-inductance is proportional to the square of the number of turns in a coil, and the mutual inductance is proportional to the number of turns. As such, all inductances will be known for the three fault scenarios.

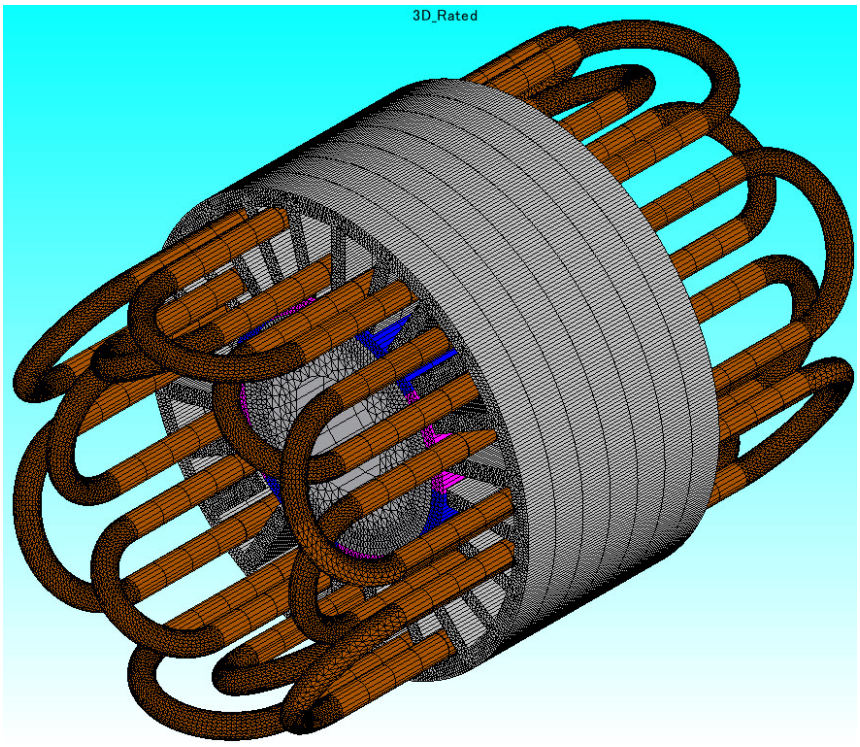

Fig. 7.45 A 3D FE model of the 24-slot 8-pole SPM machine.

7.3.4 Branch and Faulty Currents

To validate the proposed fault model, all the three fault scenarios (single-turn, half-a-coil, and one-coil short-circuit faults) have been carried out under different speeds and loads. It is found that the measured and simulated results generally match well.

As mentioned earlier, it is sufficient to use the Magtrol Model 3411 torque display instead of a position encoder to record the speed information because the 2.2kW dc machine has a good torque-speed characteristic to reduce the speed ripple caused by the 150W 24-slot 8-pole SPM machine prototype. In addition, the Magtrol Model 3411 torque display also have a BNC connector for torque output. Thus, the speed, current and torque waveforms can be displayed on the monitor of the 16-channel Yokogawa DL850 oscilloscope simultaneously. In addition, to record these quantities before and after the faults, the trigger function of the oscilloscope has to be changed. Finally, after all the measured data are saved, the different time delays of speed, torque and currents have to be considered to make all the transients occur at the same time.

7.3.4.1 One-Coil Short-Circuit Fault

The rotor speed over the time interval between 0.45s and 0.55s under the one-coil short-circuit fault is shown in Fig. 7.46. The data over 1s period have been saved and the transient occurs at about 0.5s according to the setting of the trigger function of the oscilloscope. Although the rotor speed recorded by the Magtrol Model 3411 torque display is not as accurate as that recorded by the position encoder, it has been deemed as acceptable to use it as the main input to the Simulink model to validate the proposed fault model. The 3-phase rheostat in Fig. 7.38 is set to be 1.2Ω and it is connected to the 3-phase terminals of this prototype machine to limit the amplitude of the branch and phase currents when the one-coil short-circuit fault is introduced. The measured and predicted branch currents are shown in Fig. 7.47.

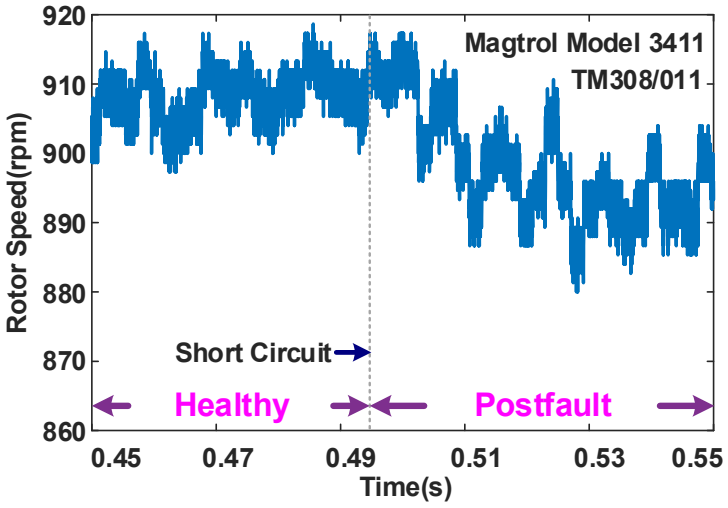

Fig. 7.46 Rotor speed under the one-coil short-circuit fault of the 24-slot 8-pole machine prototype.

Generally, there are good agreements between the measured and simulated branch currents. The relative errors of current amplitudes are less than 10%. It should be mentioned that the predicted branch and phase currents by using the 3D FE nonlinear and measured inductances are very similar. Therefore, only the predicted results using the measured inductances have been provided in Fig. 7.47 and Fig. 7.48. It can be seen from Fig. 7.47 that the branch currents of the faulty phase A are greatly affected, but the branch currents of the remaining healthy phases B and C are slightly changed. However, the changes in the branch currents seem to be more obvious than those in the 3-phase currents as shown in Fig. 7.48. In Fig. 7.48, the amplitudes of the 3-phase currents do not change too much but the amplitude of the faulty phase A clearly become smaller, from 7.8A to 6.6A.

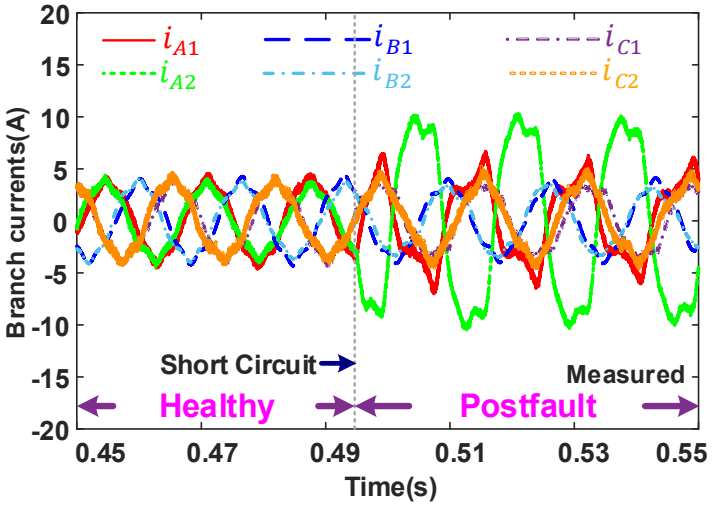

(a) Measured branch currents

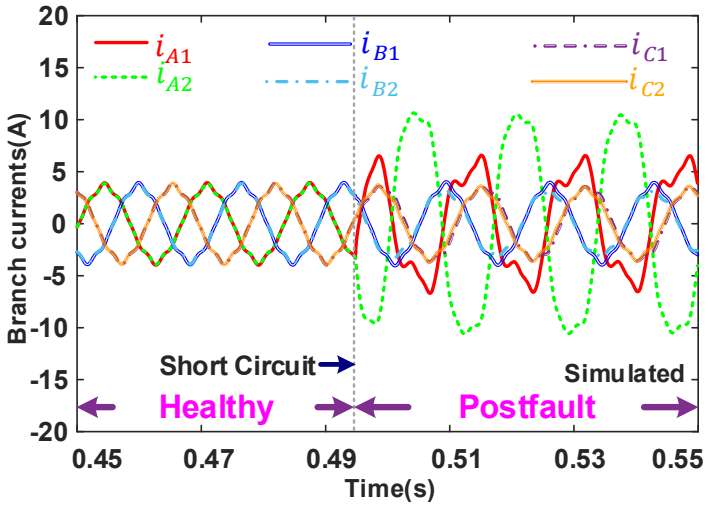

(b) Predicted branch currents

Fig. 7.47 Branch currents of the 24-slot 8-pole machine prototype under the one-coil short-circuit fault.

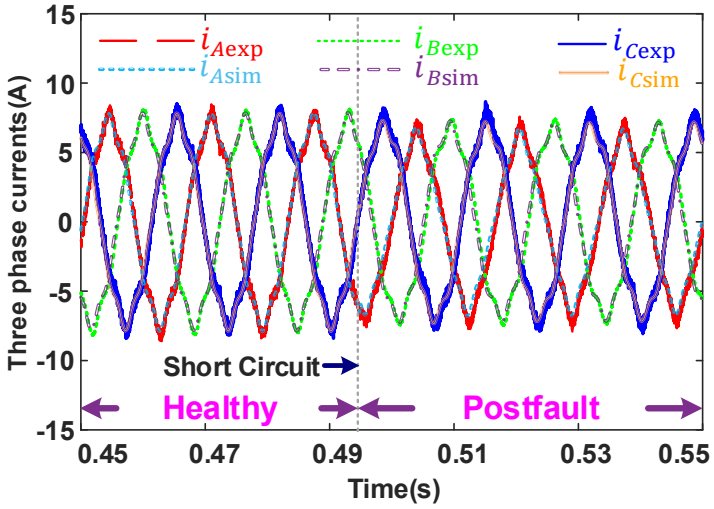

Fig. 7.48 Measured and predicted 3-phase currents of the 24-slot 8-pole machine prototype under the one-coil short-circuit fault.

To compare against the measured i_{A1f}, the predicted fault currents i_{A1f} in the short-circuited coil (using both 3D FE and measured inductances) have also been shown in Fig. 7.49. The relative error of the amplitude of the measured and simulated currents in the short-circuited coil is a little greater, up to 30%. This is mainly because the current probes shown in Fig. 7.38 are very close to each other, and the large currents flowing through them will cause interference to the measurements. This kind of interference can be reduced when the current probes are farther apart, as shown in Fig. 7.50. With less interference between the current probes, the measured currents are much closer to the simulated ones, as shown in Fig. 7.51. The relative

error now is about 10%. However, in Fig. 7.38, there was not much space on the desk to separate the current probes farther apart.

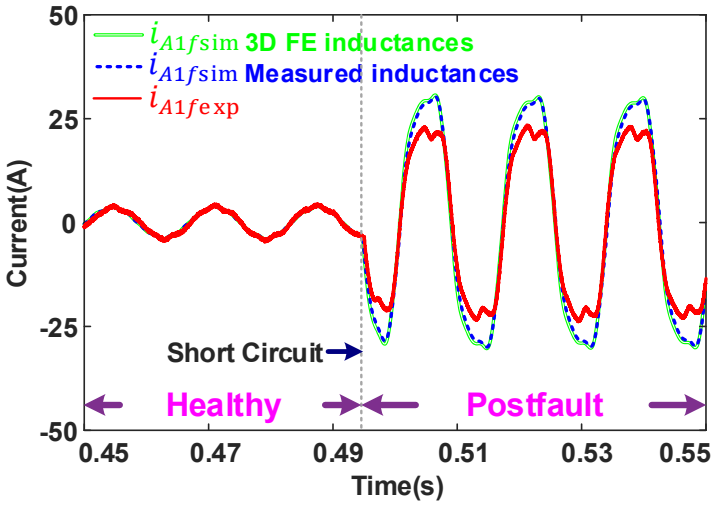

Fig. 7.49 Predicted and measured fault currents (i_{A1f}) of the 24-slot 8-pole machine prototype in the short-circuited coil.

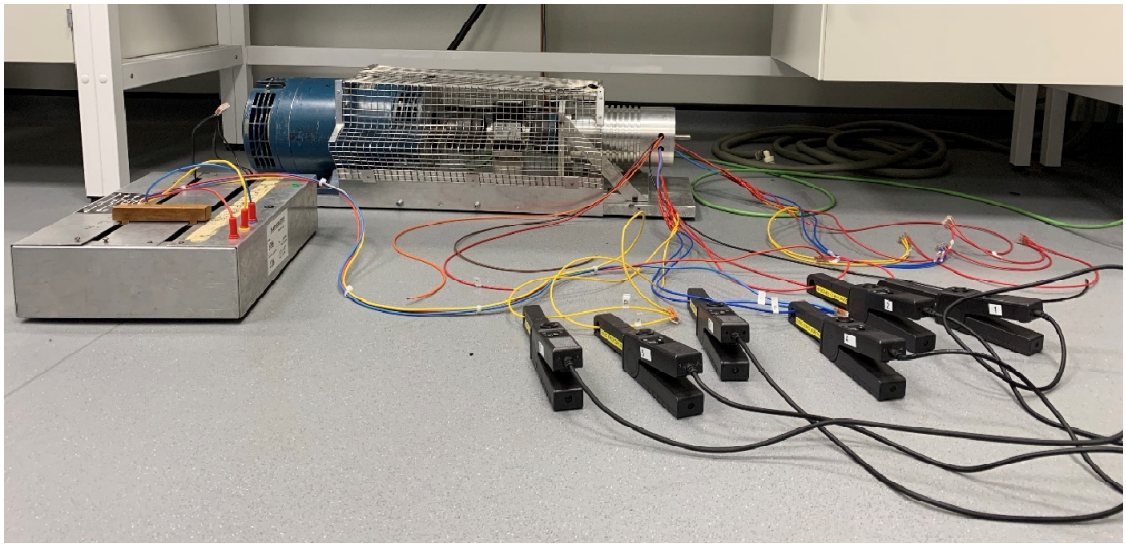

Fig. 7.50 Test rig setup on the ground.

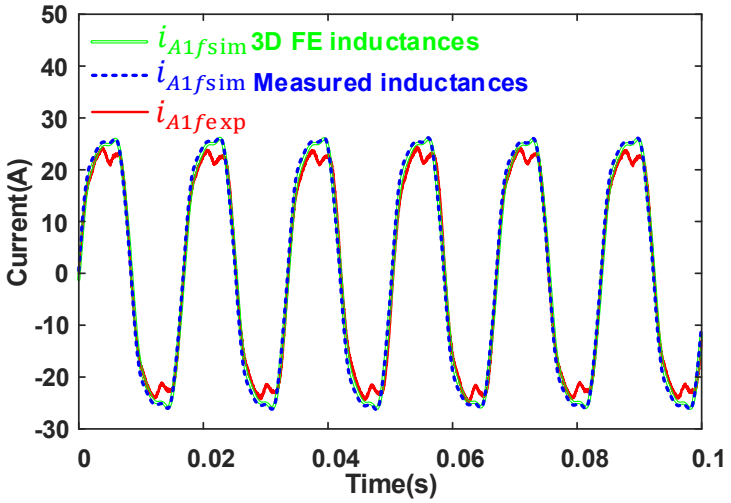

Fig. 7.51 Predicted and measured fault currents (i_{A1f}) under the one-coil short-circuit fault when the test rig is on the ground.

7.3.4.2 Half-a-Coil Short-Circuit Fault

When carrying out the experiments under the half-a-coil short-circuit fault, the 3-phase rheostat with $R_{load} = 1.2\Omega$ is also connected to the 3-phase terminals of this prototype machine to limit the amplitude of the branch and phase currents to keep electrical safety. The speed and current data have also been collected when the average rotating speed of the prototype machine is about 900rpm. At this speed, the branch currents and phase currents have been recorded and shown in Fig. 7.52 and Fig. 7.53, respectively. It should also be mentioned that the predicted branch and phase currents by using the 3D FE nonlinear and measured inductances in the fault model are almost the same. Therefore, only the predicted results using the measured inductances have been provided in Fig. 7.52 and Fig. 7.53.

It can be seen from Fig. 7.52 that the measured and predicted branch currents match well, this is the same for the measured and predicted three phase currents as shown in Fig. 7.53. Compared with the one-coil short-circuit fault, the half-a-coil short-circuit fault causes less significant changes in the branch currents and 3-phase currents, therefore it is more difficult to detect this fault.

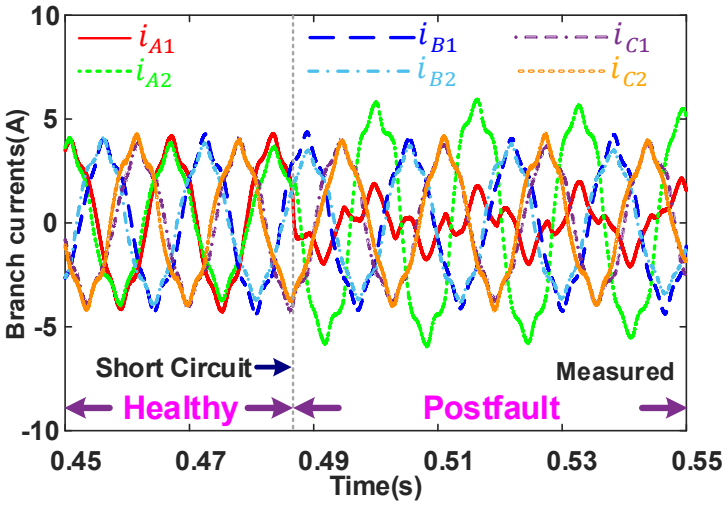

(a) Measured branch currents

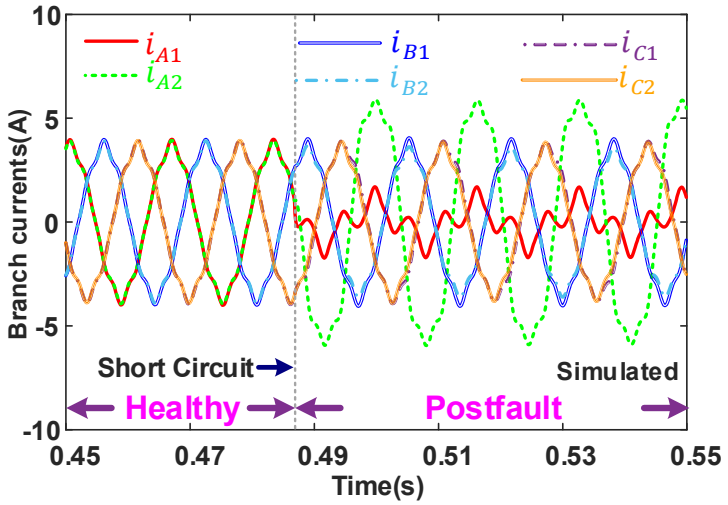

(b) Predicted branch currents

Fig. 7.52 Branch currents of the 24-slot 8-pole machine prototype under the half-a-coil short-circuit fault.

The measured and predicted fault currents i_{A1f} in the short-circuited turns are shown in Fig. 7.54. Again, the predicted i_{A1f} using the 3D FE and measured inductances are both provided in Fig. 7.54. A good agreement between the measured and predicted results can be observed. Although it is difficult to detect this fault, the fault current i_{A1f} in the short-circuited turns is still very high, around 5.6 times the rated current. This means that early detection is still very important to protect the machine windings from burning out.

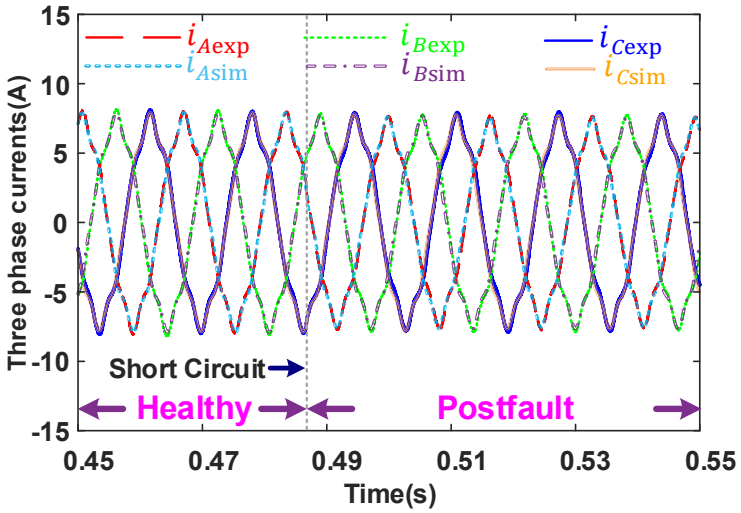

Fig. 7.53 Measured and predicted 3-phase currents of the 24-slot 8-pole machine prototype under the half-a-coil short-circuit fault.

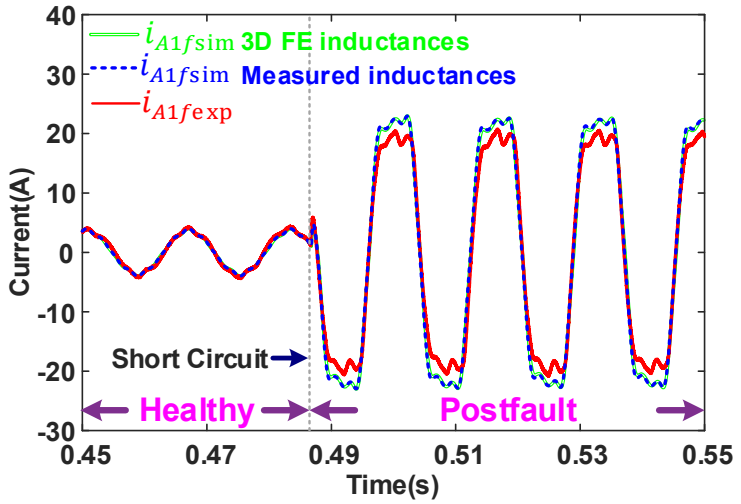

Fig. 7.54 Predicted and measured fault currents (i_{A1f}) of the 24-slot 8-pole machine prototype in the short-circuited turns.

7.3.4.3 Single-turn Short-Circuit Fault

The single-turn short-circuit fault with the 3-phase rheostat having $R_{load} = 1.2\Omega$ has also been carried out when the rotor speed is at about 900rpm. The corresponding branch currents and phase currents are shown in Fig. 7.55 and Fig. 7.56.

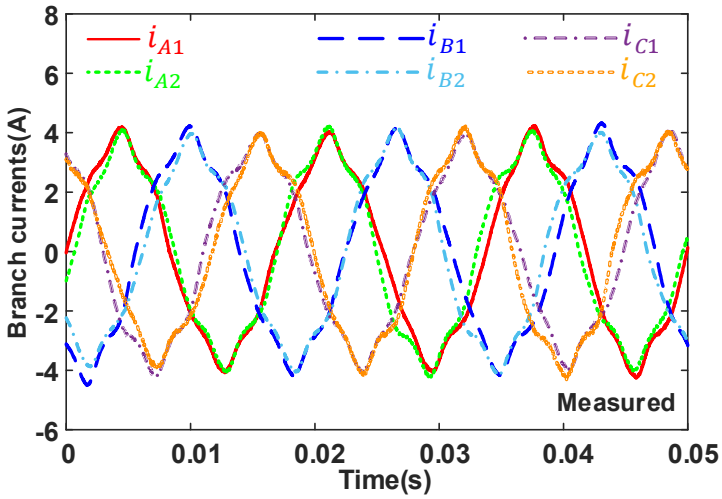

(a) Measured branch currents

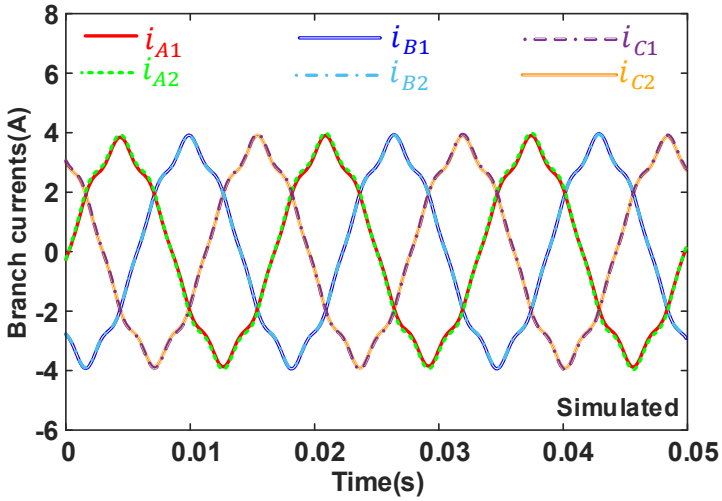

(b) Predicted branch currents

Fig. 7.55 Branch currents of the 24-slot 8-pole machine prototype under the single-turn short-circuit fault.

It can be seen from Fig. 7.55 and Fig. 7.56 that the branch currents and phase currents are hardly changed. It is worth mentioning that there is negligible difference (less than 10%) in the predicted branch and phase currents by using the 3D FE nonlinear and measured inductances in the fault model. To make the plots in Fig. 7.55 clearer, only the simulated results using the measured inductances have been provided. In addition, compared with the one-coil and half-a-coil short-circuit currents, the single-turn short-circuit current shown in Fig. 7.57 is much smaller, from greater than 20A to 8.6A. This is mainly because for this 24-slot 8-pole machine, the single-turn short-circuit current is quite sensitive to the value of R_f. In this case, $R_f = 0.032\Omega \neq 0\Omega$, which is about 6 times the resistance of short-circuited turns ($R_{Af} = 0.005\Omega$), meaning that a full single-turn short-circuit fault will not occur in practice.

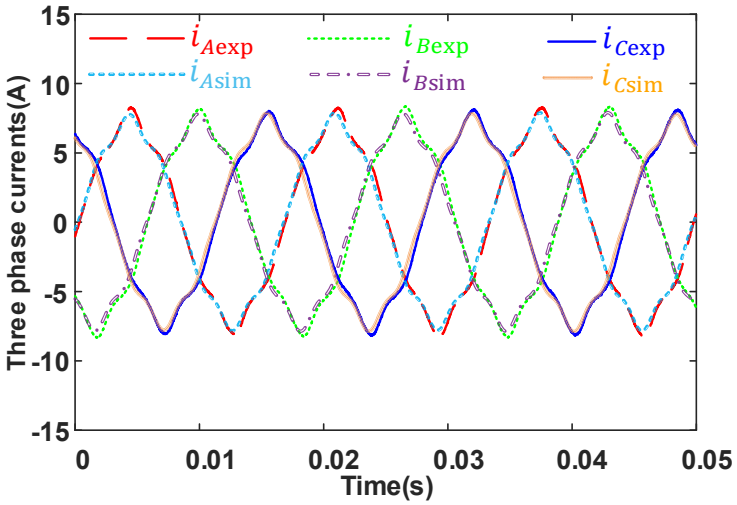

Fig. 7.56 Measured and predicted 3-phase currents of the 24-slot 8-pole machine prototype under the single-turn short-circuit fault.

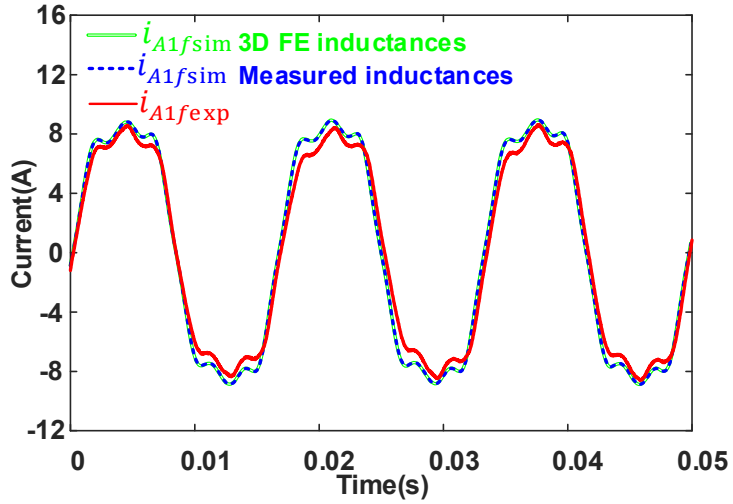

Fig. 7.57 Predicted and measured fault currents (i_{A1f}) of the 24-slot 8-pole machine prototype in the short-circuited single turn.

7.3.4.4 Different Loads and Speeds

To further validate the fault model, more tests at different loads and speeds under the half-a-coil short-circuit fault have also been carried out, and the results are shown in Fig. 7.58. It can be seen that the measured currents (amplitude) in the short-circuited turns A11_fm and faulty phase A with two different resistive loads (no-load and 1.2Ω) and different rotor speeds match well with the simulations. Therefore, together with other results in the previous sections, it can be concluded that the accuracy of the proposed fault model has been fully validated.

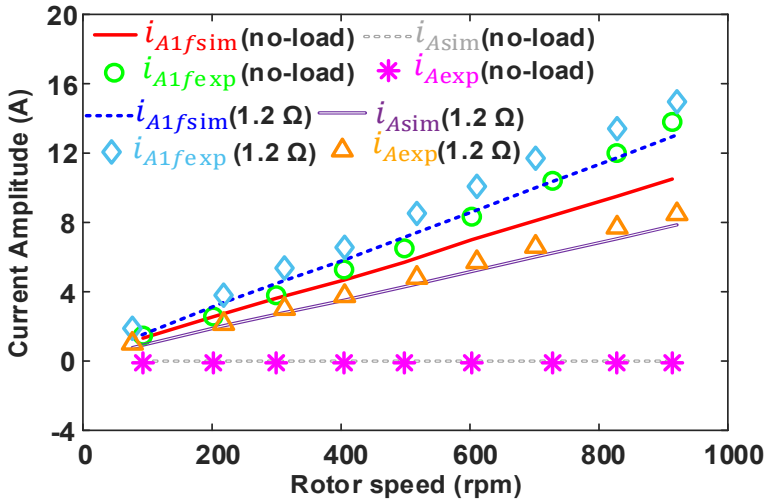

Fig. 7.58 Amplitudes of currents of short-circuited turns and faulty phase of the 24-slot 8-pole machine prototype under different resistive loads and speeds.

7.4 Conclusion

A series of fault experiments on two different machine prototypes, i.e., 12-slot 4-pole SPM machine and 24-slot 8-pole SPM machine have been carried out to validate the proposed fault models for the SPM machines with different series-parallel winding configurations. The generally good agreements between the measured and simulated results fully validate the accuracy of the proposed fault models. The analytical fault model proposed in this thesis can be very useful for developing model-based fault detection and mitigation strategies for large wind power generators. For these machines, the modelling methods like direct FE or magnetic equivalent circuit can be very time-consuming. In addition, it can also be used to evaluate the fault-tolerant capabilities of the SPM machines with different winding configurations.

Chapter 8 General Conclusions

8.1 Introduction

This thesis developed some general and simple analytical models in a concise block matrix form for PM wind generators with series, parallel and series-parallel coil connections under inter-turn short-circuit (ITSC) faults. More attention has been paid to the series-parallel coil connection as it is often used in large offshore wind power generators. The fault model has been divided into two parts, i.e., the part of the healthy machine model uses branch currents as state variables and the faulty part is represented by the current in the external short-circuited path and the inductances between the short-circuited turns and every branch winding. In this way, it is found that the multiphase Clarke transformation can be used to simplify the fault model with FE linear and nonlinear inductances because all branch inductance matrices are circulant matrices. In the process of model simplification, the healthy machine model using branch currents as state variables has been proven to be equivalent to that using 3-phase currents as state variables, which gives more physical insights into the healthy machine models. Direct FE and Simulink simulations have been carried out on the 96-slot 32-pole SPM machine with different series-parallel coil connections to validate the developed fault models and model simplification method. In addition, the developed fault models have also been validated experimentally using two different machine prototypes.

Simulations for large-power SPM wind generators such as the 500kW and 3MW SPM machines under ITSC fault have also been carried out based on the developed fault model and model simplification method. Two studies, i.e., the scaling effect and the influence of fault location, have been carried out and it is found that the large-power SPM wind generators are vulnerable to ITSC faults when relatively small number of turns are short-circuited and the single-turn short-circuit fault at the top of stator slots (slot opening) is the worst-case scenario.

It is worth mentioning that the proposed fault model and the model simplification method are generic and may be applied to other types of non-PM machines and also their multiphase counterparts with practical winding configurations. When the calculation of inductances in the fault model is difficult, FEM can be used to consider the influence of shapes and locations of the copper conductors on the corresponding inductance values. Thus, the proposed fault model and model simplification method combine both advantages of the analytical and FE models to generate simulation results with an adequate accuracy in a shorter time.

Based on the developed fault model and model simplification method, the electromagnetic performance of SPM machines such as the phase currents, branch currents, current in the short-circuited turns, torque can be predicted when the SPM machines are supplied by voltage sources. Generally, the 3-phase currents and the developed torque will change slightly under ITSC faults, although the branch currents and current in the short-circuited turns may change significantly. High-fidelity fault models can also be built for all SPM machines used in offshore wind power applications to consider all the fault scenarios under different operation conditions and to form database that can be used to find fault indicators during fault diagnostics. Such database would be useful and will be difficult to be obtained only based on measurements. This is because although ITSC faults can be studied by experiments, all the fault scenarios especially some extreme fault scenarios such as full single-turn short-circuit fault cannot be considered. Therefore, the analytical fault model together with the model simplification method can be very useful for developing model-based fault detection methods for large wind power generators if current signals are used to extract the fault indicators. It may also be useful for developing fault mitigation strategies and comparing the fault-tolerant capability of different machines such as the SPM machines with non-modular and modular overlapping windings as investigated in chapter 6. For these large-power machines, other modelling methods like FE or magnetic equivalent circuit can be very time-consuming and performing fault tests may be difficult.

8.2 Future Work

In this thesis, the magnetic equivalent circuit (MEC) modelling for the SPM machines under faulty conditions has not been considered. However, MEC models have been proven to be an interesting alternative to classical circuit models that are often used for the controller design. MEC models can include the effect of magnetic saturation and all space harmonics on machine behaviours, although they are more complex than the corresponding circuit models, they are much simpler than the corresponding FE models. Therefore, they are trade-offs between model complexity and accuracy. If real-time and accurate predictions of machine behaviours under healthy and faulty conditions are desired, they could be promising alternatives. In addition, they will be very useful especially when the commercial FE software is not available due to the consideration of cost reduction, as this has been studied in [31], [32], [90], [92], [94]–[97]. Luckily, the mathematical knowledge and skills required by the magnetic equivalent circuit models of electrical machines are almost the same as what had been used in this thesis, i.e., solving combined systems consisting of large numbers of differential equations and algebraic equations. Therefore, the main focus can then be put on the understanding of the basic concepts.

In addition, fault detection and mitigation have not been studied in this thesis. These two aspects are really very important in practice. When the developed fault model is interfaced with PWM converters to simulate the machine performance under real operating conditions, the effectiveness of some fault detection and mitigation strategies proposed by researchers can be validated easily. In the next stage, how to propose effective fault detection methods will be studied. It should be mentioned that multi-parameter monitoring and sensor fusion would become the only practical solutions for condition monitoring and fault diagnosis of electrical machines [8], thus relying on one method to detect and discriminate faults in most applications would not be sufficient.

Modelling of other internal faults, like the phase-to-ground short-circuit fault, ITSC faults considering the multi-turn, multi-strand coil structure, and ITSC faults between coils or phases, would be easier based on the research work carried out in this thesis. Therefore, they can be studied further and would be part of our future works.

References

[1] V. Yaramasu, B. Wu, P. C. Sen, S. Kouro, and M. Narimani, "High-power wind energy conversion systems: State-of-the-art and emerging technologies," *Proc. IEEE*, vol. 103, no. 5, pp. 740–788, May 2015.

[2] Global Wind Energy Council (GWEC), "Global Wind Report 2022," 2022. [Online]. Available: https://gwec.net/gwecs-latest-reports/

[3] B. Lu, Y. Li, X. Wu, and Z. Yang, "A review of recent advances in wind turbine condition monitoring and fault diagnosis," in *2009 IEEE Power Electronics and Machines in Wind Applications*, Jun. 2009, pp. 1–7.

[4] M. R. Wilkinson, F. Spinato, and P. J. Tavner, "Condition Monitoring of Generators & Other Subassemblies in Wind Turbine Drive Trains," in *2007 IEEE International Symposium on Diagnostics for Electric Machines, Power Electronics and Drives*, Sep. 2007, pp. 388–392.

[5] "The Inside of a Wind Turbine," *Energy.gov*. https://www.energy.gov/eere/wind/inside-wind-turbine-0 (accessed Feb. 03, 2019).

[6] GE Renewable Energy, "Haliade 150-6MW Offshore Wind Turbine." https://www.ge.com/renewableenergy/wind-energy/offshore-wind/offshore-turbine-haliade-150-6mw (accessed Apr. 27, 2023).

[7] F. Blaabjerg, M. Liserre, and K. Ma, "Power electronics converters for wind turbine systems," *IEEE Trans. Ind. Appl.*, vol. 48, no. 2, pp. 708–719, Mar. 2012.

[8] N. M. A. Freire and J. Marques Cardoso Antonio, "Fault detection and condition monitoring of PMSGs in offshore wind turbines," *Machines*, vol. 9, no. 11, p. 260, Oct. 2021.

[9] H. Badihi, Y. Zhang, B. Jiang, P. Pillay, and S. Rakheja, "A comprehensive review on signal-based and model-based condition monitoring of wind turbines: fault diagnosis and lifetime prognosis," *Proc. IEEE*, vol. 110, no. 6, pp. 754–806, Jun. 2022.

[10] V. Yaramasu and B. Wu, *Model Predictive Control of Wind Energy Conversion Systems*. in IEEE Press Series on Power Engineering. Wiley, 2017.

[11] S. Nandi, H. A. Toliyat, and X. Li, "Condition monitoring and fault diagnosis of electrical motors--a review," *IEEE Trans. Energy Convers.*, vol. 20, no. 4, pp. 719–729, Dec. 2005.

[12] A. Bellini, F. Filippetti, C. Tassoni, and G. Capolino, "Advances in diagnostic techniques for induction machines," *IEEE Trans. Ind. Electron.*, vol. 55, no. 12, pp. 4109–4126, Dec. 2008.

[13] A. Gandhi, T. Corrigan, and L. Parsa, "Recent advances in modeling and online detection of stator interturn faults in electrical motors," *IEEE Trans. Ind. Electron.*, vol. 58, no. 5, pp. 1564–1575, May 2011.

[14] R. M. Tallam, S. B. Lee, G. C. Stone, G. B. Kliman, J. Yoo, T. G. Habetler, and R. G. Harley, "A survey of methods for detection of stator-related faults in induction machines," *IEEE Trans. Ind. Appl.*, vol. 43, no. 4, pp. 920–933, Jul. 2007.

[15] A. Siddique, G. S. Yadava, and B. Singh, "A review of stator fault monitoring techniques of induction motors," *IEEE Trans. Energy Convers.*, vol. 20, no. 1, pp. 106–114, Mar. 2005.

[16] S. Grubic, J. M. Aller, B. Lu, and T. G. Habetler, "A survey on testing and monitoring methods for stator insulation systems of low-voltage induction machines focusing on turn insulation problems," *IEEE Trans. Ind. Electron.*, vol. 55, no. 12, pp. 4127–4136, Dec. 2008.

[17] M. Riera-Guasp, J. A. Antonino-Daviu, and G. Capolino, “Advances in electrical machine, power electronic, and drive condition monitoring and fault detection: state of the art,” *IEEE Trans. Ind. Electron.*, vol. 62, no. 3, pp. 1746–1759, Mar. 2015.
[18] S. B. Lee, G. C. Stone, J. Antonino-Daviu, K. N. Gyftakis, E. G. Strangas, P. Maussion and C. A. Platero, “Condition monitoring of industrial electric machines: state of the art and future challenges,” *IEEE Ind. Electron. Mag.*, vol. 14, no. 4, pp. 158–167, Dec. 2020.
[19] S. Choi, M. S. Haque, M. T. B. Tarek, V. Mulpuri, Y. Duan, S. Das, V. Garg, D. M. Ionel, M. A. Masrur, B. Mirafzal, and H. A. Toliyat, “Fault diagnosis techniques for permanent magnet ac machine and drives-a review of current state of the art,” *IEEE Trans. Transport. Electrific.*, vol. 4, no. 2, pp. 444–463, Jun. 2018.
[20] T. Orlowska-Kowalska, M. Wolkiewicz, P. Pietrzak, M. Skowron, P. Ewert, G. Tarchala, M. Krzysztofiak, and C. T. Kowalski, “Fault diagnosis and fault-tolerant control of PMSM drives-state of the art and future challenges,” *IEEE Access*, vol. 10, pp. 59979–60024, Jun. 2022.
[21] A. H. Bonnett and C. Yung, “Increased efficiency versus increased reliability,” *IEEE Ind. Appl. Mag.*, vol. 14, no. 1, pp. 29–36, Jan. 2008.
[22] ABB Report, “Motors don’t just fail...do they? A guide to preventing failure.” [Online]. Available: https://new.abb.com/docs/librariesprovider53/about-downloads/motors_ebook.pdf?sfvrsn=4
[23] B. Li, Y. Tipsuwan, and J. C. Hung, “Neural-network-based motor rolling bearing fault diagnosis,” *IEEE Trans. Ind. Electron.*, vol. 47, no. 5, pp. 1060–1069, Oct. 2000.
[24] F. Immovilli, A. Bellini, R. Rubini, and C. Tassoni, “Diagnosis of bearing faults in induction machines by vibration or current signals: a critical comparison,” *IEEE Trans. Ind. Appl.*, vol. 46, no. 4, pp. 1350–1359, Jul. 2010.
[25] X. Gong and W. Qiao, “Bearing fault diagnosis for direct-drive wind turbines via current-demodulated signals,” *IEEE Trans. Ind. Electron.*, vol. 60, no. 8, pp. 3419–3428, Aug. 2013.
[26] M. D. Prieto, G. Cirrincione, A. G. Espinosa, J. A. Ortega, and H. Henao, “Bearing fault detection by a novel condition-monitoring scheme based on statistical-time features and neural networks,” *IEEE Trans. Ind. Electron.*, vol. 60, no. 8, pp. 3398–3407, Aug. 2013.
[27] L. Frosini, C. Harlişca, and L. Szabó, “Induction machine bearing fault detection by means of statistical processing of the stray flux measurement,”*IEEE Trans. Ind. Electron.*, vol. 62, no. 3, pp. 1846–1854, Mar. 2015.
[28] F. Cheng, C. Wei, L. Qu, and W. Qiao, “Fault diagnosis of wind turbine gearbox using DFIG stator current analysis,” in *2016 IEEE Energy Conversion Congress and Exposition (ECCE)*, Sep. 2016, pp. 1–7.
[29] G. M. Joksimovic and J. Penman, “The detection of inter-turn short circuits in the stator windings of operating motors,” *IEEE Trans. Ind. Electron.*, vol. 47, no. 5, pp. 1078–1084, Oct. 2000.
[30] R. M. Tallam, T. G. Habetler, and R. G. Harley, “Transient model for induction machines with stator winding turn faults,”*IEEE Trans. Ind. Appl.*, vol. 38, no. 3, pp. 632–637, May 2002.
[31] C. Gerada, K. J. Bradley, M. Sumner, P. Wheeler, S. Picker, J. Clare, C. Whitley, and G. Towers, “The results do mesh,” *IEEE Ind. Appl. Mag.*, vol. 13, no. 2, pp. 62–72, Mar. 2007.
[32] P. Naderi, “Modified magnetic-equivalent-circuit approach for various faults studying in saturable double-cage-induction machines,” *IET Electr. Power Appl.*, vol. 11, no. 7, pp. 1224–1234, Apr. 2017.

[33] J. Penman, H. G. Sedding, B. A. Lloyd, and W. T. Fink, “Detection and location of interturn short circuits in the stator windings of operating motors,” *IEEE Trans. Energy Convers.*, vol. 9, no. 4, pp. 652–658, Dec. 1994.
[34] A. J. M. Cardoso, S. M. A. Cruz, and D. S. B. Fonseca, “Inter-turn stator winding fault diagnosis in three-phase induction motors, by Park’s vector approach,” *IEEE Trans. Energy Convers.*, vol. 14, no. 3, pp. 595–598, Sep. 1999.
[35] G. B. Kliman, R. A. Koegl, J. Stein, R. D. Endicott, and M. W. Madden, “Noninvasive detection of broken rotor bars in operating induction motors,”*IEEE Trans. Energy Convers.*, vol. 3, no. 4, pp. 873–879, Dec. 1988.
[36] A. Bellini, F. Filippetti, G. Franceschini, C. Tassoni, and G. B. Kliman, “Quantitative evaluation of induction motor broken bars by means of electrical signature analysis,” *IEEE Trans. Ind. Appl.*, vol. 37, no. 5, pp. 1248–1255, Sep. 2001.
[37] M. E. H. Benbouzid and G. B. Kliman, “What stator current processing-based technique to use for induction motor rotor faults diagnosis?,” *IEEE Trans. Energy Convers.*, vol. 18, no. 2, pp. 238–244, Jun. 2003.
[38] H. Henao, H. Razik, and G.- Capolino, “Analytical approach of the stator current frequency harmonics computation for detection of induction machine rotor faults,” *IEEE Trans. Ind. Appl.*, vol. 41, no. 3, pp. 801–807, May 2005.
[39] J. A. Antonino-Daviu, M. Riera-Guasp, J. R. Folch, and M. P. M. Palomares, “Validation of a new method for the diagnosis of rotor bar failures via wavelet transform in industrial induction machines,” *IEEE Trans. Ind. Appl.*, vol. 42, no. 4, pp. 990–996, Jul. 2006.
[40] S. Nandi, R. M. Bharadwaj, and H. A. Toliyat, “Performance analysis of a three-phase induction motor under mixed eccentricity condition,” *IEEE Trans. Energy Convers.*, vol. 17, no. 3, pp. 392–399, Sep. 2002.
[41] G. M. Joksimovic, “Dynamic simulation of cage induction machine with air gap eccentricity,” *IEE Proc., Electr. Power Appl.*, vol. 152, no. 4, pp. 803–811, Jul. 2005.
[42] X. Li, Q. Wu, and S. Nandi, “Performance Analysis of a Three-Phase Induction Machine With Inclined Static Eccentricity,” *IEEE Trans. Ind. Appl.*, vol. 43, no. 2, pp. 531–541, Mar. 2007.
[43] A. Ceban, R. Pusca, and R. Romary, “Study of rotor faults in induction motors using external magnetic field analysis,” *IEEE Trans. Ind. Electron.*, vol. 59, no. 5, pp. 2082–2093, May 2012.
[44] P. Naderi and A. Shiri, “Rotor/stator inter-turn short circuit fault detection for saturable wound-rotor induction machine by modified magnetic equivalent circuit approach,” *IEEE Trans. Magn.*, vol. 53, no. 7, pp. 1–13, Jul. 2017.
[45] J. Faiz, S. M. M. Moosavi, M. B. Abadi, and S. M. A. Cruz, “Magnetic equivalent circuit modelling of doubly-fed induction generator with assessment of rotor inter-turn short-circuit fault indices,” *IET Renew. Power Gener.*, vol. 10, no. 9, pp. 1431–1440, Oct. 2016.
[46] Y. Gritli, L. Zarri, C. Rossi, F. Filippetti, G. Capolino, and D. Casadei, “Advanced diagnosis of electrical faults in wound-rotor induction machines,” *IEEE Trans. Ind. Electron.*, vol. 60, no. 9, pp. 4012–4024, Sep. 2013.
[47] Y. Gritli, C. Rossi, D. Casadei, F. Filippetti, and G. Capolino, “A diagnostic space vector-based index for rotor electrical fault detection in wound-rotor induction machines under speed transient,” *IEEE Trans. Ind. Electron.*, vol. 64, no. 5, pp. 3892–3902, May 2017.
[48] B. M. Ebrahimi and J. Faiz, “Feature extraction for short-circuit fault detection in permanent-magnet synchronous motors using stator-current monitoring,” *IEEE Trans. Power Electron.*, vol. 25, no. 10, pp. 2673–2682, Oct. 2010.

[49] L. Romeral, J. C. Urresty, J. R. Ruiz, and A. G. Espinosa, “Modeling of surface-mounted permanent magnet synchronous motors with stator winding interturn faults,” *IEEE Trans. Ind. Electron.*, vol. 58, no. 5, pp. 1576–1585, May 2011.
[50] K. Kim, J. Park, J. Hur, and B. Kim, “Comparison of the fault characteristics of IPM-type and SPM-type BLDC motors under inter-turn fault conditions using winding function theory,” *IEEE Trans. Ind. Appl.*, vol. 50, no. 2, pp. 986–994, Mar. 2014.
[51] P. Naderi, “Magnetic-equivalent-circuit approach for inter-turn and demagnetisation faults analysis in surface mounted permanent-magnet synchronous machines using pole specific search-coil technique,” *IET Electr. Power Appl.*, vol. 12, no. 7, pp. 916–928, Aug. 2018.
[52] M. A. Awadallah, M. M. Morcos, S. Gopalakrishnan, and T. W. Nehl, “Detection of stator short circuits in VSI-fed brushless DC motors using wavelet transform,” *IEEE Trans. Energy Convers.*, vol. 21, no. 1, pp. 1–8, Mar. 2006.
[53] B. Vaseghi, B. Nahid-Mobarakeh, N. Takorabet, and F. Meibody-Tabar, “Modeling of non-salient PM synchronous machines under stator winding inter-turn fault condition: dynamic model - FEM model,” in *2007 IEEE Vehicle Power and Propulsion Conference*, Sep. 2007, pp. 635–640.
[54] J. Farooq, S. Srairi, A. Djerdir, and A. Miraoui, “Use of permeance network method in the demagnetization phenomenon modeling in a permanent magnet motor,” *IEEE Trans. Magn.*, vol. 42, no. 4, pp. 1295–1298, Apr. 2006.
[55] B. M. Ebrahimi and J. Faiz, “Demagnetization fault diagnosis in surface mounted permanent magnet synchronous motors,” *IEEE Trans. Magn.*, vol. 49, no. 3, pp. 1185–1192, Mar. 2013.
[56] B. M. Ebrahimi and J. Faiz, “Demagnetization fault diagnosis in surface mounted permanent magnet synchronous motors,” *IEEE Transactions on Magnetics*, vol. 49, no. 3, pp. 1185–1192, Mar. 2013.
[57] J. R. R. Ruiz, A. G. Espinosa, L. Romeral, and J. Cusidó, “Demagnetization diagnosis in permanent magnet synchronous motors under non-stationary speed conditions,” *Electr. Power Syst. Res.*, vol. 80, no. 10, pp. 1277–1285, May 2010.
[58] J. Hong, S. Park, D. Hyun, T. Kang, S. B. Lee, C. Kral, and A. Haumer, “Detection and classification of rotor demagnetization and eccentricity faults for PM synchronous motors,” *IEEE Trans. Ind. Appl.*, vol. 48, no. 3, pp. 923–932, May 2012.
[59] H. Chen, R. Qu, J. Li, and D. Li, “Demagnetization performance of a 7 MW interior permanent magnet wind generator with fractional-slot concentrated windings,” *IEEE Trans. Magn.*, vol. 51, no. 11, pp. 1–4, Nov. 2015.
[60] J. Faiz and H. Nejadi-Koti, “Demagnetization fault indexes in permanent magnet synchronous motors—An overview,” *IEEE Trans. Magn.*, vol. 52, no. 4, pp. 1–11, Apr. 2016.
[61] G. Choi, Y. Zhang, and T. M. Jahns, “Experimental verification of rotor demagnetization in a fractional-slot concentrated-winding PM synchronous machine under drive fault conditions,” *IEEE Trans. Ind. Appl.*, vol. 53, no. 4, pp. 3467–3475, Jul. 2017.
[62] J. Faiz and I. Tabatabaei, “Extension of winding function theory for nonuniform air gap in electric machinery,” *IEEE Trans. Magn.,* vol. 38, no. 6, pp. 3654–3657, Nov. 2002.
[63] U. Kim and D. K. Lieu, “Magnetic field calculation in permanent magnet motors with rotor eccentricity: without slotting effect,” *IEEE Trans. Magn.*, vol. 34, no. 4, pp. 2243–2252, Jul. 1998.
[64] U. Kim and D. K. Lieu, “Magnetic field calculation in permanent magnet motors with rotor eccentricity: with slotting effect considered,” *IEEE Trans. Magn.*, vol. 34, no. 4, pp. 2253–2266, Jul. 1998.

[65] D. G. Dorrell, M. Hsieh, and Y. Guo, “Unbalanced magnet pull in large brushless rare-earth permanent magnet motors with rotor eccentricity,” *IEEE Trans. Magn.*, vol. 45, no. 10, pp. 4586–4589, Oct. 2009.
[66] B. M. Ebrahimi, J. Faiz, and M. J. Roshtkhari, “Static-, dynamic-, and mixed-eccentricity fault diagnoses in permanent-magnet synchronous motors,”*IEEE Trans. Ind. Electron.*, vol. 56, no. 11, pp. 4727–4739, Nov. 2009.
[67] Y. Li, Q. Lu, Z. Q. Zhu, L. J. Wu, G. J. Li, and D. Wu, “Analytical synthesis of air-gap field distribution in permanent magnet machines with rotor eccentricity by superposition method,” *IEEE Trans. Magn.*, vol. 51, no. 11, pp. 1–4, Nov. 2015.
[68] K. Alewine and W. Chen, “A review of electrical winding failures in wind turbine generators,” *IEEE Elect. Insul. Mag.*, vol. 28, no. 4, pp. 8–13, Jul. 2012.
[69] A. H. Bonnett and G. C. Soukup, “Cause and analysis of stator and rotor failures in three-phase squirrel-cage induction motors,” *IEEE Trans. Ind. Appl.*, vol. 28, no. 4, pp. 921–937, Jul. 1992.
[70] A. H. Bonnett, “Root cause methodology for induction motors: a step-by-step guide to examining failure,” *IEEE Ind. Appl. Mag.*, vol. 18, no. 6, pp. 50–62, Nov. 2012.
[71] B. A. Welchko, T. A. Lipo, T. M. Jahns, and S. E. Schulz, “Fault tolerant three-phase AC motor drive topologies: a comparison of features, cost, and limitations,” *IEEE Trans. Power Electron.*, vol. 19, no. 4, pp. 1108–1116, Jul. 2004.
[72] B. A. Welchko, T. M. Jahns, and S. Hiti, “IPM synchronous machine drive response to a single-phase open circuit fault,” *IEEE Trans. Power Electron.*, vol. 17, no. 5, pp. 764–771, Sep. 2002.
[73] B. A. Welchko, T. M. Jahns, W. L. Soong, and J. M. Nagashima, “IPM synchronous machine drive response to symmetrical and asymmetrical short circuit faults,” *IEEE Trans. Energy Convers.*, vol. 18, no. 2, pp. 291–298, Jun. 2003.
[74] G. Choi and T. M. Jahns, “PM synchronous machine drive response to asymmetrical short-circuit faults,” *IEEE Trans. Ind. Appl.*, vol. 52, no. 3, pp. 2176–2185, May 2016.
[75] G. Choi and T. M. Jahns, “Investigation of key factors influencing the response of permanent magnet synchronous machines to three-phase symmetrical short-circuit faults,” *IEEE Trans. Energy Convers.*, vol. 31, no. 4, pp. 1488–1497, Dec. 2016.
[76] Electrical Apparatus Service Association, Inc, *Failures in Three-Phase Stator Windings*, 1985. [Online]. Available: https://easa.com/resources/failures-in-three-phase-stator-windings
[77] S. B. Lee, J. Yang, K. Younsi, and R. M. Bharadwaj, “An online groundwall and phase-to-phase insulation quality assessment technique for AC-machine stator windings,” *IEEE Trans. Ind. Appl.*, vol. 42, no. 4, pp. 946–957, Jul. 2006.
[78] G. C. Stone, I. Culbert, E. A. Boulter, and H. Dhirani, *Electrical Insulation for Rotating Machines: Design, Evaluation, Aging, Testing, and Repair*, 2nd ed. in IEEE Press Series on Power Engineering. Wiley, 2014.
[79] M. Mostafaei and J. Faiz, “An overview of various faults detection methods in synchronous generators,” *IET Electr. Power Appl.*, vol. 15, no. 4, pp. 391–404, Apr. 2021.
[80] H. Kim, T. Kong, S. B. Lee, T. Kang, N. Oh, Y. Kim, S. Park, C. Lim, G.C. Stone, “Experience with stator insulation testing and turn/phase insulation failures in the power generation industry,” *IEEE Trans. Ind. Appl.*, vol. 54, no. 3, pp. 2225–2236, May 2018.
[81] T. Griffith, A. H. Bonnett, B. Lockley, C. Yung, and C. Nyberg, “Revisions to IEEE standard 1068,” *IEEE Ind. Appl. Mag.*, vol. 17, no. 1, pp. 26–35, Nov. 2010.
[82] G. Klempner and I. Kerszenbaum, *Handbook of large turbo-generator operation and maintenance*, 3rd ed., vol. 91. John Wiley & Sons, 2018.

[83] H. A. Toliyat and T. A. Lipo, “Transient analysis of cage induction machines under stator, rotor bar and end ring faults,” *IEEE Trans. Energy Convers.*, vol. 10, no. 2, pp. 241–247, Jun. 1995.
[84] P. P. Reichmeider, C. A. Gross, D. Querrey, D. Novosel, and S. Salon, “Internal faults in synchronous machines. I. the machine model,” *IEEE Trans. Energy Convers.*, vol. 15, no. 4, pp. 376–379, Dec. 2000.
[85] A. Gandhi, T. Corrigan, and L. Parsa, “Recent advances in modeling and online detection of stator interturn faults in electrical motors,” *IEEE Trans. Ind. Electron.*, vol. 58, no. 5, pp. 1564–1575, May 2011.
[86] X. Tu, L. Dessaint, M. E. Kahel, and A. O. Barry, “A new model of synchronous machine internal faults based on winding distribution,” *IEEE Trans. Ind. Electron.*, vol. 53, no. 6, pp. 1818–1828, Dec. 2006.
[87] X. Tu, L. Dessaint, N. Fallati, and B. D. Kelper, “Modeling and real-time simulation of internal faults in synchronous generators with parallel-connected windings,” *IEEE Trans. Ind. Electron.*, vol. 54, no. 3, pp. 1400–1409, Jun. 2007.
[88] B. Gu, J. Choi, and I. Jung, “Development and analysis of interturn short fault model of PMSMs with series and parallel winding connections,” *IEEE Trans. Power Electron.*, vol. 29, no. 4, pp. 2016–2026, Apr. 2014.
[89] H. Qian, H. Guo, and X. Ding, “Modeling and analysis of interturn short fault in permanent magnet synchronous motors with multistrands windings,” *IEEE Trans. Power Electron.*, vol. 31, no. 3, pp. 2496–2509, Mar. 2016.
[90] G. Forstner, A. Kugi, and W. Kemmetmüller, “A magnetic equivalent circuit based modeling framework for electric motors applied to a PMSM with winding short circuit,” *IEEE Trans. Power Electron.*, vol. 35, no. 11, pp. 12285–12295, Nov. 2020.
[91] C. Gao, K. Lv, J. Si, H. Feng, and Y. Hu, “Research on interturn short-circuit fault indicators for direct-drive permanent magnet synchronous motor,” *IEEE J. Emerg. Sel. Top. Power Electron.*, vol. 10, no. 2, pp. 1902–1914, Apr. 2022.
[92] H. W. Derbas, J. M. Williams, A. C. Koenig, and S. D. Pekarek, “A comparison of nodal- and mesh-based magnetic equivalent circuit models,” *IEEE Trans. Energy Convers.*, vol. 24, no. 2, pp. 388–396, Jun. 2009.
[93] B. Vaseghi, N. Takorabet, and F. Meibody-Tabar, “Fault analysis and parameter identification of permanent-magnet motors by the finite-element method,”*IEEE Trans. Magn.*, vol. 45, no. 9, pp. 3290–3295, Sep. 2009.
[94] V. Ostovic, *Dynamics of saturated electric machines*. Springer Science & Business Media, 1989.
[95] M. Amrhein and P. T. Krein, “3-D magnetic equivalent circuit framework for modeling electromechanical devices,” *IEEE Trans. Energy Convers.*, vol. 24, no. 2, pp. 397–405, Jun. 2009.
[96] J. Faiz, H. Nejadi-Koti, and A. H. Exiri, “Inductance-based inter-turn fault detection in permanent magnet synchronous machine using magnetic equivalent circuit model,” *Electr. Power Compon. Syst.*, vol. 45, no. 9, pp. 1016–1030, Jun. 2017.
[97] J. Faiz and M. Ghasemi-Bijan, “Estimation of induction machine inductances using three-dimensional magnetic equivalent circuit,” *IET Electr. Power Appl.*, vol. 9, no. 2, pp. 117–127, Feb. 2015.
[98] O. A. Mohammed, Z. Liu, S. Liu, and N. Y. Abed, “Internal short circuit fault diagnosis for PM machines using FE-based phase variable model and wavelets analysis,” *IEEE Trans. Magn.*, vol. 43, no. 4, pp. 1729–1732, Apr. 2007.
[99] B. Vaseghi, B. Nahid-mobarakh, N. Takorabet, and F. Meibody-Tabar, “Inductance identification and study of PM motor with winding turn short circuit fault,” *IEEE Trans. Magn.*, vol. 47, no. 5, pp. 978–981, May 2011.

[100] T. W. Nehl, F. A. Fouad, and N. A. Demerdash, "Determination of saturated values of rotating machinery incremental and apparent inductances by an energy perturbation method," *IEEE Trans. Power App. Syst.**, vol. PAS-101, no. 12, pp. 4441–4451, Dec. 1982.
[101] N. A. Demerdash and T. W. Nehl, "Electric machinery parameters and torques by current and energy perturbations from field computations. I. Theory and formulation," *IEEE Trans. Energy Convers.*, vol. 14, no. 4, pp. 1507–1513, Dec. 1999.
[102] N. A. O. Demerdash and J. F. Bangura, "Characterization of induction motors in adjustable-speed drives using a time-stepping coupled finite-element state-space method including experimental validation," *IEEE Trans. Ind. Appl.*, vol. 35, no. 4, pp. 790–802, Jul/Aug. 1999.
[103] J. F. Bangura and N. A. Demerdash, "Simulation of inverter-fed induction motor drives with pulse-width modulation by a time-stepping coupled finite element-flux linkage-based state space model," *IEEE Trans. Energy Convers.*, vol. 14, no. 3, pp. 518–525, Sep. 1999.
[104] N. A. Demerdash and T. W. Nehl, "Electric machinery parameters and torques by current and energy perturbations from field computations. II. Applications and results," *IEEE Trans. Energy Convers.*, vol. 14, no. 4, pp. 1514–1522, Dec. 1999.
[105] D. C. White and H. H. Woodson, *Electromechanical Energy Conversion*. in The M.I.T. core curriculum program in electrical engineering. Wiley, 1959.
[106] P. Krause, O. Wasynczuk, and S. D. Sudhoff, *Analysis of Electric Machinery and Drive Systems*, 2nd ed. in IEEE Press Series on Power Engineering. Wiley, 2002.
[107] S. Umans, A. Fitzgerald, and C. Kingsley, *Electric Machinery*, 7th ed. McGraw-Hill Higher Education, 2013.
[108] G. R. Slemon and A. Straughen, *Electric Machines*. Addison-Wesley Pub. Co., 1980.
[109] X. Wang, Y. Sun, B. Ouyang, W. Wang, Z. Zhu, and D. Howe, "Transient behaviour of salient-pole synchronous machines with internal stator winding faults," *IEE Proc., Electr. Power Appl.*, vol. 149, no. 2, pp. 143–151, Mar. 2002.
[110] M. Dai, A. Keyhani, and T. Sebastian, "Fault analysis of a PM brushless DC motor using finite element method," *IEEE Trans. Energy Convers.*, vol. 20, no. 1, pp. 1–6, Mar. 2005.
[111] L. S. Maraaba, Z. M. Al-Hamouz, and M. A. Abido, "Mathematical modeling, simulation and experimental testing of interior-mount LSPMSM under stator inter-turn fault," *IEEE Trans. Energy Convers.*, vol. 34, no. 3, pp. 1213–1222, Sep. 2019.
[112] D. S. B. Fonseca, C. M. C. Santos, and A. J. M. Cardoso, "Stator faults modeling and diagnostics of line-start permanent magnet synchronous motors," *IEEE Trans. Ind. Appl.*, vol. 56, no. 3, pp. 2590–2599, Mar. 2020.
[113] Z. Sun, J. Wang, D. Howe, and G. Jewell, "Analytical prediction of the short-circuit current in fault-tolerant permanent-magnet machines," *IEEE Trans. Ind. Electron.*, vol. 55, no. 12, pp. 4210–4217, Dec. 2008.
[114] C. Gao, K. Lv, J. Si, P. Su, and C. Gan, "A physical faulty model based on coil sub-element for direct-drive permanent magnet synchronous motor," *IEEE Access*, vol. 7, pp. 151307–151319, Oct. 2019.
[115] F. Wu, P. Zheng, and T. M. Jahns, "Analytical modeling of interturn short circuit for multiphase fault-tolerant PM machines with fractional slot concentrated windings," *IEEE Trans. Ind. Appl.*, vol. 53, no. 3, pp. 1994–2006, Jun. 2017.
[116] J. A. Haylock, B. C. Mecrow, A. G. Jack, and D. J. Atkinson, "Operation of fault tolerant machines with winding failures," *IEEE Trans. Energy Convers*, vol. 14, no. 4, pp. 1490–1495, Dec. 1999.

[117] A. J. Mitcham, G. Antonopoulos, and J. J. A. Cullen, “Implications of shorted turn faults in bar wound PM machines,” *IEE Proc., Electr. Power Appl.*, vol. 151, no. 6, pp. 651–657, Nov. 2004.
[118] P. Arumugam, T. Hamiti, and C. Gerada, “Modeling of different winding configurations for fault-tolerant permanent magnet machines to restrain interturn short-circuit current,” *IEEE Trans. Energy Convers.*, vol. 27, no. 2, pp. 351–361, Jun. 2012.
[119] N. Bianchi, M. Dai Pré, L. Alberti, and E. Fornasiero, *Theory and Design of Fractional-Slot PM Machines*. in IEEE IAS tutorial corse notes. Cleup, 2007.
[120] A. M. EL-Refaie, “Fractional-slot concentrated-windings synchronous permanent magnet machines: Opportunities and challenges,” *IEEE Trans. Ind. Electron.*, vol. 57, no. 1, pp. 107–121, Jan. 2010.
[121] A. M. El-Refaie, “Fault-tolerant permanent magnet machines: a review,” *IET Electr. Power Appl.*, vol. 5, no. 1, pp. 59–74, Jan. 2011.
[122] W. Zhao, L. Xu, and G. Liu, “Overview of permanent-magnet fault-tolerant machines: Topology and design,” *CES Trans. Electr. Mach. Syst.*, vol. 2, no. 1, pp. 51–64, Mar. 2018.
[123] B. Prieto, M. Martínez-Iturralde, L. Fontán, and I. Elosegui, “Fault-tolerant permanent magnet synchronous machine – phase, pole and slot number selection criterion based on inductance calculation,” *IET Electr. Power Appl.*, vol. 9, no. 2, pp. 138–149, Feb. 2015.
[124] W. Lee and G. Choi, “A comprehensive review of fault-tolerant ac machine drive topologies: Inverter, control, and electric machine,” in *2021 IEEE 13th international symposium on diagnostics for electrical machines, Power Electronics and Drives (SDEMPED)*, IEEE, 2021, pp. 269–275.
[125] T. Kim, H. Lee, and S. Kwak, “The internal fault analysis of brushless dc motors based on the winding function theory,” *IEEE Trans. Magn.*, vol. 45, no. 5, pp. 2090–2096, May 2009.
[126] M. Ojaghi and V. Bahari, “Rotor damping effects in dynamic modeling of three-phase synchronous machines under the stator interturn faults—winding function approach,” *IEEE Trans. Ind. Appl.*, vol. 53, no. 3, pp. 3020–3028, May 2017.
[127] Z. T. Mei, G. J. Li, Z. Q. Zhu, R. Clark, A. Thomas, and Z. Azar, “Scaling effect on inter-turn short-circuit of PM machines for wind power application,” in *2021 IEEE International Electric Machines and Drives Conference (IEMDC)*, 2021, pp. 1–8.
[128] B. Ge, S. Xiao, Z. Liu, D. Tao, and X. Sun, “Improved model of synchronous generators internal faults based on circuit-coupled FEM,” *IEEE Trans. Energy Convers.*, vol. 32, no. 3, pp. 876–884, Sep. 2017.
[129] M. Zafarani, E. Bostanci, Y. Qi, T. Goktas, and B. Akin, “Interturn short-circuit faults in permanent magnet synchronous machines: An extended review and comprehensive analysis,” *IEEE J. Emerg. Sel. Top. Power Electron.*, vol. 6, no. 4, pp. 2173–2191, Dec. 2018.
[130] A. Berzoy, A. A. S. Mohamed, and O. Mohammed, “Impact of inter-turn short-circuit location on induction machines parameters through FE computations,” *IEEE Trans. Magn.*, vol. 53, no. 6, pp. 1–4, Jun. 2017.
[131] B. Sen, J. Wang, and P. Lazari, “A high-fidelity computationally efficient transient model of interior permanent-magnet machine with stator turn fault,” *IEEE Trans. Ind. Electron.*, vol. 63, no. 2, pp. 773–783, Feb. 2016.
[132] A. Sarikhani and O. A. Mohammed, “Inter-turn fault modeling of a variable speed PM wind generator using physics-based approach,” in *2011 IEEE International Electric Machines Drives Conference (IEMDC)*, May 2011, pp. 636–641.
[133] J. K. Tangudu, T. M. Jahns, A. M. El-Refaie, and Z. Q. Zhu, “Segregation of torque components in fractional-slot concentrated-winding interior PM machines using frozen

permeability," in *2009 IEEE Energy Conversion Congress and Exposition*, Sep. 2009, pp. 3814–3821. doi: 10.1109/ECCE.2009.5316039.
[134] J. R. Hendershot and T. J. E. Miller, *Design of Brushless Permanent-Magnet Machines*. Motor Design Books, 2010.
[135] T. A. Lipo, *Analysis of Synchronous Machines*, 2nd ed. CRC Press, 2012.
[136] M. B. K. Bouzid, G. Champenois, A. Maalaoui, and S. Tnani, "Efficient simplified physical faulty model of a permanent magnet synchronous generator dedicated to stator fault diagnosis Part I: faulty model conception," *IEEE Trans. Ind. Appl.*, vol. 53, no. 3, pp. 2752–2761, May 2017.
[137] P. J. Davis, *Circulant Matrices*. in Monographs and textbooks in pure and applied mathematics. Wiley, 1979.
[138] J. Huang, M. Kang, J. Yang, H. Jiang, and D. Liu, "Multiphase machine theory and its applications," in *2008 International Conference on Electrical Machines and Systems*, 2008, pp. 1–7.
[139] A. G. Yepes, J. A. Riveros, J. Doval-Gandoy, F. Barrero, Ó. Lopez, B. Bogado, M. Jones, and E. Levi, "Parameter identification of multiphase induction machines with distributed windings—Part 1: Sinusoidal excitation methods," *IEEE Trans. Energy Convers.*, vol. 27, no. 4, Art. no. 4, Dec. 2012.
[140] Z. T. Mei, G. J. Li, Z. Q. Zhu, R. Clark, A. Thomas, and Z. Azar, "Modelling and Analysis of Inter-Turn Short-Circuit Fault of PM Machines with Parallel-Connected Coils," *IEEE Trans. Energy Convers.*, pp. 1–11, 2023.
[141] Z. T. Mei, G. J. Li, Z. Q. Zhu, R. Clark, A. Thomas, and Z. Azar, "Scaling effect on inter-turn short-circuit fault of PM machines for wind power application," *IEEE Trans. Ind. Appl.*, vol. 59, no. 1, pp. 789–800, Feb. 2023.
[142] D. K. Kana Padinharu,G. J. Li, Z. Q. Zhu, M. P. Foster, D. A. Stone, A. Griffo, R. Clark, A. Thomas, "Scaling effect on electromagnetic performance of surface-mounted permanent-magnet Vernier machine," *IEEE Trans. Magn.*, vol. 56, no. 5, pp. 1–15, May 2020.
[143] J. Faiz, H. Nejadi-Koti, and Z. Valipour, "Comprehensive review on inter-turn fault indexes in permanent magnet motors," *IET Electr. Power Appl.*, vol. 11, no. 1, pp. 142–156, Jan. 2017.
[144] J. Zhang, W. Zhan, and M. Ehsani, "Diagnosis and fault-tolerant control of permanent magnet synchronous motors with interturn short-circuit fault," *IEEE Trans. Control Syst. Technol.*, pp. 1–8, 2023.
[145] U. Shipurkar, H. Polinder, and J. A. Ferreira, "Modularity in wind türbine generator systems — Opportunities and challenges," in *2016 18th European Conference on Power Electronics and Applications (EPE'16 ECCE Europe)*, 2016, pp. 1–10.
[146] S. Bomben, G. Mottershead, I. Kerszenbaum, and G. Klempner, *Handbook of Large Hydro Generators: Operation and Maintenance*. John Wiley & Sons, 2021.
[147] Z. Q. Zhu, "A simple method for measuring cogging torque in permanent magnet machines," in *2009 IEEE Power Energy Society General Meeting*, 2009, pp. 1–4.